

STUDIES OF JET FLOW IN ENCLOSURES

STUDIES OF JET FLOW IN ENCLOSURES

By

DAVID ANDREW JOHNSON, M. Eng.

A Thesis

Submitted to the School of Graduate Studies

in Partial Fulfilment of the Requirements

for the Degree

Doctor of Philosophy

McMaster University

© Copyright by David Andrew Johnson, June 1994

DOCTOR OF PHILOSOPHY (1994)
(Mechanical Engineering)

McMASTER UNIVERSITY
Hamilton, Ontario

TITLE: Studies of Jet Flow in Enclosures

AUTHOR: David Andrew Johnson, B. Eng. (McMaster University)
M. Eng. (McMaster University)

ADVISOR: Professor P.E. Wood

NUMBER OF PAGES: xvii, 231

Abstract

The flow of jets in confining enclosures has significant application in many engineering processes. In particular, two jet flows have been studied; the impingement of axisymmetric jets in a confined space and a turbulent inlet wall jet in a confining enclosure.

The impingement of axisymmetric jets in a cavity has been examined using flow visualization, laser Doppler anemometry, and numerical simulations. When the flow field was examined under various geometrical and fluid parameters several flow regions were found, depending on the geometrical and fluid parameters. Initially, a steady flow field existed for all arrangements for $Re_d < \sim 90$ but subsequent increments in the fluid velocity caused an oscillating flow field to emerge. The onset of the oscillations and the upper limit of finite oscillations were found to be a function of the nozzle diameter to chamber dimension ratio. Although steady numerical simulations predicted the steady flow field well, steady simulations of the oscillating flow field over-predicted the peak axial velocities. The oscillating flow field is considered to be a class of self-sustaining oscillations where instabilities in the jet shear layer are amplified because of feed back from pressure disturbances in the impingement region.

The turbulent wall jet in a cavity has been studied using flow visualization, laser Doppler anemometry (LDA), particle streak velocimetry (PSV) and numerical simulations. Instantaneous PSV measurements agreed well with time averaged LDA

measurements. Two dimensional simulations using an algebraic stress turbulence model (ASM) were in better agreement with the experimental data than two and three dimensional simulations using a $k - \epsilon$ turbulence model in the wall jet region. A wall jet growth rate was found to be 54% higher than a wall jet in stagnant surroundings due to the enclosure boundaries.

Acknowledgements

I would like to thank my supervisor Dr. P.E. Wood and Dr. A.N. Hrymak for their support of my studies while an employee at McMaster and Dr. P.E. Wood for his continued support and guidance of my research. I would also like to thank the Gates Rubber Company and the URIF program for previous support and the Natural Sciences and Engineering Research Council of Canada for their financial support of my studies. The assistance of technicians Bill Warriner, Justyna Derkach, and Paul Gatt and summer students Shawn Taylor and Martin Lehman is gratefully acknowledged and the superb editorial scrutiny of my father aided my thesis preparation immensely although any errors, technical or grammatical are all mine.

I am also thankful for the support and encouragement of my wife Donna and children Rachel, Hannah, and William during this work.

Table of Contents

1.0 Introduction	1
2.0 Literature Survey	3
2.1 Introduction	3
2.2 Opposed Jet Flows Modelling Reaction Injection Molding	14
2.3 Opposed Jet Flows Modelling Side Dump Combustors	21
2.4 Unconfined Opposed Jet Flows	29
2.5 Impinging Jet Flows	34
2.6 Oscillations	36
2.7 Summary	42
3.0 Experimental Techniques	43
3.1 Flow Visualization	43
3.1.1 Dye visualizations	43
3.1.2 Particle streak flow visualization	43
3.1.3 Laser Induced Fluorescence (LIF)	48
3.2 Laser Doppler Anemometry (LDA)	49
3.2.1 System Description	51
3.3 Particle Image Velocimetry (PIV)	52
3.4 Experimental Conditions	57
3.4.1 Experimental Details - Flow Visualization	60
3.4.2 Experimental Details - Laser Doppler Anemometry	64
3.4.3 Optical Correction	65
4.0 Numerical Technique	69
4.1 Grid	69
4.2 Boundary Conditions	70
5.0 Results	73
5.1 Pre Oscillatory Behaviour	73
5.1.1 Flow Visualization $Re_d < \sim 90$	73
5.1.2 Laser Doppler Anemometry $Re_d < \sim 90$	76
5.2 W Velocity Measurements	87
5.3 Flow Development	99
5.4 Oscillations	103
5.4.1 Introduction	103

5.4.2 Visualization of Oscillations	104
5.4.3 Quantitative Oscillation Determination	106
5.5 Post Regular Oscillatory Behaviour	122
5.6 Commercial Nozzles with adjustable screw and needle assembly	126
5.6.1 Flow Visualization	126
5.6.2 LDA studies	128
5.6.3 Effect of Mix Head Diameter D	138
5.6.4 Effect of Head Distance H	138
5.6.5 Effect of Needle Position N	139
5.6.6 Developing Jet Condition	139
5.6.7 Variation of Fluid Parameters	144
5.6.7.1 Unequal Flow Rates	145
5.6.7.2 Unequal Viscosities	147
5.6.8 Geometrical Modifications	148
5.6.8.1 Restricted Equal Flow Rate Cases - Flow Visualization	149
5.6.8.2 Restricted Equal Flow Rate Cases - LDA Study ...	152
5.6.8.3 Restricted Unequal Flow Rate Cases	153
5.6.9 Summary - Commercial Nozzles	156
 6 Conclusions - Impinging Jets	 157
 7.0 Recirculating Flow in a Cavity	 159
7.1 Introduction	159
7.1.1 Recirculating Flow	160
7.1.2 Turbulent Wall Jets	164
7.1.3 Present Study	167
7.1.4 Optical Image Velocimetry	168
7.2 Experimental Work	170
7.2.1 Apparatus	170
7.2.2 Flow Visualization	172
7.2.3 Laser Doppler Anemometry	173
7.2.4 Particle Streak Velocimetry	174
7.2.4.1 Obtaining Images	174
7.2.4.2 Imaging	176
7.2.4.3 Processing Images	177
7.3 Numerical Simulation	179
7.3.1 Solution Procedure	179

7.4 Results and Discussion	182
7.4.1 Flow Visualization	182
7.4.2 Wall Jet	187
7.4.3 Entire Cavity	191
7.5 Conclusions and Recommendations	218
8.0 Conclusions and Recommendations	220
References	223
Appendix A	A.1
Appendix B	B.1

Nomenclature

D	Main chamber diameter (m)	4
d	Nozzle diameter (m)	4
L_n	Nozzle length (m)	4
L_c	Main chamber length (m)	4
H	Head length (m)	4
H^*	H/D	4
D^*	D/d	4
H^*	H/L	5
L	Main chamber side length (m)	5
L^*	L/d	5
Q	volumetric flow (m^3/s)	6
Re_d	Reynolds number defined using nozzle conditions and diameter	6
U_{avg}	average fluid velocity leaving the nozzle (m/s)	6
i	index of coordinate direction ($i=1,2,3$)	7
x	coordinate in i direction	7
u	instantaneous velocity (m/s)	7
p	instantaneous pressure (Pa)	7
j	index of coordinate direction ($j=1,2,3$)	7
U_i	mean velocity in i direction (m/s)	7
u_i'	fluctuating velocity in i direction (m/s)	7
l_i	length scale (m)	9
k	turbulent kinetic energy (m^2/s^2)	9
G_k	generation term of k (kg/ms^2)	10
P_{ij}	stress production rate (m^2/s^3)	12
f	frequency of oscillation (Hz)	15
St	Strouhal number (fd/U)	15
x_j	axial distance from the nozzle (m)	20
c	speed of sound (m/s)	24
d_h	hydraulic diameter (m)	26
Re_{dh}	Reynolds number based on d_h	26
L_r	half distance between the nozzles (free jet) (m)	30
T	period of oscillation (s)	30
l	transverse height of nozzle (m)	30
Re_l	Reynolds number based on l	30
P_s	static pressure outside jets (Pa)	31
g_p	particle acceleration (m/s^2)	44
d_p	particle diameter (m)	44

f_d	frequency obtained at the detector (Hz)	50
F	focal length of lens (m)	50
L_b	beam separation distance (m)	50
l_2, l_1	particle displacements (m)	53
t_2, t_1	time (s)	53
N_I	image density parameter	55
C	mean particles per unit volume (m^{-3})	55
d_I	diameter of interrogation spot (m)	55
M	Lens Magnification	55
b	slot height (m)	164
U_E	free stream velocity (m/s)	164
U_j	average jet velocity (m/s)	164
U_m	maximum velocity (m/s)	164
$y_{1/2}$	distance from wall to location of $U_m/2$ (m)	164

Greek Symbols

θ	Nozzle incidence angle ($^{\circ}$)	4
ϕ	Nozzle separation angle ($^{\circ}$)	4
μ	absolute viscosity (kg/ms)	6
ν	kinematic viscosity (m^2/s)	6
ρ	density (kg/m^3)	6
ε	dissipation rate of turbulence energy (m^2/s^3)	9
μ_t	turbulent viscosity (kg/ms)	11
Φ_{ij}	source/sink due to pressure/strain correlation (m^2/s^3)	12
ε_{ij}	viscous dissipation tensor (m^2/s^3)	12
θ_m	momentum thickness (m)	38
ρ_p	particle density (kg/m^3)	44
λ	wavelength of the laser light (m)	50
α	angle between the laser beams ($^{\circ}$)	50
Δz_0	distance from the object plane (m)	55
η	index of refraction for material	65
$\theta_{1,2}$	angle between normal and incident beam ($^{\circ}$)	65

List of Tables

Table 2.1 Constants used in k- ϵ turbulence model	11
Table 2.2 Additional constants for MRS turbulence model	12
Table 2.3 Results of Sandell <i>et al.</i> (1985)	15
Table 2.4 Results of Nosseir and Behar (1986)	23
Table 3.1 PIV methods and reported velocities	54
Table 3.2 Experimental Models	58
Table 3.3 Flow Visualization : Equal Flow Rates	61
Table 3.4 Unequal Flow Cases : 1	61
Table 3.5 Unequal Flow Cases : 2	62
Table 3.6 Unequal Viscosity Cases : 1	62
Table 3.7 Unequal Viscosity Cases : 2	62
Table 3.8 Restricted Flow Cases : 1	63
Table 3.9 Restricted Flow Unequal Flow Cases : 1	64
Table 3.10 LDA Studies	66
Table 3.11 LDA Studies Models 1 and 2	67
Table 3.12 Developing Jet LDA conditions	67
Table 3.13 Unequal Flow Cases LDA conditions	68
Table 3.14 Restricted Flow Cases LDA conditions	68
Table 4.1 Numerical Simulations	72
Table 5.1.1 Vortex Location $Re_d = 75$	77
Table 5.1.2 Peak W^* values $Re_d = 75$	81
Table 5.1.3 Outlet W^* $Re_d = 75$	82
Table 5.2.1 W^* peak values Model 3 $d = 2$ mm	91
Table 5.2.2 W^* peak values Model 3 $d = 3$ mm	93
Table 5.2.3 W^* peak values Model 3 $d = 4$ mm	95
Table 5.4.1 Oscillation Limits $L^* = 10$ Model 3	109
Table 5.4.2 Oscillation Limits $L^* = 6.67$ Model 3	111
Table 5.4.3 Oscillation Limits $L^* = 5$ Model 3	115
Table 5.4.4 Oscillation Limits $D^* = 10.67$ Model 4	117
Table 7.1 Numerical Simulations	182
Table 7.2 Continuity Analysis LDA Data $Re_b = 1675$	203
Table 7.3 Continuity Analysis LDA Data $Re_b = 1117$	207

List of Figures

Figure 2.1 Cylindrical Model Geometry	4
Figure 2.2 Square Model Geometry	5
Figure 2.3 Commercial Nozzle Orifice	19
Figure 2.4 Symmetric and Antisymmetric Modes (from Nosseir <i>et al.</i> (1987)) ...	25
Figure 2.5 $1/2L_r$ versus Re_d equal jets (from Denshchikov <i>et al.</i> (1983))	30
Figure 2.6 Impingement Point Movement (from Ogawa <i>et al.</i> (1992))	33
Figure 2.7 Contours of Stream Function from Law and Masilyah (1984)	35
Figure 2.8 Classification of Self-Sustaining Oscillation Geometries from Rockwell and Naudascher (1979)	37
Figure 2.9 Variation of the Initial Instability Frequency with Jet Exit Velocity from Gutmark and Ho (1983)	39
Figure 2.10 Schematic Diagram of the Feedback Loop in an Impinging Jet from Ho and Nosseir (1981)	41
Figure 3.1 Light Sheet Generation	47
Figure 3.2 Schematic of LDA Optics and Electronics	51
Figure 3.3 Flow Loop Schematic	59
Figure 4.1 Numerical Grid	70
Figure 5.1.1 Model 4 $Re_d = 73$ $\mu = 52$ cP	75
Figure 5.1.2 Vector Plot of U^* , W^* in XZ plane at $Y = 0$	78
Figure 5.1.3 Contours of U^* in XZ plane at $Y = 0$	79
Figure 5.1.4 Contours of W^* in XZ plane at $Y = 0$	80
Figure 5.1.5 W^* vs Z^* at $(0,0,Z^*)$ Re_d 75, LDA Data and FLUENT Simulations ..	81
Figure 5.1.6 U^* vs X^* at $(X^*,0,0)$ LDA Data and FLUENT Simulations	83
Figure 5.1.7 W^* vs X^* at $(X^*,0,0)$ LDA Data and Fluent Simulations	84
Figure 5.1.8 W^* vs X^* at $(X^*,0,1)$ LDA Data and Fluent Simulations	85
Figure 5.2.1 W^* vs Z^* at $(0,0,Z^*)$, Model 3, $d = 2$ mm, $\mu = 50$ cP	90
Figure 5.2.2 W^* vs Z^* at $(0,0,Z^*)$, Model 3, $d = 2$ mm, $\mu = 25$ cP	90
Figure 5.2.3 W^* vs Z^* at $(0,0,Z^*)$, Model 3, $d = 3$ mm, $\mu = 50$ cP	92
Figure 5.2.4 W^* vs Z^* at $(0,0,Z^*)$, Model 3, $d = 3$ mm, $\mu = 25$ cP	92
Figure 5.2.5 W^* vs Z^* at $(0,0,Z^*)$, Model 3, $d = 4$ mm, $\mu = 50$ cP	94
Figure 5.2.6 W^* vs Z^* at $(0,0,Z^*)$, Model 3, $d = 4$ mm, $\mu = 25$ cP	94
Figure 5.3.1 W^* vs Re_d at $(0,0,1.5L)$, Model 3	102
Figure 5.3.2 z/L vs Re_d at $(0,0,z)$ Simulations for $L^* = 10$ and $L^* = 5$	103
Figure 5.4.1 W^{**} vs Time, $Re_d = 101$, Model 3, $d = 2$ mm, $\mu = 48$ cP	107
Figure 5.4.2 W^{**} vs Time, $Re_d = 121$, Model 3, $d = 2$ mm, $\mu = 48$ cP	107
Figure 5.4.3 W^{**} vs Time, $Re_d = 191$, Model 3, $d = 2$ mm, $\mu = 47$ cP	108
Figure 5.4.4 Spectral Density vs Frequency, Model 3, $d = 2$ mm	108

Figure 5.4.5 W_{rms}^* vs Z^* at $(0,0,Z^*)$ Model 3, $d = 2$ mm, $\mu = 50$ cP	110
Figure 5.4.6 W_{rms}^* vs Z^* at $(0,0,Z^*)$ Model 3, $d = 2$ mm, $\mu = 25$ cP	111
Figure 5.4.7 W_{rms}^* vs Z^* at $(0,0,Z^*)$ Model 3, $d = 3$ mm, $\mu = 50$ cP	112
Figure 5.4.8 W_{rms}^* vs Z^* at $(0,0,Z^*)$ Model 3, $d = 3$ mm, $\mu = 25$ cP	112
Figure 5.4.9 W'^* vs Time, $Re_d = 106$, Model 3, $d = 4$ mm, $\mu = 51$ cP	113
Figure 5.4.10 W'^* vs Time, $Re_d = 111$, Model 3, $d = 4$ mm, $\mu = 52$ cP	114
Figure 5.4.11 W'^* vs Time, $Re_d = 173$, Model 3, $d = 4$ mm, $\mu = 49$ cP	114
Figure 5.4.12 Spectral Density vs Frequency, Model 3, $d = 4$ mm	115
Figure 5.4.13 W_{rms}^* vs Z^* at $(0,0,Z^*)$ Model 3, $d = 4$ mm, $\mu = 50$ cP	116
Figure 5.4.14 W_{rms}^* vs Z^* at $(0,0,Z^*)$ Model 3, $d = 4$ mm, $\mu = 25$ cP	116
Figure 5.4.15 St_d vs Re_d for all cases of L^* Model 3	120
Figure 5.4.16 Oscillation frequency versus U_{avg} for all cases of L^* Model 3	121
Figure 5.5.1 U^* and W^* velocity vectors $Re_d = 500$ and $Re_d = 1000$	123
Figure 5.5.2 U^* Contours $Re_d = 500$ and $Re_d = 1000$	124
Figure 5.5.3 W^* Contours $Re_d = 500$ and $Re_d = 1000$	125
Figure 5.6.1 $Re_d = 43$ (Model 1, $H^* = 0.5$, $N = 3$ mm, $d = 2$ mm, $\mu = 32$ cP)	127
Figure 5.6.2 $Re_d = 69$ (Model 1, $H^* = 0.5$, $N = 3$ mm, $d = 2$ mm, $\mu = 32$ cP)	127
Figure 5.6.3 W^* Contours $Re_d = 304$ (Model 1, $D^* = 10.75$, $H^* = 0.5$, $N = 1$ mm, $\mu = 53$ cP)	130
Figure 5.6.4 W^* Contours $Re_d = 304$ (Model 1, $D^* = 10.75$, $H^* = 0.5$, $N = 3$ mm, $\mu = 53$ cP)	131
Figure 5.6.5 W^* Contours $Re_d = 304$ (Model 1, $D^* = 10.75$, $H^* = 0$, $N = 1$ mm, $\mu = 53$ cP)	132
Figure 5.6.6 W^* Contours $Re_d = 304$ (Model 1, $D^* = 10.75$, $H^* = 0$, $N = 3$ mm, $\mu = 53$ cP)	133
Figure 5.6.7 W^* Contours $Re_d = 325$ (Model 2, $D^* = 5$, $H^* = 0.5$, $N = 1$ mm, $\mu = 48$ cP)	134
Figure 5.6.8 W^* Contours $Re_d = 325$ (Model 2, $D^* = 5$, $H^* = 0.5$, $N = 3$ mm, $\mu = 48$ cP)	135
Figure 5.6.9 W^* Contours $Re_d = 325$ (Model 2, $D^* = 5$, $H^* = 0$, $N = 1$ mm, $\mu = 48$ cP)	136
Figure 5.6.10 W^* Contours $Re_d = 325$ (Model 2, $D^* = 5$, $H^* = 0$, $N = 3$ mm, $\mu = 48$ cP)	137
Figure 5.6.11 Jet Development U^* vs Y^* $Re_d = 275$	140
Figure 5.6.12 Jet Development U/U_{max} vs $y/y_{(U_{max}/2)}$ $Re_d = 275$	142
Figure 5.6.13 Jet Development I vs Y^* at $X_j^* = 0.5$ $Re_d = 275$	143
Figure 5.6.14 Jet Development I vs Y^* for $X_j^* = 1-4$ $Re_d = 275$	144
Figure 5.6.15 Jet Development I vs Y^* at $X_j^* = 4.5$ $Re_d = 275$	144

Figure 5.6.16	W^* Contours Unequal Flow Rates, left side $Re_d = 458$ right side $Re_d = 217$	147
Figure 5.6.17	Flow Visualization Particle Tracings for Flow Restriction XZ plane $Y = 0$, $C^* = 0.5$, $H^* = 0.5$	150
Figure 5.6.18	Flow Visualization Particle Tracings for Flow Restriction XZ plane $Y = 0$	151
Figure 5.6.19	Flow Visualization Particle Tracings for Flow Restriction XZ plane $Y = 0$, $C^* = 1.0$, $H^* = 0$	152
Figure 5.6.20	W^* Contours Flow Restriction, $Re_d = 300$ ($\mu = 50$ cP, Model 1, $D^* = 10.75$, $H^* = 0.5$, $C^* = 0.5$, $N = 3$ mm, $d = 2$ mm)	153
Figure 5.6.21	Flow Visualization Particle Tracings for Flow Restriction Unequal Flow Rates XZ plane $Y = 0$	154
Figure 5.6.22	Flow Visualization Particle Tracings for Flow Restriction Unequal Flow Rates XZ plane $Y = 0$	155
Figure 7.1	Plane Turbulent Wall Jet (Launder and Rodi, 1983)	167
Figure 7.2	Recirculating Flow Cavity, Inset: Inlet Area Close up	171
Figure 7.3	Schematic of Flow Loop - Recirculating Flow	172
Figure 7.4	Schematic of PSV Arrangement	176
Figure 7.5	Computational Grid - Recirculating Cavity 44x40	181
Figure 7.6	Flow Visualization - Entire Cavity $Re_b = 1675$	184
Figure 7.7	Flow Visualization - Inlet Area $Re_b = 1675$	185
Figure 7.8	Flow Visualization - Slot Inlet XZ Plane $Re_b = 1675$	186
Figure 7.9	Flow Visualization - XZ Plane at $(-.30,.075)$ $Re_b = 1675$	187
Figure 7.10	Wall Jet - U/U_j versus y/b $Re_b = 1675$	188
Figure 7.11	Wall Jet $Re_b = 1675$ - $y_{1/2}/b$ versus x/b	190
Figure 7.12	Wall Jet $Re_b = 1675$ - U_m/U_j versus x/b	190
Figure 7.13	Velocity Vectors LDA Data $Re_b = 1675$	191
Figure 7.14	Contours of Velocity LDA Data $Re_b = 1675$	193
Figure 7.15	Velocity Vectors PSV Data $Re_b = 1675$	194
Figure 7.16	$Re_b = 1675$ 2D FLUENT k - ϵ Simulation 44x40 Grid - Mean Velocity	196
Figure 7.17	$Re_b = 1675$ 2D FLUENT k - ϵ Simulation 86x78 Grid - Mean Velocity	196
Figure 7.18	$Re_b = 1675$ 2D FLUENT k - ϵ Simulation 44x40 Grid - Contours	197
Figure 7.19	$Re_b = 1675$ 2D FLUENT k - ϵ Simulation 86x78 Grid - Contours	197
Figure 7.20	$Re_b = 1675$ 3D FLUENT k - ϵ Simulation 30x40x15 Grid - Mean Velocity	197

Figure 7.21	$Re_b = 1675$ 2D FLUENT ASM Simulation 86x78 Grid - Mean Velocity	198
Figure 7.22	$Re_b = 1675$ 2D FLUENT ASM Simulation 86x78 Grid - Contours	199
Figure 7.23	U versus y at $x = 0.06$ m $Re_b = 1675$	200
Figure 7.24	U versus y at $x = .12$ m $Re_b = 1675$	201
Figure 7.25	U versus y at $x = .18$ m $Re_b = 1675$	201
Figure 7.26	U versus y at $x = .24$ m $Re_b = 1675$	202
Figure 7.27	V versus x at $y = .075$ m $Re_b = 1675$	204
Figure 7.28	U versus z $Re_b = 1675$	205
Figure 7.29	U/U_j versus y, $Re_b = 1675$ and 1117, $x = .06$ m	209
Figure 7.30	U/U_j versus y, $Re_b = 1675$ and 1117, $x = .12$ m	209
Figure 7.31	U/U_j versus y, $Re_b = 1675$ and 1117, $x = .18$ m	210
Figure 7.32	U/U_j versus y, $Re_b = 1675$ and 1117, $x = .24$ m	210
Figure 7.33	Contours of Kinetic Energy Entire Cavity - LDA Data $Re_b = 1675$	212
Figure 7.34	Contours of Kinetic Energy Entire Cavity - 44x40 2D k - ϵ Simulation $Re_b = 1675$	212
Figure 7.35	Contours of Kinetic Energy Entire Cavity - 86x78 2D k - ϵ Simulation $Re_b = 1675$	213
Figure 7.36	Contours of Kinetic Energy Entire Cavity - 30x40x15 3D k - ϵ Simulation $Re_b = 1675$	213
Figure 7.37	Contours of Kinetic Energy Entire Cavity - 86x78 2D ASM Simulation $Re_b = 1675$	214
Figure 7.38	Kinetic Energy versus y at $x = .06$ m, $Re_b = 1675$	215
Figure 7.39	Kinetic Energy versus y at $x = .12$ m, $Re_b = 1675$	216
Figure 7.40	Kinetic Energy versus y at $x = .18$ m, $Re_b = 1675$	216
Figure 7.41	Kinetic Energy versus y at $x = .24$ m, $Re_b = 1675$	217
Figure A5.2.1	W^* versus Z^* Model 3, $d = 2$ mm, $\mu = 50$ cP	A.2
Figure A5.2.2	W^* versus Z^* Model 3, $d = 2$ mm, $\mu = 50$ cP	A.2
Figure A5.2.3	W^* versus Z^* Model 3, $d = 2$ mm, $\mu = 50$ cP	A.3
Figure A5.2.4	W^* versus Z^* Model 3, $d = 2$ mm, $\mu = 50$ cP	A.3
Figure A5.2.5	W^* versus Z^* Model 3, $d = 2$ mm, $\mu = 50$ cP	A.4
Figure A5.2.6	W^* versus Z^* Model 3, $d = 3$ mm, $\mu = 50$ cP	A.4
Figure A5.2.7	W^* versus Z^* Model 3, $d = 3$ mm, $\mu = 50$ cP	A.5
Figure A5.2.8	W^* versus Z^* Model 3, $d = 4$ mm, $\mu = 50$ cP	A.5
Figure A5.2.9	W^* versus Z^* Model 3, $d = 4$ mm, $\mu = 50$ cP	A.6
Figure A5.2.10	W^* versus Z^* Model 3, $d = 4$ mm, $\mu = 50$ cP	A.6
Figure A5.2.11	W^* versus Z^* Model 3, $d = 4$ mm, $\mu = 50$ cP	A.7
Figure A5.2.12	W^* versus Z^* Model 3, $d = 4$ mm, $\mu = 50$ cP	A.7

Figure A5.2.13 W^* versus Z^* Model 3, $d = 4$ mm, $\mu = 25$ cP	A.8
Figure A5.2.14 W^* versus Z^* Model 3, $d = 4$ mm, $\mu = 25$ cP	A.8
Figure A5.2.15 W^* versus Z^* Model 3, $d = 4$ mm, $\mu = 25$ cP	A.9
Figure A5.2.16 W^* versus Z^* Model 3, $d = 4$ mm, $\mu = 25$ cP	A.9
Figure B7.1 Velocity Vectors LDA Data $Re_b = 1117$	B.2
Figure B7.2 Velocity Vectors 44x40 2D $k - \epsilon$ Simulation $Re_b = 1117$	B.3
Figure B7.3 Velocity Vectors 86x78 2D $k - \epsilon$ Simulation $Re_b = 1117$	B.4
Figure B7.4 Velocity Vectors 30x40x15 3D $k - \epsilon$ Simulation $Re_b = 1117$	B.5
Figure B7.5 U versus y at x = .06 m $Re_b = 1117$	B.6
Figure B7.6 U versus y at x = .12 m $Re_b = 1117$	B.6
Figure B7.7 U versus y at x = .18 m $Re_b = 1117$	B.7
Figure B7.8 U versus y at x = .24 m $Re_b = 1117$	B.7
Figure B7.9 V versus x at y = .075 m $Re_b = 1117$	B.8
Figure B7.10 U versus z $Re_b = 1117$	B.8
Figure B7.11 Kinetic Energy Contours LDA Data $Re_b = 1117$	B.9
Figure B7.12 Kinetic Energy Contours 44x40 2D $k - \epsilon$ Simulation $Re_b = 1117$..	B.10
Figure B7.13 Kinetic Energy Contours 86x78 2D $k - \epsilon$ Simulation $Re_b = 1117$..	B.11
Figure B7.14 Kinetic Energy Contours 30x40x15 3D $k - \epsilon$ Simulation $Re_b =$ 1117	B.12
Figure B7.15 Kinetic Energy versus y at x = .06 m $Re_b = 1117$	B.13
Figure B7.16 Kinetic Energy versus y at x = .12 m $Re_b = 1117$	B.13
Figure B7.17 Kinetic Energy versus y at x = .18 m $Re_b = 1117$	B.14
Figure B7.18 Kinetic Energy versus y at x = .24 m $Re_b = 1117$	B.14

1.0 Introduction

The flow of jets in confining enclosures has significant application in many engineering processes. In particular, two jet flows have been studied; the impingement of axisymmetric jets in a confined space and a turbulent inlet wall jet in a confining enclosure.

The impingement of axisymmetric jets in a confined space in laminar and turbulent regions is a situation which finds application in such areas as an impingement mix head for reaction injection molding (RIM), the side inlet ramjet combustor, the particle crystallizer, and combustion furnaces in pulp and paper mills. Typically the engineering applications of RIM involve the mixing of very viscous liquids in a mix head with moderate Reynolds numbers. The side inlet ramjet combustor is used in high velocity subsonic gas flows where mixing of combustible fuels gives large Reynolds numbers. Geometrically these problems are very similar and the approach taken for their analysis includes using flow visualization, laser Doppler anemometer (LDA) velocity measurements and numerical simulations.

Recirculating flow in an enclosure with an inlet wall jet is important to environmental studies, ventilation and power generation. Two cases of Re_b were examined using flow visualization, laser Doppler anemometry (LDA), particle streak velocimetry (PSV), and numerical simulations using the $k - \epsilon$ and algebraic stress

(ASM) turbulence models. Since the primary motivation for these studies was to provide an experimental database for recirculating flows with inlet wall jets the application of PSV to this flow demonstrated the technique and extended the experimental database. Numerical simulations of the flow using the anisotropic ASM turbulence model gave better predictions than a standard $k - \epsilon$ turbulence model.

2.0 Literature Survey

2.1 Introduction

The impingement of axisymmetric jets in a confined space in laminar and turbulent regions is a situation which finds application in such areas as an impingement mix head for reaction injection molding (RIM), the side inlet ramjet combustor, the particle crystallizer, and combustion furnaces in pulp and paper mills.

Typically the engineering applications of RIM involve the mixing of very viscous liquids in a mix head with moderate Reynolds numbers. The side inlet ramjet combustor is used in high velocity subsonic gas flows with mixing of combustible fuels giving large Reynolds numbers. Geometrically these problems are very similar and the approach taken for their solution is similar. The general configuration for a cylindrical chamber is shown in Figure 2.1 and a configuration for a square cross section chamber is shown in Figure 2.2.

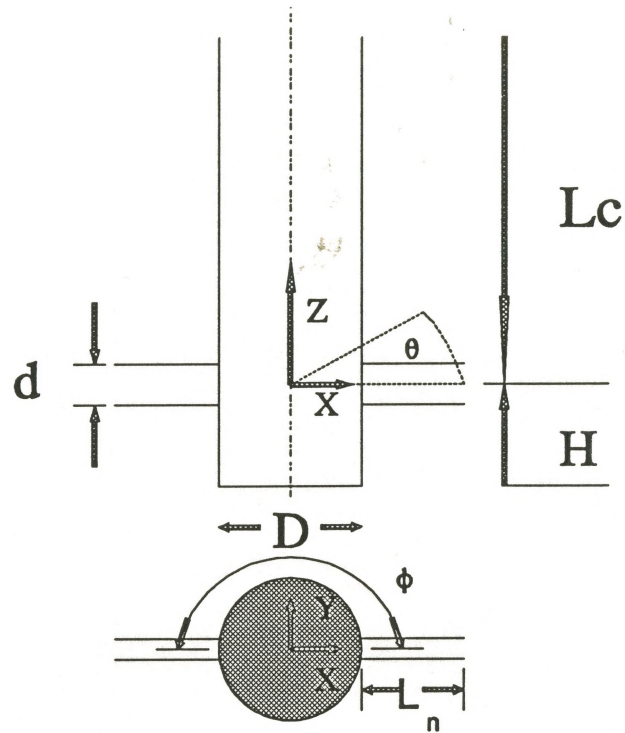


Figure 2.1 Cylindrical Model Geometry

D	Main chamber diameter (m)
d	Nozzle diameter (m)
L_n	Nozzle length (m)
L_c	Main chamber length (m)
H	Head length (m)
θ	Nozzle incidence angle ($^\circ$)
ϕ	Nozzle separation angle ($^\circ$)
H^*	H/D
D^*	D/d

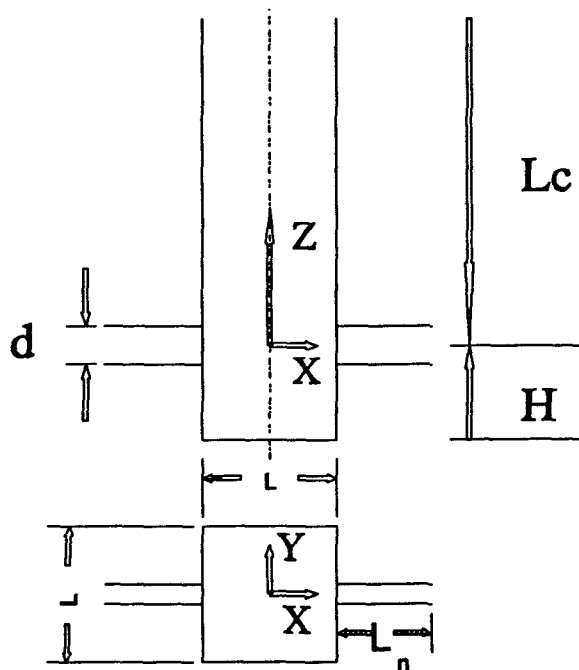


Figure 2.2 Square Model Geometry

H^*	H/L
L	Main chamber side length (m)
L^*	L/d

For all specified problems, a fluid flows from a nozzle into a chamber of enlarged area and flows out of the chamber. A jet, formed when fluid issues from the nozzle on one side, impinges onto a similar jet formed when fluid issues from the opposed nozzle. Upon impingement, a flow field is created which forces the fluid from the chamber. The dimensionless group used to characterize the flow is the Reynolds number which is based on the nozzle diameter, the fluid kinematic viscosity and the volumetric flow rate.

$$Re_d = \frac{U_{avg} d}{\nu} = \frac{4\rho Q}{\pi\mu d} \quad 2.1$$

Q	volumetric flow rate (m ³ /s)
Re _d	Reynolds number defined using nozzle conditions and diameter
U _{avg}	average fluid velocity leaving the nozzle (m/s)
μ	absolute viscosity (kg/ms)
ν	kinematic viscosity (m ² /s)
ρ	density (kg/m ³)

Opposed jet impingement can be considered to be a composite of several flow structures such as the free jet, a curved shear layer, a stagnating impingement flow, a radial jet flow, recirculating flow and developing conduit flow. All of these flow structures have been studied separately in some detail by many researchers.

Amalgamation of all these components leads to a complex flow field. Initially, at low Re_d a steady flow region exists with all components represented. The Re_d studied in this work ranges from 25 to 1,000 which is normally considered to be in the laminar, transition to turbulent and fully turbulent regions.

The physical equations governing the flow are detailed below. Equations are

developed for a constant density, isothermal fluid.

Continuity

$$\frac{\partial u_i}{\partial x_i} = 0 \quad 2.2$$

where

- i index of coordinate direction (i=1,2,3) and summation over repeated indices is implied
- x coordinate in i direction
- u instantaneous velocity
- p instantaneous pressure (Pa)

Momentum

$$\frac{\partial u_j}{\partial t} + \frac{\partial(u_i u_j)}{\partial x_i} = \nu \frac{\partial}{\partial x_i} \left(\frac{\partial u_i}{\partial x_j} + \frac{\partial u_j}{\partial x_i} \right) - \frac{1}{\rho} \frac{\partial p}{\partial x_j} \quad 2.3$$

or, using the chain rule and applying equation 2.2

$$\frac{\partial u_j}{\partial t} + u_i \frac{\partial u_j}{\partial x_i} = \nu \frac{\partial^2 u_j}{\partial x_i \partial x_i} - \frac{1}{\rho} \frac{\partial p}{\partial x_j} \quad 2.4$$

where

- j index of coordinate direction (j=1,2,3)

For the turbulent cases the usual approach is to decompose the instantaneous terms into mean and fluctuating components.

$$u_i = U_i + u_i' \quad 2.5$$

where

- U_i mean velocity in i direction
- u_i' fluctuating velocity in i direction

$$U_i = \lim_{T \rightarrow 0} \frac{1}{T} \int_{t_0}^{t_0+T} u_i dt \quad 2.6$$

Using this decomposition, the continuity and momentum equations become

$$\frac{\partial U_i}{\partial x_i} = 0 \quad \frac{\partial u_i'}{\partial x_i} = 0 \quad 2.7$$

and

$$U_i \frac{\partial U_j}{\partial x_i} = \nu \frac{\partial}{\partial x_i} \left(\frac{\partial U_j}{\partial x_i} + \frac{\partial U_i}{\partial x_j} \right) - \frac{1}{\rho} \frac{\partial P}{\partial x_i} - \frac{\partial (\overline{u_i' u_j'})}{\partial x_i} \quad 2.8$$

where $\overline{\rho u_i' u_j'}$ is called the Reynolds stress term.

The Reynolds stress terms are the source of the difficulty in the solution of turbulent problems. The set of equations (2.7), (2.8) contains four equations but potentially up to ten unknowns. This situation is known as the "closure problem".

Turbulence Modelling

In order to close the set of equations, several proposals have been made to mathematically model the Reynolds stresses. A review of these can be found in Launder and Spalding (1972). The models discussed for these studies are the k - ε two equation model, the algebraic stress model (ASM) and mean Reynolds stress model (MRS).

The k - ε model combines a length scale with the turbulent energy scale to form a turbulent diffusivity.

In this case, the length scale is determined from the viscous dissipation

$$\epsilon = \frac{k^2}{l_s^3} \quad 2.9$$

where

- ϵ dissipation rate of turbulence energy (m^2/s^3)
- l_s integral length scale
- k turbulent kinetic energy (m^2/s^2), where

$$k = \frac{\overline{u_j' u_j'}}{2} \quad 2.10$$

An equation for the kinetic energy balance may be obtained by multiplying the instantaneous momentum equation with u_j and using equation 2.2

$$\frac{D}{Dt} \frac{u_j u_j}{2} = \nu \frac{\partial}{\partial x_i} u_j \left(\frac{\partial u_j}{\partial x_i} + \frac{\partial u_i}{\partial x_j} \right) - \nu \frac{\partial u_j}{\partial x_i} \left(\frac{\partial u_i}{\partial x_j} + \frac{\partial u_j}{\partial x_i} \right) - \frac{1}{\rho} \frac{\partial}{\partial x_j} (p u_j) \quad 2.11$$

where the first term on the right side results from the viscous stresses, the second term is the viscous dissipation and the last term is the pressure work. Using Reynolds decomposition and time averaging yields a transport equation for k :

$$\begin{aligned} \frac{D}{Dt} \frac{\overline{u_j' u_j'}}{2} &= \nu \frac{\partial}{\partial x_i} \overline{u_j' \left(\frac{\partial u_j'}{\partial x_i} + \frac{\partial u_i'}{\partial x_j} \right)} - \nu \frac{\partial u_j'}{\partial x_i} \left(\frac{\partial u_i'}{\partial x_j} + \frac{\partial u_j'}{\partial x_i} \right) \\ &- \frac{\partial}{\partial x_i} \frac{\overline{u_i' u_j' u_j'}}{2} - \overline{u_j' u_i'} \frac{\partial U_j}{\partial x_i} - \frac{1}{\rho} \frac{\partial}{\partial x_j} \overline{p' u_i'} \end{aligned} \quad 2.12$$

where the first term is the viscous diffusion, the second term is the dissipation, the

third term is the turbulent transport, the fourth term is the production and the last term is the pressure work term.

Defining

$$\epsilon = \nu \overline{\frac{\partial u'_j}{\partial x_i} \left(\frac{\partial u'_i}{\partial x_j} + \frac{\partial u'_j}{\partial x_i} \right)} \quad 2.13$$

and

$$k = \frac{\overline{u'_j u'_j}}{2} \quad , \quad 2.14$$

then model differential transport equations for k and ϵ are obtained with the assumption that a gradient diffusion mechanism applies are obtained (Launder and Spalding 1974)

$$\frac{\partial}{\partial t}(\rho k) + \frac{\partial}{\partial x_i}(\rho u_i k) = \frac{\partial}{\partial x_i} \left[\frac{\mu_t}{\sigma_k} \frac{\partial k}{\partial x_i} \right] + G_k - \rho \epsilon \quad 2.15$$

$$\frac{\partial}{\partial t}(\rho \epsilon) + \frac{\partial}{\partial x_i}(\rho u_i \epsilon) = \frac{\partial}{\partial x_i} \left[\frac{\mu_t}{\sigma_\epsilon} \frac{\partial \epsilon}{\partial x_i} \right] + c_1 \frac{\epsilon}{k} G_k - c_2 \rho \frac{\epsilon^2}{k} \quad 2.16$$

where G_k generation term of k

$$G_k = \mu_t \left(\frac{\partial u_j}{\partial x_i} + \frac{\partial u_i}{\partial x_j} \right) \frac{\partial u_j}{\partial x_i} \quad 2.17$$

$$\mu_t = \rho C_\mu \frac{k^2}{\epsilon} \quad 2.18$$

μ_t turbulent viscosity

The values commonly used for the constants in the above equations which were not altered are (Launder and Spalding 1972):

Table 2.1 Constants used in k-ε turbulence model

C_1	C_2	C_μ	σ_k	σ_ϵ
1.44	1.92	0.09	1.0	1.3

An assumption of the k - ε model is that the flow field is homogeneous leading to an isotropic eddy diffusivity (equation 2.19). For opposed jets this may not be the case because of the large variations in the velocities and turbulent intensities in the region of impingement.

An alternative would be the mean Reynolds stress model (MRS) which uses differential equations to solve for all the components of the Reynolds stresses $\overline{u_i' u_j'}$. A typical MRS model is that of Launder *et al.* (1975)

$$\frac{\partial \overline{u_i' u_j'}}{\partial t} + U_k \frac{\partial \overline{u_i' u_j'}}{\partial x_k} = \frac{\partial}{\partial x_k} \left[\frac{\mu_t}{\sigma_k} \frac{\partial \overline{u_i' u_j'}}{\partial x_k} \right] + P_{ij} + \Phi_{ij} - \epsilon_{ij} \quad 2.19$$

where

P_{ij} stress production rate

$$P_{ij} = - \left[\overline{u_i' u_k'} \frac{\partial u_j}{\partial x_k} + \overline{u_j' u_k'} \frac{\partial u_i}{\partial x_k} \right] \quad 2.20$$

Φ_{ij} source/sink due to pressure/strain correlation

ϵ_{ij} viscous dissipation tensor

and Launder *et al.* (1975) model these as

$$\Phi_{ij} = -C_3 \frac{\epsilon}{k} \{ \overline{u_i' u_j'} - \frac{2}{3} \delta_{ij} k \} - C_4 \{ P_{ij} - \frac{1}{3} \delta_{ij} P_{kk} \} \quad 2.21$$

$$\epsilon_{ij} = \frac{2}{3} \delta_{ij} \epsilon \quad 2.22$$

Table 2.2 Additional constants for MRS turbulence model

C_3	C_4
1.5	0.4

This model can be computationally time consuming as partial differential equations are solved for all the non-zero Reynolds stresses.

A model of intermediate complexity is the algebraic stress model (ASM) which eliminates the gradients of the dependent variables which appear in the first three terms of the MRS (rate of change, convective transport, and diffusive transport) and replaces them by algebraic expressions (Rodi 1984).

$$\frac{D \overline{u_i' u_j'}}{Dt} - \text{diff}(u_i' u_j') = \frac{\overline{u_i' u_j'}}{k} \left\{ \frac{Dk}{Dt} - \text{diff}(k) \right\} \quad 2.23$$

The k- ϵ and the ASM modelling approaches will be used to compare with the results obtained experimentally.

Solution Procedure (FLUENT 1989)

The commercial computer code FLUENT is used to solve the governing differential equations subject to appropriate boundary conditions. FLUENT uses a control volume method in which the governing equations are discretized. All dependent variables are located at the cell centre, except velocities, which are located at the cell boundaries in a "staggered" grid. A power law differencing scheme is used to interpolate between grid points and calculate derivatives of flow variables. Time derivatives are integrated in a fully implicit manner. Wall functions are used at the boundaries close to the wall. The discretized equations are solved with a semi-implicit iterative scheme to converge at the solution. This solution method is extensively described in Patankar (1980).

2.2 Opposed Jet Flows Modelling Reaction Injection Molding

Reaction Injection Molding (RIM) is a rapid mixing process in a mix chamber of two or more liquid pre-polymers which then flow into a mold to form a solid polymer part. The process has many advantages, such as lower energy requirements in comparison to thermoplastic injection molding and production of large detailed parts. For most RIM systems, mixing is carried out through directly opposed jet to jet impingement of the reactant streams. The reactant streams may have viscosity ratios as high as 20:1, and flow rate ratios as high as 10:1 depending on the properties of the reactants and the reaction stoichiometry. Stable efficient mixing is paramount to the quality of parts produced with RIM as poorly mixed materials will cause spatial variation in the physical properties and the variation in the physical appearance of a finished molded part. Typically, mix chambers are cylindrical and 10-15 mm in diameter using nozzles to form the jets close to the closed end, head region of the chamber (Figure 2.1). The closed end is also the top of the clean-out piston used to remove the polymer from the nozzle region upon completion of the shot. The nozzles may be of an annular configuration with needles allowing some variation of the opening. After mixing the mixed fluid then leaves the open end of the chamber to enter the mold. Important geometrical parameters are: the chamber diameter, the jet nozzle diameters, the annular opening of the nozzles (if applicable) and the location of the nozzles relative to the closed end of the chamber.

Summaries of previous studies of RIM mix heads are provided in Oertel (1985) and Macosko (1989). Commercial applications may have Re_d vary from

approximately 100 to 1000, but 300-500 is considered a normal operating range to give adequate mixing within the mix head.

A variety of techniques have been used to quantify the effect of the Re_d on the flow field. Previous researchers have quantified the mixing under varying conditions using adiabatic temperature rise (Lee *et al.*, (1980), Sebastian and Boukobbal (1986)) and polymerized tracer material (Kolodziej *et al.*, 1982). Visualization of the flow patterns by Sandell *et al.* (1985) in a water based system in a mix chamber (D^* (D/d) = 5.5, $d = 9.5$ mm, nozzles angled at $\theta = 30^\circ$, aimed at the head region H^* (H/D) = 0.73) has shown an oscillating impingement region above $Re_d = 150$. At $Re_d = 250$ the oscillation was reported to have larger amplitude and higher frequency as measured by replaying video tapes and observing the region between the nozzle inlet and head region. Observations of the oscillation frequency versus Re_d are given in Table 2.3.

Table 2.3 Results of Sandell *et al.* (1985)

Re_d	f (Hz)	St (fd/U)
250	0.16 ± 0.03	0.048
400	0.63	0.12
560	1.1	0.15
720	1.5	0.16

where

f frequency of oscillation (Hz)
 St Strouhal number (fd/U)

Between Re_d of 400 to 700 there was limited visual improvement in mixing, as observed by a vanishing dye technique in water. Generally, the flow became less

steady when increasing the Re_d or increasing the distance from the nozzles to the closed end (H). A similar study using water in two model mix chambers (square L^* (L/d) = 12, d = 10 mm, round D^* = 5, d = 20 mm, θ = 0°) is reported by Akaike *et al.* (1986) who have used hydrogen bubbles and dye to visualize the flow. Their findings indicate stable non fluctuating flow when $Re_d < 200$, an unstable impingement surface $200 < Re_d < 500$, and a stable impingement surface with upstream and downstream fluctuations for $Re_d > 500$. Lee *et al.* (1980) use a viscous, glycerine water mixture (0.3 Pa s) in a mix chamber (D^* = 3.18, d = 1.0 mm) to obtain flow visualization photographs for various flow rates. They note that above a Re_d of 150, the flow is very three-dimensional with strong vortical motion. Wood *et al.* (1991) have confirmed these observations in a model mix head (D^* = 10.67, d = 2.38 mm, ϕ = 180° , H^* = 0-1) using flow visualization, velocity measurements and three-dimensional computer simulation. They found steady impingement below $Re_d = 75$ while at larger values of Re_d an instability in the impingement surface grows and oscillates. Experimentally, above $Re_d = 150$ the jets do not always directly impinge, although computer simulations showed steady oscillations from $Re_d = 100 - 300$ for $H^* = 0.5$ and $H^* = 1.0$. Subsequent three-dimensional steady and unsteady simulations by Yeo (1993) show asymmetric pressure contours at the point of impingement for $Re_d = 75$ ($D^* = 10$, $\phi = 180^\circ$) which become less symmetric with increasing Re_d . Computational grid refinement was found to alter the solution significantly. Three dimensional unsteady simulations by Ho (1992) ($D^* = 10$, $\phi = 180^\circ$) examined the impingement oscillations, distances to fully developed flow, unequal nozzle flow rates and the effect

of nozzle inlet angles. These simulations show an increase in the amplitude of oscillation from $Re_d = 125$ to $Re_d = 200$ and only marginal increase to $Re_d = 300$. A slight increase in distance to fully developed flow with increasing H^* from $H^* = 0$ up to $H^* = 0.5$ was found for $Re_d = 50$ and the axial distance to a fully developed flow ($H^* = 0.25$) condition was found to increase dramatically with increasing Re_d . The location of the impingement point for unequal flow rate ratios was found for a flow rate ratio of 1:1.5 at $X^* = 3.5$ ($-5. > X^* < 5.$) and for the flow rate ratio of 1:2 at $X^* = 4.3$ ($-5. > X^* < 5.$). Small increments in the nozzle inlet angles ($\theta = 0^\circ$ to -6°) showed a steady decrease in the amplitude of oscillation at $Re_d = 125$.

LDA measurements reported by Yu *et al.* (1991) indicate an increase in axial (Z) plane weighted average rms (root mean square)

$$u' = \sqrt{\frac{1}{(N-1)} \sum (u_i - U)^2} \quad 2.24$$

velocities with a decrease of D^* or a decrease in H^* in model mix chambers ($D^* = 3.09, 4.32, 6.05$; $d = 8.1$ mm, $H = 11,31$ mm) using a water and syrup solution with Re_d ranging from 140 - 5400. Maximum axial (Z) plane weighted average rms velocities were found with a jet momentum ratio $R = 1$ where jet momentum ratio R is defined as:

$$R = \frac{\rho_1 \left(\frac{Q_1}{d_1}\right)^2}{\rho_2 \left(\frac{Q_2}{d_2}\right)^2} \quad 2.25$$

Studies show that any transient disturbance in the flow field coming from the impingement point dissipates after several mix head diameters downstream of the impingement point and the flow becomes similar to fully developed laminar pipe flow.

In an effort to model these results, Tucker and Suh (1980) assume that the flow above or at a "critical" Reynolds number provides good large scale mixing and compared this region to a transition from laminar to turbulent flow. As the region of intensely mixed fluid is small (2-3 D above the impingement point) the mixing energy input from the jets was assumed to be fully turbulent for calculation purposes, reducing the eddy size such that the mixing length scale l_m is equal to the scale of the Kolmogoroff length microscale η_k .

$$\eta_k \sim \left(\frac{v^3}{\epsilon}\right)^{1/4} \quad 2.26$$

These arguments lead to the relationship

$$\frac{l_m}{d} \sim Re_d^{-3/4} \quad 2.27$$

which shows that as Re_d increases the mixing length scale decreases resulting in improved mixing. This result has not been experimentally confirmed, as a plateau value of Re_d is reached such that an increment in the Re_d will not significantly improve the mixing. This model is only valid for turbulent flow and it is questionable

whether at these Re_d that turbulent flow exists as the inlet Re_d drops significantly in the mix chamber due to the increased chamber diameter. Aside from the question of turbulence, the approach assumes that the input energy (essentially pressure work) will be entirely dissipated over the volume where mixing occurs (lumped analysis). It does not allow for any variation in dissipation in the volume. Simulations by Yeo (1993) show the only regions of significant dissipation occur in the jet shear layer and in the impingement region.

There are few studies of the flow patterns for mix heads having nozzles that include a screw and needle assembly to create an annular opening. A high pressure drop (at the upper limit of reactant injection pressure) across the nozzle is needed to provide good mix quality (Muller and Sochtig 1987). Figure 2.3 shows a simplified schematic of the region within the mix head near the L'Orange nozzle orifice. This configuration is typical of a number of commercial RIM mix heads.

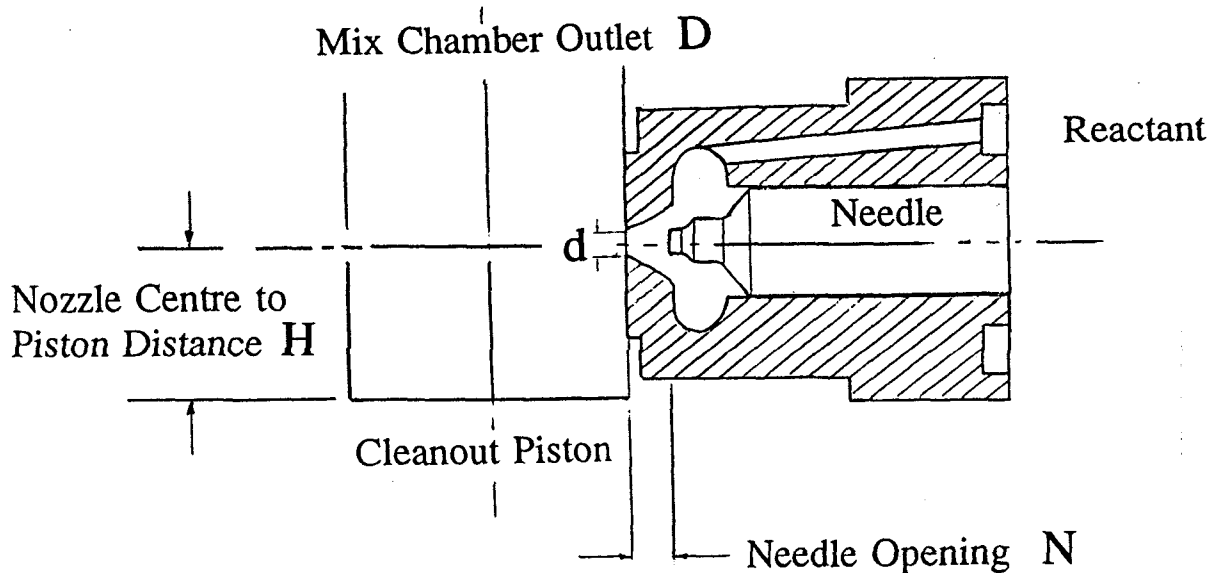


Figure 2.3 Commercial Nozzle Orifice

For either a commercial nozzle, or a long entry length nozzle, the jet as it develops with unbounded distance should approach a fully developed, self similar profile like that of Schlichting (1968) for a fully developed parabolic nozzle outlet profile. The similarity solution to the boundary layer equations assumes the circular jet issues from a minute nozzle into an unbounded area. The velocity within the boundary layer is defined:

$$u = \frac{3}{8\pi} \frac{J}{\mu x_j} \frac{1}{(1+0.25\xi^2)^2} \quad 2.28$$

where

$$\xi = \sqrt{\frac{3}{16\pi}} \sqrt{\frac{J}{\rho \nu x_j} y} \quad 2.29$$

and the momentum of the jet is

$$J = 2\pi\rho \int_0^{\infty} u^2 y dy \quad 2.30$$

where x_j is the axial distance from the nozzle $X_j^* = x_j/d$.

Akaike and Nemoto (1988) have reported results from a submerged laminar water jet of $Re_d = 100$ to 600 issuing from a short 10 mm diameter nozzle (24 mm diameter tapered to 10 mm over 25 mm and 5 mm of 10 mm diameter nozzle) into an unrestricted area. A potential core existed at $X_j^* = 2$ and the fully developed Schlichting similarity profile was approached at $X_j^* = 10$. Their experimental results may be more applicable to the commercial nozzle design, since no development length is present in either case.

2.3 Opposed Jet Flows Modelling Side Dump Combustors

For the side-dump ramjet combustor, Re_d values are typically $O(10^5)$. Previous studies have examined combustion stability as a significant performance parameter. Stability of the combustion process seems to depend on the areas of recirculation in the head region and oscillations in the pressure fields which occur at the point of jet to jet impingement. Large pressure oscillations have detrimental effects on the combustion process. Acoustical oscillations can affect the inlet pressure conditions and enhance vibration and heat transfer problems. Stull *et al.* (1985) investigated the flow patterns present in a model combustor with the nozzles for the jets 90° degrees apart ($\phi = 90^\circ$) entering the main chamber at an inlet angle θ of -45° (angled toward outlet). The main chamber was 152 mm in diameter and the rectangular nozzles were 50x70 mm. A similar combustor was used with variable inlet angles of -30° , -45° and -60° for actual combustion tests. For the flow visualization case reported, water was used as the working fluid with a Re_d of 1.8×10^5 with a head height of 50 mm ($H^* = 1/3$). Air was injected in the nozzle to form bubbles 50 mm before the main chamber with illumination provided with a slit of white light (~ 3 mm thick). Photographs at various chamber heights revealed an area of recirculation in the head region which was bistable (two possible stable configurations) and two counter rotating helical vortices trailing downstream from the nozzle inlet. As well, variation of the head height from 0 to 100 mm altered the flow pattern in the head area but had no significant effect on the flow field downstream of the nozzle position. In the actual

combustion tests, the nozzle inlet angle had little effect on overall combustor performance and oscillations were not found for most operating conditions. When found, oscillation amplitudes increased when; air temperature decreased, main chamber length decreased, fuel-air ratio increased, nozzle inlet angle decreased, and chamber exit diameter increased. The oscillation frequencies were found to be in the 100-325 Hz range and could be increased when: air temperature increased, chamber length decreased, nozzle entry angle decreased, and chamber exit diameter increased. The flow field was compared with steady state computational predictions using a $k - \epsilon$ turbulence model with 11×10 nodes in cross section and 3500 nodes in total, modelling one half of the combustor assuming symmetry. The flow patterns above the nozzle inlet were found to agree well with the flow visualization studies but poor agreement was obtained for the head region where bistable oscillatory conditions would make agreement poor.

In a similar study, Nosseir and Behar (1986) used a model with opposed rectangular planar nozzles ($L^* = 1.25 - 2.50$, $\phi = 180^\circ$, $H^* = 0-2$) on a water table (one free surface) to simulate the side dump combustor. The average Re_d based on the nozzle width was 3000. Coloured dye was injected into the flow at various locations and hydrogen bubbles were generated on a grid to illuminate the flow patterns present. Oscillations in the flow were detected using a laser beam and photo cell at a fixed location which would be interrupted by the passage of the dye at that location. Flow visualization results were similar to those of Stull *et al.* (1985) in that at one instant one jet would be deflected into the head area and then deflected out while the other jet

would be deflected into the head area in an "almost periodic and out of phase" manner. As well, above the nozzle area, in the main chamber, vortices were generated which alternated between clockwise and counter clockwise rotation similar to the above work. The strength of the vortices was found to fluctuate with the oscillation of the jets into the head area (phase locked). A non dimensional frequency (Strouhal Number = fd/U) was given for variations in velocity and head length. Measurements were obtained above the impingement region using video analysis and laser light interruption. Increases in head length were found to cause a decrease in the Strouhal number.

Table 2.4 Results of Nosseir and Behar (1986) $L^* = 2$, $H^* = 1$

Re	St
800	0.14
1600	0.17
2000	0.22
2700	0.17-0.21
3300	0.25

These values are in agreement with some of the results of Sandell *et al.* (1985) discussed previously. The recirculation patterns observed differ from the nozzle studies of Sandell *et al.* (1985) and Stull *et al.* (1985) in some respects due to the geometric configuration studied.

In order to eliminate some of the geometrical effects of the side dump combustor Nosseir *et al.* (1987) modelled the side dump combustor as two nozzles impinging head on in an unconfined space with the only limitation being two parallel

flat plates holding the nozzles. Air was the working fluid and both nozzle velocities were carefully controlled to ensure uniform flow velocities. Flow visualization using tufts suspended on wires between the two plates characterized the flow. It was found that the head on impingement was highly unstable with a period of oscillation of 0.5 - 1 s. Oscillation in the jets occurred with two well-defined modes of oscillation; the symmetric and antisymmetric modes as shown in Figure 2.4. On a long time average the oscillations became axisymmetric. Pressure variation on the plates was recorded in order to determine the location of wall reattachment away from the impingement area. Pressure was at a minimum at the point of reattachment although pressure fluctuations were 40% of the minimum value. At 220 and 515 Hz significant low frequencies were found which were independent of plate separation distance H_s and high frequencies (885-5138 Hz) which were a function of H_s . Good agreement was obtained between the high frequency range and values of the resonant frequency between the plates from the standing wave equation.

$$2\pi f_h = \left(\frac{c}{H_s}\right)(N\pi) \quad 2.31$$

c speed of sound
N 1,2,3....

The 220 Hz frequency was found to be a natural frequency of the plate dimension. The 515 Hz frequency was possibly the result of the structure of the jets interacting with the plates, similar to the fluctuating reattachment point found in a backward facing step (Troutt *et al.* 1984) or the "flapping" of the shear layer because

of the passage of coherent structures (Eaton and Johnston 1980), as it was only measured inside the separated region before reattachment. A feedback mechanism based on upstream propagation of pressure waves from the point of impingement forces the shear layer near the nozzle exit. This concept is discussed in a later section.

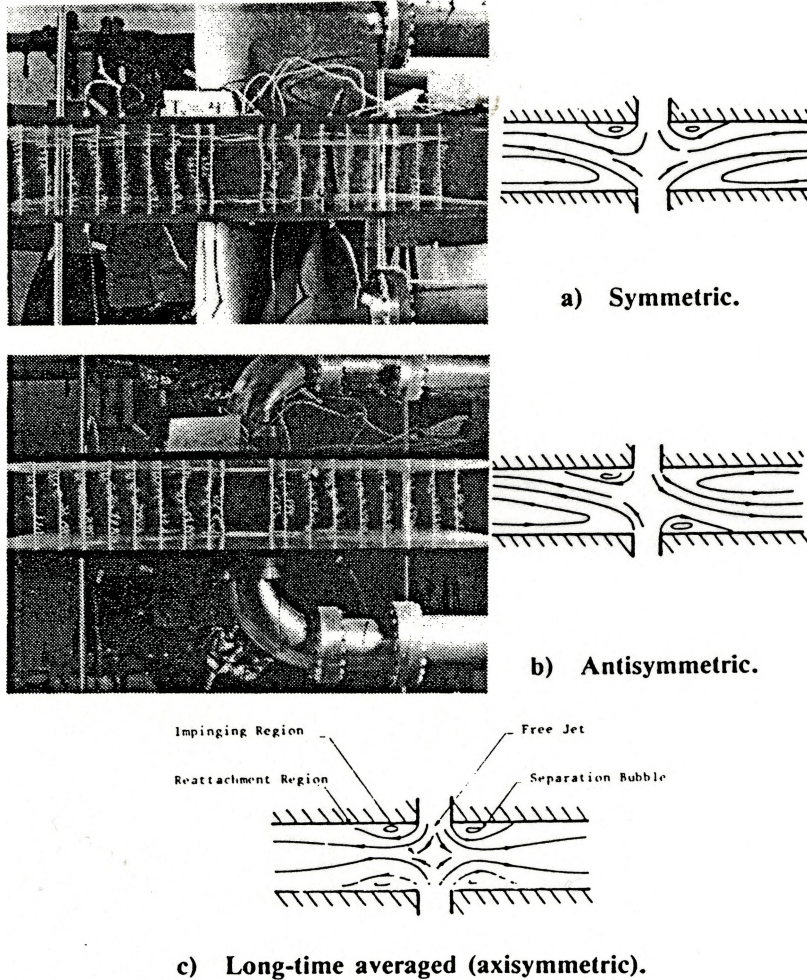


Figure 2.4 Symmetric and Antisymmetric Modes (from Nosseir *et al.* (1987))

Turbulence parameters have been experimentally determined in two cases of a model side dump combustor by Liou and Wu (1988) and Liou *et al.* (1990) using laser Doppler anemometry (LDA). The model in the first case had two opposed rectangular

inlets (35x47 mm, $\phi = 180^\circ$) entering at an angle θ of -60° and a main chamber diameter (D) of 100 mm with a variable length head region which was fixed at 50 mm ($H^* = 0.5$) for these experiments. Air was used as the working fluid and the Re_{dh} was 2.5×10^4 where

$$d_h = 4 * \frac{\text{nozzle cross sectional area}}{\text{cross section perimeter}} \quad 2.32$$

d_h hydraulic diameter
 Re_{dh} Reynolds number based on d_h

In the second case of Liou *et al.* (1990) two short opposed rectangular nozzles (15x120 mm, $\phi = 180^\circ$) entered a rectangular model (LxW 30x120 mm) making the nozzle the entire depth of the main chamber similar to the model of Nosseir and Behar (1986). The head length was potentially variable but was fixed at 30 mm ($H^* (H/L) = 1.0$). Air was again used as the working fluid and the Re_{dh} was 2.3×10^4 . A single component LDA was used for the measurements which were taken on the jet axis and at 90° to the jet axis for 9 axial (z) combustor planes in the first case and 11 axial (z) combustor planes in the second case. Because of the inlet angle θ of -60° the stagnation point or central impingement point was found to be at 0.46 D above the inlet nozzles in the first case and at 0.28 L for the second case of head on impingement. Below the impingement area in the combustor head two asymmetric vortices were measured in the plane of the nozzles and four counter rotating vortices 90° to the nozzles for the first case, while only two counter rotating vortices were found below the impingement stagnation point in the second case. Above the nozzle inlets, two vortices formed on the walls of the chamber in the second case. Flow

became unidirectional, 4 D downstream in both cases and was extrapolated to fully developed flow at 13 D downstream of the nozzles in the first case. In the second case, measurements of the transverse velocity revealed a bimodal distribution of velocities in the region of 0.1 L to 1.1 L similar to those observed by Nosseir *et al.* (1987) and Stull *et al.* (1985) where the oscillation of flow into the head region alternated between the jets. Between the nozzle inlets and 1.0 D or L, the turbulence measured was highly inhomogeneous and anisotropic. In particular, the axial turbulent intensity in the region where the jets collided was five times the transverse turbulent intensity. This would partially account for the poor agreement with a previous two dimensional $k - \epsilon$ turbulence model prediction which assumes isotropic turbulence. In a study of the effect of the head height H on the stagnation point and the areas of reattachment above the inlet nozzles it was found that H does not affect either the stagnation point or the reattachment points in the second case. The flow rates into the head and into the reattachment points were evaluated for various H. A maximum for the head flow rate was found for $H^* = 0.5$ and the flow rate then decreased to $H^* = 0.75$, where it remained essentially constant. The first case was modelled using a steady algebraic Reynolds stress (ASM) model in subsequent papers by Liou and Hwang (1989) and Liou *et al.* (1992). An unequally spaced finite difference grid $9 \times 10 \times 40$ in the x, ϕ , and z directions was used to model one quarter of the combustor. This assumes that the flow field is symmetric about the nozzle axis and 90° to the nozzle axis. However, previous work has shown this not to be the case because of impingement area oscillation. Mean flow velocities generally agreed with

experimental results within 15 % although the peak axial velocity (W) was under predicted by 54 % apparently because of asymmetric flow conditions, although a probable explanation is the assumption of steady flow simulations for an unsteady flow field. In the second work (Liou *et al.*, (1992)), in which a comparison of various turbulence models was detailed, the algebraic stress model gave the best agreement with experimental data although the $k - \epsilon$ model also predicted the trends qualitatively. Measured inlet values gave better agreement than a uniform inlet profile, as would be expected.

A flow visualization study was performed by Miao *et al.* (1989) similar to the study of Nosseir and Behar (1986) and the second case of Liou *et al.* (1990) where the opposed inlet nozzles (200x50 mm) enter at $\theta = 0^\circ$ and are the same depth as the main chamber ($W \times W$ 200x200 mm) giving a Re_{dh} of 8×10^3 . The head length was fixed at 200 mm ($H^* = 1$). An Argon Ion laser was used to create a light sheet to illuminate cross sections where 60 μ m aluminum oxide particles traced the flow. The particles were injected from holes in the sides of the inlet nozzles. Similar observations were made regarding the low speed recirculating cells in the head region and the shear layers formed at the recirculation areas above the nozzle inlets. It was postulated that there is a coupling between the streamwise vortices in the main flow and the separated flows developed above the nozzle inlets.

The effect of the inlet angle on the mean flow and turbulent characteristics in a model side dump combustor was studied by Manjunath *et al.* (1991) and Manjunath *et al.* (1992). Four inlet angles with nozzles aimed at the chamber exit ($\theta = -30^\circ, -45^\circ, -$

60° and -75°) were examined ($Re_1 = 10^5$, $H = 0$, $L/l = 3.22$, $l = 49$ mm) in planar jets the entire depth of the chamber. For $\theta = -30^\circ$ and -45° the measured W velocity and kinetic energy were much higher in the initial region $z/l < 6$ and uniform conditions were attained faster than the larger inlet angles as the maximum velocities decayed rapidly. For all inlet angles the initial region was found to be anisotropic with the axial W_{rms} velocities approximately twice the V_{rms} values. The slow decay of W_{rms} for large inlet angles indicated a gradual mixing process in comparison with the intense mixing at small inlet angles indicated by the rapid drop in all rms values.

2.4 Unconfined Opposed Jet Flows

Oscillations have also been observed in impinging jets with no boundary restrictions. Denshchikov *et al.* (1978) and Denshchikov *et al.* (1983) report self-sustained oscillations in two opposed free jets issuing from nozzles 50-200 mm ($2L_f$) apart in a submerged water tank. The flow was visualized with ink added to the jets and recorded with a movie camera. A dimensionless group T/T^* was used to compile the results.

$$T^* = \frac{\rho(2L_f)^2}{\mu} \quad 2.33$$

L_f half distance between the nozzles (free jet)
 μ Absolute viscosity
 ρ density

For equal momentum jets the expression became

$$\frac{T}{T^*} = 0.34 Re_l^{-1.0} \left(\frac{l}{2L_f}\right)^{0.45} \quad 2.34$$

T period of oscillation
 l transverse height of nozzle
 Re_l Reynolds number based on l

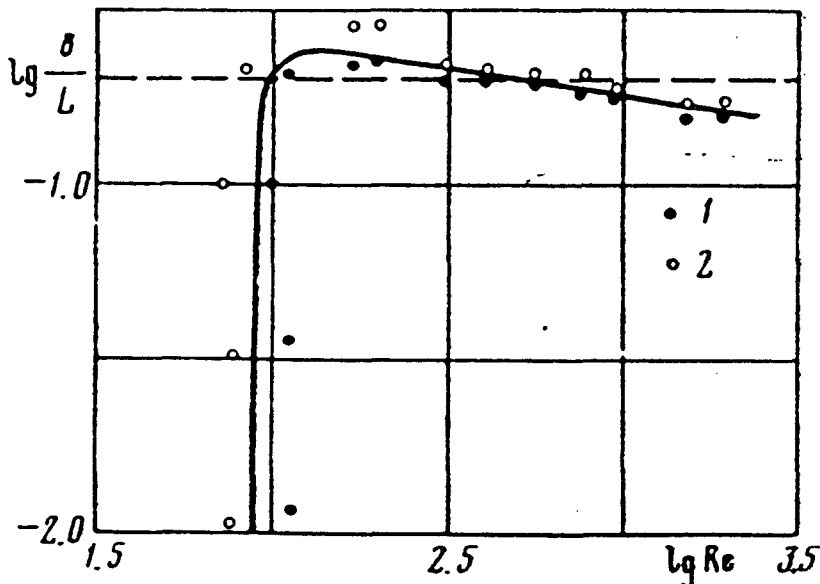


Figure 2.5 $1/2L_f$ versus Re_l equal jets (from Denshchikov *et al.* (1983)) ○ no oscillations, • oscillations

For values of Re_l less than 90-100 self-sustained oscillations were absent for all values of $1/2L_f$ and for $100 < Re_l < 4800$ the presence of oscillations depended on the value of $1/2L_f$. A neutral stability curve as a function of $1/2L_f$ and Re_l is shown in Figure 2.5.

A similar study was reported by Ogawa and Maki (1986) and subsequently by Ogawa *et al.* (1992) where air flowed through two 28.2 mm diameter opposed nozzles

($Re_d O(10^4)$). In the first case primarily pressure variation was measured as one jet impinged on a flat plate located at various distances from the nozzle exit and velocity measurements were obtained for various jet to jet separation distances ($2L_j/d = 0.35$ to 5.32). In the second paper an attempt was made to correlate the point of impingement between the two jets with the momentum ratio of the nozzles. The point of impingement was determined through the use of a hot wire anemometer located 20 mm from the jet axis (-z direction) which was moved parallel to the jet axis to determine the highest axial (w) velocity. The location corresponding on the jet axis was taken as the impingement point. The momentum of the jet can be found from the Bernoulli equation along a stream line.

$$\frac{1}{2}U^2 + \frac{P}{\rho} + \frac{1}{2}\overline{u^2} = constant \quad 2.35$$

Combined with the assumption of isotropy

$$\frac{P}{\rho} = \frac{P_a}{\rho} - \overline{u^2} \quad 2.36$$

P_a static pressure outside jets

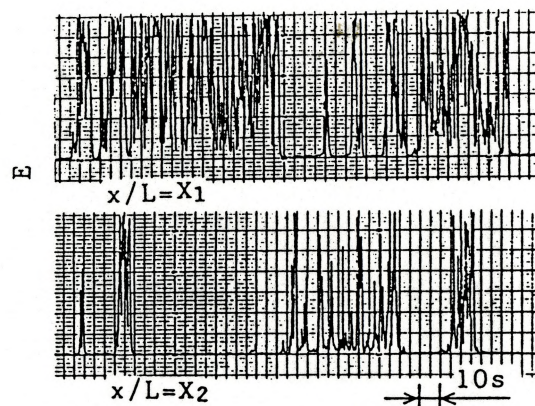
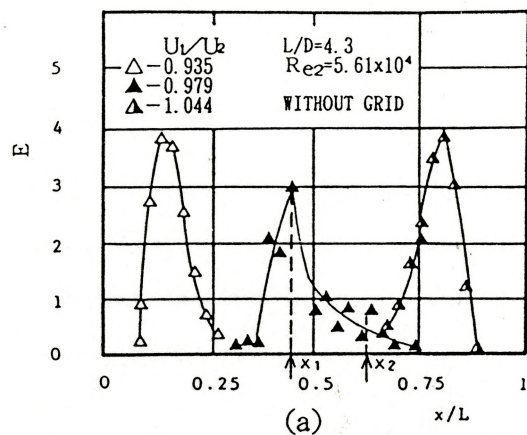
These equations lead to an estimate of the momentum of the jet at the jet centre.

$$\frac{1}{2}\rho(U^2 - \overline{u^2}) + P_a = constant \quad 2.37$$

The results for two nozzle designs are shown in Figure 2.6 which essentially show that for low turbulent intensity fluid issuing from the nozzle the impingement point can be determined from the momentum ratio but for higher turbulent intensities

it can not solely be determined from the momentum ratios. The second paper (Ogawa *et al.* (1992)) found that if the mass flow ratios differed significantly (e.g. when the impingement point was near one of the nozzles) the impingement point was relatively stable ($L_e/d = 2.15$ and 4.29). When mass flow rates were approximately unity a bistable impingement point was found. The variation was attributed to variation in ($\overline{U-u'^2}$) because of similar velocity profiles from both nozzles but differing fluctuating velocity profiles caused by insertion of grids in one nozzle only. Frequency of impingement area movement was not discussed.

Becker *et al.* (1988) found complex frequency spectra with no regular oscillations in an opposed jet apparatus with jets 6.22 mm in diameter separated by 340 mm ($L_e/d = 27.3$) with volumetric air velocities of 17.8 m/s giving a Re_d of 6900. L_e/d was found to be a significant operating parameter affecting turbulence and mixing at the point of impingement more so for $L_e/d < 12$. For large L_e/d the effect of initial flow parameters on the impingement zone was found to be negligible.



(b) Output of a hot-wire anemometer

Figure 2.6 Impingement Point Movement (from Ogawa *et al.* (1992))

2.5 Impinging Jet Flows

The opposed jet configurations studied in this work is found to have characteristics which are similar to previously documented impinging flows. In particular, the presence of flow regions such as steady flow, and oscillatory flow has been studied extensively for some geometric arrangements.

Initial approaches to opposed jet flows considered the similarity between opposed jets and a single jet impinging on a flat plate (Powell (1961), Nosseir and Behar (1986)). Many cases of jet impingement on a flat surface have been documented in the laminar [Deshpande and Vaishnav (1982), Law and Masliyah (1984)] and turbulent [Wolfshtein (1970), Beltaos and Rajaratnam (1973), Gutmark *et al.* (1978)] regions. Some similarities exist between these cases and the present opposed jet case, such as the existence of a free jet region, an impingement region and, for low Re_d cases, a recirculating region. Flat plate impingement differs in that a wall jet develops along the plate boundary away from the impingement region, while a radial jet develops from the impingement region in the opposed jets; no laminar flat plate impingement studies have detailed an oscillating impingement region. Laminar jet impingement on a flat plate has been numerically simulated by Deshpande and Vaishnav (1982) (Re_d 0-2000, $L_p/d = 1.5$ and 2) where L_p is the distance from the nozzle exit to the plate. For $0 < Re_d < 1000$ a recirculating toroidal vortex adjacent to the nozzle exit was found and at $Re_d \geq 1000$ the vortex no longer existed. The vortex centre moved toward the plate for $Re_d \leq 25$ and in the radial direction away

from the stagnation point for $Re_d > 25$. A similar study by Law and Masliyah (1984) ($400 < Re_d < 1900$, $L_p/d = 2$ and 4) with the addition of an upper confining surface parallel to the impingement plate showed a similar toroidal vortex filling the confining cavity. The vortex grew in the radial direction and the vortex centre moved in the radial direction with increasing Re_d . In contrast to the unconfined impingement study above, the toroidal vortex existed over the entire range of Re_d studied. Contours of stream function from their simulations are shown in Figure 2.7.

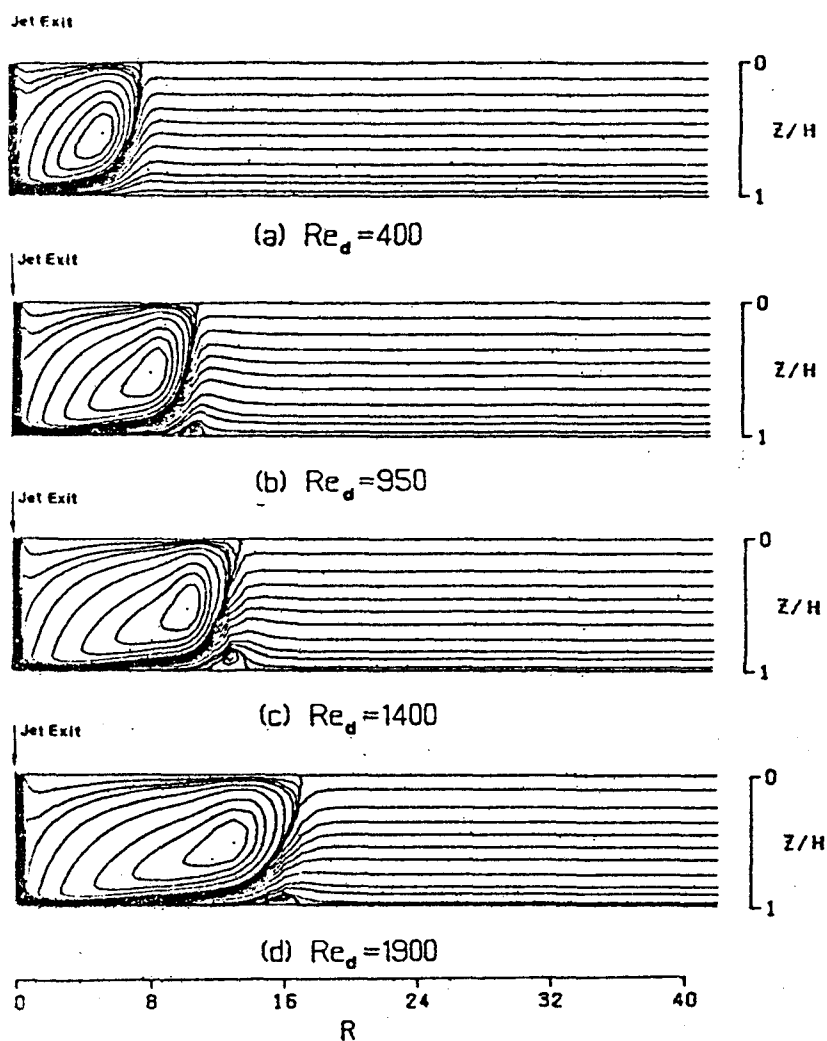


Figure 2.7 Contours of Stream Function from Law and Masliyah (1984)

2.6 Oscillations

Initially, the mechanism controlling the movement of the impingement region in the opposed jet case was considered to be a class of the Coanda effect in which a free jet develops oscillations due to alternating side wall attachments (Murai *et al.* 1989). The jet movement in the mix head case is not as significant as that seen with free jets in a channel and the frequency of oscillation of the free jet is typically very small. Studies of suddenly enlarged channels, similar to the jet entry into the chamber of the opposed jets, show recirculation filling the expanded area and instability in the wall reattachment areas leading to asymmetric flow patterns. Numerical simulations by Shapira *et al.* (1990) for channel expansion ratios (D^* or L^* in the opposed jet case) of 1:2 and 1:3 and expansion angles of 7° - 90° reveal that, as the expansion ratio decreases, the flow remains stable for higher Re_d . In this case, stable refers to a symmetric flow pattern and unstable refers to an asymmetric flow pattern. For an expansion ratio of 1:3 and an expansion angle of 90° the symmetric flow pattern was found to be unstable for $Re_d = 82.6$. The transition from symmetric to asymmetric flow was found to be smooth and non-oscillatory.

Self-sustained oscillations in impinging jet flows where a jet impinging on an object or surface develops regular self sustaining oscillations have been reviewed by Rockwell and Naudascher (1978,1979). A graphic classification scheme based on the jet and the impinged surface from the Rockwell and Naudascher (1979) review is shown in Figure 2.8. In all of these cases, several interacting events are necessary for the occurrence and maintenance of oscillations. Steady flow will occur below a

critical value of Re_d , as disturbances will be damped (Naudascher (1967)).

Subsequently, disturbances in the impingement region are fed back to the unstable free shear layer of the jet. These disturbances cause increased vorticity fluctuations in the shear layer. Consequent downstream amplification of the shear layer vorticity fluctuations aids the production of disturbances in the impingement region.

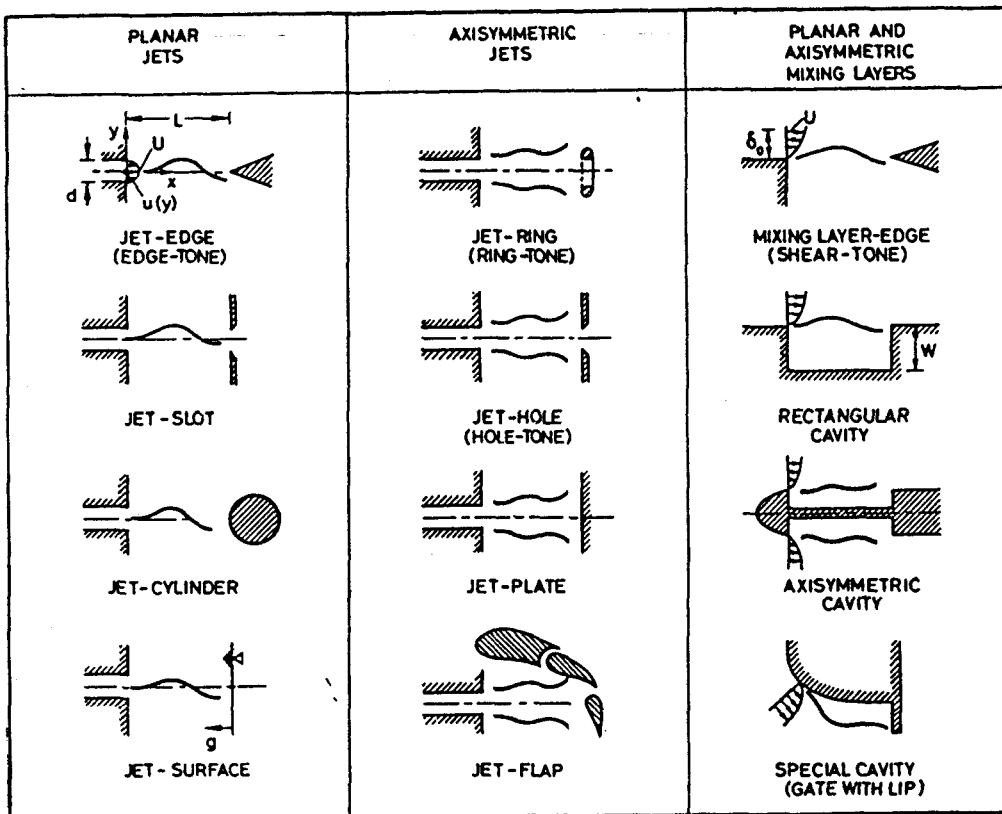


Figure 2.8 Classification of Self-Sustaining Oscillation Geometries from Rockwell and Naudascher (1979)

Theoretical predictions of the growth of a disturbance in the initial free finite thickness shear layer originating at the nozzle lip found certain frequencies to be unstable (Michalke 1965). The most amplified frequency f_o forms a constant Strouhal number based on the initial momentum thickness θ_{mo} and the jet exit velocity U where

$$St_o = \frac{f_o \theta_{mo}}{U} = 0.017 \quad 2.38$$

the momentum thickness θ_m (Schlichting 1968) is defined by

$$\theta_m = \int_{y=0}^{+\infty} \frac{u}{U} \left(1 - \frac{u}{U}\right) dy \quad 2.39$$

θ_m momentum thickness (m)

where u is the velocity at the point y in the velocity profile. θ_m is a function of the Re_d and the distance from the nozzle x and θ_{mo} is defined as the initial momentum thickness at the nozzle lip where $x = 0$. As

$$\theta_{mo} \propto \frac{1}{\sqrt{U}} \quad 2.40$$

then

$$f_o \propto U^{\frac{3}{2}} \quad 2.41$$

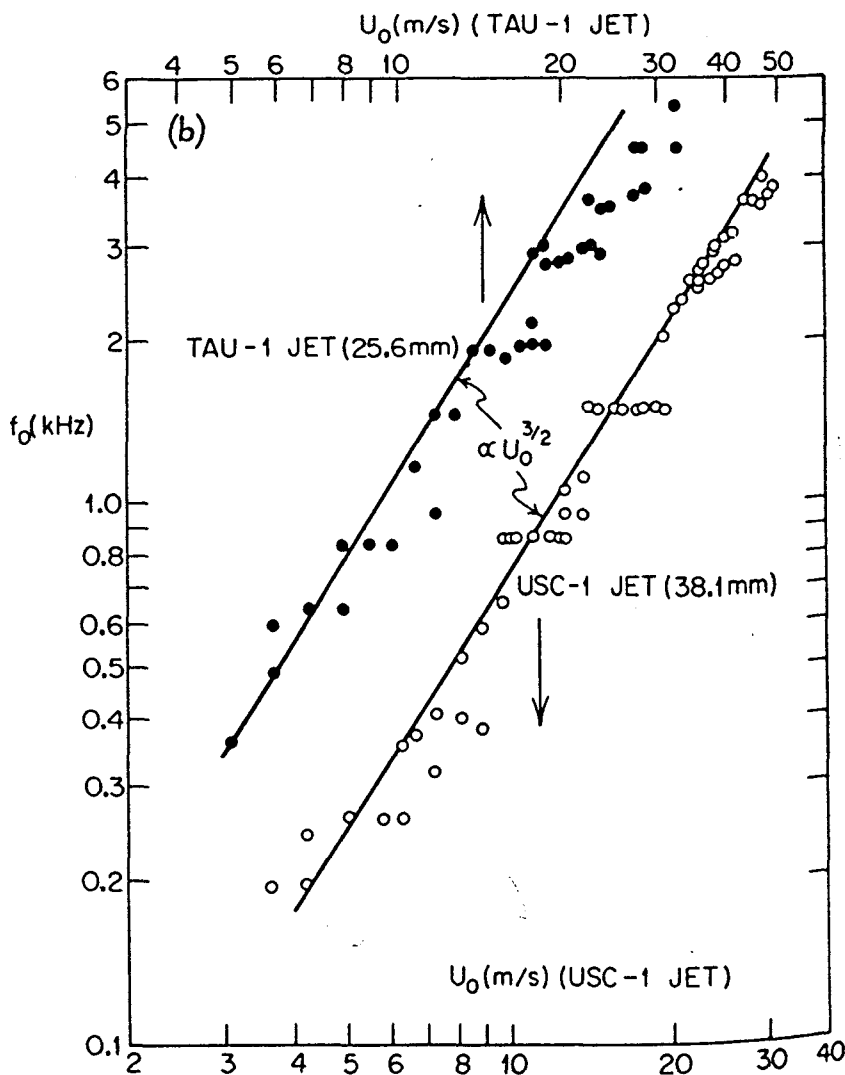


Figure 2.9 Variation of the Initial Instability Frequency with Jet Exit Velocity from Gutmark and Ho (1983)

A review of previous instability studies in free turbulent jets is reported and Gutmark and Ho (1983), who found a significant scatter in the St_0 (.01 - .018) reported in the literature. Their measurements close to the nozzle ($x/d = 0.3$) showed the dependence of frequency on velocity $U^{3/2}$ as shown in Figure 2.9. Significant variation in their St_0 with Re_d led to the discovery of an extremely small upstream

disturbance and the conclusion that "a minute amount of spatially coherent disturbance can cause the scatter in the instability frequency" and "the development of the entire shear layer up to the end of the potential core may be affected by initial conditions".

The flow system presently under study, the opposed jet configuration, is not specifically outlined in the Rockwell and Naudascher (1979) review (Figure 2.8). Although the closest example is perhaps the jet-plate configuration, this implies a solid impingement surface which does not exist here.

The impingement of a subsonic turbulent jet on a flat plate has been investigated by Ho and Nosseir (1981). Their experimental work found evidence of a phase lock between downstream and upstream travelling waves, creating a closed feedback loop required for self sustained oscillations. Variation in the plate to nozzle distance was found to cause frequency stages in the resonant Strouhal number ($St_f = f_d/U$) typical of self sustained flows. The St_f would decrease with increasing plate to nozzle distance until a St_f minima of 0.3 was reached at which point the St_f would jump to an increased level. The resonant frequencies were found to be an order of magnitude smaller than the initial instability frequencies, and the shear layer thickened because of multiple mergings of the coherent structures downstream of the nozzle or *collective interaction*. A schematic of the feedback loop proposed by Ho and Nosseir (1981) is shown in Figure 2.10. The described feedback mechanism will only function in an unstable flow region and the extent of the region will depend on the strength of the feedback, which is controlled by the boundary conditions (Naudascher (1967)).

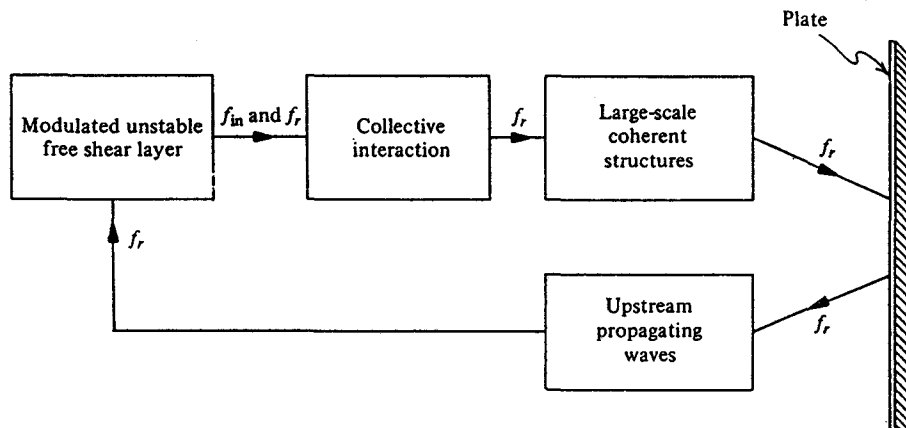


Figure 2.10 Schematic Diagram of the Feedback Loop in an Impinging Jet from Ho and Nasseir (1981)

The present case concerning oscillations in the opposed jet impingement area of a confined cavity has not been previously addressed in the literature. In particular, the influence of the fluid interface of the impingement area and the effect of the wall boundaries will alter the oscillatory mechanism, even though components of the described feedback mechanism are present, such as the initial shear layer instability and upstream propagating pressure waves from the impingement region.

2.7 Summary

As a summary of previous work, stable conditions and self-sustained oscillations have been found in geometrically similar opposed jet studies with widely varying Re_d and St . The cases where the Re_d is of $O(10^2-10^3)$ shows instabilities in an impingement surface above and below the geometric point of impingement while for studies with $Re_d > O(10^3)$ the visualized structure changes somewhat in that a similar region below the impingement region has been documented while helical vortices have been visualized above the impingement point. Unconfined opposed jets are also reported to have oscillatory behaviour, depending on nozzle parameters such as separation distance, diameter and momentum ratio a situation suggesting that other geometrical parameters are insignificant for oscillatory behaviour.

3.0 Experimental Techniques

3.1 Flow Visualization

Several flow visualization techniques have been developed in order to qualitatively analyze the flow field present under various experimental conditions.

3.1.1 Dye visualizations

For dye visualizations, dye (BASF) soluble in mineral oil is added in bulk to the fluid entering from one nozzle of the mix chamber or it was injected with a syringe at a specific location before the inlet nozzle. Illumination was provided by a white spot light. For cases of $Re_d > 90$, the dye technique gave poor results as the dye would rapidly mix with the clear fluid so that dye at the wall obscured the impingement area, making visualization difficult.

3.1.2 Particle streak flow visualization

Particle streak flow visualization was more successful, as the fluid is seeded with polystyrene particles (60 μm mean diameter) which, when illuminated with a light source and photographed or video taped, reveal the characteristics of the flow.

A major criterion for the selection of particles is their ability to follow the flow under all conditions. Stoke's law is normally used to evaluate the particle size required as

the Reynolds number based on particle slip should be small; it is subject to the following assumptions: inertia forces on particles of fluid neglected in comparison with shearing forces due to viscosity (only possible if Re very small); no boundary surface affecting flow; particle a rigid sphere; steady motion, only particle moving; no slip between fluid and particle.

Drag force opposing motion

$$D_s = 3\pi \mu \Delta u d \quad 3.1$$

$$\frac{\pi}{6}d^3\rho_s g = \frac{\pi}{6}d^3\rho_f g + 3\pi\mu\Delta u d \quad 3.2$$

$$\Delta u = \frac{d_p^2(\rho_p - \rho_f) g_p}{18 \mu} \quad 3.3$$

where

Δu	particle slip velocity ($u_p - u$)
g_p	particle acceleration
d_p	particle diameter
ρ_p	particle density

Now if the fluid is moving with a variable velocity the Basset Boussinesq

Oseen approximation modified by Tchen (Durst *et al.* 1981) is used.

$$\frac{\pi}{6}d^3\rho_s \frac{dv_s}{dt} = \frac{\pi}{6}d^3\rho_f \frac{dv_f}{dt} + 3\pi\mu d(v_f - v_s) + \frac{1}{2} \frac{\pi}{6}d^3\rho_f \left(\frac{dv_f}{dt} - \frac{dv_s}{dt} \right) \quad 3.4$$

$$+ \frac{3}{2} d^2 \sqrt{\pi \mu \rho_f} \int_{t_0}^t \left(\frac{dv_f}{dt} - \frac{dv_s}{dt} \right) \frac{dt}{\sqrt{t-t_0}} + F_e \quad 3.5$$

where the terms describe:

1. Force required to accelerate sphere
2. Pressure gradient in the fluid surrounding the sphere caused by fluid acceleration
3. Viscous drag force
4. Force to accelerate the apparent mass of the particle relative to the fluid (potential flow)
5. Basset history integral - drag force arising from deviation of flow pattern from steady state (increase of instantaneous flow resistance)
6. External forces

This approximation is subject to the following assumptions: turbulence homogeneous and steady; domain of turbulence infinite; spherical small particles and Stokes law applies; particle small compared with the smallest wavelength present in the turbulence; during motion of particle same fluid particles in the neighbourhood.

For these studies the following simplifications apply:

$$\rho_f \approx \rho_s$$

$$0 = \frac{3}{2} \frac{\pi}{6} d^3 \rho \left(\frac{dV_f}{dt} - \frac{dV_s}{dt} \right) + 3\pi \mu d (V_f - V_s) \quad 3.6$$

Relative velocity $U = V_f - V_s$ gives

$$\frac{dU}{dt} + \frac{1}{\tau} U = 0 \quad \tau = \frac{\frac{3}{2} \frac{\pi}{6} d^3 \rho}{3\pi \mu d} = \frac{\rho d^2}{12\mu} \quad 3.7$$

$$U(t) = U(0) e^{-\frac{t}{\tau}} \quad 3.8$$

Typical values for τ are $O(10^{-6})s^{-1}$ giving a slip velocity of $O(10^{-9})$ m/s for (t 10^{-4} s).

Particle Shape

The above analysis applies only to spherical shapes. Results will apply qualitatively to other shapes by using equivalent volume sphere and particle shape factor $\lambda=(A/A_s)$

$$d_s = \left(\frac{6V}{\pi}\right)^{\frac{1}{3}} \quad A_s = \pi d_s^2 \quad 3.9$$

A correction factor must be applied to the drag coefficient. As the particle deviates further from a sphere the predictions will have less value.

Additional Constraints

Additional constraints are imposed in using particles for laser Doppler anemometry: they must scatter enough light to be detectable and provide a good signal to noise ratio. For flow visualization they must reflect enough light to be visible to the recording medium.

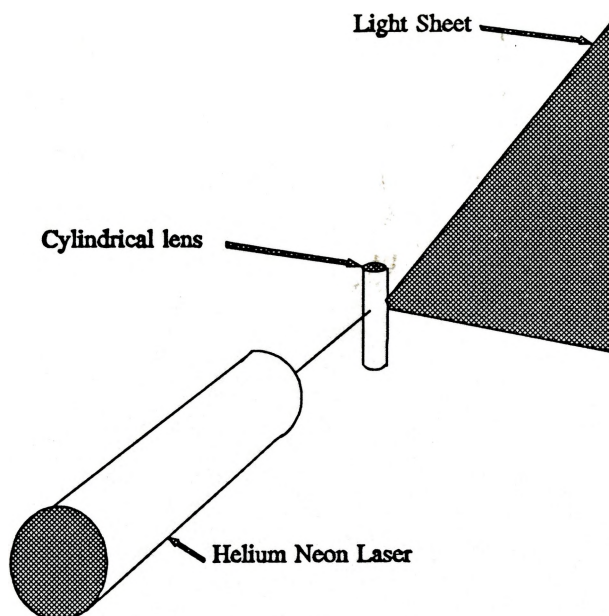


Figure 3.1 Light Sheet Generation

Illumination was provided with a white light source for visualizing the entire chamber or through the use of a Helium Neon (HeNe) (Spectra Physics 15 mW) or Argon Ion (Coherent 6 W) laser for planes of light. A light sheet was created from the laser beam using several techniques such as a cylindrical lens, a rotating mirror, or an oscillating mirror. The cylindrical lens expands the beam in one direction only creating a sheet of light typically 1-2 mm thick (Figure 3.1). All of these methods proved invaluable for probing specific areas of the impingement region.

3.1.3 Laser Induced Fluorescence (LIF)

Laser induced fluorescence (LIF) is a similar situation to adding a soluble dye to the fluid for visualization but has the benefit that the dye is not visible under normal visible light conditions. Dyes which are water soluble such as Fluorescein and Rhodamine have been investigated previously and the technique is well developed. Using carefully controlled initial dye concentrations it is possible to measure the decay in concentration as fluorescent intensity varies. Walker (1985) has examined a slow co-flowing free jet in water using this technique. A dye (BASF Fluorol Yellow 088) was used, which is soluble in the mineral oil used as the working fluid. Normally, the volume of oil issuing from one jet was thoroughly premixed with the dye and the other volume of oil from the opposed jet was free of dye. The dyed oil fluoresced in the main chamber with the Argon laser source giving well defined flow patterns throughout the chamber. Flow visualizations were recorded with a CCD video camera (Panasonic MF 552) and SVHS video tape recorder (Panasonic) and still photographs were obtained with a Nikon F2 35 mm camera with 400-1600 ASA slide film. The disadvantage of this technique is that the "clean" oil is gradually used up as the dye is inseparable from the oil whereas the advantages are that no injection of the dye is required which can disturb the flow and the premixed dye gives uniform mixing throughout the chamber.

3.2 Laser Doppler Anemometry (LDA)

Laser Doppler Anemometry (LDA) was used as a measurement tool in the investigation of impingement mixing. Reviews of the theory and methods are provided in Drain (1980) and Durst *et al.* (1981).

The method consists of splitting a laser beam into two equal intensity beams separated by a distance L_b ; the beams then pass through a focusing lens of focal length F to cross at the measurement point located in the flow of interest. Simplistically, the crossed beams can be thought of as creating a fringe pattern of light and dark bands because of the interference of the two light waves. Small particles (0.1-10 μm), present in the flow either through natural occurrence or through artificial seeding scatter the light from both beams when passing through light and dark bands. The frequency of the scattered light from particle reflection is doppler shifted in proportion to its velocity and is detectable only when combined with the incident beams. The reflected light is focused on to a photomultiplier, which converts light intensity to a frequency modulated current from which the frequency difference is resolved. The frequency is related to the particle velocity through:

$$f_d = \frac{2u}{\lambda} \sin\left(\frac{\alpha}{2}\right) \quad 3.10$$

where

f_d frequency obtained at the detector
 λ wavelength of the laser light
 U particle velocity to be measured
 α angle between the laser beams

$$\alpha = 2 \tan^{-1}\left(\frac{\left(\frac{L_b}{2}\right)}{F}\right) \quad 3.11$$

where

F focal length of lens
 L_b beam separation distance

The system as described has no way of determining the direction of flow of the particle as it crosses the "fringes". To overcome this ambiguity one of the beams is shifted by a known frequency such that the previously stable interference pattern of light and dark fringes is now a moving interference pattern. A particle moving with the fringes will have an increased frequency, while a particle moving away from the fringe movement will have a decreased frequency. In this way the direction of particle movement may be resolved. There are several methods of providing frequency shifting but the one used in the present work is a Bragg cell, which is an acousto-optic cell which shifts the light frequency by 40 MHz. LDA provides high spatial and temporal resolution but on a point by point basis.

stage that could be positioned within ± 5 microns.

The signal from the photomultiplier is in the form of an amplitude varying current signal crossing zero amplitude as fringes are traversed. High and low pass filters are set to eliminate extraneous signals and the settings are dependent on the range of expected frequencies (velocities). The counter essentially times the number of zero crossings of, in this case, 8 fringes to determine the passage time. A comparator circuit compares the time for 8 fringes with the time for the initial 5 fringes and the data is rejected if it is outside the allowable difference (3% in this case). Incoming data rate is indicated on the counter and the percentage validated of the incoming data is also indicated. Both of these indicators fluctuated significantly depending on many factors including the location of the probe volume, system alignment, and particle velocities. Data from the counter processor is transferred to the computer with the Dostek 1400a (Dostek, 1987) computer interface utilizing sample and hold circuitry at a user specified sample rate. Stored data is subsequently processed to determine velocity parameters.

3.3 Particle Image Velocimetry (PIV)

A recent development in the measurement of fluid velocity parameters is Particle Image Velocimetry (PIV). It has the advantage over other measurement techniques in that an entire flow field is recorded at one instant instead of point to point measurements with such instruments as the LDA or hot wire anemometers. In

reality it is an extension of flow visualization with the addition that quantitative results may be obtained from this method. These results have only become obtainable with the advent of economical image digitization techniques and high speed computer processing software. There are currently two major methods of PIV and numerous variations of the technique. State of the art reviews by Adrian (1986),(1991), Buchave (1992) and others detail the methods employed.

For all methods, a flow field containing seeding particles is illuminated with a strong light source. Images are obtained of the particle movements from which displacement information is obtained. As the time interval between images is known, an instantaneous velocity may be obtained.

$$u = \lim_{t_2 \rightarrow t_1} \frac{l_2 - l_1}{t_2 - t_1} \quad 3.12$$

where

l_2, l_1 particle displacements
 t_2, t_1 time

Sequential images are obtained by strobing the light source with a known frequency, chopping the light source with a rotating mechanical aperture, chopping the light source with an acoustic optic modulator (similar to the Bragg cell used in LDA work), scanning the area with a rotating mirror or using a pulsed laser as the light source. The limitations of the above "chopping" techniques are that a finite amount of light is available and in order to capture the movement of one particle, the particle displacement should be small, which means that most of the light intensity is wasted and this limits these techniques to low speed flows. Below is a listing of the

technique employed and the maximum velocity reported in a selection of current papers.

Table 3.1 PIV methods and reported velocities

Technique	Maximum Velocity (m/s)	Reference
HYCAM - Video digitized	1	Racca(1988)
Photographs - Video digitized	.1	Liu (1991)
Photographs - Mechanical Strobe	.2 .05	Kawahashi (1989) Willert (1991)
Bragg Cell controlled pulse Ar ion laser	10 1 3.4 2	Marko (1985) Cenedese (1990) Khalighi (1989) Winter (1987) Adamczyk (1988)
Video (Frame Speed (1/30) sec)	.4 .001	Camp (1990) Hassan (1991)

The pulsed laser technique uses all the available light intensity for the pulses but pulse separation is not infinitely variable and the high cost of these lasers has precluded their general acceptance.

The difference in technique selected depends on the method to obtain the images, the particle concentration, and the processing method.

Adrian (1991) has defined an image-density parameter N_I such that

$$N_I = C \Delta z_o \frac{\pi d_I^2}{4M^2} \quad 3.13$$

where

N_I image density parameter
 C mean particles per unit volume

Volume of the interrogation spot

Δz_0 distance from the object plane
 π pi
 d_I diameter of interrogation spot
 M Lens Magnification

If the particle concentration is low enough ($N_I \ll 1$), individual particles can be tracked and the displacement of individual particles can be obtained commonly called particle streak velocimetry (PSV). This method can be time consuming unless an automated procedure is employed, such as the one described by Kerstens (1986),(1988). Otherwise, with $N_I \gg 1$ there will be many particle images at the interrogation spot, individual resolution will be impossible and another technique must be employed.

For $N_I \gg 1$ many images can be found at each interrogation spot. In this method a single frame photograph with multiple light pulses is taken of the spot. Particle displacement is small between pulses (10^{-6} to 10^{-3} m Adrian). The processed negative is then analyzed using one of several methods, the most common being Youngs' fringes. Essentially a two-dimensional Fourier transform of the image is formed when a laser beam strikes the interrogation spot causing each pair of particle images to create an interference pattern of light and dark bands. Random displacements will lead to random interference patterns but particle pairs with similar displacement directions will reinforce the interference pattern. As the interrogation

spot is small (~1 mm diameter), the directional error is also small. Several methods are available to analyze the Youngs' fringes but the most common seems to be to acquire the interference pattern with a digital CCD camera and perform a fast Fourier transform (FFT) on the fringe spacing-intensity distribution image.

The advantage of the PIV technique is that it records an instantaneous two dimensional image but requires a great deal of processing time to recover the velocity vectors present. As well, no time history of the flow is available as images are separated by a large amount of time in comparison to LDA or HWA results. Three dimensional PIV has been attempted using stereoscopic images (Sinha (1992), Arroyo and Greated (1991)) or camera defocusing (Willert and Gharib (1992)) but processing time and alignment difficulties have prevented wide acceptance.

3.4 Experimental Conditions

In order to experimentally analyze the flow patterns present, several clear acrylic models have been made with varying geometrical parameters. Acrylic was chosen as the construction material as its index of refraction ($\eta_a = 1.49$) is close to that of the mineral oils ($\eta_o = 1.4622$ @24.6 °C) used in the experimental work and it allows light passage through the chamber for LDA and flow visualization studies. Index of refraction matching is important to minimize optical distortion. Round chamber models were constructed from solid blocks of acrylic with the appropriate chamber diameter bored out of the solid block. Commercial RIM nozzle blocks were fit to the chamber in models 1 and 2 and nozzles were bored in the solid block in the case of model 4. Square chamber models were constructed of 6.35 mm thick acrylic sheet bonded together with the nozzles constructed separately and fastened to the model. Table 3.2 is a list of models used where:

d	nozzle opening diameter
D	main chamber diameter (cylindrical models)
D*	dimensionless chamber diameter (D/d)
H	head length (distance from nozzle centre to closed end of chamber)
H*	dimensionless head length (H/D) or (H/L)
L	main chamber width (square models)
L_c	length of chamber above nozzle centre
L_n	length of nozzle
L*	dimensionless chamber width (L/d)

Table 3.2 Experimental Models

#	D,L (mm)	chamber	d (mm)	L_c	H^*	L_n
1	21.5	round	*1	6.25 D	0.0 *2	*1
	21.5	round	*1	6.25 D	0.5 *2	*1
2	10.0	round	*1	10.5 D	0.0 *2	*1
	10.0	round	*1	10.5 D	0.5 *2	*1
3	20.0	square	2	6.25 L	0.5	> 10 d
	20.0	square	3	6.25 L	0.5	> 10 d
	20.0	square	4	6.25 L	0.5	> 10 d
4	25.4	round	2.4	6 D	variable	5.5 d

All dimensions in mm

1. Constructed to accept commercially available Impianti nozzles which have an adjustable flow control needle with no straight nozzle length as shown in Figure 2.3. Nominal openings of 1 mm and 2 mm are available.
2. Inserts were constructed to vary the head length. H^* is the Z distance from $Z = 0$ to the surface of the head divided by the chamber diameter D. $H^* = 0$ means that the head surface is flush with the bottom of the nozzle openings ($H=d/2$).

In addition to the above models a constriction or "choke" was fabricated for Model 1. The "choke" fit the bore diameter (21.5 mm) and had an concentric inside diameter of 10.0 mm. It could be placed at any Z distance in the model, the distance characterized by C^* the Z distance above $Z = 0$ divided by the chamber diameter D. The purpose of the choke was to alter the chamber area and increase the pressure in the impingement area.

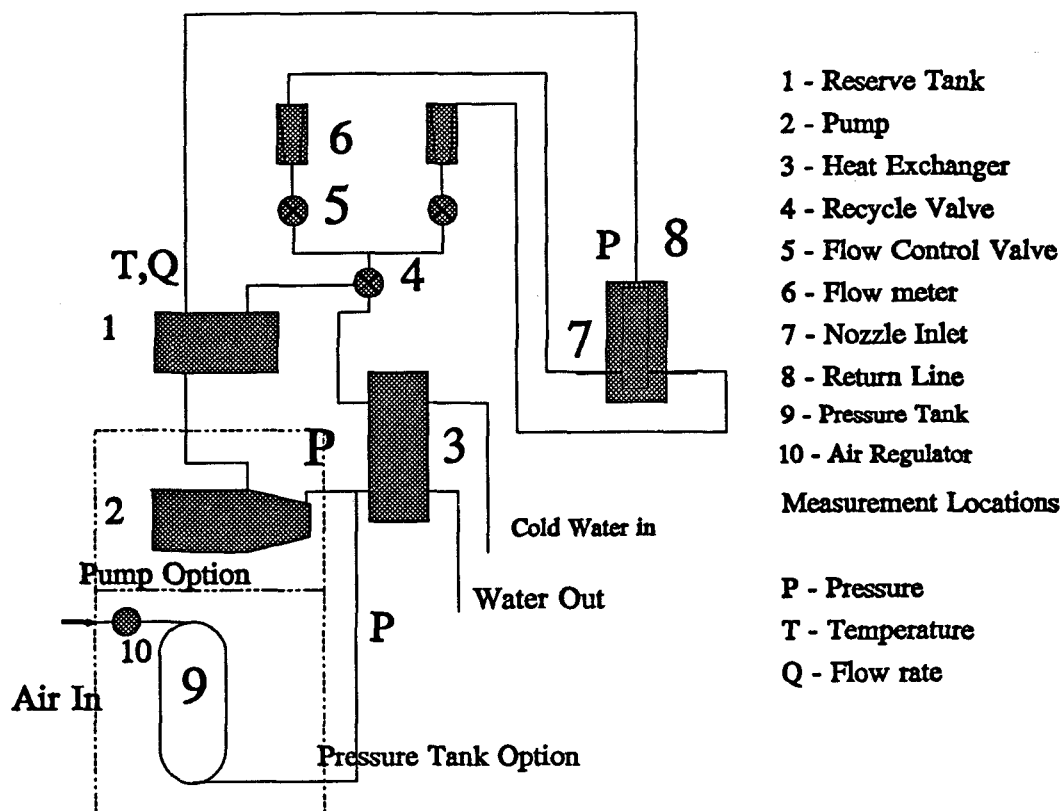


Figure 3.3 Flow Loop Schematic

The flow loop is shown schematically in Figure 3.3. Two fluid delivery systems were implemented. In the first system, fluid is held in reserve tanks above the pumps. Two pumps are available but only one loop will be described. The variable speed progressing cavity pump (Moyno # 33104) drew fluid from the reserve tank and pumped it through accumulators to dampen pulsations to the heat exchanger (counter flow type). Flow then went to a control valve which adjusted the amount of recycle back to the reserve tank, the remainder splitting and flowing to two needle valves and variable area rotameters (Brooks 8602-162153) before proceeding to the nozzle inlets. Outlet from the model chamber was directed back to the reserve tank

where the flow rate was obtained with a stopwatch and graduated cylinder. System pressure was monitored at the pump (gauges) and after the accumulators with pressure transducers with input to the computer during data collection; chamber pressure was monitored at the chamber outlet. The reserve tanks were constantly stirred to maintain uniform temperature and the temperature was monitored at the chamber outlet to the reserve tank. In the second system the pumps were eliminated and the flow was driven by constant pressure from a large reservoir through the flow meters to the model in order to eliminate any external effects due to pump frequencies. In both cases pressure oscillations were recorded during data collection, using a pressure transducer input to the computer.

Mineral oil $\rho = 840 \text{ kg/m}^3 @ 25^\circ\text{C}$ (Esso ISOPAR M R 2056 and other suppliers) was used as the representative fluid because of the wide range of viscosities obtainable (1-400 cP), the stability of the oil, and of paramount importance, the close agreement between the index of refraction for acrylic ($n_{\text{acr}} = 1.4893$ and mineral oil $n_{\text{oil}} = 1.4622 @ 24.6^\circ\text{C}$). Viscosities were obtained with a Brookfield LVT viscometer.

3.4.1 Experimental Details - Flow Visualization

Initially, for all cases examined, flow visualization was performed to determine areas of interest for further investigation and subsequent analysis with the LDA. The results of these flow visualizations were recorded on SVHS (Panasonic) video tape recorder from a colour 8 mm video camera (Sony V9) or from a black and white CCD

camera (Panasonic MF 552). Playback of the images was available with slow motion frame by frame analysis. Still photographs were also obtained using slide film (Kodak Ektachrome) or black and white print film (Kodak TMAX and others). Table 3.3 details flow visualization studies performed for cases where both nozzle inlets had equal flow rates and equal viscosity.

Table 3.3 Flow Visualization: Equal Flow Rates

Model	Re_d range	μ (cP)	Technique	Recording Med.
1	50 - 400	10 -60	1,2,3	Photographs and Video
2	50 - 300	10-60	1,2,3	"
3	50 - 300	4-2000	1,2	"
4	20 - 300	10-50	1,2	"

1. Polystyrene particles and laser light sheet
2. Laser induced fluorescence (Fluorescent dye)
3. Dye and white light

Tables 3.4,3.5 summarize flow visualization studies performed where the viscosities were the same but the flow rates were not identical at both nozzles.

Table 3.4 Unequal Flow Cases : 1

Model	Re_d	μ (cP)	H^*	N (mm)	d (mm)	D^*
1	217	45.5	0.5	1,3	2	10.75
	458	45.5		1,3	2	

Table 3.5 Unequal Flow Cases : 2

Model	Re_d	Q_1/Q_2	μ (cP)	H^*	d (mm)	N (mm)	D^*
1	100 - 300	2 - 10	40 - 60	0	2	1	10.75
1	100 - 300	2 - 10	40 - 60	0	2	3	10.75
1	100 - 300	2 - 10	40 - 60	0.5	2	1	10.75
1	100 - 300	2 - 10	40 - 60	0.5	2	3	10.75
2	30 - 300	2 - 10	40 - 60	0	2	1	10.75
2	30 - 300	2 - 10	40 - 60	0	2	3	10.75
3	40 - 300	1.73	33	0.0	2.38	-	10.67

Table 3.6, 3.7 summarize cases where the viscosities were not the same at each nozzle.

Table 3.6 Unequal Viscosity Cases : 1

Model	Re_d	μ (cP)	H^*	N (mm)	d (mm)	D^*
1	103-225	32.0	0.5	1	2	10.75
	61-138	54.4		1	2	

Table 3.7 Unequal Viscosity Cases : 2

Model	Re_d	μ (cP)	H^*	N (mm)	d (mm)	D^*
1	82-202	18.0	0.5	1	2	10.75
	33-65	54.4		1	2	

Tables 3.8, 3.9 summarize cases where a constriction was placed in the main chamber.

Table 3.8 Restricted Flow Cases : 1

Model	Re_d	μ (cP)	C^*	H^*	d (mm)	N (mm)	D^*
1	100 - 300	20 - 50	0.25	0 0.5 1.0	2	1	10.75
1	100 - 300	20 - 50	0.5	0 0.5 1.0	2	1	10.75
1	100 - 300	20 - 50	1.0	0 0.5 1.0	2	1	10.75
1	100 - 300	20 - 50	0.25	0 0.5 1.0	2	3	10.75
1	100 - 300	20 - 50	0.5	0 0.5 1.0	2	3	10.75
1	100 - 300	20 - 50	1.0	0 0.5 1.0	2	3	10.75

Table 3.9 Restricted Flow Unequal Flow Cases : 1

Model	Re_d 1,2	μ (cP)	C^*	H^*	d (mm)	N (mm)	D^*
1	140 - 320 76 - 150	20 - 50	0.25	0 0.5 1.0	2	1	10.75
1	140 - 320 76 - 150	20 - 50	0.5	0 0.5 1.0	2	1	10.75
1	140 - 320 76 - 150	20 - 50	1.0	0 0.5 1.0	2	1	10.75
1	140 - 320 76 - 150	20 - 50	0.25	0 0.5 1.0	2	3	10.75
1	140 - 320 76 - 150	20 - 50	0.5	0 0.5 1.0	2	3	10.75
1	140 - 320 76 - 150	20 - 50	1.0	0 0.5 1.0	2	3	10.75

3.4.2 Experimental Details - Laser Doppler Anemometry

Once visual records of the flow fields were recorded, LDA measurements were obtained at predetermined locations for the axial (W) and jet plane (U) velocity components. Normally, 10,000 validated data points were collected at each measurement location for each component at a constant predetermined frequency. Data collected was stored in binary form until it was later processed to determine statistical results and frequency spectra. Factors which affect data collection in LDA, such as velocity biasing and optical corrections, are well documented. Measuring points within a flow with different velocities can lead to velocity biasing. When the

velocity is high the number of particles passing the measurement volume is much higher than the number of particles passing the measurement volume at lower velocities; hence any averaging of the collected data will be biased towards the higher velocities. Methods to avoid velocity biasing and articles questioning the reality of biasing are common (Edwards 1979). Craig *et al.* (1986) detail a method of Stevenson *et al.* (1983) which suggests increasing the seeding rate at a constant sampling interval until no further reduction in the measured velocity is seen; however, this method is not useful if it must be attempted at each measurement location. Stevenson *et al.* (1983) state laminar flows and low turbulence intensity flows do not have significant biasing, as the error is proportional to the square of the turbulence intensity. To avoid the possibility of this problem, data is sampled at regular intervals less than the incoming data rate.

3.4.3 Optical Correction

When light in air travels through a denser medium the light is refracted towards the normal. The relationship is described by Snells' law

$$\eta_1 \sin \theta_1 = \eta_2 \sin \theta_2 \quad 3.14$$

where

- η index of refraction for material
- $\theta_{1,2}$ angle between normal and incident beam

For LDA purposes this means that measurements obtained inside a model will require correction to determine the location of the measurement volume. For the

square model geometry (Model 3) both beams are refracted by an equal amount and the calculation is straightforward. For round model geometries, the correction becomes more difficult because of the unequal path length travelled by each beam: an iterative procedure is required to locate the intersection of the beams.

Another difficulty in obtaining measurements with the LDA is the fluctuating data rate resulting from the fluctuating particle count. This obstacle is overcome through constant frequency data collection.

Table 3.10 details LDA measurements obtained with models 3 and 4 (straight nozzles).

Table 3.10 LDA Studies Models 3 and 4

Model	Re_d range	Coverage	μ (cP)	L^*, D^*	H^*
3	30 - 400	2,3	23 - 200	5	0.5
3	30 - 400	2,3	23 - 200	6.67	0.5
3	30 - 400	2,3	23 - 200	10	0.5
3	75 - 1000	1	15 - 50	5	0.5
3	75 - 1000	1	15 - 50	10	0.5
4	75 - 150	3	23	10.67	0
4	75 - 150	3	23	10.67	0.25
4	75 - 150	3	23	10.67	0.5
4	50 - 150	2	48	10.67	0.5 0

1. Entire model 10,000 data/pt
2. Axial Velocity Profiles 10,000 data/pt
3. Frequency Analysis 8,000 data/pt

Table 3.11 details measurements obtained using models 1 and 2 which use

commercial nozzles. The Re_d values were selected based on normal mix head operating conditions.

Table 3.11 LDA Studies Models 1 and 2

Model	Re_d	μ (cP)	H^*	D^*	N (mm)
1	304	53	0.0	10.75	1
1	304	53	0.0	10.75	3
1	304	53	0.5	10.75	1
1	304	53	0.5	10.75	3
2	325	48	0.0	5.0	1
2	325	48	0.0	5.0	3
2	325	48	0.5	5.0	1
2	325	48	0.5	5.0	3

Measurements were made at $Z^* = 0$ along the jet axis in the Y plane for the case detailed in Table 3.12. Commercial nozzles were used which have an adjustable pin which restricts the flow while open and completely closes the opening when the injection process is complete. The nozzle cross section is shown in Figure 2.3 and consists of three inlet flow tubes entering a chamber before the sharp edge nozzle exit. Detailed U measurements were made along the y axis for 10 x values to determine the jet characteristics at a representative Re_d .

Table 3.12 Developing Jet LDA conditions

Model	Re_d	μ (cP)	H^*	D^*	N (mm)	d (mm)
1	275	60.0	0.5	10.75	3	2

LDA measurements were obtained for the case of unequal flow rates listed in Table 3.13. As in the equal flow commercial nozzle cases, values were selected to represent those found in practice.

Table 3.13 Unequal Flow Cases LDA conditions

Model	Re_d	μ (cP)	H^*	D^*	N (mm)	d (mm)
1	217	45.5	0.5	10.75	1	2
	458	45.5	0.5	10.75	1	2

The LDA study using a flow restriction is outlined in Table 3.14 using model

1. A typical value of Re_d was chosen.

Table 3.14 Restricted Flow Cases : LDA conditions

Model	Re_d	μ (cP)	C^*	H^*	d (mm)	N (mm)	D^*
1	300	50	0.5	0.5	2	3	10.75

4.0 Numerical Technique

Three dimensional simulations were carried out for various cases, using the commercial CFD code FLUENT (1991). These simulations were used to model the opposed jets in a confined chamber because of the inadequacy of previous studies in predicting the flow patterns using symmetry planes to model one quarter of the chamber. Flow visualization results described in a later section show that the flow structure is three dimensional for all but the lowest values of Re_d .

The code solves the fundamental equations governing the flow using a finite volume numerical procedure. In essence, the region of interest is divided into a finite number of control volumes. In each control volume the partial differential equations are discretized to form sets of non-linear, inter-related algebraic equations which are solved iteratively. The procedure is detailed in Patankar (1980).

4.1 Grid

For the modelling of the square chamber geometry a non uniform three dimensional finite difference grid was selected using grid densities similar to those of Yeo (1993); then a concentration of grids was located close to the area of the jets issuing from the nozzles and in the area where the impingement of the jets would take place. The grid used is shown in Figure 4.1.

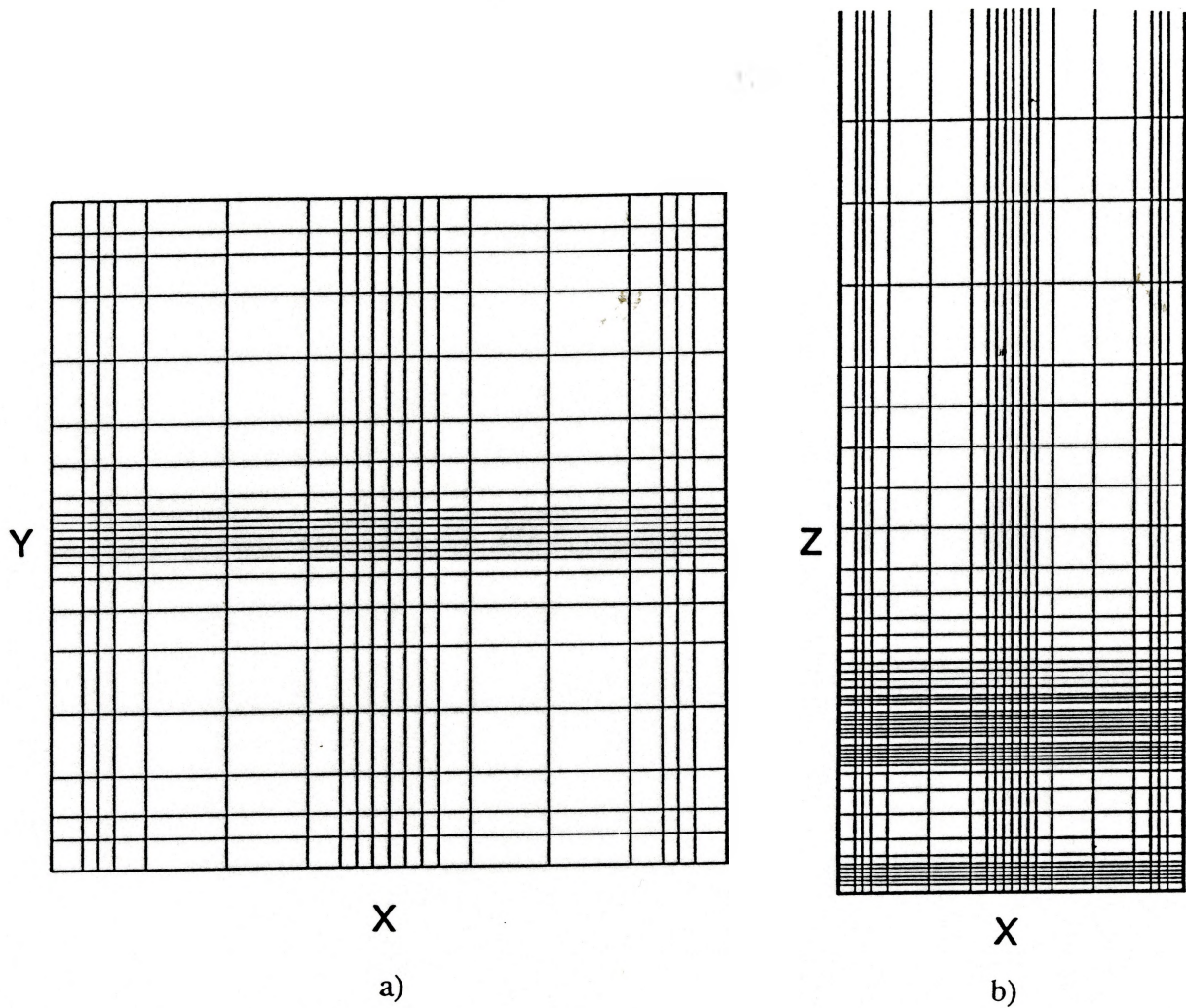


Figure 4.1 Numerical Grid (a) (left side) XY plane (b) XZ plane

4.2 Boundary Conditions

For the inlet boundary condition the circular nozzle inlet is approximated on the rectangular grid and a fully developed pipe flow profile is applied as the inlet condition. 7×7 grids were used for the $21 \times 23 \times 52$ cases and 7×14 grids were used for

the 21x23x102 cases for the inlet nozzles.

$$u=2u_{avg}\left(1-\left(\frac{r}{R}\right)^2\right) \quad 4.1$$

Simulations with a uniform average velocity were also carried out. Poor agreement with experimental results, in particular the peak values of W^* and outlet flow values, led to the fully developed circular pipe flow profile being used for the nozzle inlets.

The chamber outlet was located 20 L from the point of impingement to ensure fully developed flow at the outlet. Flow inlet conditions were also checked using the outlet area average flow as an indication of an appropriate inlet flow rate. All other boundaries were specified as no slip wall conditions. Properties used for the simulations were $\rho = 840 \text{ kg/m}^3$, $\mu = .05 \text{ kg/ms}$ @ 20°C , which is representative of the mineral oil used in the experimental studies; although simulations using water properties showed identical results when made dimensionless with the inlet velocity. Table 4.1 details the numerical simulations.

Table 4.1 3-D Numerical Simulations

Model	Re_d	Grid (x,y,z)	H^*	L^*	Numerical Solution Method
3	50 - 300 steps of 25, 1000	21x23x102	0.5	10	steady laminar
3	50 - 300 steps of 25	21x23x102	0.5	5	steady laminar
3	1000, 2000, 5000	21x23x52	"	10	Turbulent steady k - ϵ
"	1000, 5000	"	"	10	Turbulent steady ASM
"	75, 125, 150	"	"	10	transient laminar

Converged steady solutions were obtained for all cases of $Re_d < 300$ and $Re_d = 1000$. For $300 < Re_d < 1000$ converged steady solutions were not found. The convergence criterion was defined as the sum of all residuals should be less than 10^{-3} . As the flow visualizations revealed an unsteady flow field for $Re_d > \sim 90$, unsteady numerical simulations were obtained for values of $Re_d \geq 100$. Time dependent solutions for a similar geometry ($D^* = 10$, $H^* = 0.5$ and 1.0) have recently been reported by Yeo (1993).

5.0 Results

Experimental results indicated that the division of results should be based on flow field behaviour based on Reynolds number. All models exhibited stationary flow fields for certain values of Re_d , regular oscillatory flow fields for higher Re_d , and irregular flow fields following oscillatory behaviour.

5.1 Pre Oscillatory Behaviour

Opposed jet impingement can be considered a composite of several flow structures such as the free laminar jet, a curved shear layer, a stagnating impingement flow, a radial jet flow, recirculating flow and developing conduit flow. All of these flow structures have been studied separately in some detail by many researchers. Amalgamation of all these components leads to a complex flow field. Initially at low values of Re_d a steady flow regime exists with all components represented producing a complex flow field.

5.1.1 Flow Visualization $Re_d < \sim 90$

For all models (1-4) (Table 3.3) for all flow conditions the flow field of $Re_d < \sim 90$ was seen to be stationary and unaffected even by sudden transient changes in fluid velocities such as those caused artificially by tapping on the jet inlet line. In this instance the flow field was temporarily disrupted but would return after the transient

had passed. The two jets remained cylindrical with an insignificant amount of spreading to just before the point of impingement for $Re_d > 50$. At values of Re_d below this value the flow field differed in that the jets did not impinge but turned and flowed toward the outlet. For $Re_d > 50$ particle streaks from either jet side were observed to reach the geometric centre of the chamber. At the chamber centre a small "disc" was observed where the jets collide and spread out in the radial direction with the jet centre line axis as the origin. The observed disc had a diameter not significantly larger than the jet diameter (in YZ plane) and a thickness (X direction) less than 1 d. From this disc the fluid flowed radially outward in all directions in the form of a free radial jet losing velocity and spreading in width. Impingement of the fluid from the disc on the chamber bottom causes the fluid to divide and flow along the chamber bottom. In the plane of the jets, fluid flows along the chamber bottom and up the wall surface creating a rotating vortex driven by the incoming jet and the downward disc flow. Particles and air bubbles are occasionally observed to remain in this vortex for long periods of time with transient flow unable to dislodge them. A similar phenomenon occurs above the jets with the exception that there is no physical upper bound confinement, although the fluid leaving the disc loses velocity and is re-entrained by the jet-disc structure. The upper vortex pair was always observed to be larger than the lower vortex pair. In the plane of the disc and perpendicular to the jet axis the fluid was observed to flow outwards in all directions from a source of roughly jet diameter dimensions. In the plane through the XY axis at $Z=0$ the fluid was seen to impinge and flow outward to the chamber walls and then follow the chamber wall

to the incoming jet forming two pairs of rotating vortices. A typical example of a stable flow field is shown in Figure 5.1.1 using Model 4 where $Re_d = 73$ and $\mu = 52$ cP created using the particle streak - laser light sheet method.

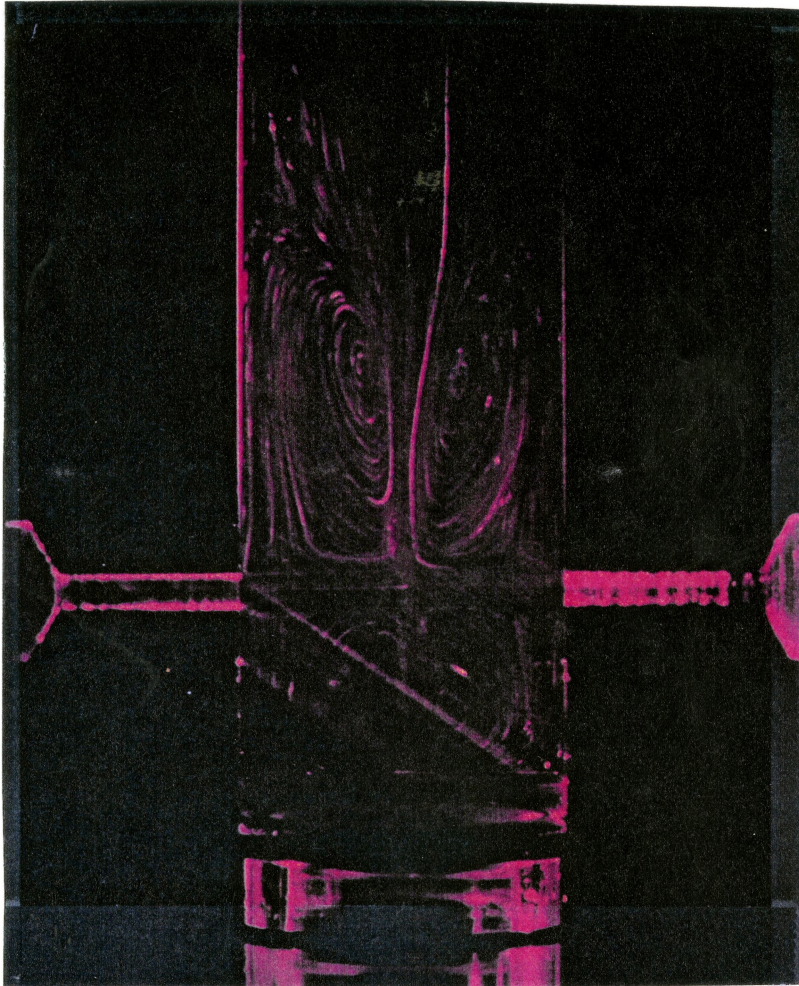


Figure 5.1.1 Model 4 $Re_d = 73$ $\mu = 52$ cP

When one jet is dyed with fluorescent dye, very little interaction was observed between the jet fields when the field is illuminated with the argon laser exciting the dyed fluid using the LIF technique. Undyed fluid is seen to remain in the vortices above and below the undyed jet for the entire duration of the video taping.

Thus, the steady flow field may be described as two opposed jets creating a

fluid disc at their point of impingement which releases fluid at its periphery, causing a toroidal shape with recirculating vortices extending to the chamber boundaries or to the edge of recirculation, in the case of the chamber outlet.

5.1.2 Laser Doppler Anemometry $Re_d < \sim 90$

Data from the representative case $Re_d = 75$ ($L^* = 10$, $d = 2$ mm, $\mu = 35$ cP, Model 3) is presented in Figure 5.1.2. The XZ plane at $Y = 0$ is presented. Because of optical access difficulties LDA data is unobtainable close to the periphery of the model. A numerical simulation of the same condition ($Re_d = 75$, $L^* = 10$, $d = 2$ mm, Model 3) is presented adjacent to the experimental data. Velocities have been made dimensionless with the average inlet velocity and two dimensional particle path lines laid over the velocity vectors beginning at the nozzle inlet. Although the vortices below the jets are seen to be in close agreement, the simulation predicts the vortices above the jets to be closer to the jets than the experimental data suggests. The sparseness of experimental data in this region could be a factor in the accurate determination of the core of the vortices. The location of the vortex core is detailed in Table 5.1.1 from flow visualization photographs, LDA measurements, and FLUENT numerical simulations.

Table 5.1.1 Vortex Location $Re_d = 75$

	Lower	Vortex	Upper	Vortex
	X^*	Z^*	X^*	Z^*
Flow Visualization	1.3	-3.7	1.5	6.5
LDA data	1.2	-3.3	2.2	8.6
Numerical Simulation	1.0	-3.6	1.2	7.5

In the figure below the particle path line showing the flow in the Z direction shows slight curvature in the experimental case near the upper vortices and only marginal curvature in the simulation.

Contours of U^* are presented for the same case in Figure 5.1.3. Overall agreement is close, with the simulation predicting the $U^* = 0$ contour very well. The penetration distance of the incoming jets to the point of impingement also agrees well and the simulation shows a contour of $U^* = 0$ running vertically along the Z axis; whereas the experimental work shows a slight curvature, as seen previously in the particle path lines. W^* contours are shown in Figure 5.1.4. Again overall agreement is good with the simulations predicting the contours very well. The increase in W^* at the point of impingement is well predicted, as are the $W^* = 0$ contour lobes above the jets defining the recirculation areas.

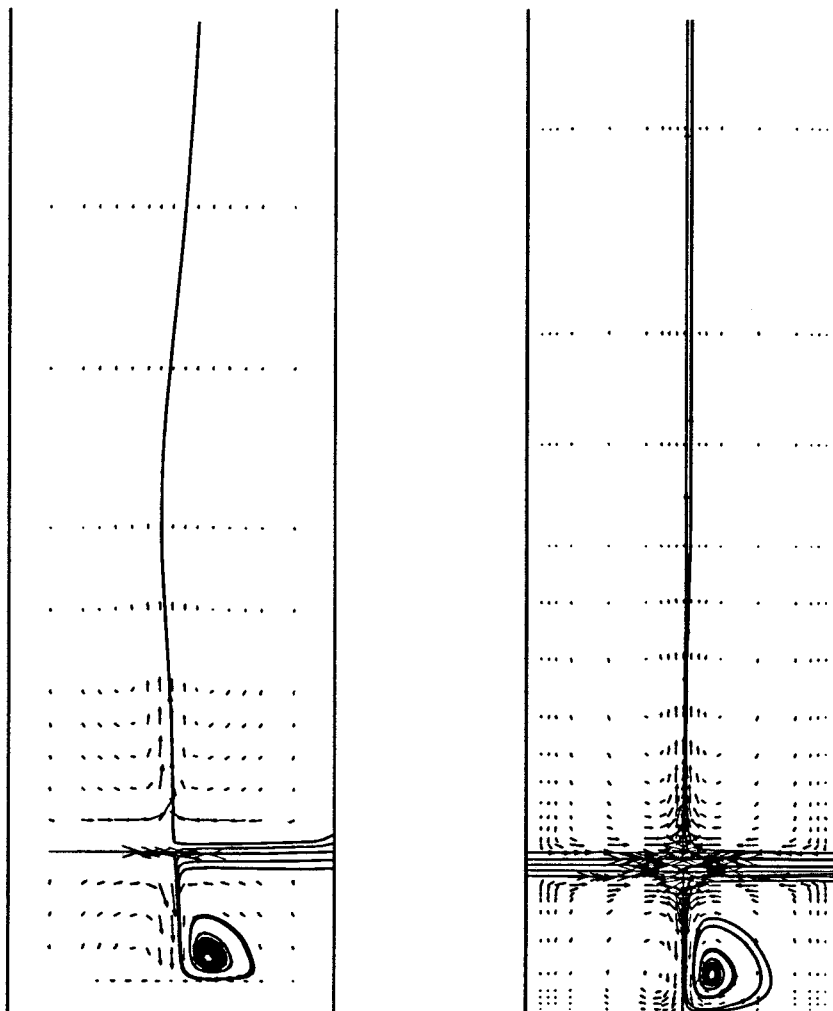


Figure 5.1.2 Vector Plot of U^* , W^* in XZ plane at $Y = 0$ (a) left side LDA data $Re_d = 75$ ($L^* = 10$, $d = 2$ mm, $\mu = 35$ cP, Model 3), (b) right side FLUENT simulation $Re_d = 75$. Dimensionless unit vector 0.25

The experimental data show a flow field which has some curvature in the W^* flow above the jets, although the simulation for $Re_d = 75$ shows a flow field which is symmetric about the impingement Z plane.

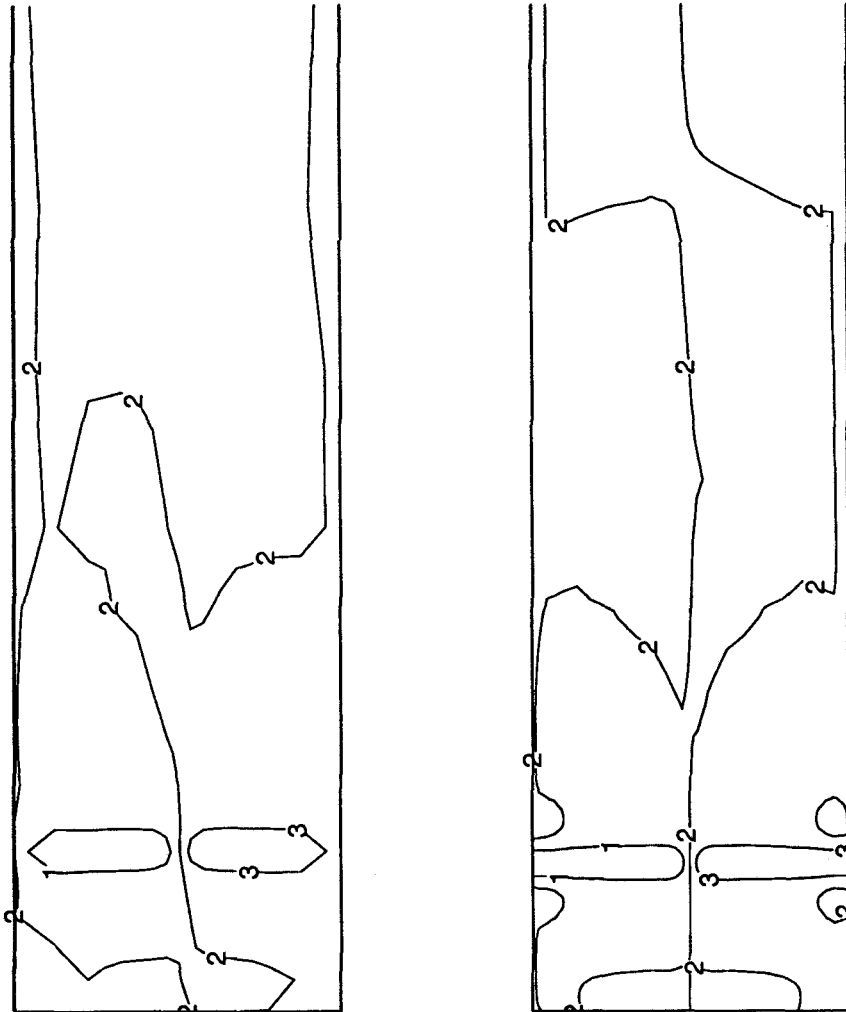


Figure 5.1.3 Contours of U^* in XZ plane at $Y = 0$ (a) left side LDA data $Re_d = 75$ ($L^* = 10$, $d = 2$ mm, $\mu = 35$ cP, Model 3), (b) right side FLUENT simulation $Re_d = 75$. Dimensionless contour values: 1 $U^* = -0.5$, 2 $U^* = 0$, 3 $U^* = 0.5$

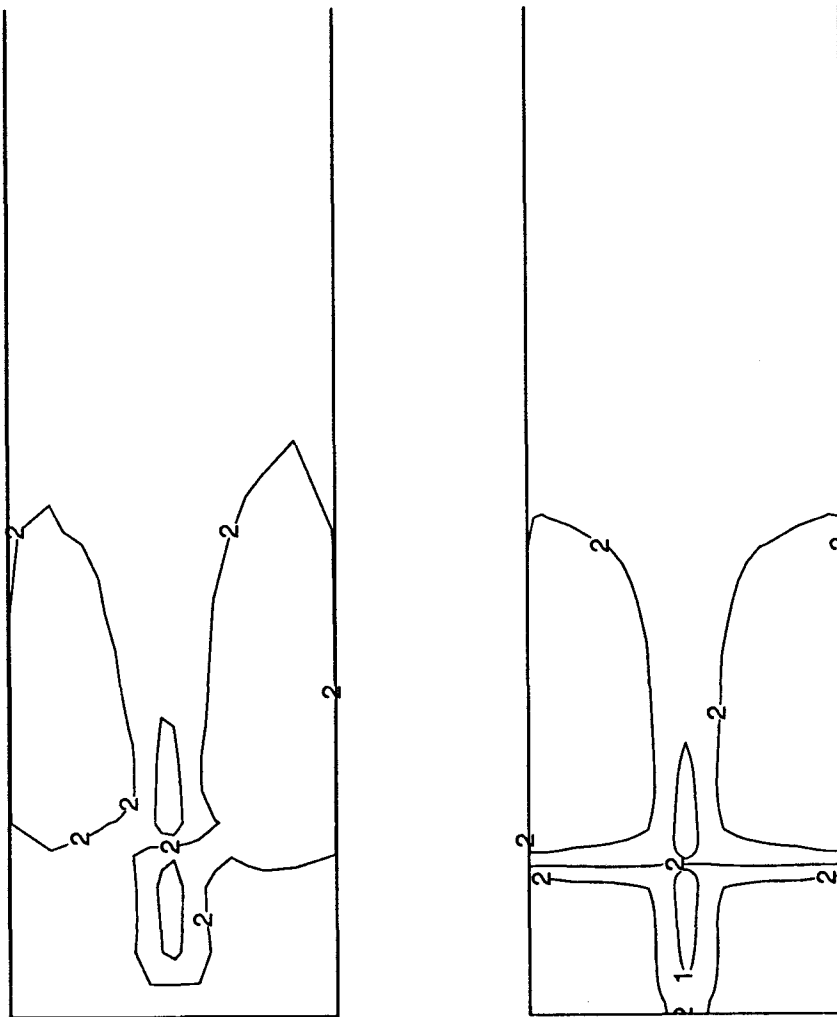


Figure 5.1.4 Contours of W^* in XZ plane at $Y = 0$ (a) left side LDA data $Re_d = 75$ ($L^* = 10$, $d = 2$ mm, $\mu = 35$ cP, Model 3), (b) right side FLUENT simulation $Re_d = 75$. Dimensionless contour values: 1 $W^* = -0.25$, 2 $W^* = 0$, 3 $W^* = 0.25$

Figure 5.1.5 shows experimental data and numerical simulation results for W^* vs Z^* at $(0,0,Z^*)$ (i.e. axial velocity along the chamber axis). The simulation for $Re_d = 50$ is included on the plot for reference. The simulation predicts W^* well, although the peak W^* attained is over predicted by 22% above the jets and over predicted by 16%

below the jets.

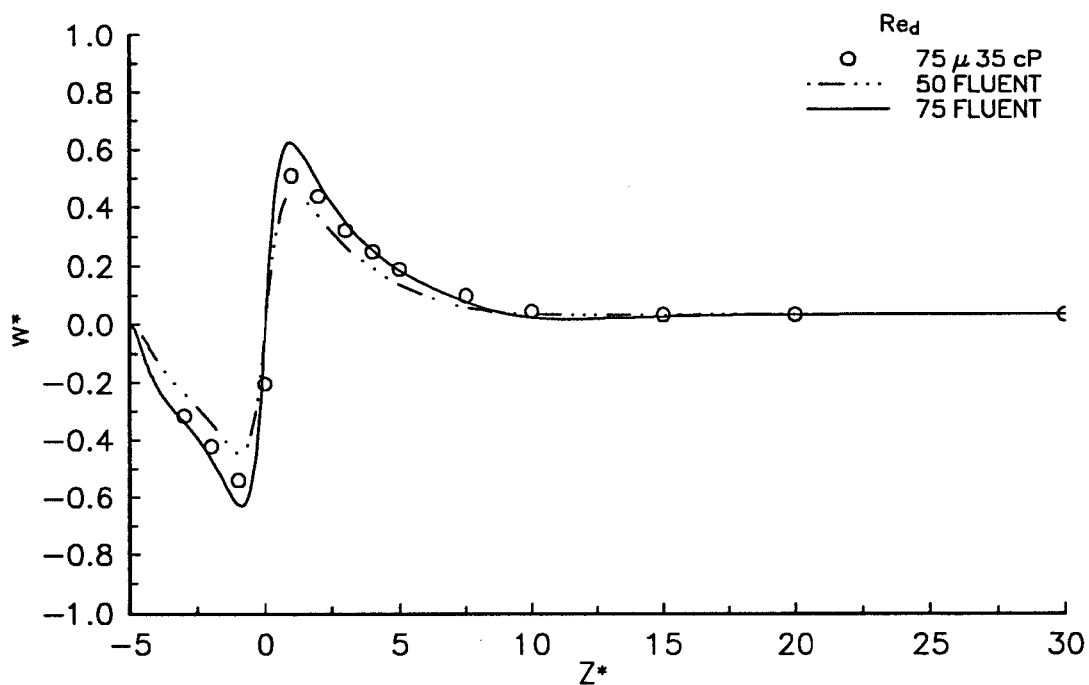


Figure 5.1.5 W^* vs Z^* at $(0,0,Z^*)$ $Re_d = 75$, LDA Data and FLUENT Simulations

The peak W^*_{max} and its location are given in Table 5.1.2 for $Re_d = 75$.

Table 5.1.2 Peak W^* values $Re_d = 75$

	Location Z^*	W^*_{max}
LDA data	1.0	0.5105
FLUENT simulation	0.9375	0.6251
LDA data	-1.0	-0.5400
FLUENT simulation	-0.9063	-0.6295

This disagreement may be more a function of the LDA data missing the peak

value location than an over prediction by the simulation. The outlet W^* values agree well. The LDA data (average velocity based on measured volumetric flow rate) is 0.3% below the theoretical fully developed value and the simulations are 3% above the theoretical value. Numerical simulations have inlet values which are also 3% above the theoretical value because of the modelling of the inlet condition on the orthogonal grid. A parabolic inlet profile was applied to an approximation of a circular orifice. Values of W^* at the outlet are tabulated in Table 5.1.3.

Table 5.1.3 Outlet W^* $Re_d = 75$

	W^* at $Z^* = 30$
Theoretical	0.3283
LDA data	0.3272
FLUENT Simulation	0.3383

A profile of the jet velocity U^* versus X^* is shown in Figure 5.1.6. The simulation at $(X^*, 0, 0)$ over-predicts the velocity profile away from the geometric impingement area. Analysis of the experimental W^* data revealed that a significant negative velocity ($-W^*$) existed at the predicted point of impingement, a result which agreed well with the simulation at $Z^* = -0.132$. For this reason the U^* simulation results at $Z^* = -0.132$ are included on the plot. The U^* profile 0.132 Z^* below the jets is identical to the profile at $Z^* = 0$ in the region of the point of impingement, but varies from $Z^* = 0$ away from the impingement point. The simulation results at $Z^* = -0.132$ are in better agreement with the experimental results and suggest that the geometrical positioning of the model may have been in error by 2.7% in the Z^*

direction.

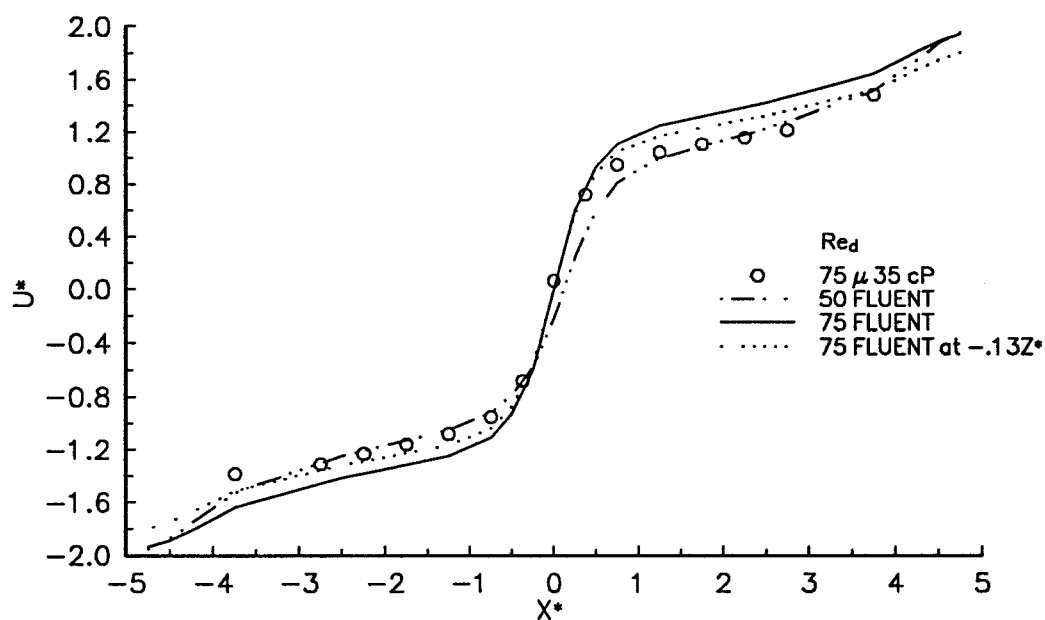


Figure 5.1.6 U^* vs X^* at $(X^*, 0, 0)$ LDA Data and FLUENT Simulations

As further confirmation of this apparent location error, the W^* vs X^* for $Z^* = 0$ results are presented in Figure 5.1.7. The experimental data show a significant negative W^* peak at $X^* = 0$. The simulation at $X^* = 0$ shows a very small peak at the same point. Results from the simulation at $-0.132 Z^*$ are in much better agreement with the data which show an asymmetric value at $0.5 > X^* > 0$.

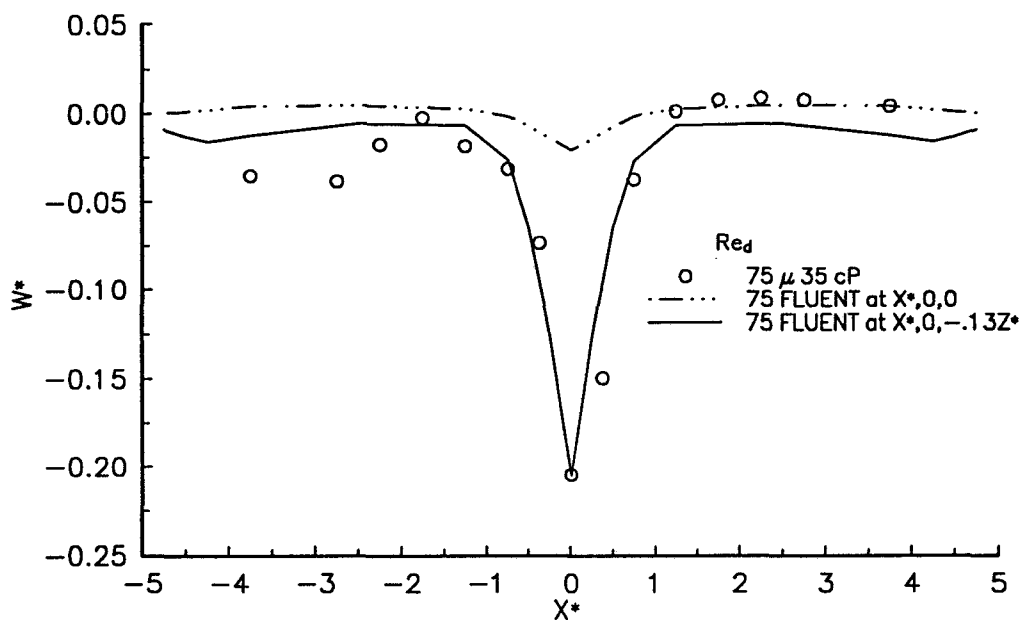


Figure 5.1.7 W^* vs X^* at $(X^*, 0, 0)$ LDA Data and Fluent Simulations

The agreement between the simulation and the data is further reinforced by the plot of W^* vs X^* at $Z^* = 1$ (Figure 5.1.8). The simulation is seen to over-predict the peak value at $X^* = 0$ but, as the slope of W^* is very steep for $-1 < X^* < 1$, the possibility exists that the peak experimental value was missed. Other values are in excellent agreement, with the exception of a skewed value at $X^* = -0.5$, which is probably due to the skewed impingement disc as observed previously.

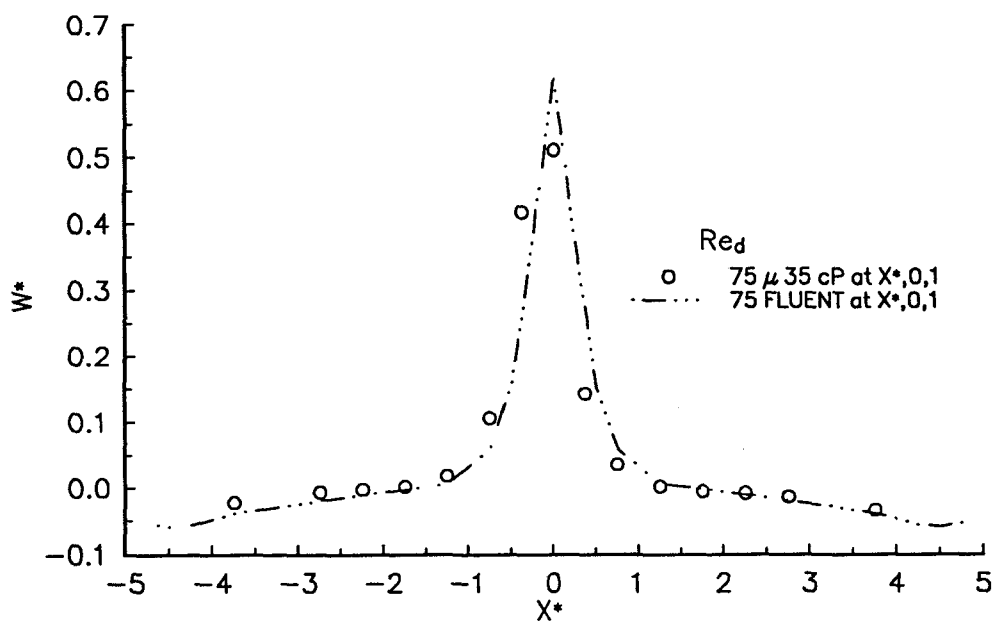


Figure 5.1.8 W^* vs X^* at $(X^*, 0, 1)$ LDA Data and Fluent Simulations

A steady flow field has been documented for $Re_d < \sim 90$ for all models examined (1-4) through the use of flow visualization and laser Doppler anemometer velocity measurements. Transient perturbations were damped by the flow structures present. Here numerical simulations of the flow field agree well with the experimental data. These Re_d are somewhat lower than those previously documented for steady flow, but previous flow visualization studies have no concrete definition of steady flow. Values of $Re_d = 204$ ($L^* = 12$ and $D^* = 10$, $d = 10$ mm) were considered steady by Akaike *et al.* (1986) although their flow visualizations with hydrogen bubbles in water show a curved impingement disc at the time of the photograph and $Re_d = 146$

shows significant curvature of the impingement interface. Similarly, all figures shown in Sandell *et al.* (1985) ($D^* = 5.5$, $d = 9.5$ mm, $\theta = -30^\circ$, $H^* = 0.73$) show an unsteady impingement area ($155 < Re_d < 720$), although frequency determination is only given for values of $Re_d > 250$. Tucker and Suh (1980) found that a directly opposed nozzle configuration reached a "critical" Re_d before configurations with the nozzles aimed at the head region; a finding which would explain the discrepancy with the studies by Sandell *et al.* (1985) above.

5.2 W Velocity Measurements

Measurements of axial W velocity in the impingement region have been obtained in order to clarify the structure present under three flow regimes; stable non oscillatory flow $Re_d < \sim 90$, regular oscillatory flow $90 < Re_d < \sim 150$ (depending on L^*), and post oscillatory flow $Re_d > \sim 150$. Simulations for representative Re_d have been obtained and compared with the experimental data. Experimental velocity measurements at comparable Re_d do not exist in the literature, except those few previously reported in Wood *et al.* (1991).

W velocity measurements were obtained for values of L^* (L/d) of 10, 6.67 and 5 (Model 3) for the range of Re_d from 50 - 400 in the z direction. These velocity results have been made dimensionless with the average inlet velocity obtained from flow measurements using a graduated cylinder and stopwatch ($W^* = W/U_{avg}$) and the axial distances have been made dimensionless with the inlet diameter ($Z^* = z/d$).

In an effort to collapse all W velocity profiles, a momentum parameter was developed to scale the velocities. Using the total inlet momentum from one axisymmetric inlet jet

$$M = \int_0^r u^2 y dy \quad 5.2.1$$

Assuming a parabolic inlet profile from a fully developed nozzle flow

$$u = u_{max} \left(1 - \left(\frac{y}{r}\right)^2\right) \quad 5.2.2$$

gives a total momentum for one jet of

$$M = \frac{(u_{\max})^2 r^2}{6} = \frac{(2u_{\text{avg}})^2 r^2}{6} \quad 5.2.3$$

The momentum was not found to be a better scaling factor for the W velocity measurements than U_{avg} away from the radial jet area. The true free radial jet with a momentum source composed of two circular discs of radius r_0 and separation distance h was presented by Schwarz (1963).

$$w = \left[\frac{9M^2}{32\nu} \right]^{\frac{1}{3}} [r^3 - l^3]^{-\frac{1}{3}} \text{sech}^2 \left[\frac{\left(\frac{3M}{16\nu^2} \right)^{\frac{1}{3}} r y}{(r^3 - l^3)^{\frac{2}{3}}} \right] \quad 5.2.4$$

where l is the distance to the virtual origin of the radial jet and

$$w_{\max} = \left[\frac{9M^2}{32\nu} \right]^{\frac{1}{3}} (r^3 - l^3)^{-\frac{1}{3}} \quad 5.2.5$$

This result would suggest that the w velocity at $x=0$, $y=0$ depends on the inlet velocity according to

$$w \propto u_{\text{avg}}^{\frac{4}{3}} \quad 5.2.6$$

in the region where a fully developed radial jet occurs. This analysis is based on similarity profiles and does not apply to the near nozzle region or the transition region.

Figure 5.2.1 [Additional cases for differing conditions are shown in Appendix A Figures A5.2.1-5] shows the results for a 2 mm jet using 50 cP oil. In these figures a peak W^* of 0.4 was found at 1 jet diameter ($Z^* = 1$) above the geometric point of

impingement and a peak W^* of -0.75 was found at $Z^* = 1$ below the geometric point of impingement. Figure 5.2.2 shows the results for a 2 mm jet using 25 cP oil. In these figures a peak W^* of 0.6 was found at $Z^* = 1$ above the geometric point of impingement and a peak W^* of -0.6 was found at $Z^* = 1$ below the geometric point of impingement. Sample data for $d = 2$ mm jets are presented in Table 5.2.1 which shows the symmetry of the flow above and below the geometric point of impingement for $Re_d < 157$. There is some scatter in the velocity profiles and this may be attributed to probe volume positional inaccuracy, imbalance in the momentum of the jets, and oscillation of the impingement area. Probe volume location inaccuracy was not considered to be a significant factor in the measurement scatter. There is some difficulty in obtaining ideal momentum balance conditions at the geometric centre especially for the higher Re_d cases. The normal procedure was to locate the probe volume at the geometric centre and then adjust the needle valves, while obtaining the U velocity. These adjustments were so small that the effect was not seen on the flow meters. A minimal U velocity was taken to signify a balance between the two jets. Since at higher Re_d stable conditions were not found, the jets were balanced as well as possible, allowing for the oscillation of the jet to jet interface. In these cases the mean velocity was minimized while the rms velocity was, at times, 500 times greater than the mean velocity. If this careful adjustment were not made, the velocities measured would not be on the fluid interface axis and the peak values would be less than expected.

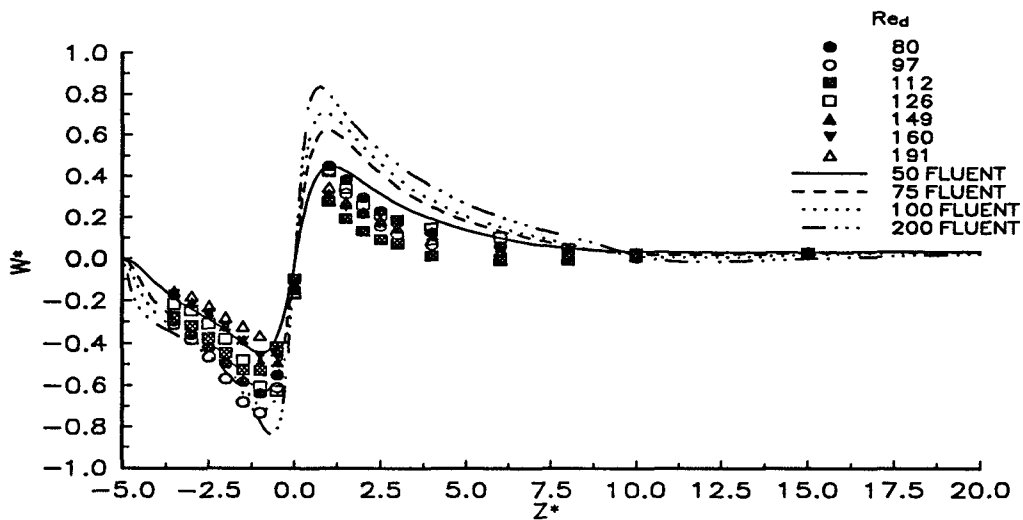


Figure 5.2.1 W^* vs Z^* at $(0,0,Z^*)$, Model 3, $d = 2$ mm, $\mu = 50$ cP

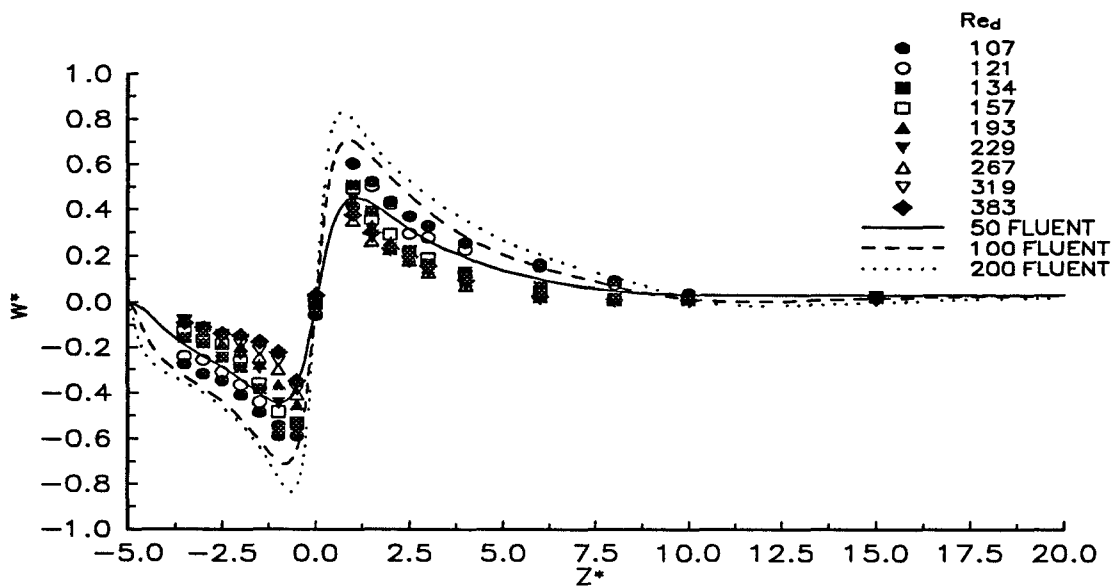


Figure 5.2.2 W^* vs Z^* at $(0,0,Z^*)$, Model 3, $d = 2$ mm, $\mu = 25$ cP

Peak W^* values and the location are given in Table 5.2.1 and peak values are symmetric about the geometric impingement point for $Re_d < 157$.

Table 5.2.1 W^* peak values Model 3 $d = 2$ mm

d 2mm	Re_d	Location Z^*	W^* peak
LDA data μ 50 cP	97**	1.0	0.427
		-1.0	-0.731
	149	1.0 -1.0	0.317 -0.486
	191	1.0 -1.0	0.346 -0.363
LDA data μ 25 cP	107**	1.0	0.604
		-1.0	-0.586
	157	1.0 -0.5	0.496 -0.531
	193	1.0 -0.5	0.425 -0.450
Simulations	50	1.063	0.450
		-0.969	-0.445
	100	0.844	0.711
		-0.844	-0.714
150	0.781	0.789	
	-0.719	-0.793	
200	200	0.719	0.833
		-0.656	-0.837

** Maximum values for all Re_d

There is generally close agreement between W^* values obtained with differing viscosities, suggesting that the Re_d and W^* are the proper scaling parameters for this flow, which is viscosity independent when the jets have the same fluid viscosity.

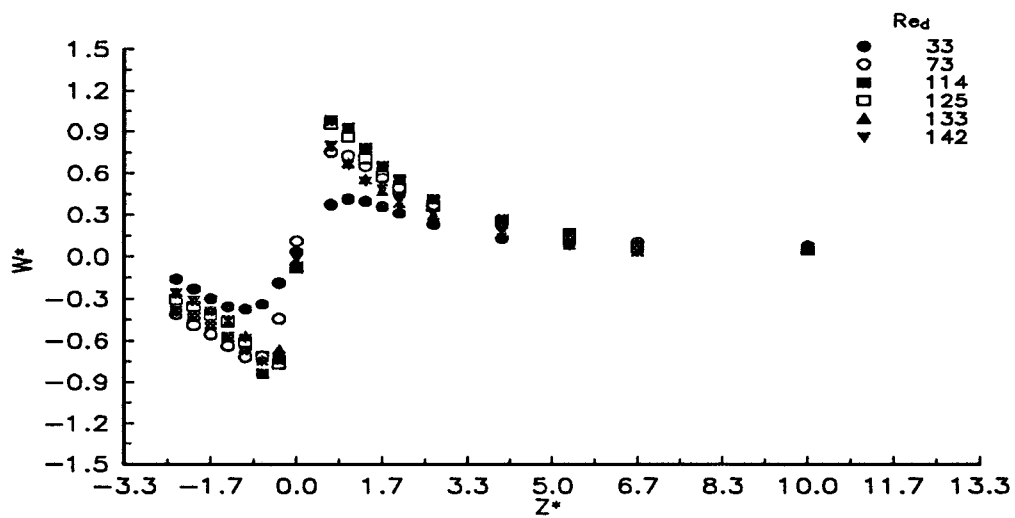


Figure 5.2.3 W^* vs Z^* at $(0,0,Z^*)$, Model 3, $d = 3$ mm, $\mu = 50$ cP

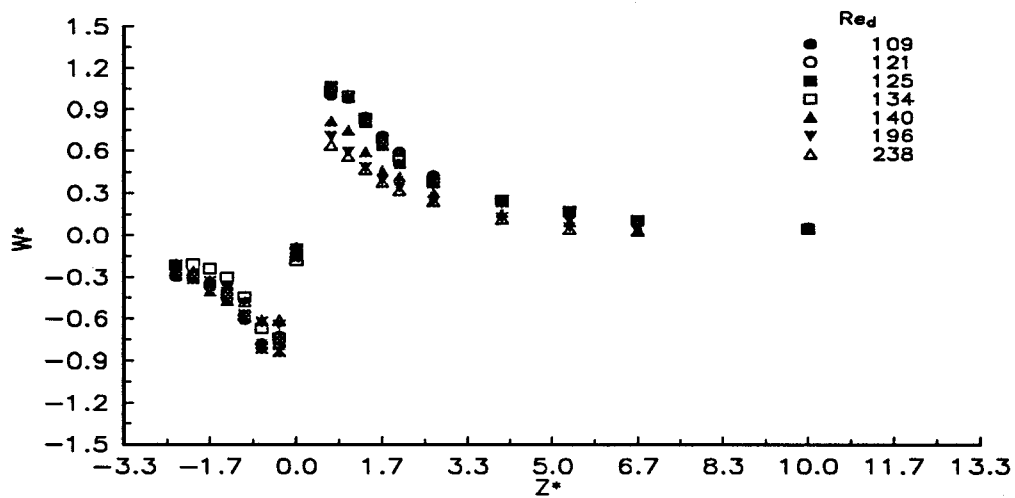


Figure 5.2.4 W^* vs Z^* at $(0,0,Z^*)$, Model 3, $d = 3$ mm, $\mu = 25$ cP

Figures 5.2.3, [Appendix A5.2.6,7] show the results for a 3 mm jet using 50 cP oil. The case of $Re_d = 33$ has been included as the profile of W^* differs greatly from the profiles of $Re_d = 50$ or greater. Figure 5.2.4 show the results for a 3 mm jet using 25 cP oil. Similar reasoning to the 2 mm case applies to the distribution of the velocity profiles. Table 5.2.2 details W^* peak values and the Z^* location and again peak values are symmetric about the geometric impingement point for $Re_d < 196$.

Table 5.2.2 W^* peak values Model 3 $d = 3$ mm

d 3mm	Re_d	Location Z^*	W^* peak
LDA data μ 50 cP	106	0.66	0.938
		-0.66	-0.825
	142	0.66	0.797
		-0.66	-0.744
Maximum**	114	0.66 -0.66	0.983 -0.832
LDA data μ 25 cP	109	0.66	1.00
		-0.66	-0.777
	140	0.66	0.816
		-0.33	-0.832
	196	0.66	0.708
		-0.33	-0.643
Maximum**	125	0.66 -0.66	1.070 -0.783

** Maximum values for all Re_d

Figures 5.2.5, [Appendix A5.2.8-12] show the results for a 4 mm jet using 50 cP oil and Figures 5.2.6, [Appendix A5.2.13-16] show the results for a 4 mm jet using 25 cP oil. Similar reasoning to the 2 mm case applies to the variance in the velocity profiles. Peak values are tabulated in Table 5.2.3.

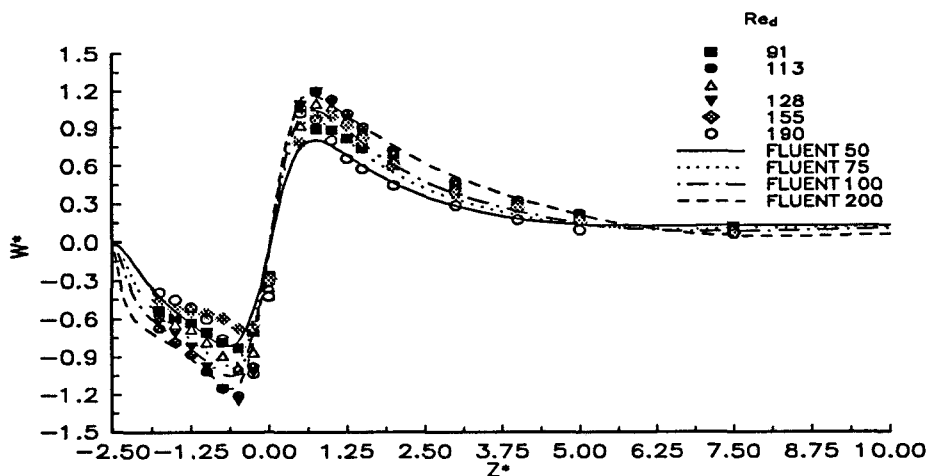


Figure 5.2.5 W^* vs Z^* at $(0,0,Z^*)$, Model 3, $d = 4$ mm, $\mu = 50$ cP

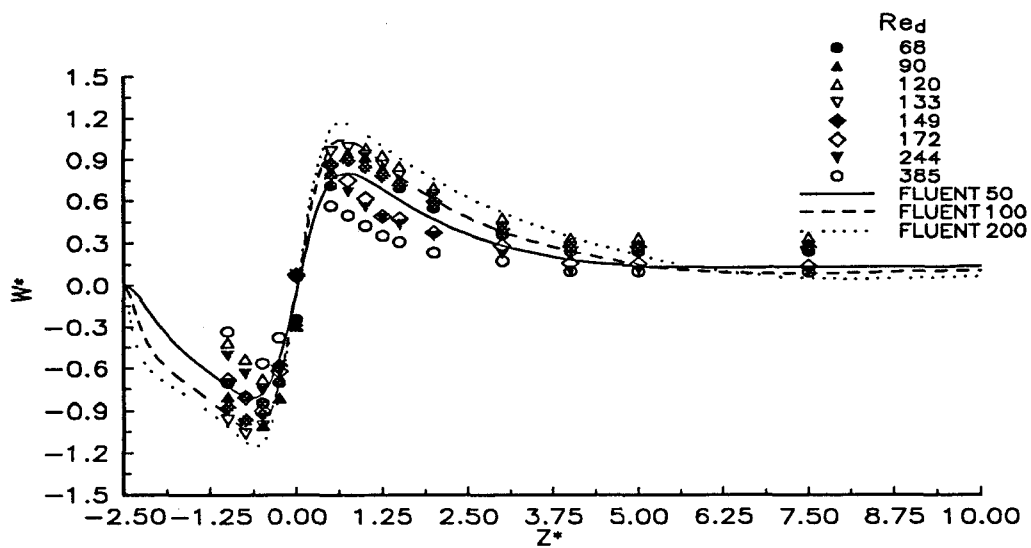


Figure 5.2.6 W^* vs Z^* at $(0,0,Z^*)$, Model 3, $d = 4$ mm, $\mu = 25$ cP

Table 5.2.3 W^* peak values Model 3 $d = 4$ mm

d 4mm	Re_d	Location Z^*	W^* peak
LDA data μ 50 cP	100	0.75	0.947
		-0.5	-0.843
	155	0.75	1.102
		-0.5	-1.104
	190	0.75	0.783
		-0.25	-0.723
Maximum**	113	0.75 -0.5	1.197 -1.211
LDA data μ 25 cP	102**	0.75	1.058
		-0.5	-1.070
	149	0.75	0.897
		-0.75	-0.961
	188	0.5	0.829
		-0.5	-0.945
Simulation	50	0.742	0.803
		-0.656	-0.812
	100	0.742	1.042
		-0.656	-1.051
	150	0.602	1.130
		-0.602	-1.126
	200	0.602	1.164
		-0.602	-1.152

** Maximum values for all Re_d

The data show that it is never the highest Re_d which attains the highest W^* . On the contrary, the low to middle range of Re_d result in the highest W^* . The range of Re_d where the peak occurs is very close to the onset of oscillatory behaviour discussed in a later section. This phenomenon makes physical sense as the average peak value from experimental work, as shown, would never reach a stationary pre oscillating

maximum as a result of the fluctuation of the impingement area which causes lower measured velocities as the "disc" moves off the z axis away from the measurement volume.

If the disc behaved as a radial laminar jet with the origin as the periphery of the disc (maximum w velocity), the velocity in the radial direction should decay as $1/r$, where r is the direction perpendicular to the jet axis. The W^* plots indicate velocity decay similar to this above and below the W^* peak and is more apparent for values above the impingement point where there is no confining surface. Below the impingement point the curve of W^* is much steeper because of the bottom surface confinement. As this region is well within the initial and developing regions of the radial jet as defined by Schwarz (1963) and detailed above, the similarity solutions do not apply directly to these cases.

Simulations of the flow field for several Re_d for $L^* = 10, 5$ (Model 3) are included on the W^* vs Z^* plots. The simulations give positive agreement for the lower values of Re_d but the simulations show a continuing increase in W^* peak with increasing Re_d . Experimentally a plateau is reached where an increase in the Re_d actually causes a decrease in the W^* peak, because the oscillatory behaviour of the impingement disc tends to distribute the momentum of the radial jet over a wider area. Examination of W_{rms}^* vs Z^* (Figures 5.4.5,5.4.6) reveals that the maximum values predicted by the simulations are quite plausible and are exceeded experimentally when W_{rms}^* is combined with W^* . The simulations, therefore, solve the steady state equations, which do not allow for fluctuation of the impingement disc with time.

Time dependent solutions were attempted using the FLUENT code although a steady state returned for all cases after an initial transient. Time dependant solutions were examined for some cases by Yeo (1993), who found a fluctuation of $0.2 W^*$ at $Z^* = 4$ in the case of $D^* = 10$ at $Re_d = 125$. Figures 5.4.5,5.4.6 agree well with this value. Ho (1992) has used an average of three unsteady time steps to define the axial velocity average in unsteady numerical simulations, citing computational time as the constraint to including more time steps in the average. Those results ($Re_d = 125$, $H^* = 0.5$, $D^* = 10$) coincide with the present experimental data.

The over prediction of peak axial velocities by the steady simulations is similar to that encountered in unsteady laminar flow around a rectangular cylinder (Duroo and Pereira (1988) and Davis *et al.* (1984)). In these cases, a steady simulation resulted in a significantly larger vortex formation behind a square cylinder, while a time average of unsteady simulations predicted a more realistic vortex formation. Duroo and Pereira conclude that "only unsteady predictions of periodic flows should be compared with time average measurements".

Data for comparison purposes is scarce, although Liou and Wu (1988) present some W velocity measurements obtained with a LDA in a model side dump combustor ($Re_{dh} = 2.49 \times 10^4$, air flow) where a maximum $V_x/U_{ref} = 1.04$ is found $1.0 D$ above the inlet arm (inlet arms at 60° toward outlet) and minimum $V_x/U_{ref} = -0.42$ is found $0.25 D$ above the inlet arm. The stagnation point was found to be at $0.42 D$ above the inlet arm.

The time averaged experimental W^* results for $L^* = 10, 6.67, 5$ indicate that a

maximum W^* peak is reached in the steady flow range which decreases with increasing Re_d . The oscillation of the impingement surface result in the decrease in the peak producing a lower average velocity. The maximum W^* peak values correspond well with the limit of steady flow and onset of oscillatory flow discussed in a later section. Steady numerical simulations do not coincide with experimental results and show steady increases in W^* peak with increasing Re_d , a difficulty previously documented for steady simulations of unsteady periodic flow fields. Previously reported unsteady simulations parallel present experimental data, although there is not a great deal of published experimental data for comparison purposes.

5.3 Flow Development

In computational modelling the flow field of the opposed jet mix head and for purposes of alternative design of mix heads, the distances for re-establishment of unidirectional flow and fully developed flow in the mix chamber are of considerable importance. For these reasons the outflow conditions for the present mix chamber are discussed.

As a test to determine whether the flow field is re-established to fully developed flow above the point of impingement, the peak on-axis value should be 2.09 times the average value based on fully developed flow in a square duct (Shah and London 1978).

For the 2 mm ($L^* = 10$ Model 3) example,

$$W_{\max_{out}} = 2.09 W_{\text{avg}_{out}} = 2.09 \frac{\pi}{200} U_{\text{avg}_{inlet}} \quad 5.3.1$$

$$\frac{W_{\max_{out}}}{U_{\text{avg}_{inlet}}} = 0.03283$$

From Figure 5.3.1, W^* versus Re_d at $Z^* = 15$, this value is nearly achieved but moves away from the theoretical value as Re_d is increased (Model 3, $L^* = 10$, $\mu = 25$ and 50 cP). Numerical simulations at the same location $Z^* = 15$ (Model 3, $L^* = 10$) also give little agreement past $Re_d = 50$ showing a higher degree of divergence as Re_d is increased. Simulations at $Z^* = 90$ (Model 3, $L^* = 10$) give excellent agreement with the theory.

Similarly for the 3 mm (Model 3, $L^* = 6.67$, $\mu = 25$ and 50 cP) case,

$$\frac{W_{\max_{out}}}{U_{avg_{inlet}}} = 0.0742 \quad 5.3.2$$

From the velocity data collected, this condition is not satisfied and all the data lie below the theoretical value at $Z^* = 10$ for all Re_d measured.

For the 4 mm (Model 3, $L^* = 5$, $\mu = 25$ and 50 cP) case,

$$\frac{W_{\max_{out}}}{U_{avg_{inlet}}} = 0.1317 \quad 5.3.3$$

The plot of W^* vs Re_d shows for $\mu = 25$ cP that W^* increases with Re_d until $Re_d = 120$ and then decreases to $Re_d = 187$ and then levels off below the fully developed flow line, although for $\mu = 50$ cP the values of W^* steadily decrease with increasing Re_d . For this condition a fully developed flow has not been achieved at $Z^* = 7.5$ (1.5 L) for all Re_d measured. Numerical simulations (Model 3, $L^* = 5$) at the same location $Z^* = 7.5$ (1.5 L) also show that fully developed flow has not been reached; there is a steady decline in W^* with increasing Re_d . Simulations at $Z^* = 46$ indicate that the flow has become fully developed.

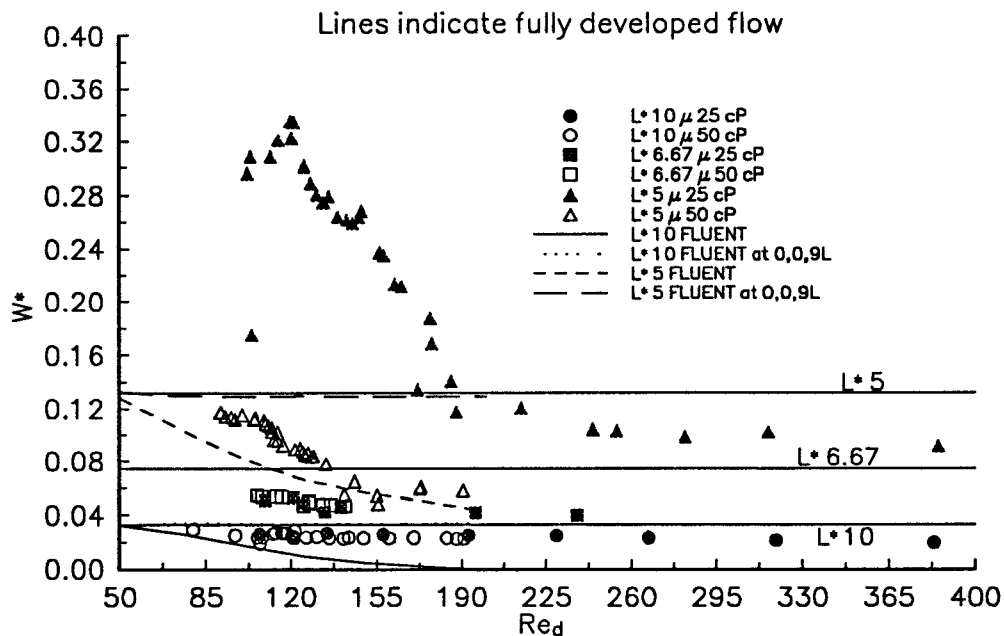


Figure 5.3.1 W^* vs Re_d at $(0,0,1.5L)$, Model 3

The development length required to achieve 5% of the theoretical fully developed value could be considered to define the length of the mixing zone. Development length versus Re_d is shown in Figure 5.3.2 for $L^* = 10$ and $L^* = 5$ (Model 3). The case of $L^* = 10$ is seen to reach the fully developed value before the $L^* = 5$ case and at the highest value of $Re_d = 200$, the fully developed value is found at 3 L for Model 3. At the same Re_d , $L^* = 5$ requires 5.6 L to reach the fully developed value. These results are in general agreement with the simulations of Ho (1992) ($D^* = 10$, $H^* = 0.25$) who found fully developed flow at 1.5D for $Re_d = 50$, 1.8D for $Re_d = 125$, 2.0D for $Re_d = 200$ and $\sim 4D$ for $Re_d = 300$; Liou and Wu,

(1988) who extrapolated to $Z/D = 13$ as the fully developed point for turbulent flow ($D/L_{hd} = 2.5$, $Re_{dh} = 2.5 \times 10^4$); and Liou *et al.* (1993), who found unidirectional flow above $z/L = 4$ and nearly fully developed flow at $z/L = 9$ for a Re_L of 4.56×10^4 ($L/w = 2$).

The determination of the point where unidirectional flow or fully developed flow occurs may be useful in computational simulations, since the outlet condition is modelled as fully developed flow. For design purposes, the location of unidirectional flow may be considered the limit of the effect of impingement mixing, as subsequent mixing will only occur because of laminar deformations.

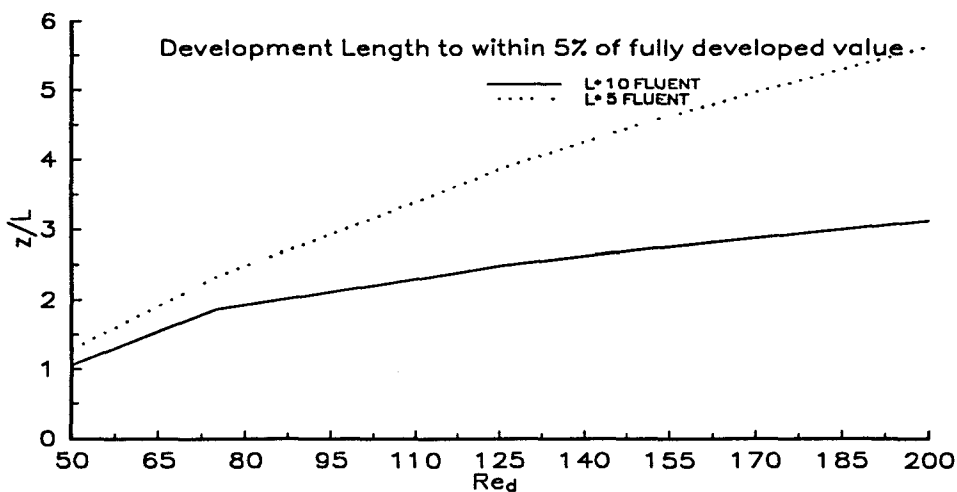


Figure 5.3.2 z/L vs Re_d at $(0,0,z)$ Simulations for $L^* = 10$ and $L^* = 5$

5.4 Oscillations

5.4.1 Introduction

A stable non-oscillatory flow field consisting of a developing jet region, an opposed jet impingement region and toroidal recirculating zones surrounding each jet has been documented for $Re_d < \sim 90$ for all cases of L^* . This flow field structure returns after transient disturbances and is well predicted computationally. Marginal increments in the jet velocities above these Re_d values caused regular oscillations of the opposed jet impingement region to occur. A well defined onset of oscillations was found, and limit values of steady oscillations were also determined. The following section discusses the oscillatory phenomenon:

Previous visualizations of the flow patterns by Sandell *et al.* (1985) in a mix chamber ($D^* = 5.5$, $\theta = 30^\circ$, $H^* = 0.73$) has shown an oscillating flow above $Re_d = 150$. At $Re_d = 250$ the oscillation had a larger amplitude and increased frequency, as measured observing the region between the nozzle inlet and head region. Observations of the oscillation frequency versus Re_d are given in Table 2.3. Between Re_d of 400 and 700 there was limited visual improvement in mixing based on a vanishing dye technique in water. Generally, the flow became less steady when increasing the Re_d or increasing the distance to the head region.

In a similar study, Nosseir and Behar (1986) used a rectangular model with opposed ($\phi = 180^\circ$) rectangular jets in a water loop to simulate the side dump combustor. The average Re_d based on the nozzle width was 3000. Oscillations in the flow were detected when the dyed fluid interrupted a laser beam at a fixed location.

The flow field visualized had no obvious impingement region, as found in the present study and, above the geometric point of impingement, vortices aligned with the chamber were observed; whereas the present study found vortices aligned with the jet axis for steady and oscillating impingement surfaces. Observations were similar to those of Stull and Craig (1985) in that at one instant one jet would be deflected into the head area and then deflected out, while the other jet would be deflected into the head area in an "almost periodic and out of phase" manner. As well, above the nozzle area in the main chamber, vortices were generated which alternated between clockwise and counter clockwise rotation similar to the above work. The strength of the vortices was found to fluctuate with the oscillation of the jets into the head area (phase locked). Values of St vs Re_d are given in Table 2.4. These values are in agreement with some of the results of Sandell *et al.* (1985) above. Wood *et al.* (1991) have confirmed these observations using laser Doppler anemometer velocity measurements and three dimensional computer simulations. They found steady impingement below $Re_d = 75$ ($D^* = 10.67$, $D = 25.4$ mm, $\phi = 180^\circ$), and at values higher than this, an instability in the impingement surface began to grow and oscillate. Experimentally, above $Re_d = 150$ the jets would not directly impinge, although the computer simulations showed steady oscillations from $Re_d = 100 - 300$.

5.4.2 Visualization of Oscillations

Oscillations in the flow field were observed in both the flow visualization

studies and the LDA experimental results for certain values of Re_d for model 3 and model 4. Before oscillations were observed, the flow field was stationary and no fluctuations were observed. Increases in the jet velocity caused small changes in the location of the recirculation area above the jets. Then, as the Re_d was increased, the centre of the recirculation area moved away from the jets toward the outlet. Small increases in the jet velocity above a certain onset value caused the jet impingement disc to oscillate with a small amplitude and low frequency. As an initial indication of oscillatory behaviour, for Model 4 at $Re_d = 98$, in the XZ plane, particles were observed to flow along the jets and then alternate between whichever upper vortex they were drawn toward. Increases in the jet velocity caused the oscillations to increase in amplitude and frequency. At $Re_d = 109$ for Model 4 the oscillations in the upper vortices were more visually apparent in the XZ plane and the location of the upper vortex was unstable, although the lower vortex did not show significant movement. In the XY plane ($Re_d = 106$ Model 4) the boundary of the impingement disc is seen to alternately wash along either chamber boundary at $(0, Y, 0)$. Increases in Re_d cause ($Re_d = 120$, Model 4) the recirculation areas above the jets alternately to roll off the configuration and flow towards the flow outlet in an irregular and unstable manner. Once the area of recirculation departs, the disc deflects into this area until the recirculation area builds up and the opposite recirculation area rolls off and flows toward the outlet, similar to the results observed by Stull and Craig (1985). Below the area of impingement the disc is directed toward the opposite jet side of the chamber; thus the disc is seen to move as a "solid" body.

Above a limit value of Re_d observation of the disc was infrequent ($Re_d = 130$, Model 4) and for some cases of L^* the jets would not directly impinge changing the structure of the flow field entirely and would not return to the original vortex structure until a significant decrease in the Re_d occurred (down to $Re_d = 98$ for Model 4). In this new structure the majority of the flow in the W^* direction occurred along the chamber boundaries, while the centre of the chamber contained an unstable recirculating "ball". For the cases where the disc was observed, it was oscillating wildly and the disc position was also seen to move along the jet axis comparable to the studies by Ogawa *et al.* (1992).

5.4.3 Quantitative Oscillation Determination

Equal time interval velocity samples were obtained using the LDA (Dostek 1987); examples of the time series representing a non-oscillatory case, an oscillating case and a post oscillatory case are shown in Figures 5.4.1-3, where W^* is the fluctuating W component (W_{mean} removed) divided by U_{avg} . In Figure 5.4.1 $Re_d = 101$, $\mu = 48$ cP the fluctuation from the mean is very small and the spectral density for this time series (Figure 5.4.4) show no oscillatory frequencies. Figure 5.4.2 shows the time series for $Re_d = 121$, $\mu = 48$ cP where significantly larger velocity oscillations are recorded with a regular pattern. The spectral density for this case (Figure 5.4.4) shows a well defined peak frequency at 24.3 Hz. The post oscillatory case $Re_d = 191$, $\mu = 47$ cP shows extreme velocity fluctuations with no well defined regularity. The spectral density for this case shows no well defined peaks (Figure 5.4.4).

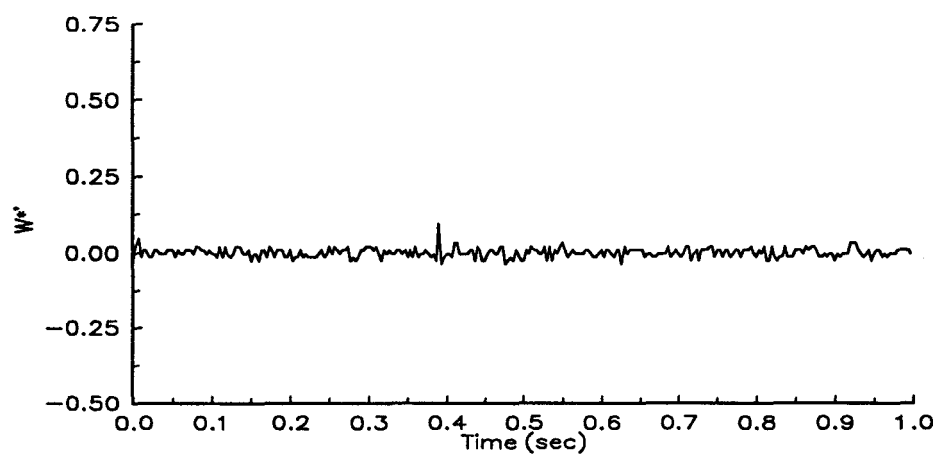


Figure 5.4.1 W^* vs Time, $Re_d = 101$, Model 3, $d = 2$ mm, $\mu = 48$ cP

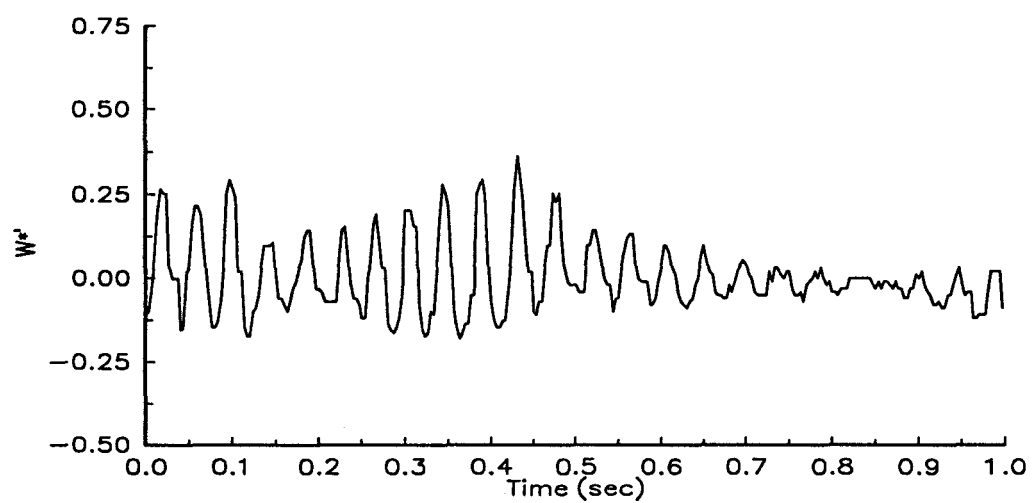


Figure 5.4.2 W^* vs Time, $Re_d = 121$, Model 3, $d = 2$ mm, $\mu = 48$ cP

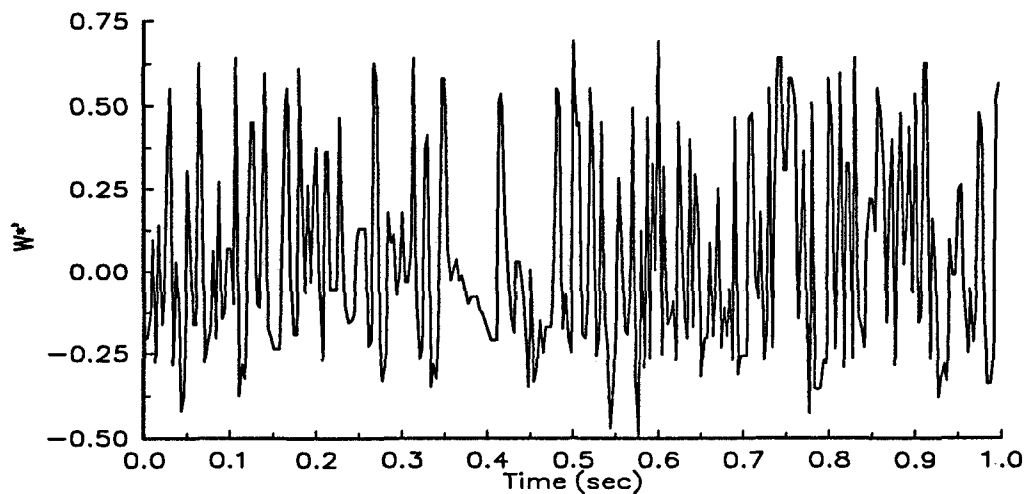


Figure 5.4.3 W^* vs Time, $Re_d = 191$, Model 3, $d = 2$ mm, $\mu = 47$ cP

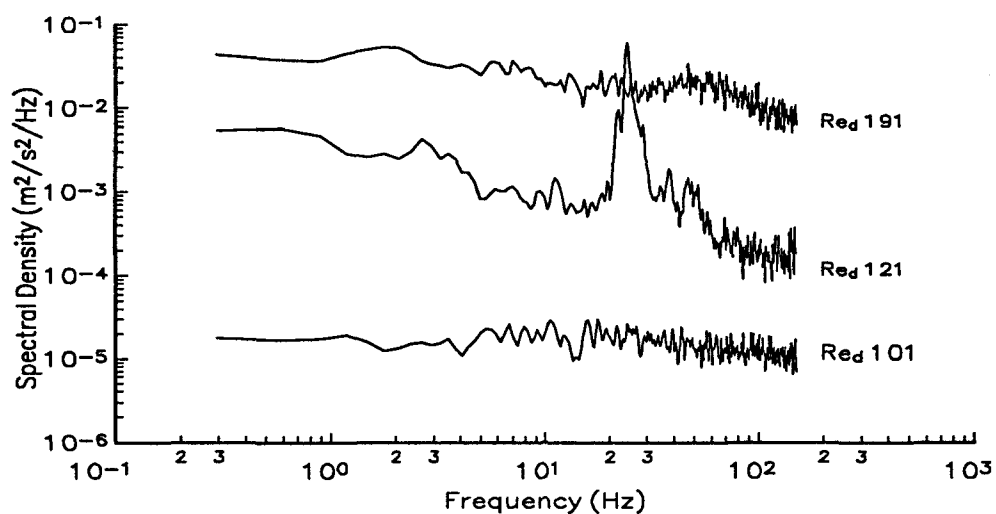


Figure 5.4.4 Spectral Density vs Frequency, Model 3, $d = 2$ mm, Complete Time Series from Figures 5.4.1-5.4.3

Using all the equal time interval velocity samples, FFT were obtained to determine the frequencies present. In this way the onset and limit of finite oscillations was determined. For the case of $L^* = 10$ (Model 3) the onset of oscillations occurred at roughly a Re_d of 106 ($\mu = 50$ cP) with a frequency of 19.3 Hz giving a Strouhal number ($St_d = fd/U_{avg}$, f - frequency, d - jet diameter, U_{avg} - average inlet velocity) of 0.012255. Marginally lower values of Re_d were devoid of any significant frequencies. Once oscillations began, the frequency increased with Re_d to the upper limit where the oscillations were irregular. Although the upper limit was determined to be $Re_d = 160$ ($\mu = 47$ cP) with a frequency of 40.7 Hz giving a Strouhal number of 0.018323, well defined oscillations were not recorded for all values of Re_d above 143. Using a lower viscosity oil, the onset of oscillations was found to be $Re_d = 110$ ($\mu = 21$ cP) with a frequency of 8.2 Hz giving a Strouhal number of 0.011887. An upper limit of oscillations was found to be $Re_d = 152$ ($\mu = 22$ cP) with a frequency of 15.2 Hz giving a Strouhal number of 0.015337.

Table 5.4.1 Oscillation Limits $L^* = 10$ Model 3

Re_d	μ (cP)	f (Hz)	St_d	
106	50	19.3	0.012255	Onset $L^* = 10$
160	47	40.7	0.018323	Limit $L^* = 10$
110	21	8.2	0.011887	Onset $L^* = 10$
152	22	15.2	0.015337	Limit $L^* = 10$

Onset of oscillations can also be seen in the plots of W_{rms}^* versus Z^* (Fig 5.4.5,6). In these plots using 50 cP oil, significant velocity fluctuations do not occur

until a Re_d of 112 has been attained. Although a limit for well-defined frequencies of Re_d 152 was found using the FFT analysis, the figure shows that the level of W_{rms}^* continues to increase beyond the limit value.

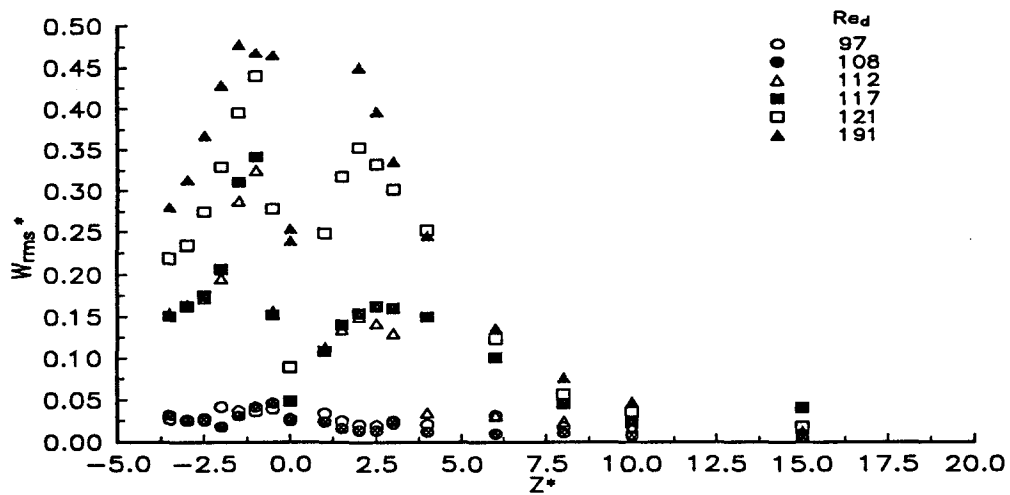


Figure 5.4.5 W_{rms}^* vs Z^* at $(0,0,Z^*)$ Model 3, $d = 2$ mm, $\mu = 50$ cP

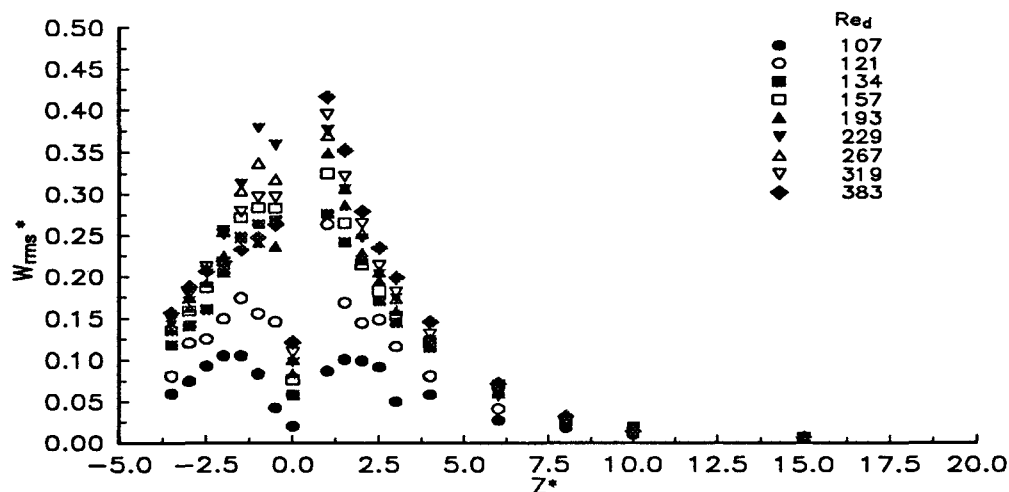


Figure 5.4.6 W_{rms}^* vs Z^* at $(0,0,Z^*)$ Model 3, $d = 2$ mm, $\mu = 25$ cP

Similar analyses were carried out for $L^* = 6.67$ Model 3 and are summarized in Table 5.4.2.

Table 5.4.2 Oscillation Limits $L^* = 6.67$ Model 3

Re_d	μ (cP)	f (Hz)	St_d	
106	50	16.7	0.024737	Onset $L^* = 6.67$
127	50	24.9	0.029616	Limit $L^* = 6.67$
109	25	9.1	0.025418	Onset $L^* = 6.67$
140	25	13.2	0.028456	Limit $L^* = 6.67$

Onset of oscillations can also be seen in the plots of W_{rms}^* versus Z^* . For the case of $L^* = 6.67$ and $\mu = 50$ cP (Figure 5.4.7) significant velocity fluctuations do not occur until a Re_d of 114 has been attained and for $\mu = 25$ cP (Figure 5.4.8) velocity fluctuations do not occur until after $Re_d = 109$.

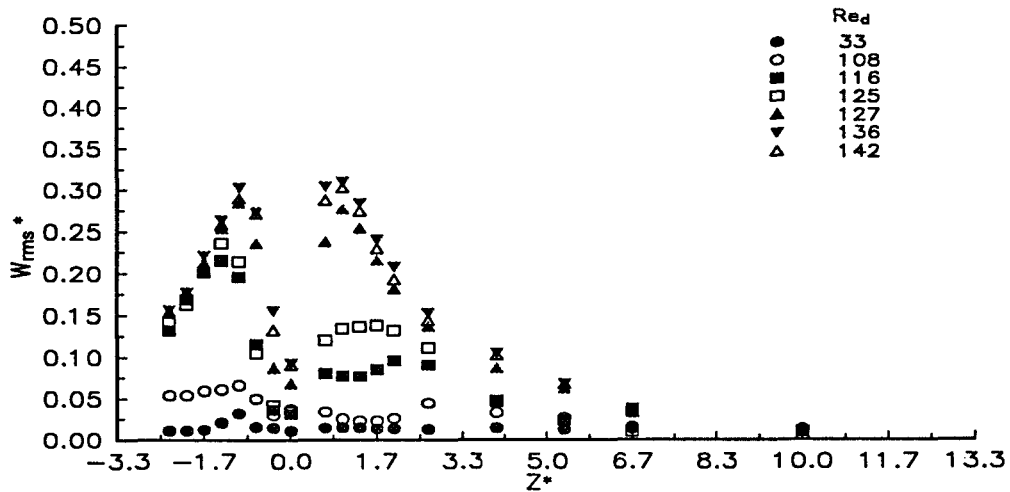


Figure 5.4.7 W_{rms}^* vs Z^* at $(0,0,Z^*)$ Model 3, $d = 3$ mm, $\mu = 50$ cP

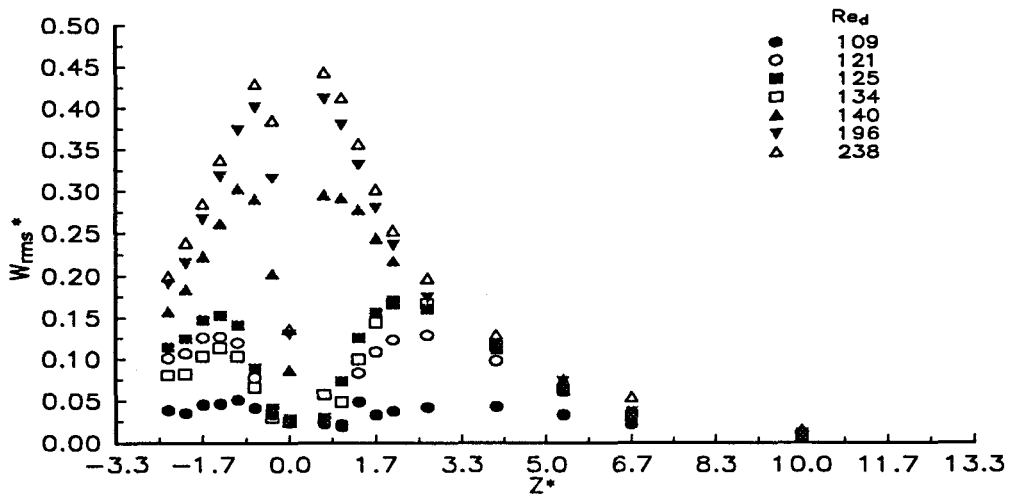


Figure 5.4.8 W_{rms}^* vs Z^* at $(0,0,Z^*)$ Model 3, $d = 3$ mm, $\mu = 25$ cP

Times series for $L^* = 5$ are shown in Figures 5.4.9-11. The case of $Re_d = 106$, $\mu = 51$ cP (Figure 5.4.9) is similar to figure 5.4.1 ($L^* = 10$, $Re_d = 101$, $\mu = 48$ cP) in

that the deviation from the mean is very small and the spectral density for this time series (Figure 5.4.12) shows no oscillatory frequencies. Figure 5.4.10 shows the time series for $Re_d = 111$, $\mu = 52$ cP, where a regular pattern begins to emerge. This Re_d is very close to the onset of the oscillations and as a result the fluctuation is not as significant as that seen in Figure 5.4.2. The spectral density for this case (Figure 5.4.12) shows a well defined peak frequency at 18.8 Hz. The limit oscillatory case $Re_d = 173$, $\mu = 49$ cP (Figure 5.4.11) shows extreme velocity fluctuations with no observable well-defined regularity. The spectral density shows no well defined peaks (Figure 5.4.12).

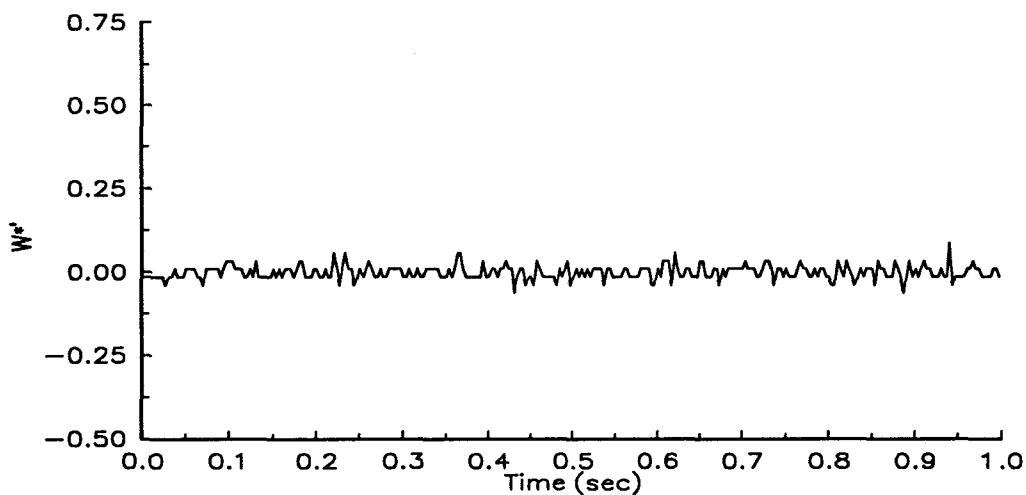


Figure 5.4.9 W^* vs Time, $Re_d = 106$, Model 3, $d = 4$ mm, $\mu = 51$ cP

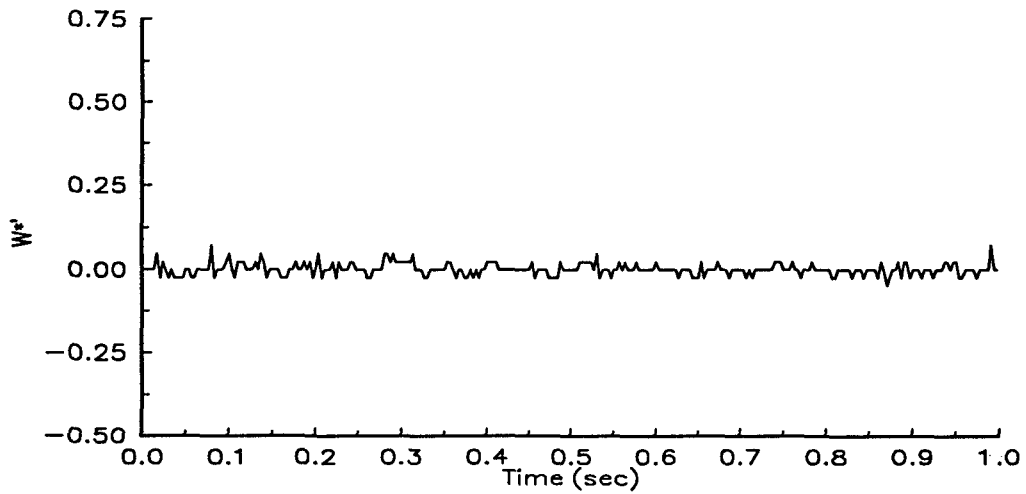


Figure 5.4.10 W^* vs Time, $Re_d = 111$, Model 3, $d = 4$ mm, $\mu = 52$ cP

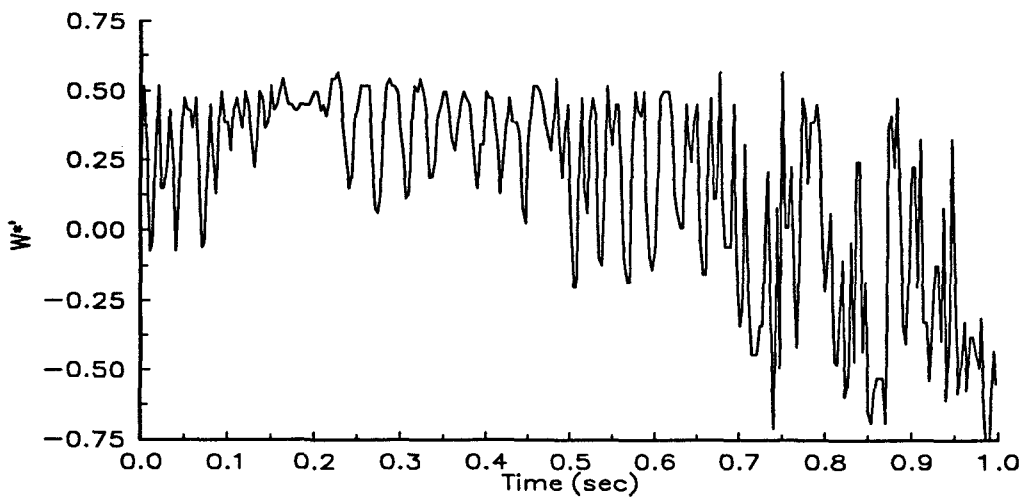


Figure 5.4.11 W^* vs Time, $Re_d = 173$, Model 3, $d = 4$ mm, $\mu = 49$ cP

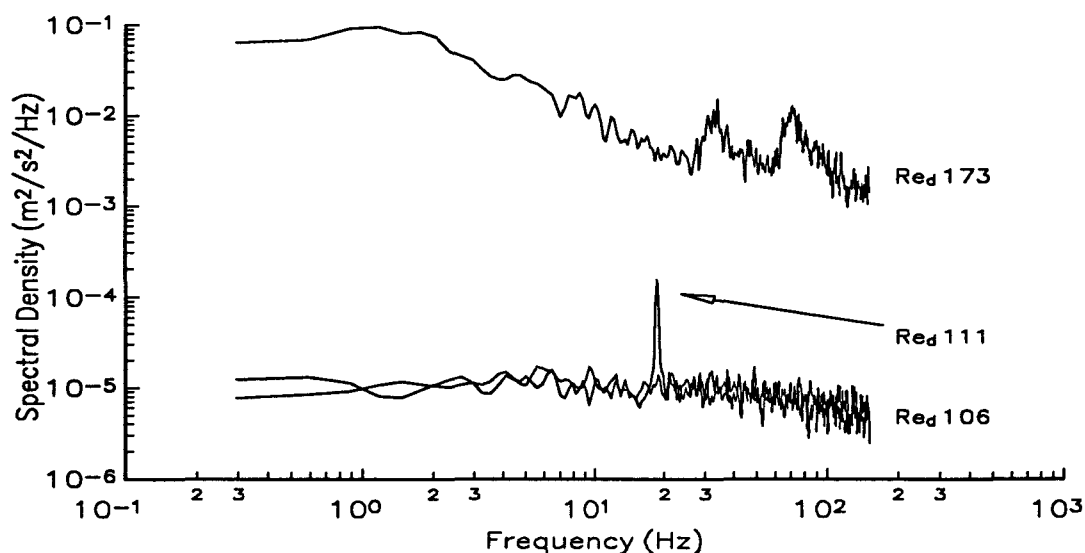


Figure 5.4.12 Spectral Density vs Frequency, Model 3, $d = 4$ mm, Complete Time Series from Figures 5.4.9-5.4.11

Table 5.4.3 Oscillation Limits $L^* = 5$ Model 3

Re_d	μ (cP)	f (Hz)	St_d	
109	51	17.9	0.043279	Onset $L^* = 5$
173	49	31.9	0.050530	Limit $L^* = 5$
120	25	9.7	0.042561	Onset $L^* = 5$
217	26	21.4	0.052089	Limit $L^* = 5$

For the case of $L^* = 5$ and $\mu = 50$ cP (Figure 5.4.13) significant velocity fluctuations did not occur until a Re_d of 117 to 121 has been attained, and at $\mu = 25$ cP (Figure 5.4.14) significant fluctuations are not seen until $Re_d = 121$; although the limit of oscillations occurred at $Re_d = 173$ although well defined oscillations were not recorded for all values of Re_d above 167.

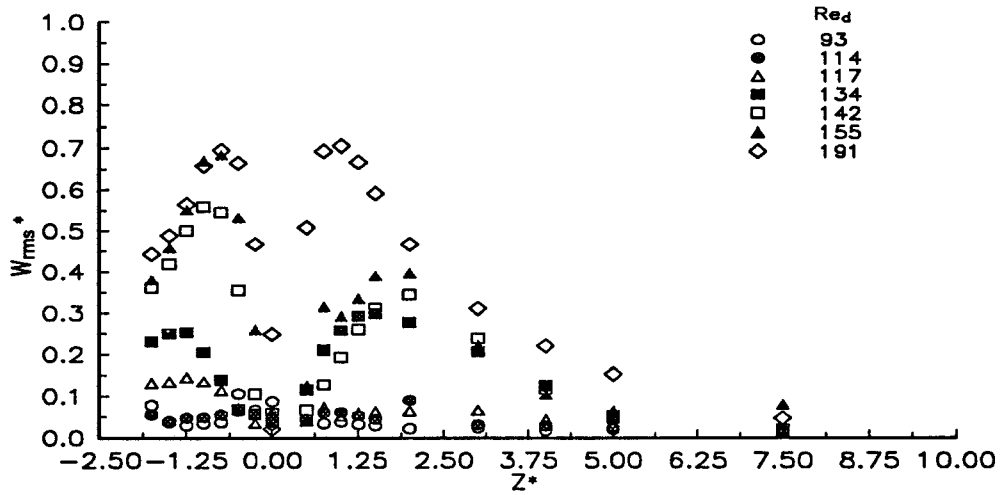


Figure 5.4.13 W_{rms}^* vs Z^* at $(0,0,Z^*)$ Model 3, $d = 4$ mm, $\mu = 50$ cP

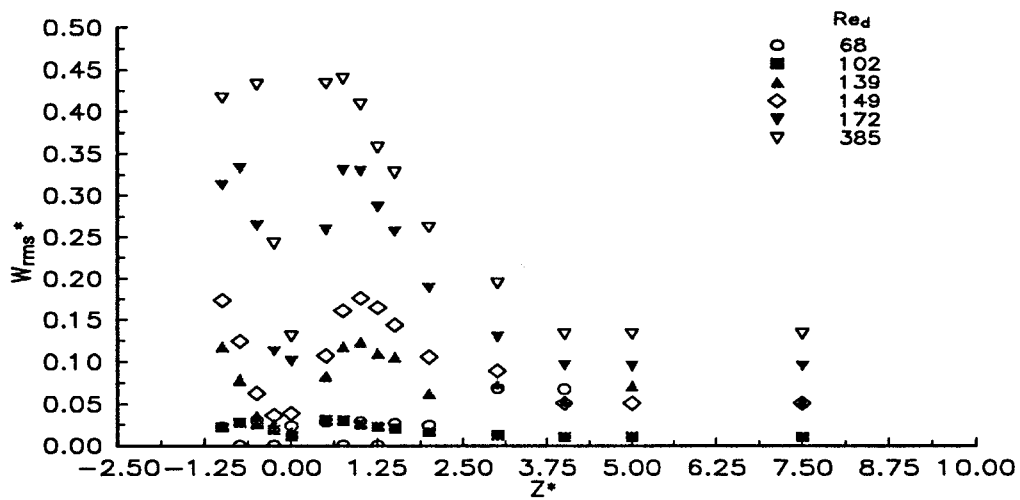


Figure 5.4.14 W_{rms}^* vs Z^* at $(0,0,Z^*)$ Model 3, $d = 4$ mm, $\mu = 25$ cP

The $D^* = 10.67$ ($H^* = 0.5$, Model 4) chamber was analyzed for oscillations and the results are presented in Table 5.4.4.

Table 5.4.4 Oscillation Limits $D^* = 10.67$ Model 4

Re_d	μ (cP)	f (Hz)	St_d	
99	23	4.1	0.0088	Onset $D^* = 10.67$
131	23	6.2	0.0099	Limit $D^* = 10.67$

St_d versus Re_d is shown in Figure 5.4.15 for all cases of L^* . This figure shows the slight increase in frequency with velocity which has been noted by Nosseir and Behar (1986) for a different geometry at much higher Reynolds number (Re 3000). The results of this plot show that the oscillations are independent of viscosity values for a given L^* ratio. As well, for the lower the value of L^* , the more delayed is the onset of oscillation and a larger range of well defined oscillations seems to indicate a more stable flow field than the higher values of L^* . For all cases of L^* (Model 3), onset of oscillations was found to occur at a higher Re_d than that previously reported by Wood *et al.* (1991) in a $D^* = 10.67$ cylindrical chamber. The data shows that L^* has a significant effect on the oscillatory behaviour in the chamber.

Initially, the mechanism controlling the oscillations was considered to be an example of the Coanda effect, in which a free jet develops oscillations because of alternating side wall attachments (Murai *et al.* 1989). The jet movement in the mix head case is not as significant as that seen with free jets in a channel and the frequency of oscillation of the free jet is typically very small.

This oscillatory motion is similar to the class of flows called self-sustained

oscillations, which occur in many flows usually with impingement on a solid object, such as the "jet-hole" or "jet-plate" (Rockwell and Naudascher, 1979). In these cases, a free shear flow impinging on a solid object creates pressure disturbances which are fed back to the shear layer, continually forcing the oscillations. Any vortical disturbances downstream of a point influence the flow dynamics at that point (Dimotakis and Brown, 1976).

In a study of a jet impinging on a solid flat plate Ho and Nousseir (1981) found the presence of oscillations resulting from an instability in the jet shear layer caused by background perturbations. These perturbations were produced downstream of the jet at the plate impingement and were fed back to the nozzle opening, where they controlled the evolution of the fluctuations. Oscillatory onset occurred when upstream travelling disturbances were in phase with downstream travelling structures. Previous work by Gutmark and Ho (1983) on free jets in air found the initial instability frequency f

$$f \propto U_{avg}^{\frac{3}{2}} \quad 5.4.1$$

(f (Hz), U_{avg} (m/s)). The present experimental data also shows this trend for all values of L^* (Model 3) (Figure 5.4.16). Gutmark and Ho (1983) have determined that a "minute amount of *spatially coherent* background perturbation is enough to affect the initial instability frequency". The generally accepted turbulent jet Strouhal number St_d (fd/U_{avg}) is in the range of 0.3 (Crow and Champagne, 1971), at least an order of magnitude greater than that found in these studies. Another fundamental Strouhal

number is the one based on initial momentum thickness θ_{mo} and the most amplified frequency (Michalke (1965)) is 0.017 ($St_\theta = f\theta_o/U_{avg}$) which is certainly in the range of the Strouhal numbers determined here; however the present momentum thickness would have to be of the same order as the nozzle diameter. The work of Gutmark and Ho (1983) also showed that St_d increased smoothly for values of $X/d = 3.5$, but the data was scattered widely for values of $X/d = 2.5$ and 5. All studies discussed above concern free turbulent jets. It is possible that the impingement area modelled as a "semi-solid" amplifies any disturbances such as those described as fluid-elastic cavities (Rockwell and Naudascher 1978), where the wall of a cavity may undergo a deflection and exert some feedback control on the shear layer.

The fact that these oscillations occur at relatively low Re_d in comparison to the turbulent (free and impinging on solid objects) jets discussed above suggests that the impingement surface plays a significant role in the onset and sustaining of the oscillations. Simulations by Yeo (1993) suggest that, at the point of stagnation, a symmetric pressure distribution is found for steady flow fields and that the pressure distribution becomes asymmetric as oscillatory motion begins.

Flow visualizations at the limit of oscillations indicate that the interface between the jets is no longer able to sustain oscillations of increasing amplitude and frequency and the jets no longer impinge directly. At this point the impingement pressure distribution is altered significantly and feedback from the interface would no longer occur.

In summary, oscillations in the impingement surface of an opposed jet mix

head were found above certain onset values of Re_d for cases of L^* . As L^* is increased the onset and limit values of Re_d were decreased. Above the limit values no regular oscillations were observed or measured and the entire structure of the flow field is altered significantly. Previous studies of self-sustained oscillations in free and impinging jets show similar characteristics and provide a theoretical framework based on pressure perturbations in the region of impingement.

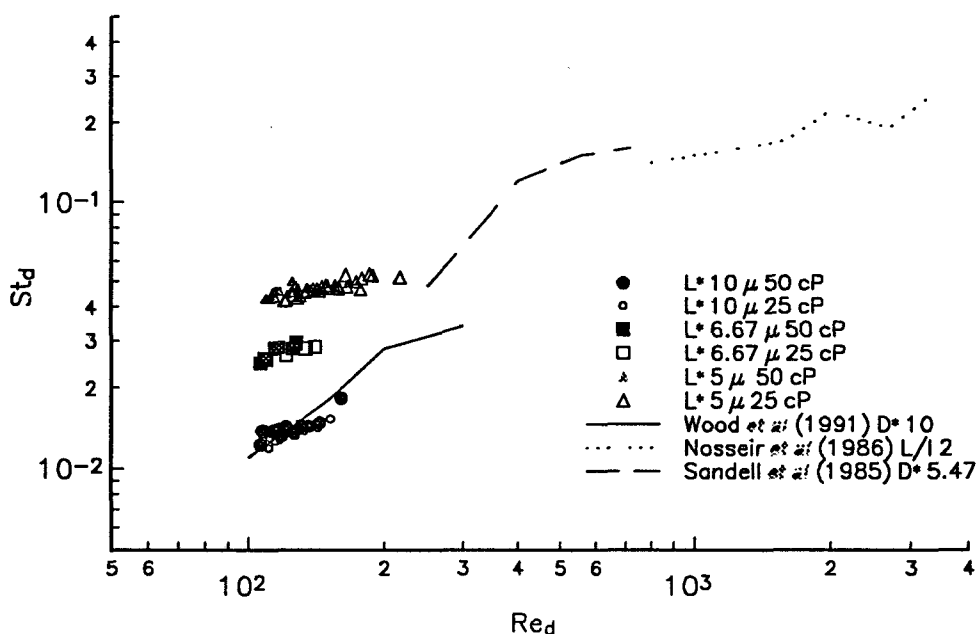


Figure 5.4.15 St_d vs Re_d for all cases of L^* Model 3 with data from Wood *et al.* (1991), Nosseir and Behar (1986), and Sandell *et al.* (1985)

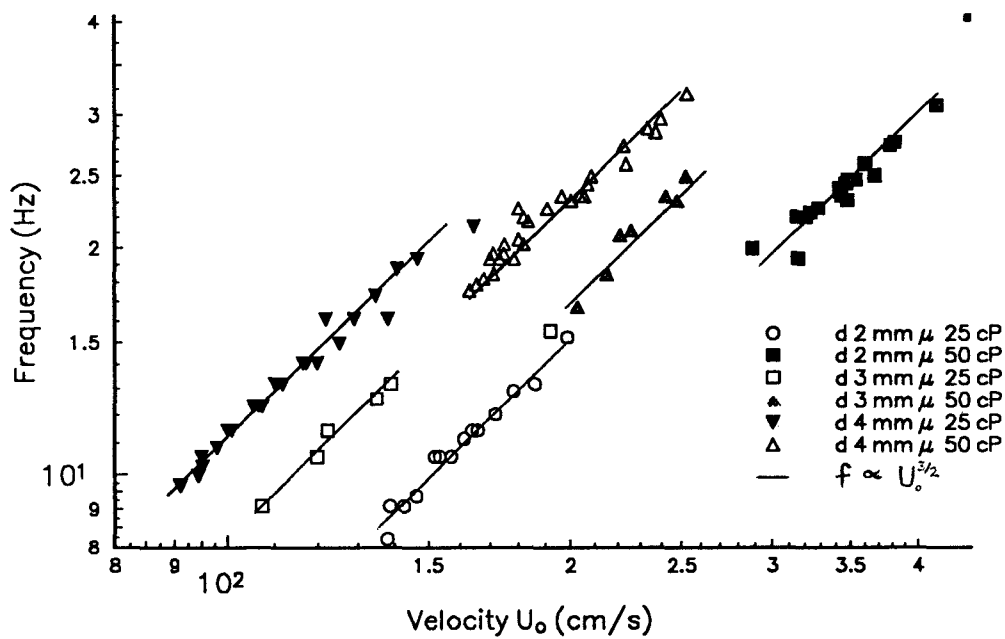


Figure 5.4.16 Oscillation frequency versus U_{avg} for all cases of L^* Model 3

5.5 Post Regular Oscillatory Behaviour

The final area of discussion is the post regular oscillatory region, where no regular oscillations were observed or measured and the flow field assumed an irregular disorganized pattern.

At Re_d above the limit value found for each case of L^* , FFT analysis showed no regular oscillations present, as did flow visualization studies, although the impingement interface continued to oscillate wildly. At these Re_d the point of impingement, which was previously stationary, began to move on the jet axis contributing to the oscillatory behaviour. This movement has also been observed by Ogawa *et al.* (1992) in turbulent ($Re_d = 5.61 \times 10^4$) opposed free jets ($L^* = 4.3$ and $L^* = 8.57$), although all the oscillations observed were only assumed to occur because of movement of the impingement point and not from the oscillation of the impingement disc about the jet axis.

In flow visualization studies no uniform flow structure was seen, although a contorted impingement surface was visible sporadically. The jets precess one another and occasionally directly impinge; however the flow far above the jets was observed to move toward the jets from a greater distance than previously noted in the case of regular oscillatory behaviour.

U^* and W^* velocity vectors from $Re_d = 500$ ($d = 2$ mm, $L^* = 10$, $\mu = 25$ cP, Model 3) and $Re_d = 1000$ ($d = 2$ mm, $L^* = 10$, $\mu = 15$ cP, Model 3) are shown in Figure 5.5.1 and contours of U^* and W^* are shown in Figures 5.5.2-3. The time-averaged results show that some structure exists where the jets collide and flow away

from the geometric centre of the chamber. $Re_d = 500$ shows some similarity to cases of much lower Re_d since a broad band of W^* flow exists above and below the geometric centre signifying an unstable impingement point in this area. Although $Re_d = 1000$ is not as comparable some characteristics are similar, such as the $-W^*$ flow below the geometric centre. Contours of W^* show a broader, higher band of velocity above and below the geometric centre. This pattern suggests increased movement of the impinging area between the jets.

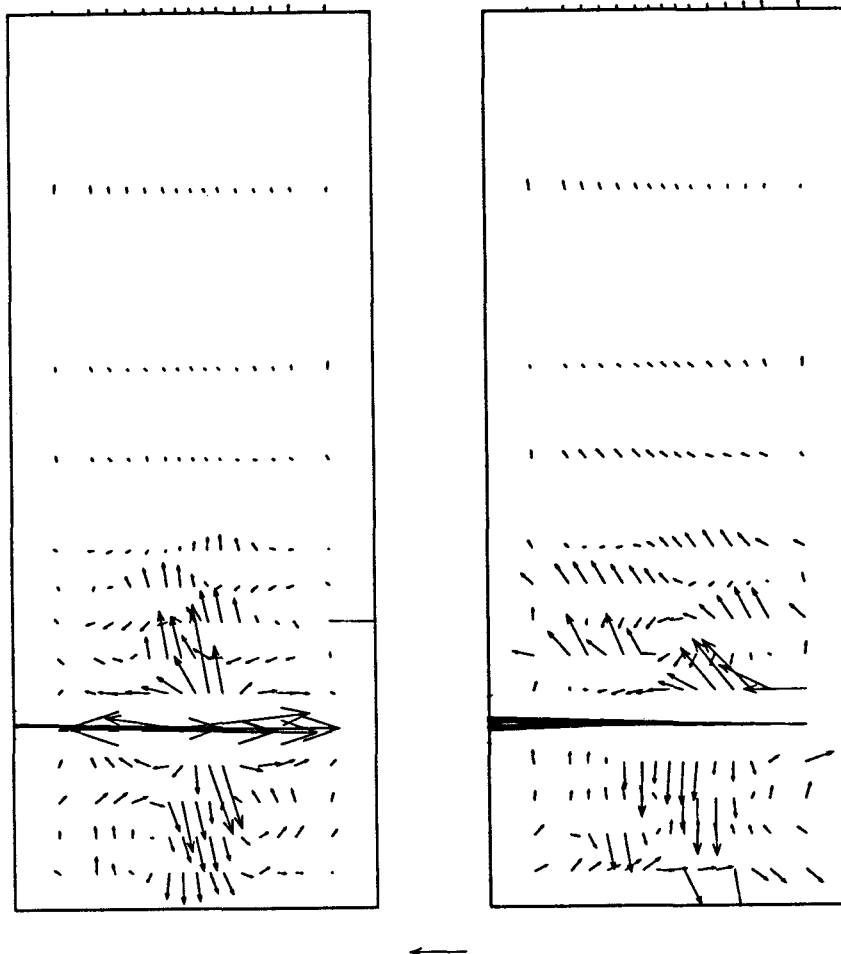


Figure 5.5.1 U^* and W^* velocity vectors $Re_d = 500$ and $Re_d = 1000$; left side $Re_d = 500$ ($d = 2$ mm, $L^* = 10$, $\mu = 25$ cP, Model 3), right side $Re_d = 1000$ ($d = 2$ mm, $L^* = 10$, $\mu = 15$ cP, Model 3)
Dimensionless velocity vector 0.25

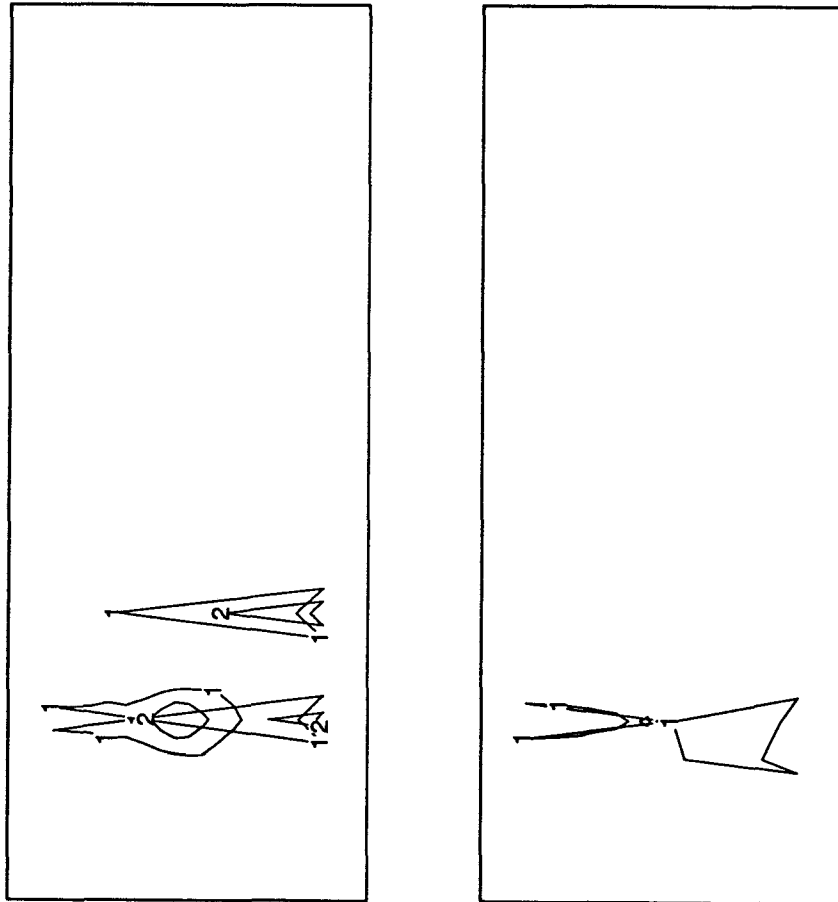


Figure 5.5.2 U^* Contours $Re_d = 500$ and $Re_d = 1000$; left side $Re_d = 500$ ($d = 2$ mm, $L^* = 10$, $\mu = 25$ cP, Model 3), right side $Re_d = 1000$ ($d = 2$ mm, $L^* = 10$, $\mu = 15$ cP, Model 3) Dimensionless contour levels 1 - 0.25 2 - 0.5

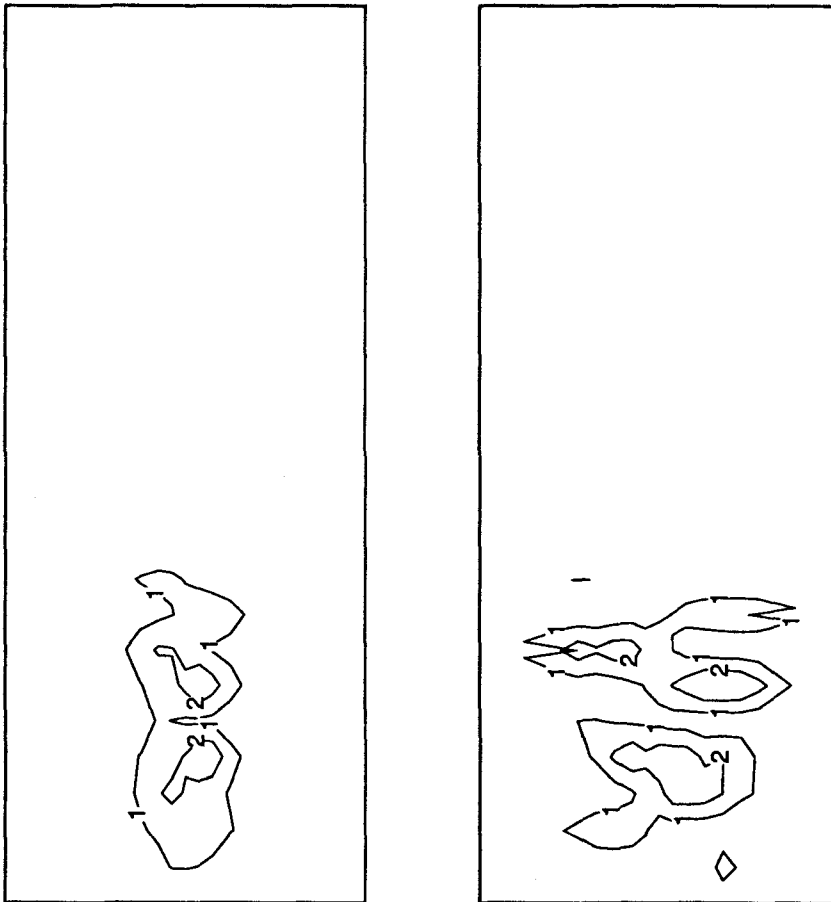


Figure 5.5.3 W^* Contours $Re_d = 500$ and $Re_d = 1000$; left side $Re_d = 500$ ($d = 2$ mm, $L^* = 10$, $\mu = 25$ cP, Model 3), right side $Re_d = 1000$ ($d = 2$ mm, $L^* = 10$, $\mu = 15$ cP, Model 3) Dimensionless contour levels 1 - 0.125 2 - 0.25

5.6 Commercial Nozzles with adjustable screw and needle assembly

5.6.1 Flow Visualization Studies

Also studied extensively were the flow patterns for mix heads having nozzles that include a screw and needle assembly to modify the opening. Although video recording was the predominant recording media, some still photographs were also obtained. Figure 5.6.1 shows Model 1, $Re_d = 43$ ($H^* = 0.5$, $N = 3$ mm, $d = 2$ mm, $\mu = 32$ cP) with the left side dyed with fluorescent dye. A centrally located impingement area is visible, as are the upper and lower recirculation zones. Figure 5.6.2 shows the same parameters for $Re_d = 69$. Again the main structure is visible, although the vortices are not as clearly defined. Above these values of Re_d the only well defined structures observed using the fluorescent dye technique are the exiting and impinging jets. At $Re_d \sim 300$ very little information can be gathered from flow visualization, particularly in the region of jet impingement as there are no visible flow structures.

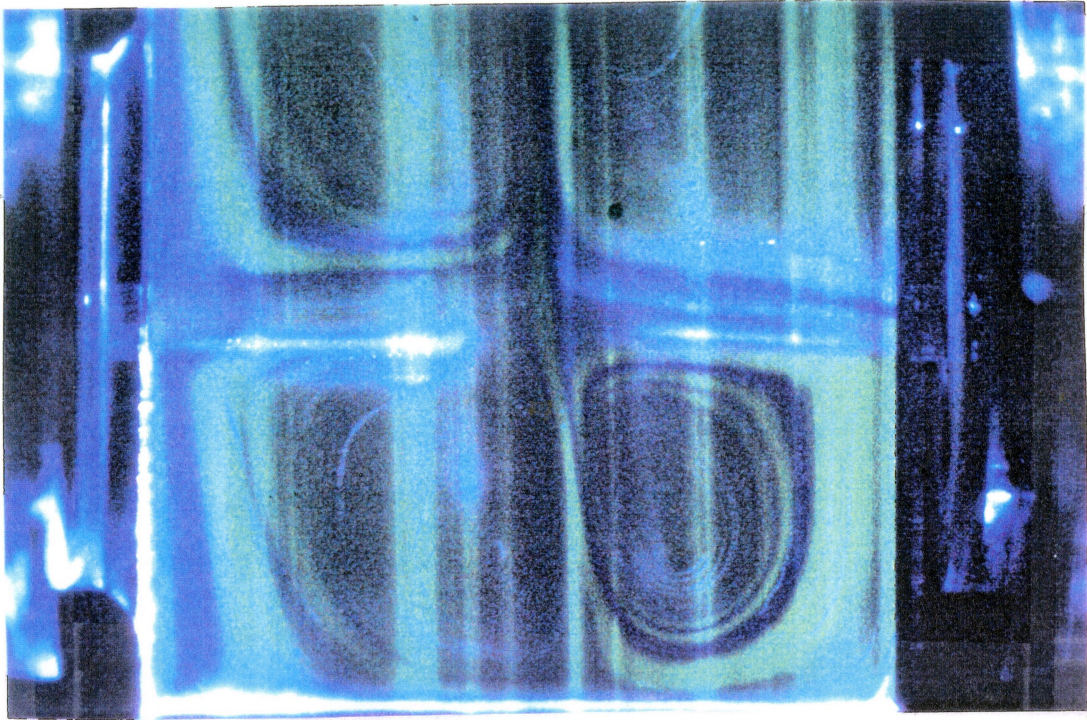


Figure 5.6.1 $Re_d = 43$ (Model 1, $H^* = 0.5$, $N = 3$ mm, $d = 2$ mm, $\mu = 32$ cP)

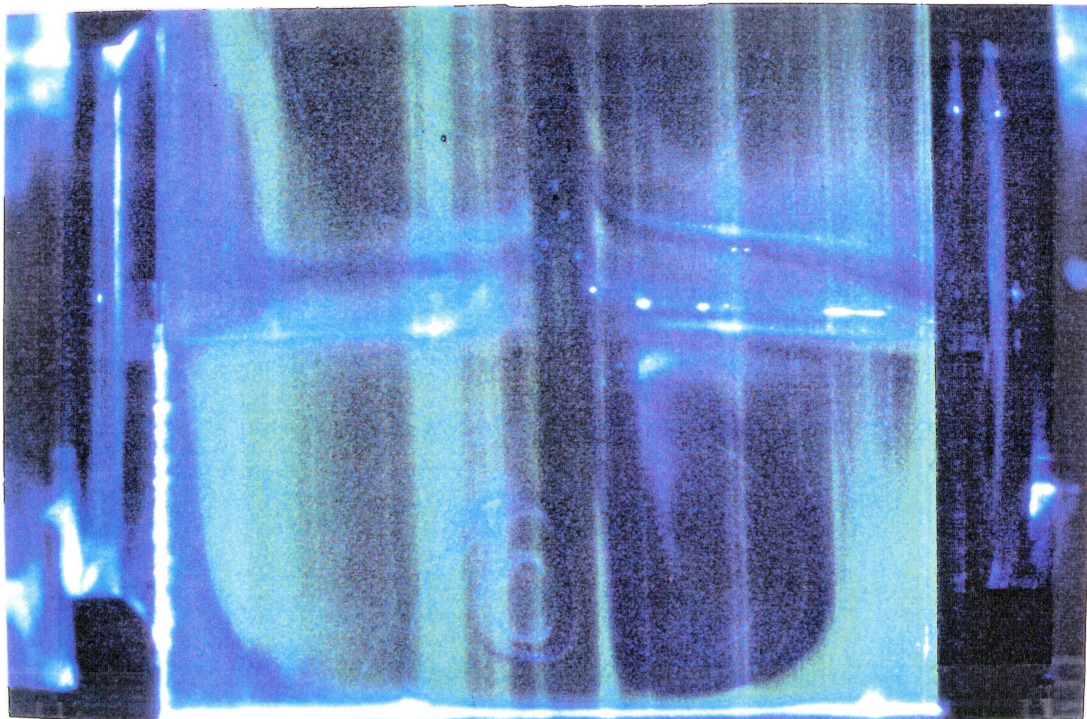


Figure 5.6.2 $Re_d = 69$ (Model 1, $H^* = 0.5$, $N = 3$ mm, $d = 2$ mm, $\mu = 32$ cP)

5.6.2 LDA studies

Studies of the entire flow field for different geometrical configurations were undertaken for the representative $Re_d \sim 300$ (Table 3.11). This value is considered to be in the normal operating region for most commercial RIM equipment. Two needle openings were selected; 1 mm (needle 1 mm from complete closure) and 3 mm, which was considered to be an opening unrestricted by the needle.

Figure 5.6.3 shows contours of W^* obtained with measurements from the LDA for model 1 ($Re_d = 304$, $D^* = 10.75$, $H^* = 0.5$, $\mu = 53$ cP) with a needle opening of 1 mm ($N = 1$ mm). The results are similar to the previous cases with straight tube nozzles: a centrally located core of high velocity fluid pierces upward at $Z^* = 1$ and the flow directly above the jets is entrained downward, forming a recirculating toroidal structure. A similar phenomenon occurs at $Z^* = -1$, although the direction of the velocities is reversed. At $Z^* = 5.375$ a small area of $-W^*$ flow can be seen. By $Z^* = 10.75$ (1 D) the flow is unidirectional and by $Z^* = 21.5$, centrally located. With the exception of a needle opening of 3 mm ($N = 3$ mm) an identical situation is shown in Figure 5.6.4. W^* in the impingement area is similar; however, the region of $-W^*$ flow extends much higher into the chamber to $Z^* = 10.75$ and unidirectional flow is not seen until after this value. Here the core of high W^* is not centrally located and extends further up into the chamber than the $N = 1$ mm case. An unsteady numerical simulation of the case $Re_d = 304$ (Model 1, $D^* = 10.75$, $H^* = 0.5$, $N = 3$ mm) by Ho (1992) agrees well with the present experimental work in that the core of $+W^*$ fluid is not centrally located, although the simulation shows higher values of W^* transferred

further up the chamber in the model. The results differ in this respect, as each experimental data point represents a time average of 10,000 velocity measurements, while the simulation is an average of three time steps from the transient solution. Unidirectional flow is achieved at approximately the same point ($Z^* = 10.75$) in both the simulations and experiments.

The next two cases ($D^* = 10.75$, $H^* = 0$, $N = 1$ mm and 3 mm, $\mu = 53$ cP) show similar behaviour (Figures 5.6.5 and 5.6.6). The $N = 1$ mm case shows a central W^* core and two adjacent $-W^*$ flow lobes above the jets ($Z^* = 1$), and the flow is unidirectional beyond $Z^* = 10.75$. The $N = 3$ mm case shows a central W^* core and lobes but does not achieve a unidirectional flow until after $Z^* = 10.75$.

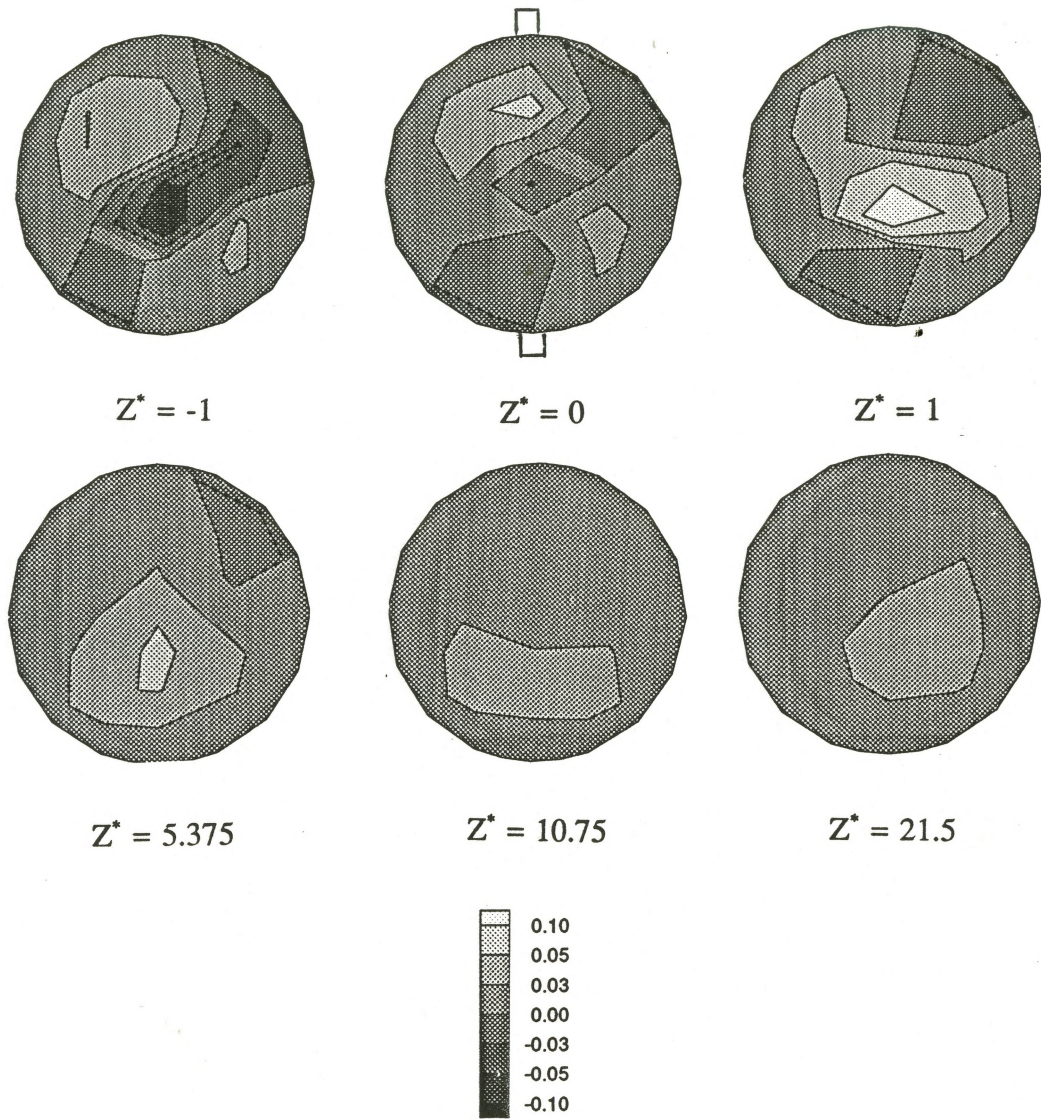


Figure 5.6.3 W^* Contours $Re_d = 304$ (Model 1, $D^* = 10.75$, $H^* = 0.5$, $N = 1$ mm, $\mu = 53$ cP)

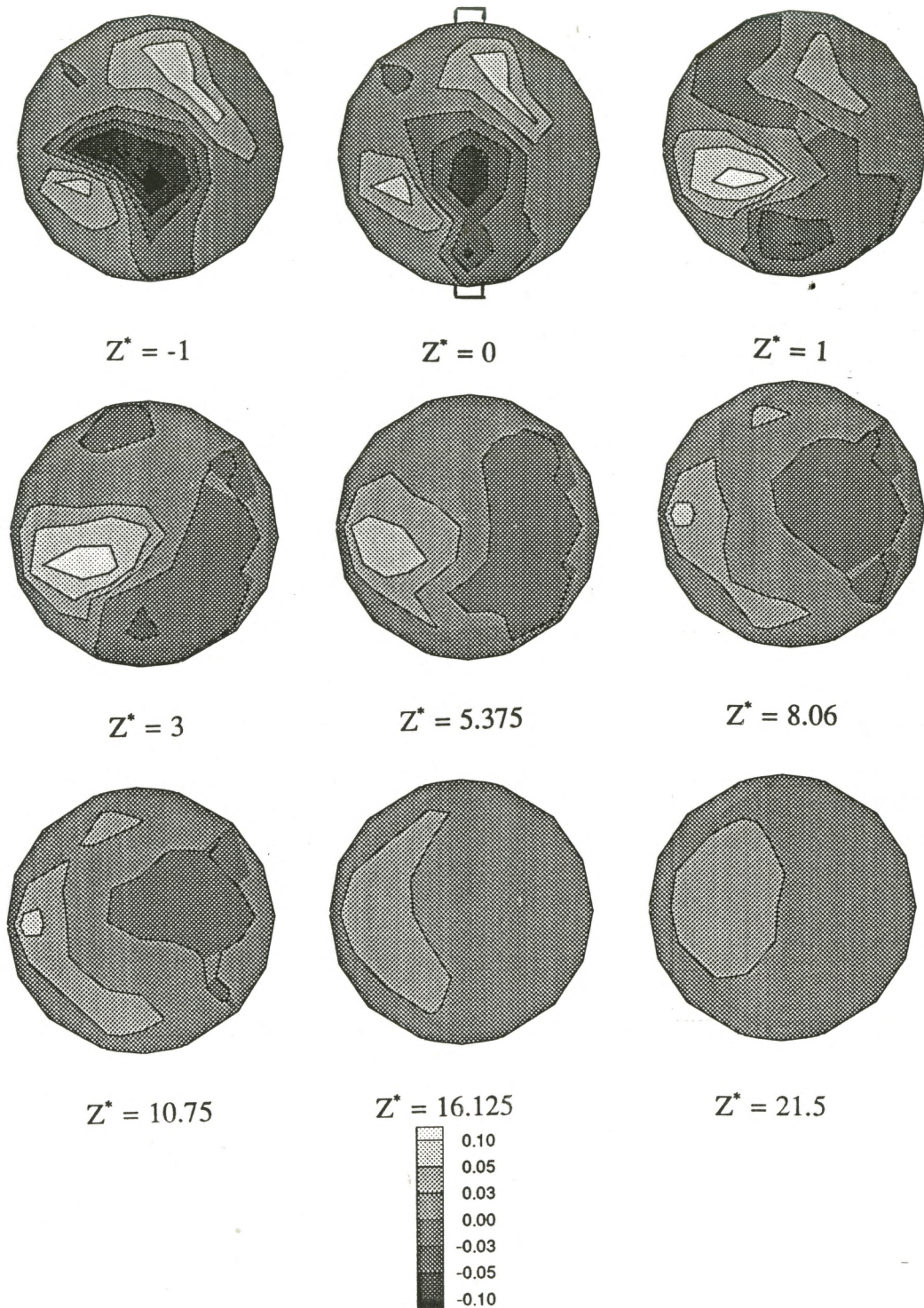


Figure 5.6.4 W^* Contours $Re_d = 304$ (Model 1, $D^* = 10.75$, $H^* = 0.5$, $N = 3$ mm, $\mu = 53$ cP)

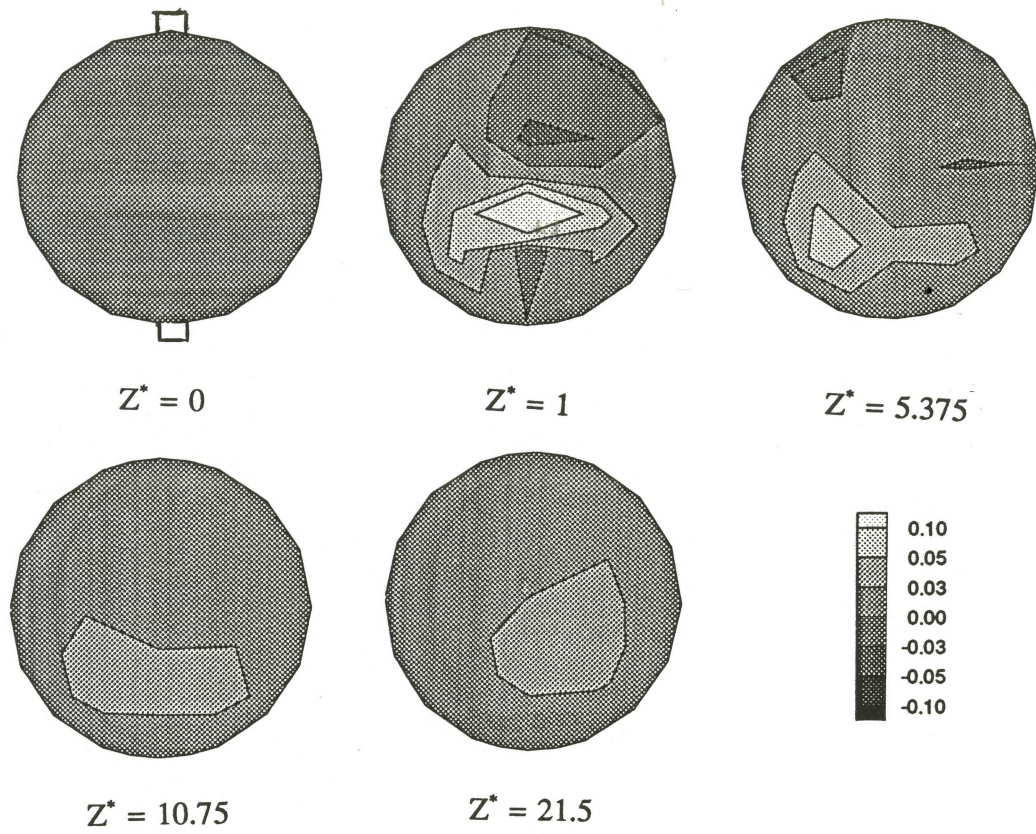


Figure 5.6.5 W^* Contours $Re_d = 304$ (Model 1, $D^* = 10.75$, $H^* = 0$, $N = 1$ mm, $\mu = 53$ cP)

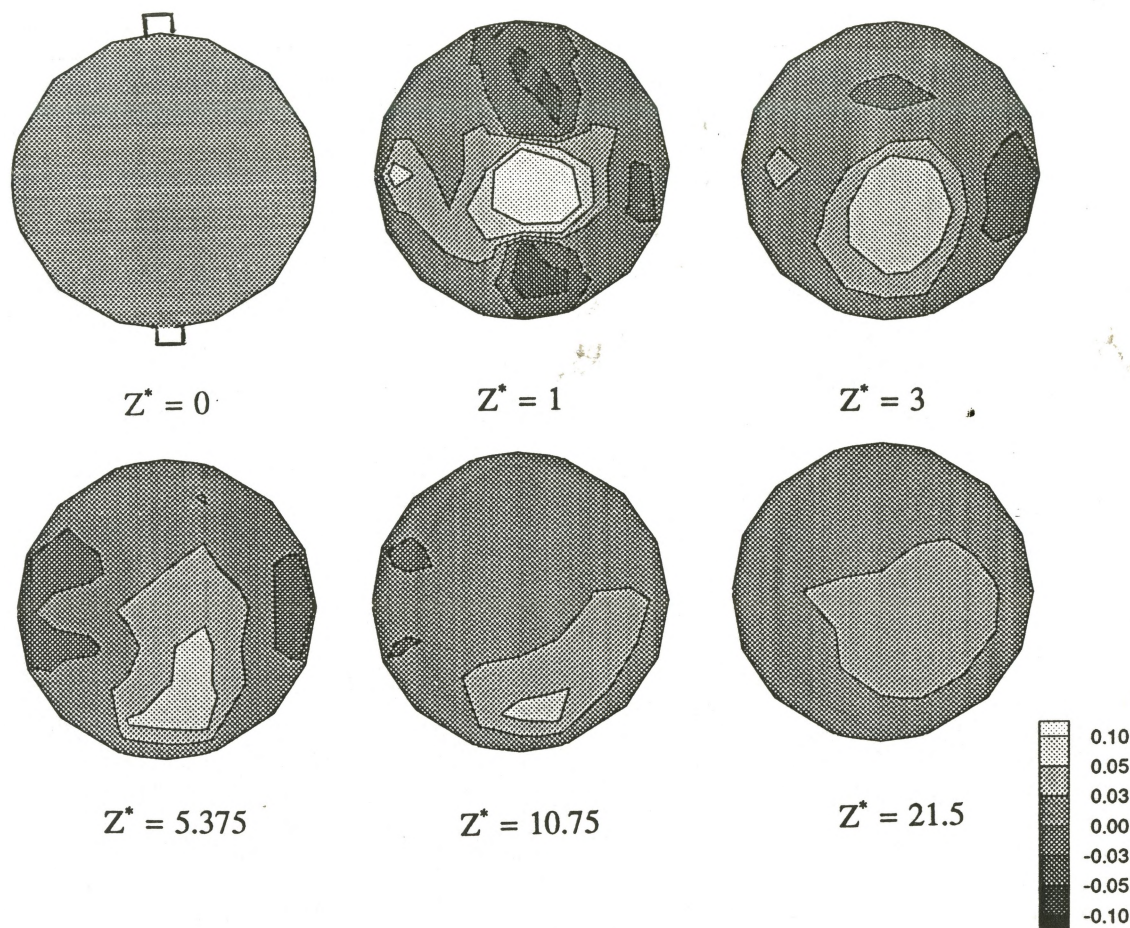


Figure 5.6.6 W^* Contours $Re_d = 304$ (Model 1, $D^* = 10.75$, $H^* = 0$, $N = 3$ mm, $\mu = 53$ cP)

Figures 5.6.7 and 5.6.8 show the results for model 2 ($Re_d = 325$, $D^* = 5$, $H^* = 0.5$, $\mu = 48$ cP) with needle openings of 1 mm ($N = 1$ mm) and 3 mm ($N = 3$ mm). These figures are quite similar and show a division of W^* in the impingement area in the $Y = 0$ plane. Above the impingement area the flow is skewed and the highest W^* occurs above the area where $-W^*$ is greatest in the impingement area. Unidirectional flow is established at $Z^* = 2.5$ ($0.5 D$) for the $N = 1$ mm case and nearly so for the $N = 3$ mm case as before although a more uniform profile is not seen until $Z^* = 10$. For

the same cases with $H^* = 0$ (Figures 5.6.9 and 5.6.10) a division between $+W^*$ and $-W^*$ at $Y = 0$ is again apparent and $-W^*$ is seen to penetrate further into z direction in comparison to the $D^* = 5 H^* = 0.5$ cases and unidirectional flow is not established until $Z^* = 5$ (1 D).

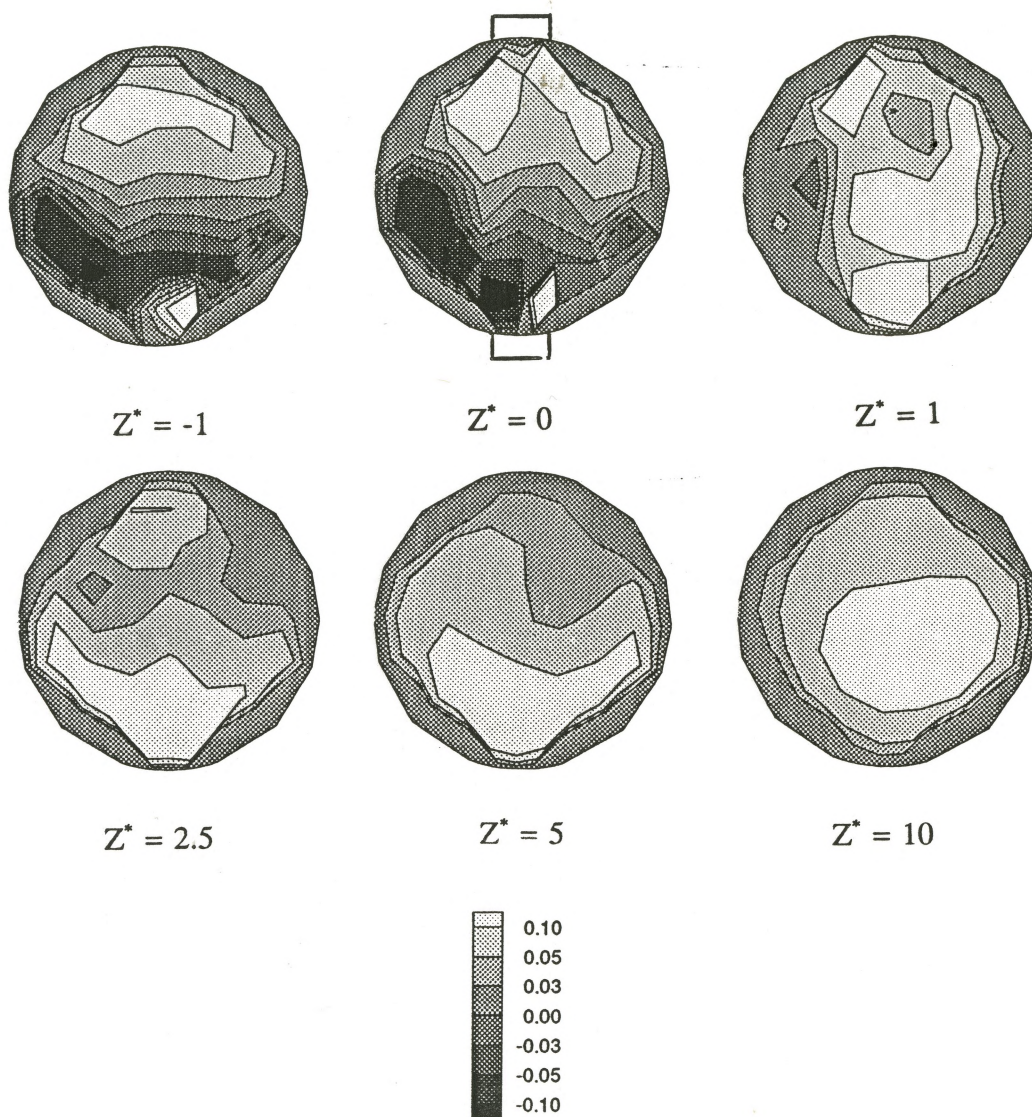


Figure 5.6.7 W^* Contours $Re_d = 325$ (Model 2, $D^* = 5$, $H^* = 0.5$, $N = 1$ mm, $\mu = 48$ cP)

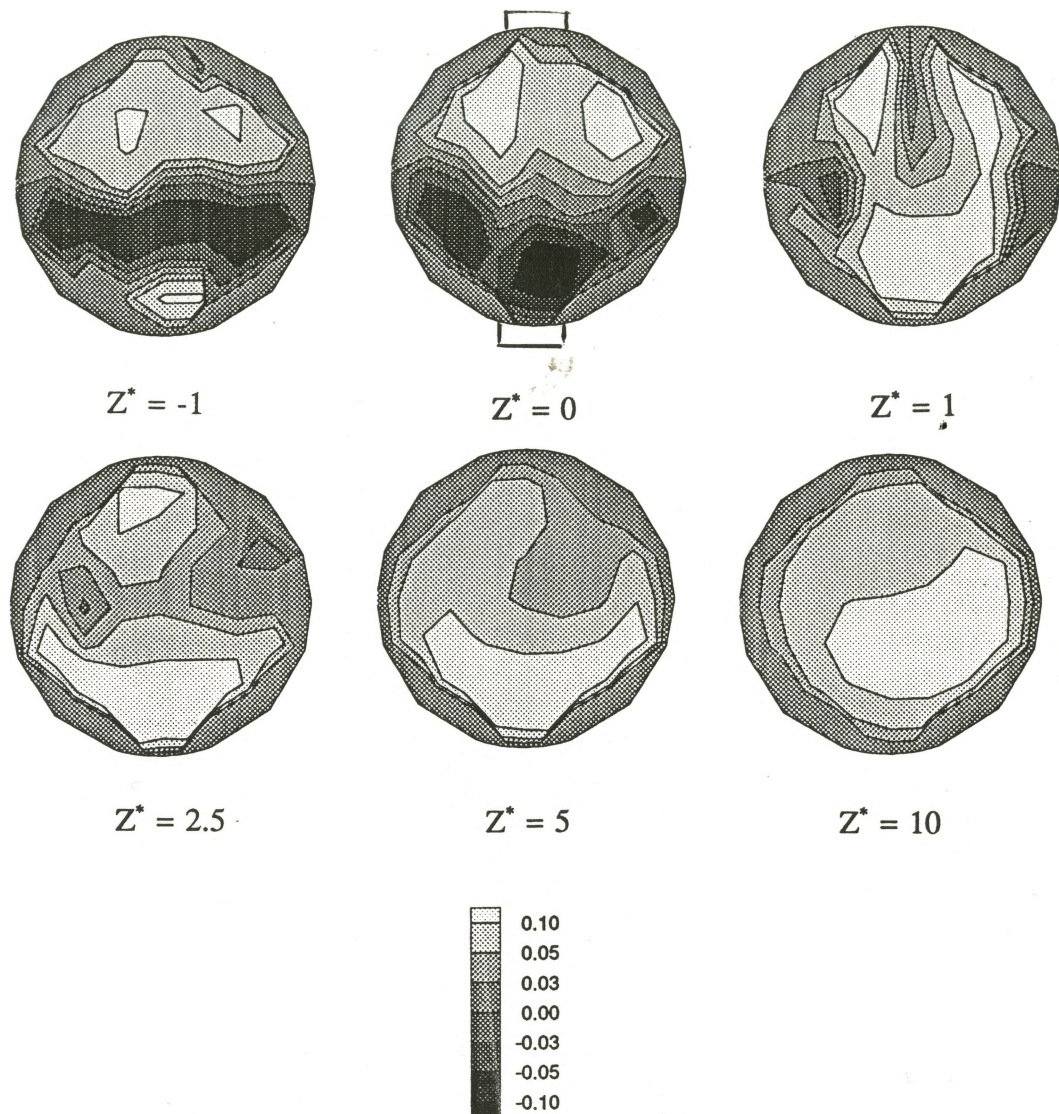


Figure 5.6.8 W^* Contours $Re_d = 325$ (Model 2, $D^* = 5$, $H^* = 0.5$, $N = 3$ mm, $\mu = 48$ cP)

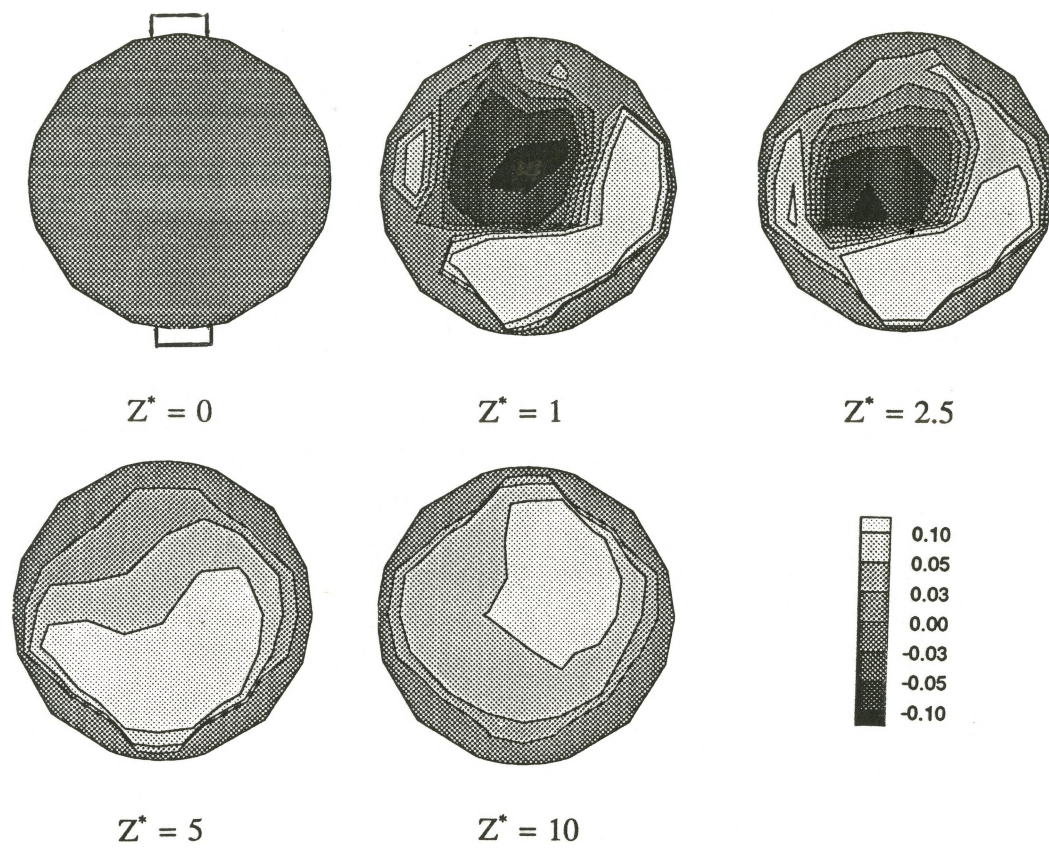


Figure 5.6.9 W^* Contours $Re_d = 325$ (Model 2, $D^* = 5$, $H^* = 0$, $N = 1$ mm, $\mu = 48$ cP)

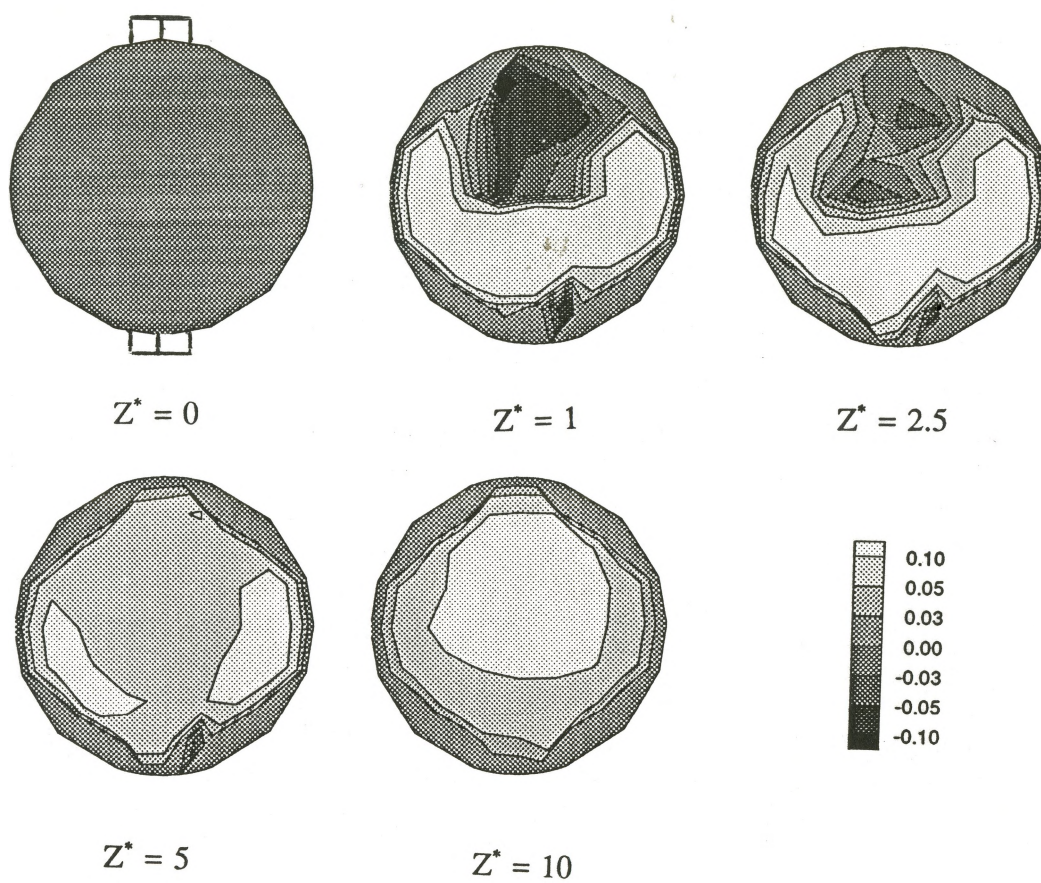


Figure 5.6.10 W^* Contours $Re_d = 325$ (Model 2, $D^* = 5$, $H^* = 0$, $N = 3$ mm, $\mu = 48$ cP)

5.6.3 Effect of Mix Head Diameter D^*

Two cases of D^* were examined; $D^* = 10.75$ and $D^* = 5$. Velocity measurements for the former case $D^* = 10.75$ show a more balanced flow field than the latter $D^* = 5$ cases in the area of impingement, although higher levels of W^* are recorded for $D^* = 5$ generally and in particular above the impingement area ($Z^* = 0$). Perhaps the most significant effect is the fact that the flow for $D^* = 5$ becomes unidirectional (no $-W^*$ velocity) at lower values of Z^* . For uniform mixing, the mixing region should be confined to as small an area as possible. Significant flow down the chamber from above the impingement point, as seen in the $D^* = 10.75$ cases, can only lead to uneven mixing in the chamber. These results are in agreement with those of Sebastian and Boukobbal (1986) who found mixing effectiveness greatly reduced for $D^* > 5$ in adiabatic temperature rise experiments, although the effect of fluid momentum ratio and D^* ratio were not separated in their studies; similar work by Lee *et al.* (1980) shows D^* has no obvious effect on the adiabatic temperature rise.

5.6.4 Effect of Head Distance H^*

The H^* position seems to have little effect past the point of impingement, since W^* contours are unaffected by H^* above $Z^* = 1$ for both cases of D^* . This result has been qualitatively documented previously by Stull *et al.* (1985), who found flow visualization patterns above the jets relatively unaffected by variations in H^* for $H^* = 0 - 0.66$, and Liou *et al.* (1990), who found the location of the impingement stagnation point and recirculation attachment points above the impingement area to be insensitive

to H^* for $H^* = 0 - 4$. Simulations by Wood *et al.* (1991) showed that oscillations of the impingement surface decreased with increasing H^* ($H^* = 0.5 - 1$) for $Re_d = 50-300$; simulations by Ho (1992), with increasing H^* from $H^* = 0$ up to $H^* = 0.5$ for $Re_d = 50$, showed a slight increase in distance to the point where flow is fully developed. Qualitative studies by Sandell *et al.* (1985), however, suggest that lower values of H^* have a stabilizing effect on the flow field, although the range of H^* studied is not given.

5.6.5 Effect of Needle Position N

When the needle restricts the nozzle opening for $N < 1.5$ mm, an annular gap is formed. In all flow visualizations and measurements no annular core or spreading of the jet occurred that was significantly different from an unrestricted nozzle; however, it was impossible to make measurements very near to the nozzle exit (less than 1 mm) to determine if an annular core existed. With the needle position at $N = 3$ mm the onset of unidirectional flow occurs at larger values of Z^* in all cases.

5.6.6 Developing Jet Condition

From flow visualization images the incoming jets are seen to remain cylindrical up to the point of impingement for a large range of Re_d ; in fact the jets are the only discernable structure at high Re_d ($Re_d > 160$).

Results of the measurements of U^* along the y axis for various x values are shown in Figure 5.6.11 (Conditions Table 3.12). In these cases X_j^* refers to the

measurements beginning at the nozzle mouth ($x_j = 0$), divided by the nozzle diameter d . Although the initial profiles ($X_j^* = 0.5, 1.0$) have some curvature in the profile $-0.5 < Y^* < 0.5$ (original jet dimensions), velocities close to $Y^* = 0$ are fairly uniform, indicating the existence of a potential core and not much spreading of the jet has occurred. The profiles are slightly skewed toward the $+y$ axis, a situation which becomes more pronounced as X_j^* is increased until at $X_j^* = 4.5$ the jet profile has disappeared and the effect of the impingement area is seen. From this figure an asymmetric skewed impingement surface is seen.

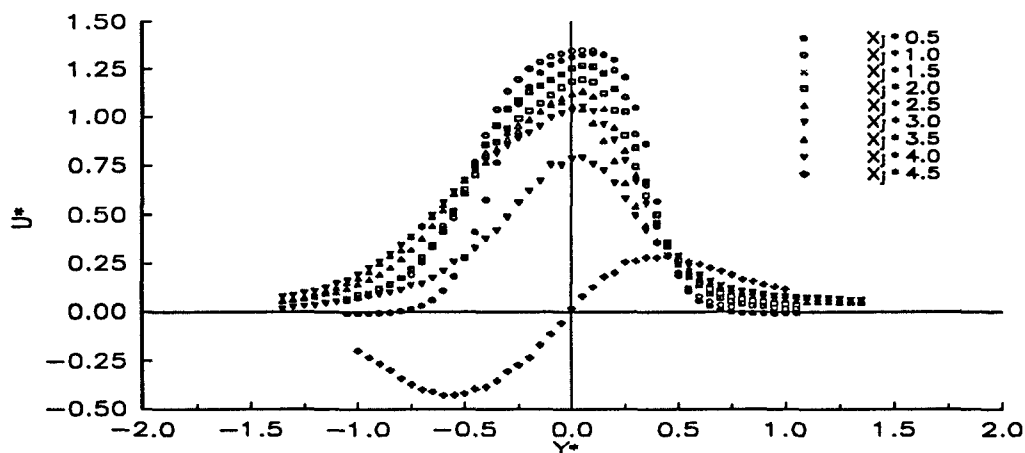


Figure 5.6.11 Jet Development U^* vs Y^* $Re_d = 275$ (Model 1, $\mu = 60$ cP, $H^* = 0.5$, $D^* = 10.75$, $N = 3$ mm, $d = 2$ mm)

Figure 5.6.12 shows U/U_{\max} for each X_j^* versus $y/y_{(U_{\max}/2)}$. As the jet develops, it should approach a fully developed profile like that of Schlichting (1968) for a fully developed parabolic nozzle outlet profile; however, from this figure it appears as though the profiles never reach the similarity profile, although the profile at $X_j^* = 3.5$ is the closest. At $X_j^* = 4.0$ the profile is skewed significantly toward the +y axis and shows little agreement to the similarity result. Akaike and Nemoto (1988) have reported results from a submerged laminar water jet of $Re_d = 100$ to 600 which issued from a short 10 mm diameter nozzle (24 mm dia. tapered to 10 mm over 25 mm and 5 mm of 10 mm diameter nozzle) into an unrestricted area. Their experimental results for $Re_d = 308$ at $X_j^* = 0$ and 2 are included in the figure for comparison; the present results at $X_j^* = 0.5$ and 1.0 agree very well with this data, although values of $10 > X_j^* > 2$ are not reported in their study.

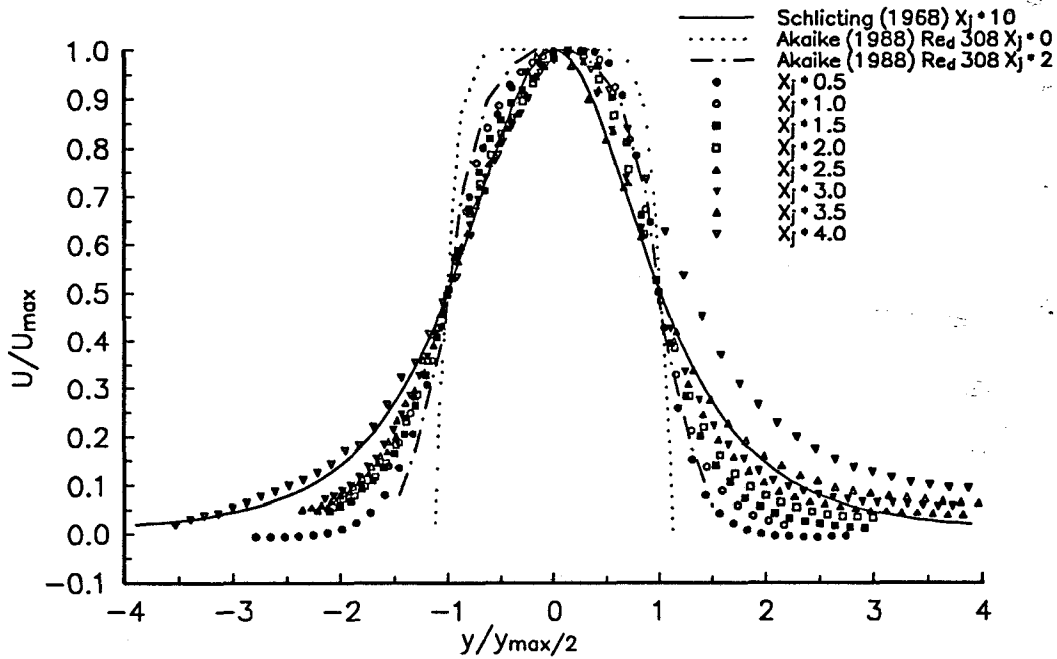


Figure 5.6.12 Jet Development U/U_{\max} vs $y/y_{(U_{\max}/2)}$ $Re_d = 275$ (Model 1, $\mu = 60$ cP, $H^* = 0.5$, $D^* = 10.75$, $N = 3$ mm, $d = 2$ mm)

Figure 5.6.13-15 shows the intensity versus Y^* for the same X_j^* where intensity I is defined as

$$I = \frac{\sqrt{u^2}}{U} \quad 5.6.1$$

I has the highest value for $X_j^* = 0.5$, partially as a result of $X_j^* = 0.5$ having some $-U^*$ flow because of jet entrainment. The peaks in the figure at $Y^* = -0.75, 0.75$ define the boundary of the $+U^*$ flow. In the core of the jet between these Y^* values, I

is extremely low; as is also true for $3.5 > X_j^* > 1.0$ in the region of the original jet diameter $-0.5 < Y^* < 0.5$. At the periphery of these values I increases dramatically. Near the point of impingement $X_j^* = 4.0$ (Figure 5.6.14) and $X_j^* = 4.5$ (Figure 5.6.15) the effect of the skewed impingement point is seen. $X_j^* = 4.0$ has a significant I for all values of $-Y^*$, probably the result of the movement of the skewed impingement interface. As seen in Figure 5.6.15 at $X_j^* = 4.5$ I increases at $Y^* = 0.0$ because of the very low velocities in this region.

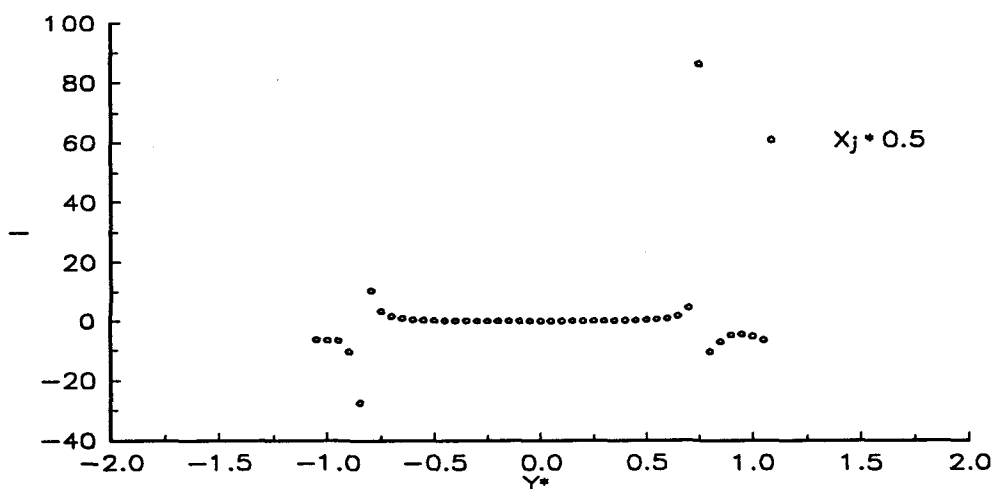


Figure 5.6.13 Jet Development I vs Y^* at $X_j^* = 0.5$ $Re_d = 275$ (Model 1, $\mu = 60$ cP, $H^* = 0.5$, $D^* = 10.75$, $N = 3$ mm, $d = 2$ mm)

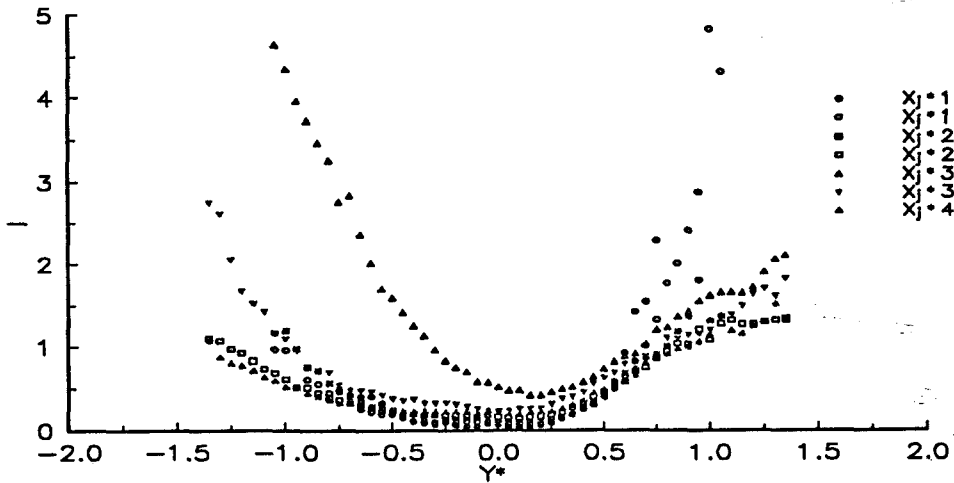


Figure 5.6.14 Jet Development I vs Y^* for $X_j^* = 1-4$ $Re_d = 275$ (Model 1, $\mu = 60$ cP, $H^* = 0.5$, $D^* = 10.75$, $N = 3$ mm, $d = 2$ mm)

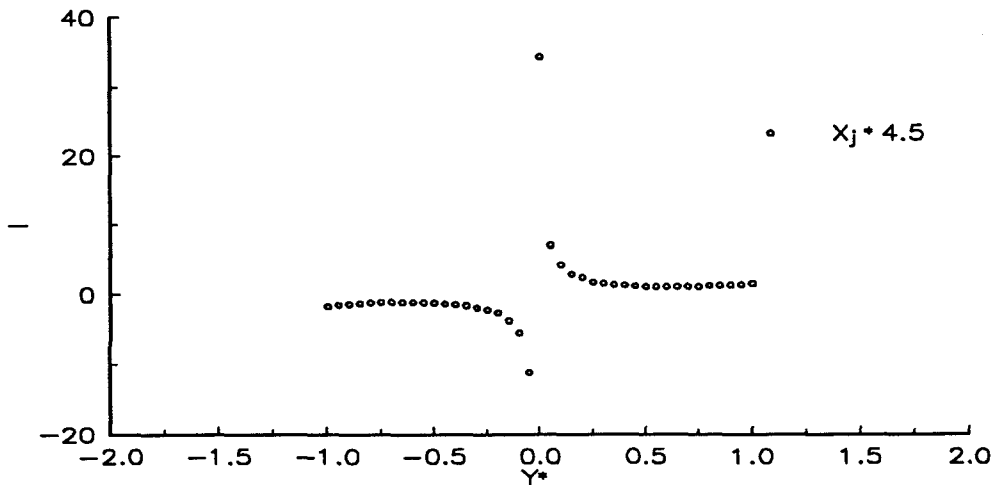


Figure 5.6.15 Jet Development I vs Y^* at $X_j^* = 4.5$ $Re_d = 275$ (Model 1, $\mu = 60$ cP, $H^* = 0.5$, $D^* = 10.75$, $N = 3$ mm, $d = 2$ mm)

5.6.7 Variation of Fluid Parameters

Frequently in industrial practice, fluid parameters are not identical at both nozzles, with the viscosity and flow rate differing significantly. Unequal flow rates were examined using both flow visualization and LDA studies.

5.6.7.1 Unequal Flow Rates

Flow visualization studies for unequal flow rates for both cases reveal a significant alteration in the location of the point of impingement. For low Re_d cases (e.g. $Re_{d1} = 50$, $Re_{d2} = 87$) the impingement point is close to the lower Re_d side. If the Re_d ratio is maintained and Re_d is increased, the impingement point moves closer to the lower Re_d side. From flow visualization images it is difficult to determine the path of the fluid issuing from the nozzle with this lower Re_d . In the XY plane at $Z = 0$ two large areas of recirculation are observed on either side of the high Re_d jet. Video analysis shows the impingement area and structure in these cases to be more stable at higher Re_d than comparable equal flow rate cases.

The LDA results for unequal flow case 1 ($N = 1$ mm) are shown in Figure 5.6.16 (Conditions Table 3.13). In this case U_{avg} was taken to be the average velocity of the combined jet conditions. Above the jets significant $-W^*$ is found for all Z^* measured (up to $Z^* = 10.75$, $1D$), indicating a large area of recirculation; the $+W^*$ flow is skewed and located around the higher velocity jet (left side of figure). There is some deflection of the higher velocity jet into the head region aiding this recirculation structure. At the $Z^* = 0$ plane the impingement point may be roughly estimated using the U velocity at $Y^* = 0$ and is found to be located at $X^* = 3.39$ ($-5.375 > X^* < 5.375$)

$U_{avg2}/U_{avg1} = 2.11$ ($Re_{d2}/Re_{d1} = 458/217$, $\mu = 45.5$ cP). Results for unequal flow rate turbulent free air jets have been detailed by Ogawa *et al.* (1992) who found for a flow rate ratio U_{avg1}/U_{avg2} of 0.935 the impingement point was located at $X^* = -1.61$ ($-2.15 > X^* < 2.15$) and for a flow rate ratio U_{avg1}/U_{avg2} of 1.044 the impingement point was located at $X^* = 1.32$ ($d = 35$ mm, $L/D = 4.3$, $Re_d = 5.61 \times 10^4$). Although the flow rate ratio is smaller, their results indicate that the relationship between flow rate ratio and impingement point is not linear and flow rate ratio may not solely be used to determine the impingement point. They also found the impingement area in unequal flow rate ratios cases to be relatively stable in comparison to the equal flow rate case. Numerical simulations reported by Ho (1992) in a cylindrical mix chamber ($D^* = 10$) for a flow rate ratio of 1:1.5 found the impingement point to be located at $X^* = 3.5$ ($-5. > X^* < 5.$) $U_{avg1}/U_{avg2} = 1.5$, and for the flow rate ratio of 1:2 found the impingement point to be located at $X^* = 4.3$ ($-5. > X^* < 5.$) $U_{avg1}/U_{avg2} = 2$.

These values are in reasonable agreement considering the unsteady nature of the flow field at these Re_d and the technique used to ascertain the impingement point.

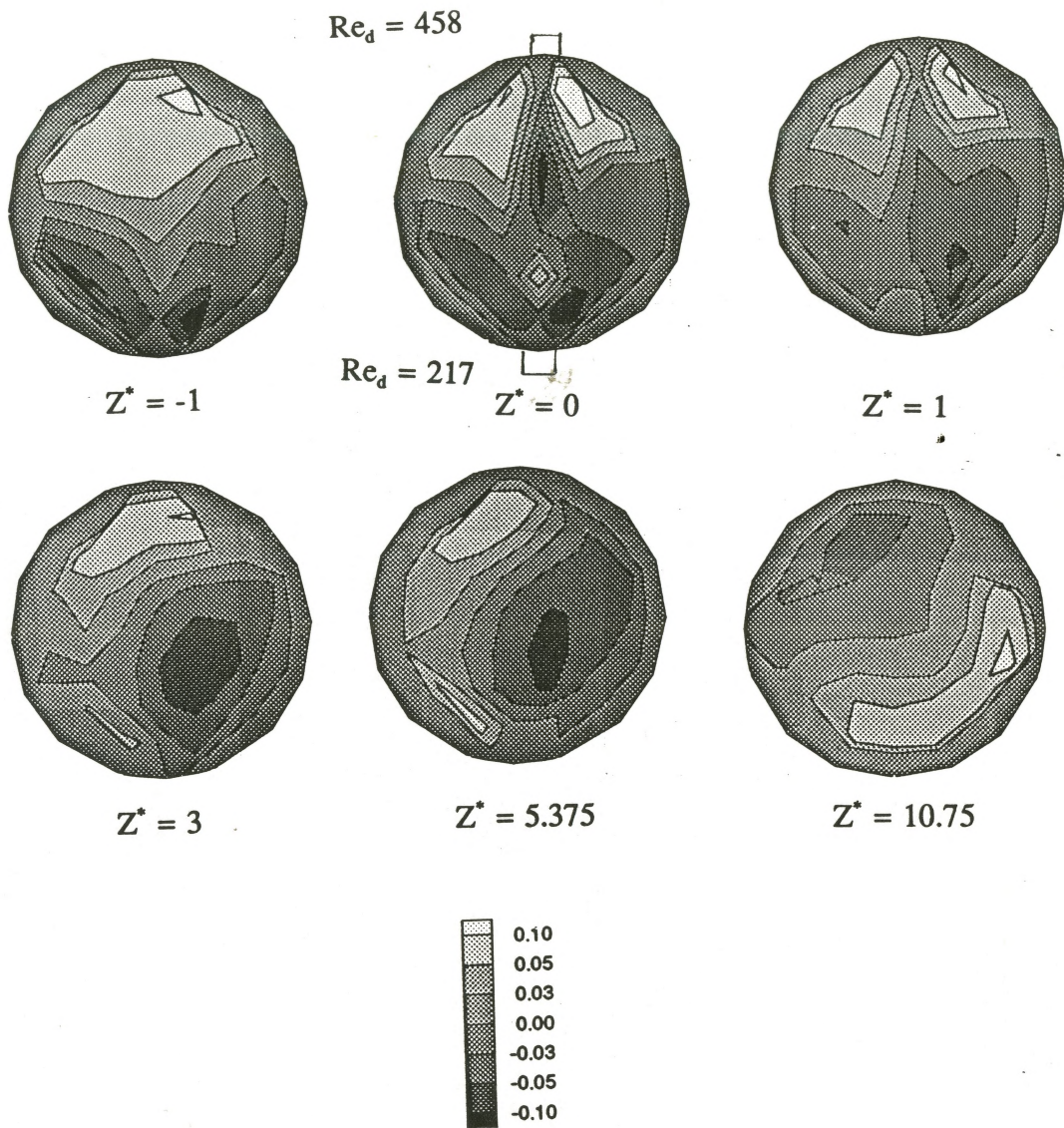


Figure 5.6.16 W^* Contours Unequal Flow Rates, top $Re_d = 458$, bottom $Re_d = 217$
 (Model 1, $D^* = 10.75$, $H^* = 0.5$, $N = 1$ mm, $d = 2$ mm, $\mu = 45.5$ cP)

5.6.7.2 Unequal Viscosities

Because of the quantities of unusable intermediate viscosity material generated during an entire LDA study, unequal viscosities were examined using flow visualization only. For the two cases studied the flow rate on both sides was equal;

therefore, the flow rate effect was eliminated. For the case of $Re_{d1} = 42$, $\mu = 49$ cP and $Re_{d2} = 105$, $\mu = 19$ cP an impingement point in the geometric centre of the chamber is observed. Above and below this point, form the more viscous jet vortices, which are similar to the equal viscosity/flow rate cases; however on the lower viscosity side no vortices form above or below the jets and the flow has no visible configuration. At Re_d above these values the higher viscosity fluid was observed to form a flowing surface in the area above the heavy viscosity jet diagonal to the surface of the piston head below the lower viscosity fluid which the lower viscosity fluid flowed against and was unable to penetrate. The jets were observed to miss and strike the opposed wall and occasionally alternate position with respect to each other. As a result of this change, the flow pattern above the jets was similar to a corkscrew with helical flow along the chamber boundary in the Z direction.

5.6.8 Geometrical Modifications

In an effort to confine the areas of recirculation and to further simulate commercial practice, a restriction was designed and placed in the chamber outlet of Model 1. The "choke", which fit the bore diameter (21.5 mm) and had a concentric inside diameter of 10.0 mm, could be placed at any Z ($C^* = Z/D$) distance in the model. Its purpose was to alter the chamber area and increase the pressure in the impingement area allowing an opportunity to "shape" the mix chamber.

5.6.8.1 Restricted Equal Flow Rate Cases - Flow Visualization

$$\underline{C^* = 0.5, H^* = 0.5}$$

With the addition of the "choke" the most significant change is the destruction of the recirculation areas above the jets. Sketches of path lines shown in Figure 5.6.17 for the conditions $Re_d = 54$, $\mu = 24$ cP, $N = 3$ mm, $C^* = 1.0$, $H^* = 0.5$, $D^* = 10.75$ of the XZ plane can be compared with Figure 5.6.1,2 of the XZ plane with no flow restriction. The lower recirculation areas are unaffected but in the unrestricted case the upper recirculation core is located at approximately $X^* = \pm 1$, $Z^* = 8$ (0.75 D) above the origin while the restricted case shows no core of recirculation and the flow is seen to come from the $X^* = \pm 5.375$, $Z^* = 5.375$ upper corner of the "choke". Furthermore a stationary impingement surface is observed at $Re_d = 135$ (Figure 5.6.17) which is higher than previously recorded for the unrestricted cases where a maximum pre-oscillatory $Re_d \sim 90$ was observed. Although at $Re_d = 202$ (Figure 5.6.17) the jets still impinge, all other defined structures have disappeared.

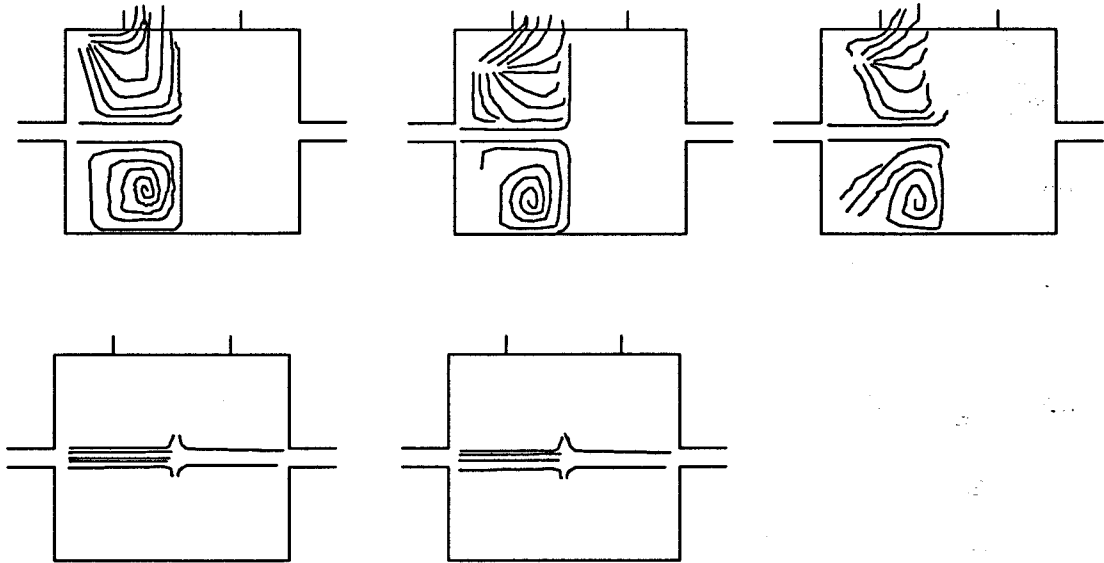


Figure 5.6.17 Flow Visualization Particle Tracings for Flow Restriction XZ plane $Y = 0$, $C^* = 0.5$, $H^* = 0.5$ ($\mu = 24$ cP, $N = 3$ mm, $D^* = 10.75$; top row $Re_d = 54$, $Re_d = 96$, $Re_d = 135$; bottom row $Re_d = 202$, $Re_d = 309$)

$C^* = 1.0$, $H^* = 0.5$

Figure 5.6.18 (bottom row) $Re_d = 97$, $N = 3$ mm, $C^* = 1.0$, $H^* = 0.5$, $D^* = 10.75$ of the XZ plane is similar to the shorter choke in that the lower recirculation areas are unaffected but a partial upper recirculation area is located near the surface of the "choke" for $Re_d < 75$ (Figure 5.6.18) which subsequently disappears as Re_d is increased. Above $Re_d = 75$ the flow again appears to enter the XZ plane in the upper corner of the confined area at $X^* \pm 5.375$, $Z^* = 10.75$. This situation is comparable to an unrestricted case where the recirculation area seldom went above $Z^* = 10.75$ (1D). An oscillating structure is present at $Re_d = 143$ (Figure 5.6.18) and no structure other than the impinging jets was observed at $Re_d = 284$.

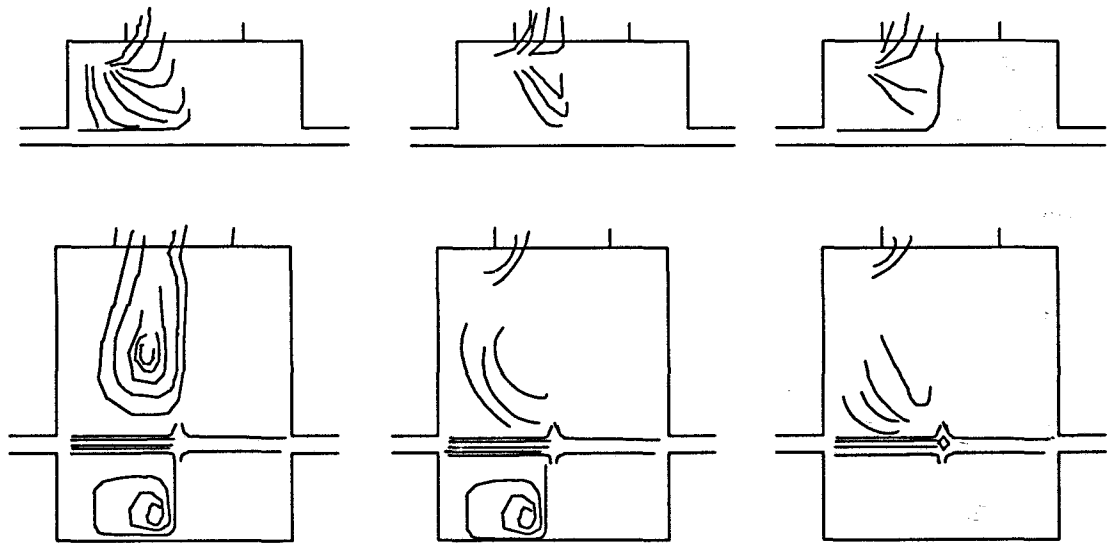


Figure 5.6.18 Flow Visualization Particle Tracings for Flow Restriction XZ plane $Y = 0$ ($\mu = 24$ cP, $N = 3$ mm, $D^* = 10.75$; top row $C^* = 0.5$, $H^* = 0$, $Re_d = 76$, $Re_d = 89$, $Re_d = 135$; bottom row $C^* = 1.0$, $H^* = 0.5$, $Re_d = 61$, $Re_d = 97$, $Re_d = 143$)

$C^* = 0.25$, $H^* = 0$

For these cases there is not a large volume before the lip of the "choke" and, as a result, significant areas of recirculation were observed in the tube blocking the +W flow.

$C^* = 0.5$, $H^* = 0$

Above the jets these cases are similar to the $C^* = 0.5$, $H^* = 0.5$ cases previously discussed, with the particle tracings appearing to originate in the upper area of the "choke". At the mouth of the "choke" they also have significant U velocity restricting the +W velocity somewhat (Figure 5.6.18 top row). Above $Re_d = 135$ no structure was identifiable.

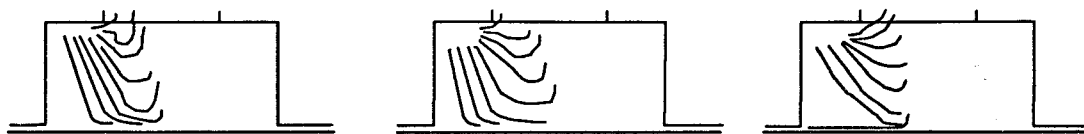


Figure 5.6.19 Flow Visualization Particle Tracings for Flow Restriction XZ plane $Y = 0$, $C^* = 1.0$, $H^* = 0$ ($\mu = 24$ cP, $N = 3$ mm, $D^* = 10.75$, from left $Re_d = 78$, $Re_d = 95$, $Re_d = 135$)

$C^* = 1.0$, $H^* = 0$

A small recirculation area is observed at $Re_d = 78$ (Figure 5.6.19) which has disappeared at $Re_d = 95$ (Figure 5.6.19). No structure was visible above $Re_d = 135$ (Figure 5.6.19)

5.6.8.2 Restricted Equal Flow Rate Cases - LDA Study

$C^* = 0.5$, $H^* = 0.5$ LDA study

Figure 5.6.20 shows contours of W^* for model 1 ($d = 2$ mm, $D^* = 10.75$, $C^* = 0.5$, $H^* = 0.5$, $N = 3$ mm, Conditions Table 3.14). The results are somewhat similar to the previous cases since a centrally located core of high velocity fluid pierces upward at $Z^* = 1$ and flows downward from above the jets. At $Z^* = 3$ areas of $-W^*$ flow can be seen surrounding the core of $+W^*$ flow. Optical limitations prevented another Z^* level from being examined. The significant alteration occurring with the addition of

the "choke" is the centralization of the flow above and below the impingement point. For all previous commercial nozzles the flow above and below $Z^* = 0$ has not been centrally located and significant $-W^*$ occurred well above $Z^* = 0$. Flow visualization and LDA data, however, reveal that the addition of a "choke" will allow a stable impingement configuration to exist at higher Re_d than in unrestricted cases, the flow is more centrally located, and it was not observed to flow up the walls of the chamber.

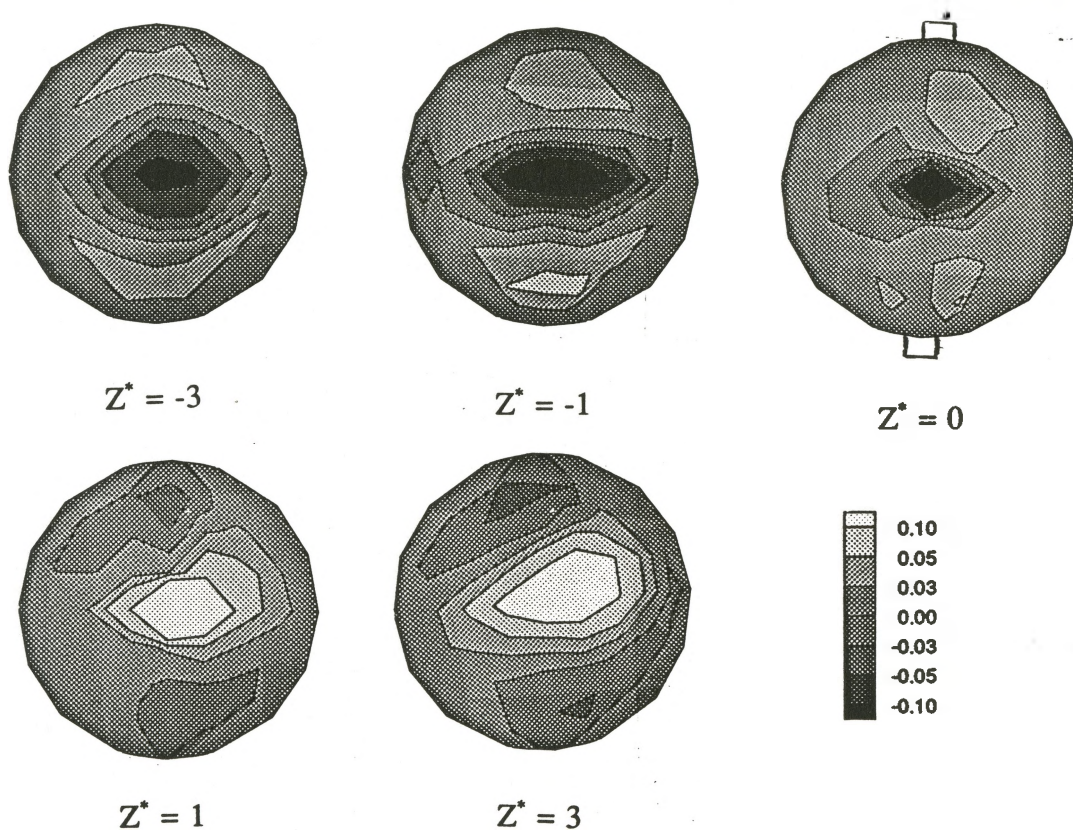


Figure 5.6.20 W^* Contours Flow Restriction, $Re_d = 300$ ($\mu = 50$ cP, Model 1, $D^* = 10.75$, $H^* = 0.5$, $C^* = 0.5$, $N = 3$ mm, $d = 2$ mm)

5.6.8.3 Restricted Unequal Flow Rate Cases

$C^* = 1.0$, $H^* = 0.5$ and $C^* = 0.5$, $H^* = 0.5$

The unequal flow rate structures visualized were significantly different than those visualized with equal flow rate cases described previously. Below $Z^* = 0$ a single vortex was observed toward the lower flow side. Above $Z^* = 0$ flow in the X direction was predominant until the lip of the "choke" where the flow altered direction and flowed in the Z direction. The particle paths seem to be folded on top of each other.

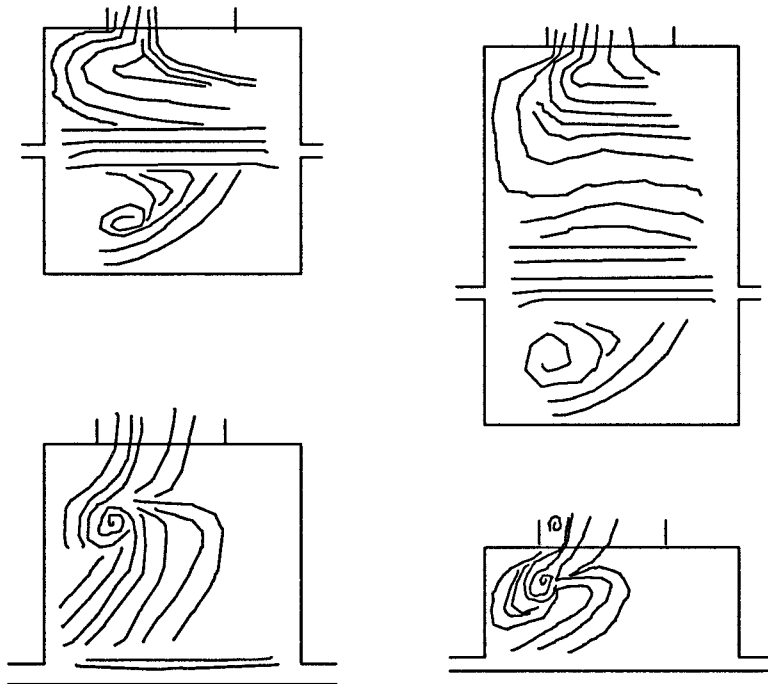


Figure 5.6.21 Flow Visualization Particle Tracings for Flow Restriction Unequal Flow Rates XZ plane $Y = 0$ ($\mu = 24$ cP, $N = 3$ mm, $D^* = 10.75$, from top row, left; $C^* = 0.5$, $H^* = 0.5$, left side $Re_d = 73$, right side $Re_d = 143$; $C^* = 1.0$, $H^* = 0.5$, left side $Re_d = 73$, right side $Re_d = 143$; bottom row, left $C^* = 1.0$, $H^* = 0.0$, left side $Re_d = 73$, right side $Re_d = 143$; $C^* = 0.5$, $H^* = 0.0$, left side $Re_d = 76$, right side $Re_d = 143$)

$C^* = 1.0$, $H^* = 0.0$ and $C^* = 0.5$, $H^* = 0.0$

In these cases a single vortex is formed above $Z^* = 0$ on the lower flow rate

side and a large vortex forms in the "choke" chamber further restricting the flow.

Above $Z = 0$ the structures visualized are not similar to the unequal flow rate cases without restrictions; however the movement of the impingement area toward the lower flow rate side is similar as is the single lower vortex. Only in the $H^* = 0$ cases was $-W^*$ flow observed above the "choke". Previously, significant $-W^*$ flow occurred at much higher Z values than observed with the restriction.

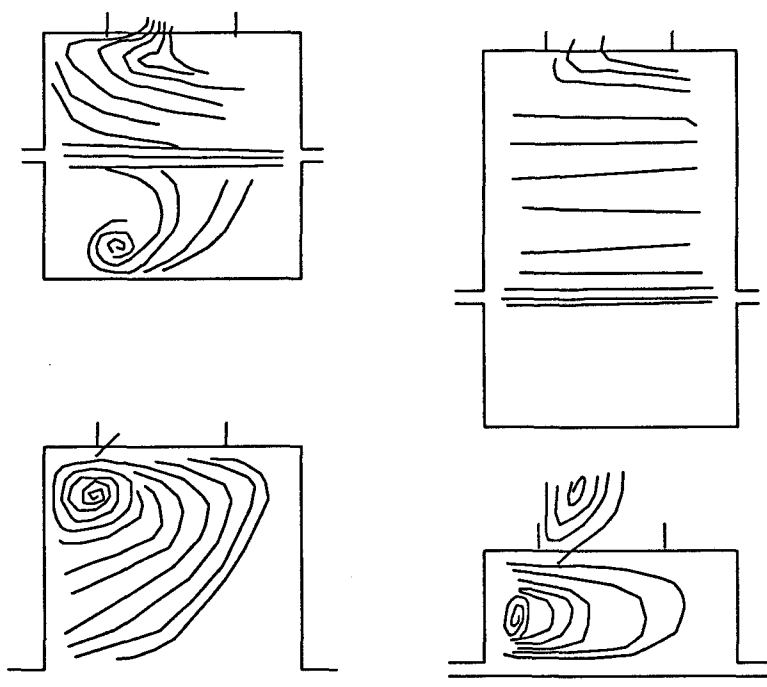


Figure 5.6.22 Flow Visualization Particle Tracings for Flow Restriction Unequal Flow Rates XZ plane $Y = 0$ ($\mu = 24$ cP, $N = 3$ mm, $D^* = 10.75$, from top row, left; $C^* = 0.5$, $H^* = 0.5$, left side $Re_d = 135$, right side $Re_d = 309$; $C^* = 1.0$, $H^* = 0.5$, left side $Re_d = 139$, right side $Re_d = 319$; bottom row, left $C^* = 1.0$, $H^* = 0.0$, left side $Re_d = 135$, right side $Re_d = 309$; $C^* = 0.5$, $H^* = 0.0$, left side $Re_d = 139$, right side $Re_d = 303$)

5.6.9 Summary - Commercial Nozzles

The effect of geometrical and fluid parameters on the velocity field of model mix heads used in reaction injection molding has been examined through laser Doppler anemometer measurements and flow visualization. Flow visualization results reveal that an unsteady three dimensional flow structure exists for $Re_d > \sim 150$ and that the opposed jets are the only structure visible at $Re_d \sim 300$. Quantitative velocity measurements obtained with a laser Doppler anemometer reveal the time averaged structure of the flow. Two different chamber diameters were examined, $D^* = 10.75$ and $D^* = 5$. The flow was found to become unidirectional at smaller axial distances (Z^*) for $D^* = 5$, while significant flow down the chamber from above the impingement point was seen in the $D^* = 10.75$ cases. In both chamber diameters the H^* position seems to have little effect past the point of impingement. These results agree well with previous studies using different techniques. The flow was found to become unidirectional at smaller axial distances (Z^*) for a restricted nozzle opening. The short nozzle was not found to have a significant effect on the jet development in an opposed jet configuration and no annular jet velocity profile was found for the nozzle needle settings examined. A flow restriction placed above the impingement point was found to have a significant effect on the flow field eliminating the upper vortices seen with no restriction present. As well, with the restriction the flow was found to be more uniform and centrally located in the chamber. Unequal flow rate ratios were found to alter the flow field significantly by moving the impingement point toward the lower momentum jet and stabilizing the flow field to some extent.

6 Conclusions - Impinging Jets

The flow field present in an opposed jet mix head has been examined using flow visualization, laser Doppler anemometer velocity measurements and three dimensional numerical simulations for several geometrical and fluid variables. Geometrical parameters investigated include chamber shape (cylindrical or rectangular), nozzle diameters, head length, nozzle needle position for commercial nozzle blocks, and flow restriction position. Fluid parameters studied include unequal nozzle flow rates and unequal nozzle viscosities.

Three distinct flow regions have been determined based on dimensionless groups formed from the geometric and fluid parameters detailed above.

The first region is a steady non-oscillatory one consisting of several flow structures such as the free laminar jet, a curved shear layer, a stagnating impingement flow, a radial jet flow, recirculating flow and developing conduit flow. Initially, for all models (1-4) and for all flow conditions, the flow field of $Re_d < \sim 90$ was stationary and only temporarily disrupted by the passage of the transient. The two jets were seen to remain cylindrical with an insignificant amount of spreading until just before the point of impingement for $Re_d > 50$. At values of Re_d below this value the jets did not impinge but flowed toward the outlet.

The onset of the second region or oscillatory phase was found to be a function of the Re_d , the ratio of the chamber characteristic dimension (L or D), and the nozzle

diameter, which form a dimensionless length group L^* or D^* . Smaller values of L^* in the range of L^* studied delayed the onset of oscillations. At the onset of oscillations the impingement disc was seen to oscillate about the jet-to-jet axis. Incremental values of Re_d caused an increase in the dimensionless frequency St_d and the amplitude of disc oscillation until a limit value was reached. Again smaller L^* values showed a delay in the limit of finite oscillations. The oscillations are postulated to occur because of pressure wave feedback from the point of jet impingement to the nozzle mouth, forcing the self-sustaining oscillations.

The third region occurred past the limit of finite oscillations. This regime was characterized by a change in the overall flow structure because, for large values of L^* , the jets no longer directly impinged. An unsteady flow field was visualized and no regular oscillations were found in velocity measurements, although the rms of the measured velocities continued to increase with increasing Re_d .

Studies of the effect of geometrical parameters in the third post regular oscillations regime were obtained using commercial nozzle blocks. Re_d typical of commercial RIM operation revealed the jets to be the only structure visible at $Re_d \sim 300$. Chamber diameter to nozzle diameter, needle position and a flow restriction were found to have a significant effect on the flow field, while the head position was found to have little effect past the point of impingement. The short nozzle was not found to have a significant effect on the jet development in an opposed jet configuration and no annular jet velocity profile was found for the nozzle needle settings examined; however unequal nozzle flow rate ratios were found to alter the flow field significantly.

7.0 Recirculating Flow in a Cavity

7.1 Introduction

This chapter studies of a jet-driven, recirculating cavity which has many important engineering applications such as ventilation, heat removal in electronic equipment, combustion chambers, and the cooling of nuclear reactor cores. Jet-driven recirculating flows arise when a jet of fluid is injected along a wall boundary creating a turbulent wall jet which drives the recirculation. The turbulent wall jet can be characterized as a "boundary layer in which, by virtue of the initially supplied momentum, the velocity over some region in the shear layer exceeds that in the free stream" (Launder and Rodi, 1983). The remainder of the cavity is a large region of recirculation, with the core of the cavity virtually stagnant.

Numerical simulations of turbulent recirculating flows are regularly used for design and analysis of complex flow fields. Although these simulations reduce the number of experiments necessary, the numerical modelling foundation must be based on experimental results, thus the primary motivation for these studies was to provide an experimental database for jet driven recirculating flow. The application of Particle Streak Velocimetry (PSV) to this flow field has also extended the database.

7.1.1 Recirculating Flow

Johnson (1988) has reviewed some studies similar to the present case and found that mean velocity profiles are generally well predicted in the cavity but turbulent energy levels were not well simulated by conventional $k - \epsilon$ turbulence models.

Baron *et al.* (1981) have examined the case of three dimensional turbulent flow caused by a jet entering a cubic cavity (.05 m side) with asymmetric entry and exit. Measurements in the cavity were obtained using a two component LDA and comparisons were made with three dimensional numerical simulations. The velocity profiles were well simulated but the turbulent energy profiles were poorly predicted and in particular the code was unable to predict the increase in turbulent energy at the inlet.

Tanaka *et al.* (1983) have examined a cylindrical vessel with a variable height intake and discharge modelling a Liquid Metal Fast Breeder Reactor (LMFBR) hot plenum. The velocity profiles were obtained using a propeller velocimeter. A numerical simulation gave good predictions of the bulk flow with the exception of poor agreement for the case of a high discharge and a low intake. Turbulent kinetic energy profiles were not obtained in this study.

Boyle and Golay (1983a) have examined a scale model of the Fast Flux Test Facility (FFTF) reactor outlet plenum. The rectangular model (.1524 X .2286 X .0608 m) studied had a vertical inlet (.0286 m wide) near the bottom and a horizontal outlet (.0191 m wide) also at the bottom of the model. The cavity was considered two

dimensional, the measurements of velocity and kinetic energy were obtained using a two component LDA, and comparisons were made with simulations predicted by the $k - \sigma$ turbulence model of Stuhmiller (1974) although the more common $k - \epsilon$ model was also used with the TEACH-T code. Using a 16 X 24 computational grid, close agreement between the measured and computed mean velocity field was observed, with the exception of the upper portion of the tank, where it was believed three dimensional effects occurred because the jet impinged on the top of the tank. The velocity gradient at the wall was not predicted well with the code, a finding probably due to too coarse a computational grid in the near wall region. The turbulent kinetic energy computed compared poorly to experimental results in magnitude and in profiles.

In a continuation of their work (Boyle and Golay, 1983b), they examined transient flow cases and compared them to turbulence model predictions.

A similar study by Ushijima *et al.* (1987) on a rectangular plenum (.052 X .045 X .05 m) compared experimental results obtained using an LDA system with three turbulence models; the $k - \epsilon$ model, the Launder Reynolds stress model (LRSM) (Launder *et al.*, 1975), and the Simplified Reynolds stress model (SRSM), all assuming two dimensional flow. The numerical simulations gave accurate predictions of bulk flow, although poor agreement was obtained at the top of the plenum because of three dimensional effects. The normal stresses $\overline{u'u'}$ and $\overline{v'v'}$ were predicted poorly by all the models used.

Following the experimental studies of Karlsson *et al.* (1992), a recent

numerical study focusing on the development and prediction of the inlet wall jet in an open channel ($Re_b = 10000$, $b = 0.010$ m, $b/H = 0.007$, $L/H = 5.0$, $W/H = 1.04$, $W/b = 145$) was reported by Andersson *et al.* (1993) using the $k - \epsilon$ and RSM turbulence models. The $k - \epsilon$ turbulence model predicted the jet velocity peak to be too close to the wall boundary, a finding which distorted the mean flow characteristics. The Reynolds stress model (RSM) used throughout agreed well with LDA data at 70 and 150 slot widths downstream, although no overall flow predictions were given. Although wall functions were used, the apparent decrease in the logarithmic region as the wall jet developed and elimination of the logarithmic region at greater than 100 inlet widths (Launder *et al.* (1981)) led Andersson *et al.* (1993) to recommend using another wall treatment. The growth rate of the wall jet was well predicted with the RSM model but over-predicted with the $k - \epsilon$ turbulence model compared with the measured results of Karlsson *et al.* (1992).

Water flow in an offset channel (outlet diagonally opposite inlet) was examined by Walter and Chen (1990,1992) using primarily flow visualization and one case of particle streak velocimetry. The channel was .115 m wide, .111 m high and .0222 m deep with an .0111 m high inlet in the vertical wall flowing horizontally adjacent to the channel bottom ($Re_b = 25 - 4600$, $b = 0.011$ m, $b/H = 0.01$, $L/H = 1.04$, $W/H = 0.2$, $W/b = 2$). The Reynolds number was based on the inlet height and the volume average inlet velocity. Similar to the inlet, the outlet was located in the opposite vertical wall and flowed horizontally adjacent to the upper surface. Flow visualization photographs were used to determine recirculation areas and stagnation points. Three

dimensional effects were evident in the asymmetry of the flow in the z direction and the cavity depth to slot height (W/b) was found to be too small for two dimensional flow.

Studies concerning room ventilation have similar aspects to the present study and are included for completeness. Nielsen *et al.* (1978) have examined flow in an offset channel ($L/H = 3.0$, $b/H = .056$, $W/H = 1.0$, $t/H = 0.16$, $w/W = 0.5$ and 1.0 , $b = .005$ m, $Re_b = 5000$ to 10000) with an outlet height (t) larger than the inlet (b) and variable width inlet (w) using LDA and $k - \epsilon$ turbulence model (TEACH code) predictions. Inlet flow along the top of the cavity drove the recirculation. In air conditioning design, maximum reverse flow velocities (flow along lower surface) experienced by occupants are important and, for a constant inlet velocity, maximum reverse flow velocities were found when b was increased or L was decreased. Close agreement between the measured and computed mean velocity field was observed, with the exception of the wall jet region and the reverse flow region, where three dimensional effects were seen. In a subsequent study, Gosman *et al.* (1980) examined three dimensional effects created by a narrow inlet slot ($w/W = 0.1$) in a similar cavity ($L/H = 3.0$, $W/H = 1.0$, $b/H = 0.1$, $t/H = 0.16$, $b = .00893$ m, $Re_b = 9000$). The mean velocity field was well predicted although neither study considered the near wall parameters. Choi *et al.* (1988) considered the enclosure inlet and outlet location in a simulation study using the $k - \epsilon$ turbulence model (TEACH code) and two dimensional flow field assumptions. The case with an inlet wall jet had a diagonally opposed outlet in a geometry similar to that of Nielsen *et al.* (1978) ($L/H = 3$, $b/H = .05$, $t/b =$

3, $Re_b = 3600$). A high pressure gradient was found where the inlet wall jet encountered the confining wall ($x = L$). The reverse flow was poorly predicted by the simulations.

7.1.2 Turbulent Wall Jets

The turbulent wall jet in unconfined spaces has been examined extensively. Reviews are presented in Launder and Rodi (1981, 1983). The wall jet is shown in Figure 7.1 from Launder and Rodi (1983) where

b	slot height (m)
U_E	free stream velocity (m/s)
U_j	average jet velocity (m/s)
U_m	maximum velocity (m/s)
$y_{1/2}$	distance from wall to location of $U_m/2$ (m).

Initial work by Glauert (1956) divided the jet into two components: the inner boundary layer region between the wall and the point of maximum velocity and the outer layer region containing the diffusing jet and the entraining fluid. Matching the inner and outer regions lead to a similarity solution where

$$u \propto x^{-1/2} \quad 7.1$$

This proportionality will apply only in the self similar region away from the entrance region. Data on the rate of growth of the outer layer for a two dimensional turbulent wall jet in stagnant surroundings has been compiled by Launder and Rodi (1981) from many studies to produce

$$\frac{dy_{1/2}}{dx} = 0.073 \pm 0.002 \quad 7.2$$

and was found to be 30% below the growth rate of a plane free jet (Rodi 1975). Cited as the cause is the damping of the turbulent velocity fluctuations normal to the wall resulting from turbulent pressure reflections from the wall. When the turbulent wall jet is in an external flow, as in the present case, the outer region has a reduced effect on the inner region and the inner region is thicker than the stagnant flow case. For a turbulent wall jet in a positive pressure gradient, Irwin (1973) has found the growth rate $dy_{1/2}/dx = 0.0436$ for $(U_m - U_E)/U_E = 1.65$. For three dimensional wall jets, the jet grows in both the x and z direction. Launder and Rodi (1981) have reviewed previous three dimensional studies and found

$$\frac{dy_{1/2}}{dx} = 0.048 \quad \frac{dz_{1/2}}{dx} = 0.26 \quad 7.3$$

although studies by Chandrasekhara Swamy and Bandyopadhyay (1975) show higher growth in the x direction $dy_{1/2}/dx \sim 0.068$ and slower growth in the z direction $dz_{1/2}/dx = 0.166$.

Within the wall jet significant differences are found in the measured turbulence values. Launder and Rodi (1983) give maximum measured values:

$$\frac{\overline{u^2}}{U_m^2} = 0.04 \quad 7.4$$

$$\frac{\overline{v^2}}{U_m^2} = 0.015 - 0.025 \quad 7.5$$

$$\frac{k}{U_m^2} = 0.04-0.05 \quad 7.6$$

which indicates $\overline{u'^2} \approx \overline{v'^2} + \overline{w'^2}$ as $k = 0.5(\overline{u'^2} + \overline{v'^2} + \overline{w'^2})$. Values for $\overline{w'^2}$ are not reported.

Numerical simulations of plane wall jets in stagnant surroundings with the standard $k - \epsilon$ turbulence model show a 30% higher rate of growth than experimental studies (Andersson *et al.*, 1993 and Launder and Rodi, (1983)). This discrepancy is due to the discussed damping of the normal velocity fluctuations in the inner region and the outer free shear region, which are not accounted for in the model. In the wall jet the position of zero shear stress and the point of maximum velocity do not coincide and the point of zero shear stress is closer to the wall. A standard $k - \epsilon$ model has coincident maximum velocity and zero shear stress and, for this reason, predicts the velocity maximum at the point of zero shear stress too close to the wall, a situation which leads to a distorted mean velocity profile. Reynolds stress transport models (RSTM) and algebraic stress models (ASM) do not have this limitation and are recommended by Launder and Rodi (1983) for wall jet prediction with the inclusion of a wall damping model.

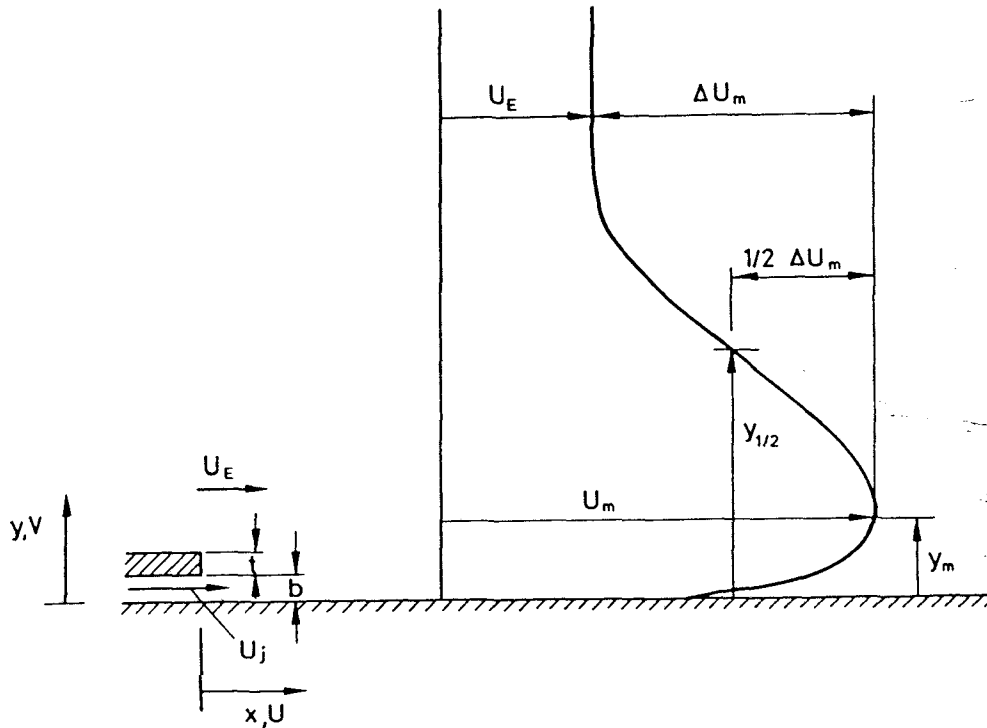


Figure 7.1 Plane Turbulent Wall Jet (Launder and Rodi, 1983)

7.1.3 Present Study

In the present study, recirculating flow in a cavity has been examined for two cases of Re_b , where Re is based on the slot height b and the average inlet jet velocity U_j .

$$Re_b = \frac{\rho U_j b}{\mu} \quad 7.7$$

The cavity had inside dimensions of $L = .30$ m, $H = .15$ m, and $W = .05$ m with an inlet slot $b = .002$ m from $(x,y,z) = (0,0,-.025)$ to $(0,.002,.025)$ m and a corresponding

outlet slot from $(x,y,z) = (0,.148,-0.025)$ to $(0,.150,.025)$ m (Figure 7.2). The cavity was designed so that large portions of the flow field would be two dimensional ($b/H = .0133$, $L/b = 150$, $L/H = 2$, $W/b = 25$). The flow field within the cavity was examined using flow visualization, laser Doppler anemometry (LDA), particle streak velocimetry (PSV) and two and three dimensional numerical simulations. Previous work (Johnson 1988) concluded that the cavity appeared to be two dimensional in the main body, but no attempt was made to quantify this further. Measurements in the third dimension have been made in an attempt to resolve this issue and three dimensional simulations have been performed. Two cases of isothermal water flow were examined $Re_b = 1675$ and $Re_b = 1117$ where Re is based on the slot height b . The extension of the work was primarily motivated to determine the suitability of particle streak velocimetry to recirculating flows and flow fields with high velocity gradients.

7.1.4 Optical Image Velocimetry

The current state of the art for optical measuring techniques has been reviewed in chapter two.

For all methods, a flow field containing seeding particles is illuminated with a strong light source. Images are obtained sequentially of the particle movements from which displacement information is obtained. As the time interval between images is known, an instantaneous velocity may be obtained.

$$u = \lim_{t_2 \rightarrow t_1} \frac{l_2 - l_1}{t_2 - t_1} \quad 7.8$$

where

l_2, l_1	particle displacements
t_2, t_1	time

For particle streak velocimetry (PSV) sequential images are obtained by strobing the light source with a known frequency, chopping the light source with a rotating mechanical aperture, chopping the light source with an acoustic optic modulator (similar to the Bragg cell used in LDA work), scanning the area with a rotating mirror or using a pulsed laser as the light source. The limitations of the above "chopping" techniques are that a finite amount of light is available and, in order to capture the movement of one particle, the particle displacement has to be small; consequently most of the light intensity is prevented from passing to the scanning area. Therefore these techniques are limited to comparatively low speed flows.

If the particle concentration is low enough ($N_f \ll 1$), individual particles can be tracked and the displacement of individual particles can be obtained.

The use of PSV in water flow in an offset channel was examined by Walter and Chen (1990,1992). A 10 mW HeNe Laser was used as the light source with a rotating disk with a coded pattern of "dot", "dash", "dot", "dot" to provide the "chopping". Velocity magnitude and direction were determined manually, using a mouse on the CCD camera captured images. One velocity vector plot is presented, for a Re_b of 105. The dynamic range of velocity magnitude (ratio of maximum to minimum) was about 50, leading to images captured at various exposure times (0.5 sec

to 14 sec) to cover the velocity range. A composite of 20 images was collected. A total error estimate of 5% of the average particle streak length was found, which included errors due to inability to determine streak end points and the rotational inaccuracy of the rotating disc. Error in the exposure interval resulting from the time required to chop the light was neglected. Flow visualization photographs were used to determine recirculation areas and stagnation points.

7.2 Experimental Work

7.2.1 Apparatus

A flow cavity was constructed from clear acrylic, having inside dimensions of $L = .30$ m, $H = .15$ m, and $W = .05$ m with an inlet slot $b = .002$ m from $(x,y,z) = (0,0,-.025)$ to $(0,.002,.025)$ m and a corresponding outlet slot from $(x,y,z) = (0,.148,-0.025)$ to $(0,.150,.025)$ m (Figure 7.2). The cavity was designed such that large portions of the flow field would be two dimensional ($b/H = .0133$, $L/b = 150$, $L/H = 2$, $W/b = 25$). A .20 m development length was provided to convert the flow inlet of .0127 m diameter to the slot dimensions.

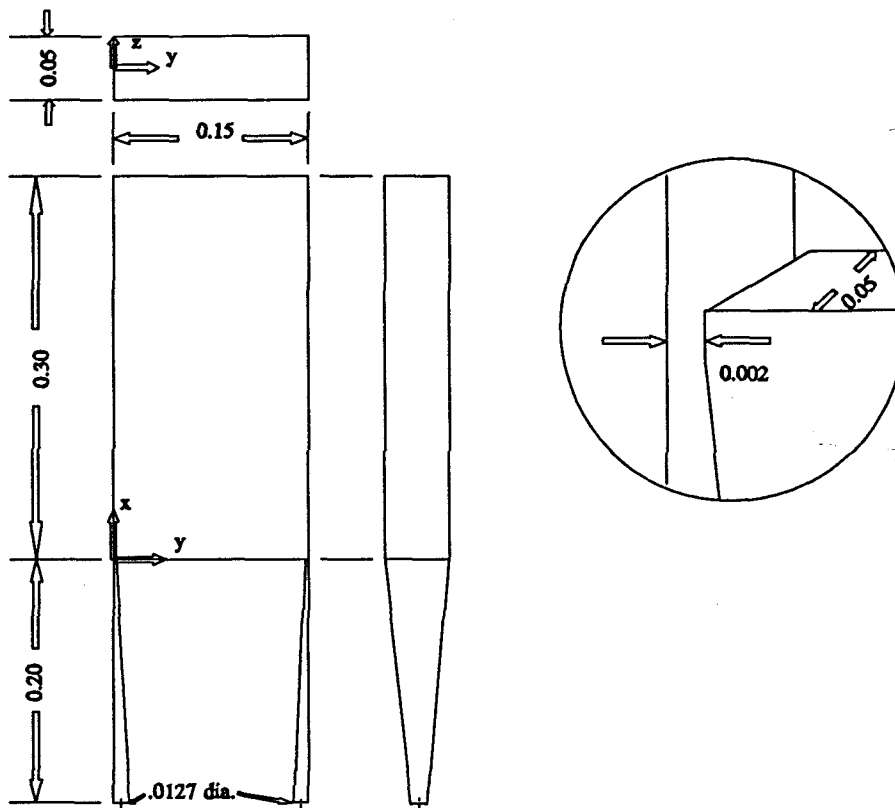


Figure 7.2 Recirculating Flow Cavity, Inset: Inlet Area Close up, All dimensions in metres

The flow cavity was connected in a water flow loop, which consisted of a head tank, pump (Little Giant 4E-34NT), bypass valve and flowmeter, the cavity and a return line to the head tank (Figure 7.3). The pump was externally water cooled and the head tank was constantly mechanically stirred. Temperature was monitored at the head tank and volumetric flow readings were obtained at the return line.

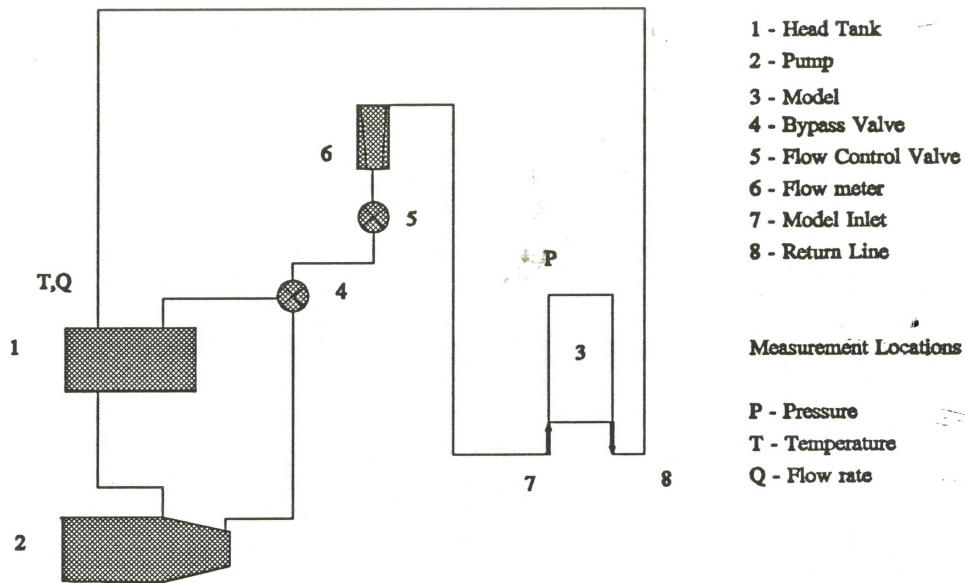


Figure 7.3 Schematic of Flow Loop - Recirculating Flow

7.2.2 Flow Visualization

Two techniques were used to visualize the flow field: a laser light sheet and particles, and a laser light sheet and fluorescent dye. The laser light sheet was used as it creates a two dimensional plane of light which may be orientated in any direction. A 6W argon ion laser (Coherent Innova I-90), at a power setting of 200 mW, was directed onto a cylindrical lens which formed a light sheet ~ 0.002 m thick and ~ 0.05 m wide. For photographs of the entire cavity a light sheet was formed using a six sided rotating mirror. Polystyrene particles (~ 60 μm mean dia.) seeded the flow for the first

technique and Fluorescein dye (Fisher Scientific) injected before the flow meter inlet was used in the second technique. A .010 m square grid was placed behind the cavity as an approximate measuring tool and as an aid in determining the extent of the incoming fluid and recirculating fluid interaction. A 35 mm camera (Nikon F3) or a CCD camera (Panasonic MF552) was used to record the images.

7.2.3 Laser Doppler Anemometry

Measurements were obtained using a Dantec 55X single component LDA system in the forward scatter mode. The system described previously in chapter 3 consisted of a 35 mW HeNe laser with a 55X12 beam expander, Bragg Cell, 55X82 beam translator and a .080 m focal length lens giving a measuring volume of length 124 μm and diameter 26 μm .

The flow cavity was mounted on the computer controlled 3-axis traversing stage described in chapter 3. At each measuring point 10000 instantaneous velocity measurements were obtained for both u and v at a constant sampling rate to minimize bias. Incoming data to the counter processor was typically of the order of 4-5 kHz with validation of 75%. No additional seeding was used for the tap water.

For measurements made at the mid plane of the z axis ($z = 0$), the location of the measuring volume was calculated using Snells' law (Section 3.4.3), and no correction was required for subsequent in-plane measurements. Since both beams had the same path length, a correction was not required. For measurements made in the z direction in the model a correction was required. Software was written again using

Snells' law to determine the coordinates for the desired locations.

Two cases have been examined for different inlet flow velocities; $Re_b = 1675$, $U_j = .72$ m/s, and $Re_b = 1117$, $U_j = .48$ m/s. For each case, measurement of the overall flow field occurred at the z dimension centre line ($z = 0$). As well, detailed measurements were obtained for all values of y at $x = .06, .12, .18, .24$ m of the U velocity and for all x values at $y = .075$ m (vertical centre line) of the V velocity. U velocities for all z values were obtained at six locations (x,y) as an aid in determining the applicability of the two-dimensional assumption. In the region of the wall jet detailed measurements were obtained at many x values for y values increasing with the distance from the inlet. In this way the entire wall jet profile was obtained.

7.2.4 Particle Streak Velocimetry

Particle streak velocimetry has two distinct components, obtaining the images from the experiment and processing the video taped images.

Method

7.2.4.1 Obtaining Images

Using this technique velocity measurements were obtained of individual particles within the flow field.

Laser

A 6W Argon Ion laser (Coherent Innova I-90) operating at 200 mW all lines was used as the light source, as discussed in the flow visualization section. The light

was directed onto the mid-plane of the recirculating cavity which was mounted on a three axis traversing stage for positioning.

Light Pulses

Pulsing of the laser light was accomplished through the use of a rotating disk of .127 m in diameter. The axis of the disk which was aligned with the laser beam, was placed between the laser and the cylindrical lens. At a radius of .057 m a pattern was drilled to allow the incident laser beam to pass through the disk. The pattern was: a drilled hole (.00238 m diameter), a rotation of 19.2° , another drilled hole (.00238 m diameter), a rotation of 19.2° , a continuous arc .00238 m wide for 19.2° , a rotation of 19.2° and a final drilled hole (.00238 m diameter) for a total angle of 76.8° on the disk. Using this pattern the light was "chopped" at a dot, dot, dash, dot pattern of known spacing for purposes of direction evaluation. The disk was directly driven by a motor at a constant speed, which was selected depending on the speed of the particles at the location under study. The variable speed DC motor driving the disk was monitored using the attached generator which gave a voltage proportional to the speed and using a strobe light for calibration and verification purposes (Figure 7.4).

Seeding Particles

In these cases polystyrene particles of nominal diameter $60\ \mu\text{m}$ (filtered between 46 and $74\ \mu\text{m}$ ($\rho = 1.1\ \text{g/cm}^3$)) were added to the water and the storage vessel was continuously stirred. Smaller particles were originally used but the streak images were not defined well enough to detect on the video tape. A discussion of seeding

particle selection is presented in chapter 3 section 3.1.2. Particles of similar size have been used by Agui and Jimenez (1987), Utami and Ueno (1987) and Walter and Chen (1992) all of whom have concluded the particles tracked the flow sufficiently.

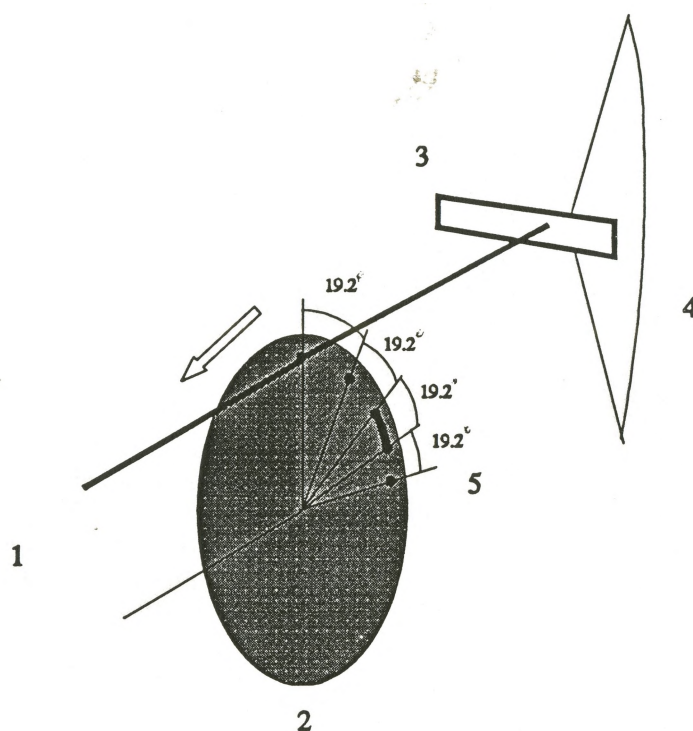


Figure 7.4 Schematic of PSV Arrangement
 1 - Argon Ion Laser Beam, 2 - Rotating Disk, 3 - Cylindrical Lens, 4 - Light Sheet Generated, 5 - Strobe Sequence

7.2.4.2 Imaging

A CCD video camera (Panasonic MF-552) with 768 X 512 pixel elements was focused onto a region of the cavity of approximately 40 mm x 40 mm. A .010 m square grid was placed behind the cavity to allow determination of the location of the video image within the cavity. The cavity was then traversed in .010 m increments

with video recording taken at each grid point. Output from the camera was recorded on a SVHS video tape recorder (Panasonic) for subsequent analysis.

Disk rotational speeds of 1800 rpm, 900 rpm and 600 rpm were used depending on the area of the cavity under investigation giving an entire streak (pattern of dot, dot, dash, dot) time period of .0071 sec, .0142 sec, and .0213 sec respectively. In regions where there was a wide range of velocities, such as at the inlet jet area where the incoming jet was at a high velocity and the entrained fluid at a much lower velocity, three distinct sets of video recordings were obtained at the three disk rotational velocities. In this way the full range of velocities could be obtained. In the centre core of the cavity, the lowest disk rotational speed was used, which was still not a long enough time period to allow significant movement of most of the particles. There was a limitation in the maximum amount of time allowed for streaks since the video frame transfer rate of the camera was 30 Hz and a complete streak must occur on the frame. This arrangement gave a minimum disk rotational speed of 384 rpm which, when used with the camera, very rarely gave usable complete streaks as the disk rotation was unsynchronized with the camera. Thus the system has a bias toward higher velocity particles at the lowest motor rotational speed.

7.2.4.3 Processing Images

The video tape record was then analyzed on a frame by frame basis. The procedure was to acquire 18 images using a frame grabber board (Data Translation DT-2853, 480 X 512 elements, 256 grey levels) at any given grid segment in the

computer memory and then to view these images individually. Software was written to perform the function of image capture, image display, cursor movement, pixel determination, grid location and streak velocity components. Initially the coordinates of the background grid were found, in order to determine the number of pixels corresponding to a length of .010 m in the x and y directions. Typically 220 pixels corresponded to a length of .010 m giving a resolution of 45 μm per pixel. Once the geometrical parameters were determined, the frames were then examined for complete particle streaks. Incomplete particle streaks were rejected; then beginning at the tail (two dots) and ending at the head (dash and single dot), complete streaks were measured manually in pixel units, using a movable cursor. This procedure was continued until all complete particle streaks had been measured on that frame before proceeding onto the next stored frame. There was not a high enough density of complete streaks to confuse the beginning and end of complete streaks.

Pixel distances found were converted to length measurements and then divided by the appropriate time period to produce u and v velocities. The velocity position was located at the geometrical mid-point of the particle streak.

Sources of Errors

The DC motor frequency when measured varied somewhat from a set rotational speed, the worst case being at a rotational speed of 600 rpm, where the motor was seen to oscillate between 597 and 603 rpm leading to error of 0.5% in the velocity. As well, the positioning of the cursor at the exact head or tail of the streak was subject to some error, since the cursor used was two pixels wide and two pixels high.

Through observation it was evident when the cursor was not covering the head or tail in some way, giving an error of ± 2 pixels. As the contribution of this error to the velocity measurement was a function of the overall length of the streak image, shorter streaks would be subject to a higher error than longer streaks. Examination of the data shows an average pixel length of 49 pixels giving an error of 4.1 %. In this flow field there was no evidence of curvature of the streaklines, which can lead to erroneous data interpretation.

7.3 Numerical Simulation

7.3.1 Solution Procedure

Subject to appropriate boundary conditions the commercial computer code FLUENT is used to solve the governing differential equations. FLUENT uses a control volume method, in which the region of interest is divided into a finite number of control volumes. In each control volume the partial differential equations are discretized to form sets of non-linear, inter-related algebraic equations which are solved iteratively. FLUENT uses either a standard $k - \epsilon$ turbulence model discussed in chapter 2, section 2.1 with model constants given in Table 2.1 or an algebraic stress model discussed in chapter 2. All dependant variables are located at the cell centre, except velocities, which are located at the cell boundaries in a "staggered" grid. A power law differencing scheme is used to interpolate between grid points and calculate derivatives of flow variables. Time is integrated in a fully implicit manner. Wall

functions are used at the boundaries close to the wall. The discretized equations are solved with a semi-implicit iterative scheme to converge to a solution.

A non-uniform grid was selected such, that a concentration of grids was located close to the walls of the cavity (Figure 7.5). Table 7.1 gives the details of the simulations. To model the inlet and outlet conditions, the slot height was divided into equally spaced divisions (seven grids for 44x40 grid cases, thirteen grids for the dense 86x78 grid cases) to which a fully developed parabolic profile with the appropriate average velocity was applied.

$$u = u_{\max} \left[1 - \left(\frac{y}{b}\right)^2\right] = 1.5u_j \left[1 - \left(\frac{y}{b}\right)^2\right] \quad 7.9$$

where b slot height (m)

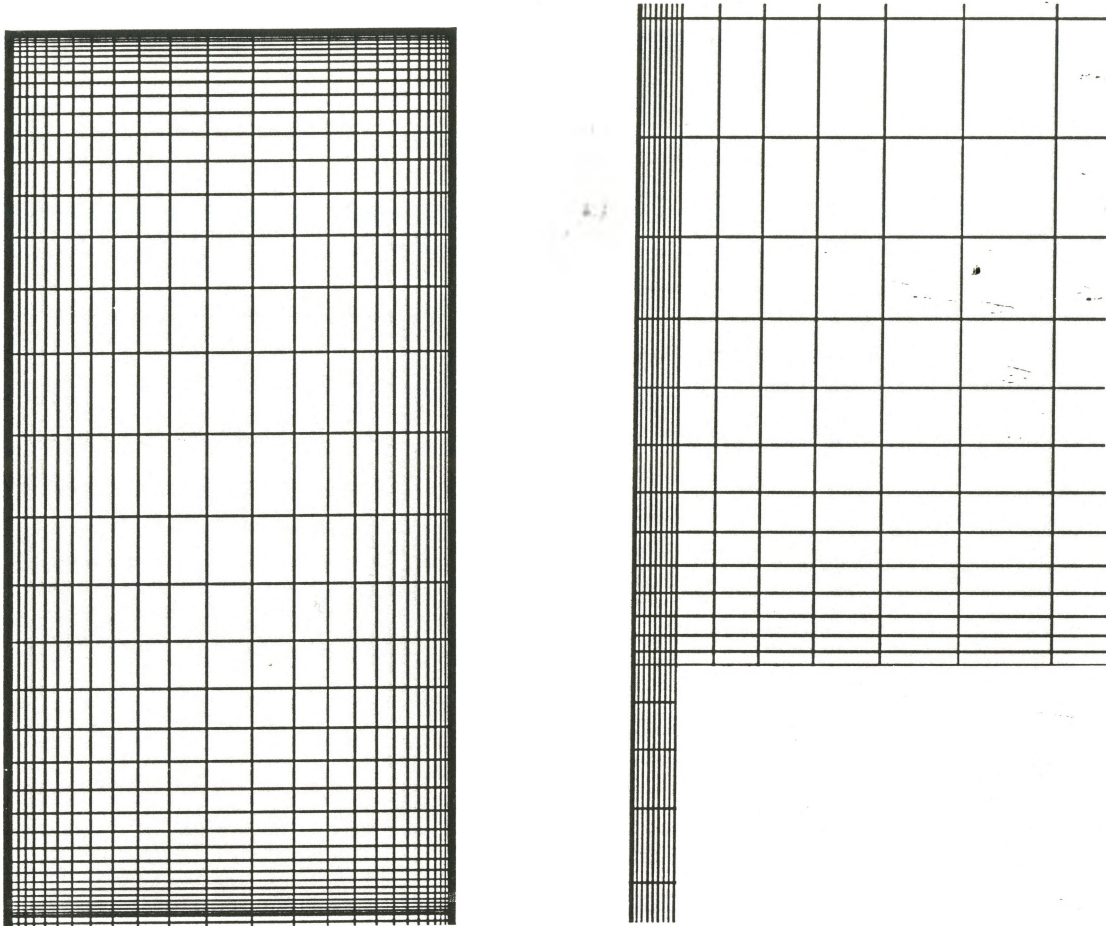


Figure 7.5 Computational Grid - Recirculating Cavity 44x40 a) entire XY plane (left side) b) inlet close up

An inlet turbulent energy k of $.007776 \text{ m}^2/\text{s}^2$ (Turbulent Intensity 10 %), $\epsilon = .00161 \text{ m}^2/\text{s}^3$ was used at the inlet as an experimental measurement was not obtainable. A uniform width (.002 m wide) development length of .02 m was added to the inlet and outlet grid section, in order to assure fully developed flow at the inlet and to allow for a fully developed flow condition at the outlet. Other boundary conditions

were that there would be no slip at all other wall surfaces. Water properties used in the simulation were $\rho = 997 \text{ kg/m}^3$, $\mu = .857 \times 10^{-3} \text{ kg/ms}$ @ 26°C (White, 1984).

For the three dimensional simulations the inlet condition was modified so that the inlet would represent a fully developed flow in a rectangular duct using the approach described by Shah and London (1978).

Table 7.1 Numerical Simulations

Model	Re_b	Grid	Turbulence Model
x,y .30,.15	1675	2D 44x40	k - ϵ
"	1117	2D 44x40	"
"	1675	2D 86x78	"
"	1117	2D 86x78	"
"	1675	2D 86x78	ASM
"	1117	2D 86x78	"
x,y,z .30,.15,.05	1675	3D 30x40x15	k - ϵ
"	1117	3D 30x40x15	"

7.4 Results and Discussion

7.4.1 Flow Visualization

Examination of photographs and video tape reveal the structure of the flow present in the cavity for $Re_b = 1675$ and $Re_b = 1117$.

Mid-Plane Two Dimensional Profiles XY Plane

For the case $Re_b = 1675$ fluid is seen to enter the cavity from the slot at $(x,y) = (0,0)$

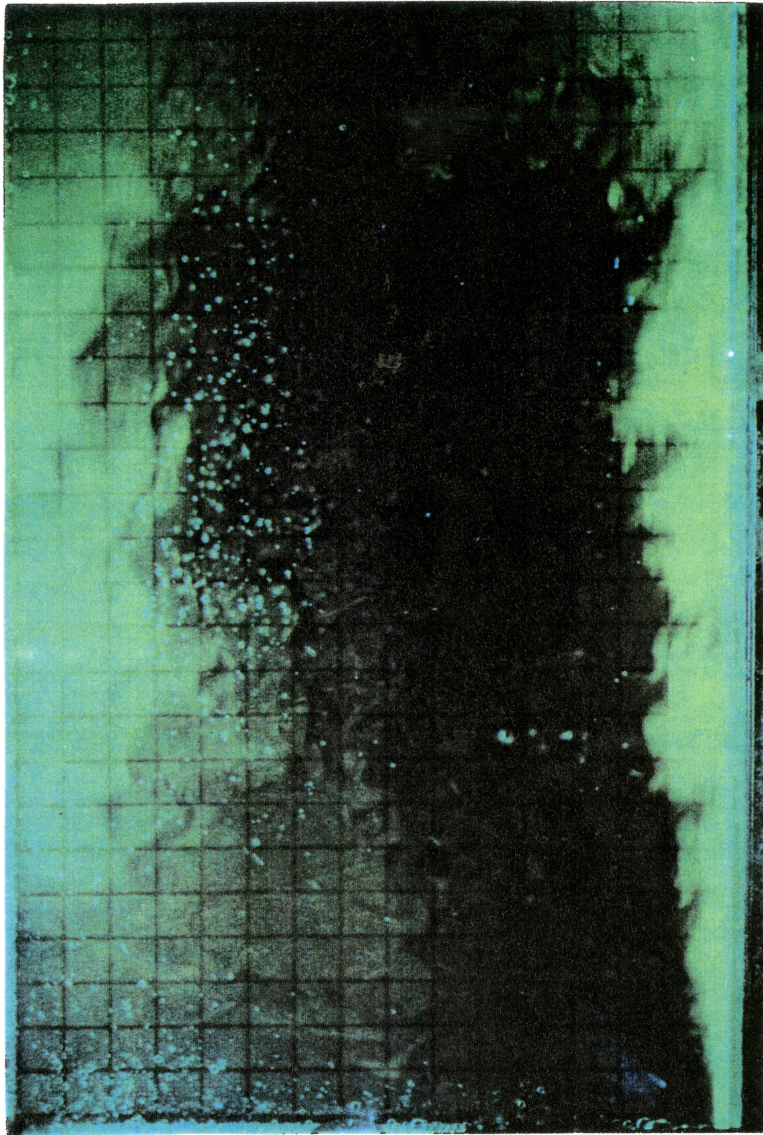


Figure 7.6 Flow Visualization - Entire Cavity $Re_b = 1675$

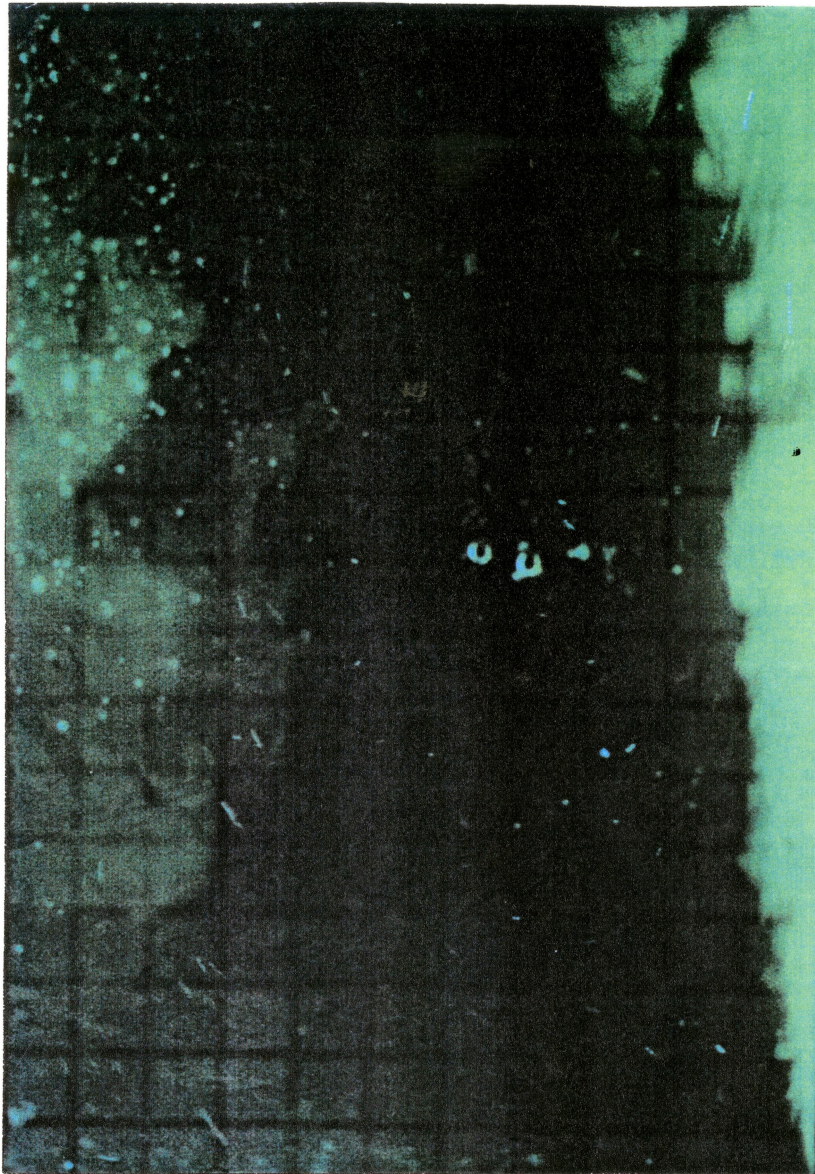


Figure 7.7 Flow Visualization - Inlet Area $Re_b = 1675$

XZ Plane

A slice taken at the slot inlet $(x,y) = (0,0)$ reveals significant turbulent bursts in the $+x$ flow direction but no evidence of three dimensional effects (Figure 7.8). A slice taken mid plane ($y = .075$ m) at $x = .20 - .30$ m reveals significant eddies in the z direction as the fluid passes along the $x = .30$ m wall (Figure 7.9). Similar eddies

are seen mid plane at $y = .075$, where the fluid passes along the $x = 0$ wall. This qualitative analysis reveals that two dimensional flow at the z centre line exists for a majority of the flow cavity, the exception being the corner areas away from the inlet and outlet.



Figure 7.8 Flow Visualization - Slot Inlet XZ Plane $Re_b = 1675$



Figure 7.9 Flow Visualization - XZ Plane at $(\sim .30, .075)$ $Re_b = 1675$

7.4.2 Wall Jet

Measurements of U for many x values have been obtained in the region of the wall jet. U/U_j versus y/b for several values of x/b are shown in Figure 7.10. The plot clearly shows the velocity decay with increasing x/b and, at $x/b = 100$, the profile is nearly flat. The free stream velocity U_E increases with increasing x/b for the region 0

$< x/b < 20$, suggesting a nonuniform effect on the growth of the jet in comparison to previous studies (Irwin, 1973) which have purposely controlled U_E .

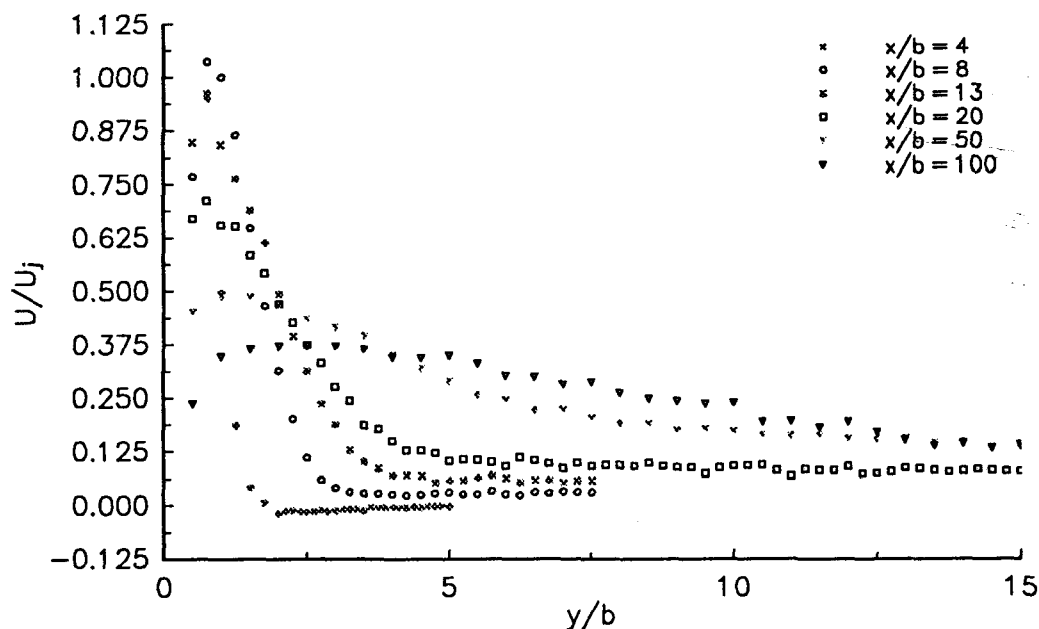


Figure 7.10 Wall Jet - U/U_j versus y/b $Re_b = 1675$

As discussed in the introduction a wall jet in stagnant surroundings has a well defined growth rate $dy_{1/2}/dx = 0.073 \pm .002$. Experimental values of $y_{1/2}/b$ versus x/b are plotted in Figure 7.11 for $Re_b = 1675$ with the corresponding simulations. The growth rate of the wall jet was found to be 0.112 which is 54 % higher than the reported growth rate of a wall jet in stagnant surroundings. The difference in the growth rate can be attributed to several factors. Previous wall jet studies in stagnant surroundings are significantly different, as they were performed with no boundary

restrictions to jet development and no flow external to the jet. The $x = .30$ m wall obviously limits the development of the wall jet and the effects are seen for $x/b > 100$. The recirculating flow caused by the confining boundaries may aid the growth of the wall jet. In the cavity, flow is nearly parallel to the $x = 0$ wall and must turn to follow the $y = 0$ wall boundary. In the region where the turning recirculating flow meets the incoming wall jet, significant interaction will occur in the jet outer free shear layer. As well, the influence of the developing boundary layer along the $z = \pm .025$ m surfaces may enhance the growth rate seen at the $z = 0$ measurement location. All boundary interactions will modify the wall jet behaviour as compared to a wall jet in stagnant surroundings. The decay of the maximum velocity U_m versus x/b is shown in Figure 7.12. Excellent agreement with the numerical simulations is found in the region of $20 < x/b < 150$. In the initial development region $x/b < 20$ there is some scatter in the experimental data since the velocity maximum in this region is very near the wall and the closest experimental measurement was 1 mm from the wall, factors leading to errors in the maximum velocity determination and the $y_{1/2}$ determination.

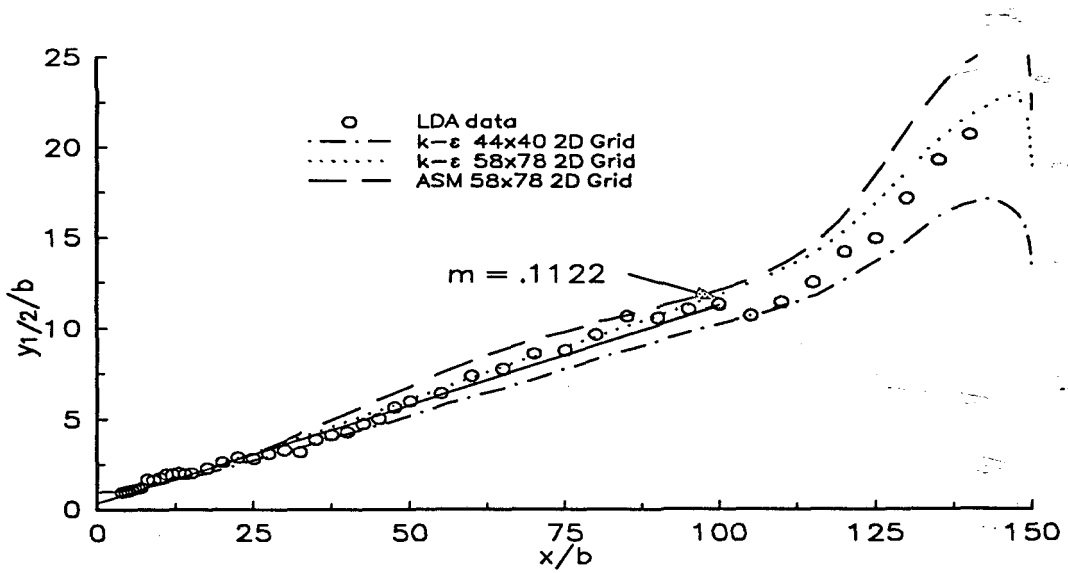


Figure 7.11 Wall Jet $Re_b = 1675 - y_{1/2}/b$ versus x/b

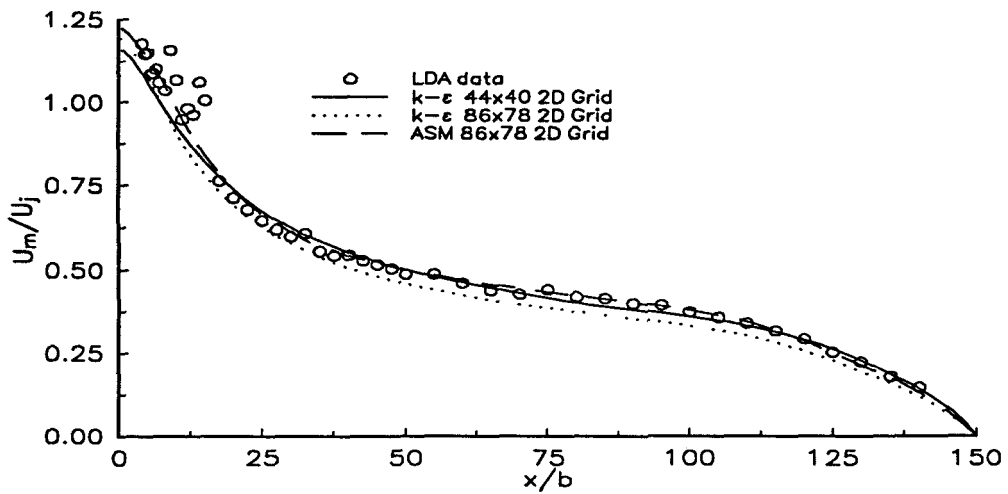


Figure 7.12 Wall Jet $Re_b = 1675 - U_m/U_j$ versus x/b

7.4.3 Entire Cavity

For each case, measurement of the overall flow field occurred at the cavity mid plane ($z = 0$). As well, detailed LDA measurements were obtained for each case at $x = .06, .12, .18, .24$ m of U velocity and at $y = .075$ m of V velocity. LDA measurements of U velocities were obtained at six locations (x,y) in the z direction as an aid in determining the applicability of the two-dimensional assumption. The experimental results were compared with the predictions of FLUENT using a standard $k - \epsilon$ turbulence model and an algebraic stress model (ASM) model. Particle streak velocities for $x = .06, .12, .18, .24$ m were obtained from the overall flow field data.

Mean Velocity

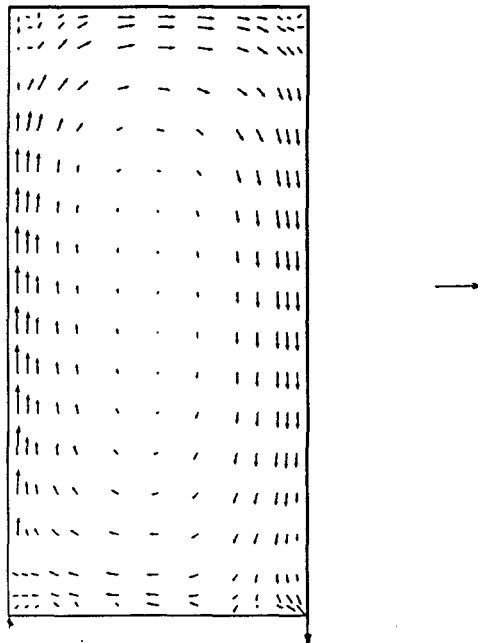


Figure 7.13 Velocity Vectors LDA Data $Re_b = 1675$ - Mean Velocity
Dimensionless Velocity Vector $U/U_j = 0.5$

Figure 7.13 shows the mean velocity LDA experimental results for the case of $Re_s = 1675$ for the overall flow field. Figure 7.14 shows the contours of U and V velocity from the LDA experimental results. Fluid entering the cavity from the slot, creates a wall jet and entrains fluid in the x direction, reducing velocity and spreading in the y direction. At $x \sim .27$ m the bulk of the fluid turns and flows along the wall ($x = .30$ m) before turning once again and flowing along the $y = .15$ m wall with lower velocity but increased width. Upon approaching the exit some fluid is drawn to the exit and the remainder turns along the $x = 0$ wall and is entrained by the incoming jet. In comparison to the flow around the walls the centre recirculating core of the cavity is stagnant. Away from the $x = 0$ inlet and outlet plane small recirculation zones exist; the area at $(.30,0)$ opposite the inlet being $\sim .020$ m in diameter, and the area at $(.30,.15)$ opposite the exit being somewhat smaller $\sim .010$ m in diameter.

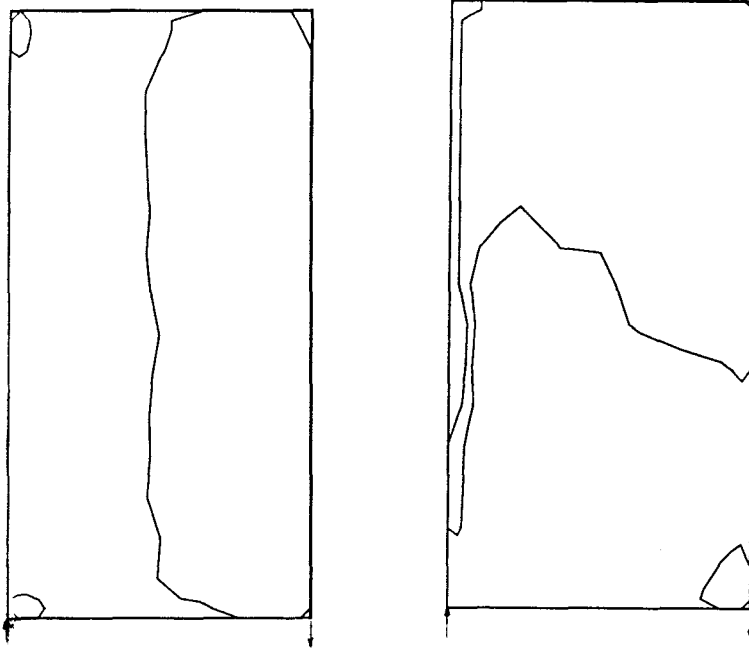


Figure 7.14 Contours of Velocity LDA Data $Re_b = 1675$ a) left side 0 Contour U velocity, b) 0 Contour V velocity

Figure 7.15 shows the results of particle streak velocity analysis. The individual randomly located velocities have been transformed to a regular grid by averaging and centrally locating all velocities within a .005 m square area. Of these 1800 areas, most contained less than 20 vectors and some, such as the central core, contained no vectors. For this reason averaging was limited and the figure represents a quasi-instantaneous picture as vectors from different grid locations were obtained at differing time periods and too few vectors were obtained at each location for a meaningful average. The manual digitization method led to some spurious velocity vectors, which were eliminated before averaging. Spurious velocity vectors were visually identified and removed only in regions where the flow had a uniform direction and the vector opposed this flow direction. As a result approximately 0.1 % of the vectors were removed. A discussion of the removal of spurious vectors from

PIV data based on local velocity statistics is discussed in Westerweel (1994). The flow field measured agrees well with the LDA experimental measurements. Contours of 0 velocity are not shown because of the scarcity of data in the central core, a situation which created meaningless contours.

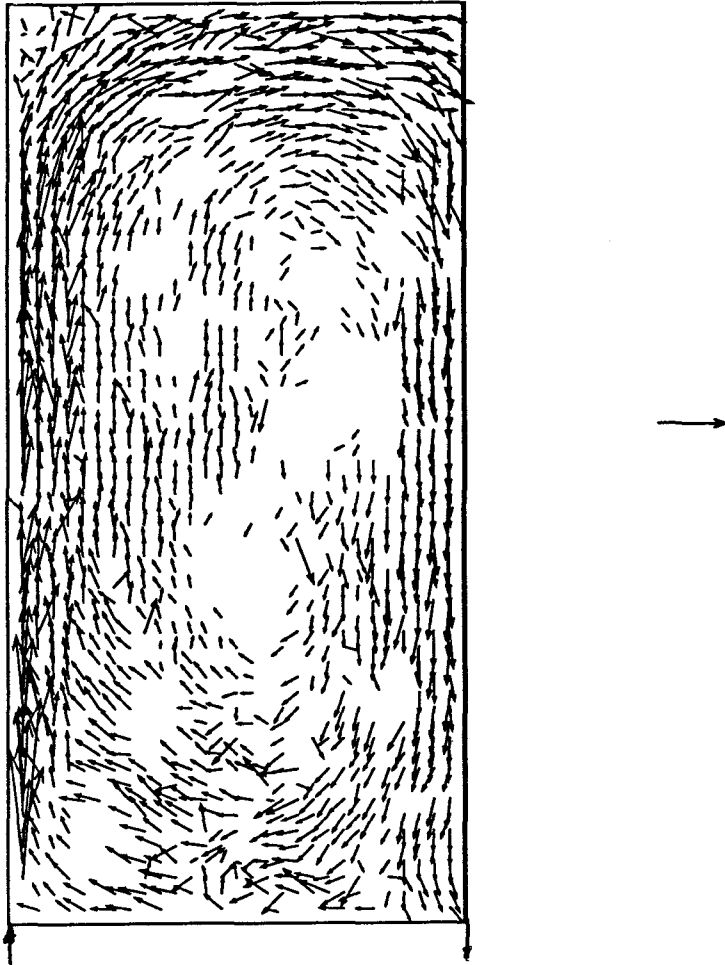


Figure 7.15 Velocity Vectors PSV Data $Re_b = 1675$ - Mean Velocity
Dimensionless Velocity Vector $U/U_j = 0.5$

The results of four simulations of the flow cavity are presented in Figures 7.16,7.17,7.20,7.21. Figure 7.16 represents a two-dimensional FLUENT $k - \epsilon$ turbulence model simulation using a 44×40 grid. Figure 7.17 is a two-dimensional

FLUENT $k - \epsilon$ turbulence model simulation using a 86×78 grid. Contours of U and V for both cases are shown in Figure 7.18 and Figure 7.19. Figure 7.20 is a three-dimensional FLUENT $k - \epsilon$ turbulence model simulation using a $30 \times 40 \times 15$ grid.

Figure 7.21 is a two-dimensional FLUENT ASM turbulence model simulation using a 86×78 grid. Contours of U and V for the ASM case is shown in Figure 7.22. The dense grid two-dimensional simulation was done to ensure that the solution was independent of the grid dimensions. The only significant difference between the $k - \epsilon$ 2D simulations is the predicted size of both recirculation zones in the corners of the $x = .30$ m wall. The dense grid simulation predicts larger recirculation zones, a finding borne out by the experimental data. The experimental data and the two-dimensional numerical simulations differ significantly from the three-dimensional simulation in that in the former two the flow toward the exit along the $y = .15$ m wall flows parallel to the wall while in the latter flow toward the exit flows on an angle toward the entrance slot. As a result the main recirculation cell in the cavity is reduced in size and skewed in shape.

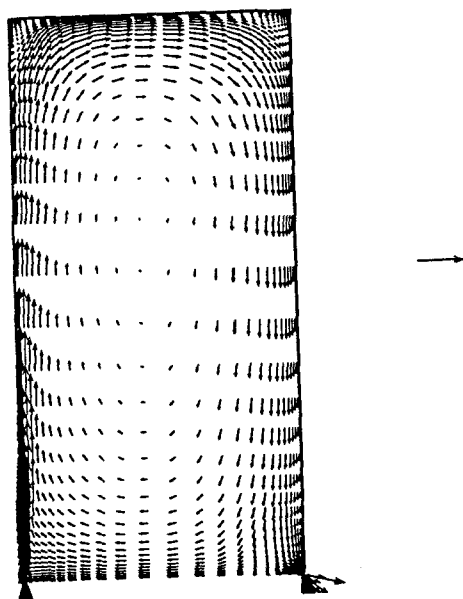


Figure 7.16 $Re_b = 1675$ 2D FLUENT $k - \epsilon$ Simulation 44x40 Grid - Mean Velocity
Dimensionless velocity vector $U/U_j = 0.5$

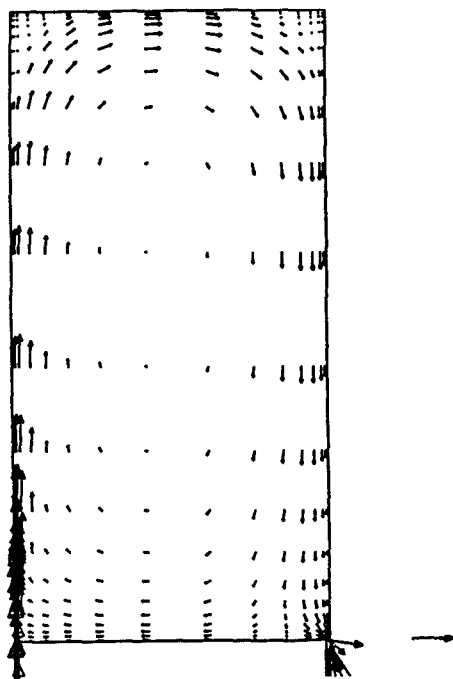


Figure 7.17 $Re_b = 1675$ 2D FLUENT $k - \epsilon$ Simulation 86x78 Grid - Mean Velocity
Dimensionless velocity vector $U/U_j = 0.5$. Grid lines removed for clarity.

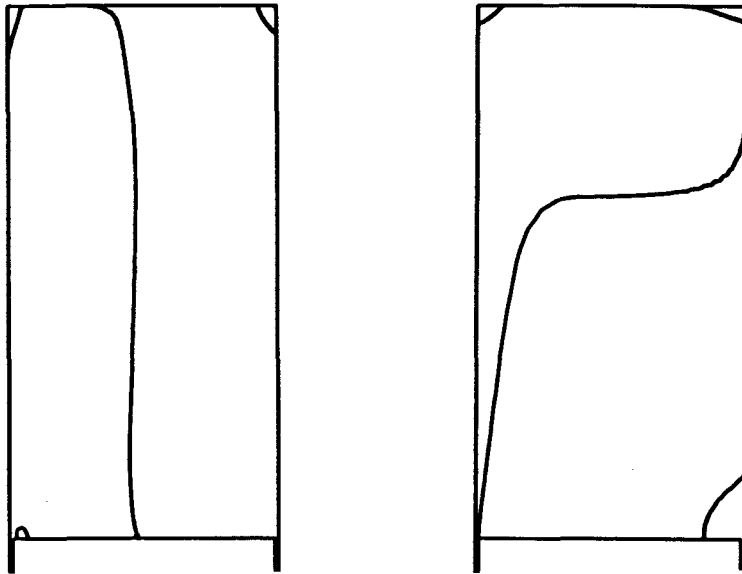


Figure 7.18 $Re_b = 1675$ 2D FLUENT $k - \epsilon$ Simulation 44x40 Grid - Contours a) left side 0 Contour U velocity, b) 0 Contour V velocity

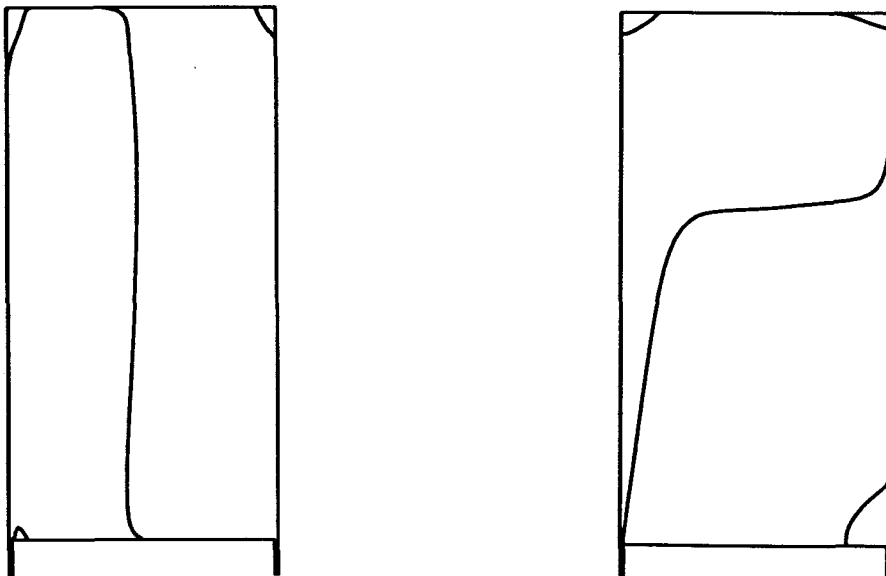


Figure 7.19 $Re_b = 1675$ 2D FLUENT $k - \epsilon$ Simulation 86x78 Grid - Contours a) left side 0 Contour U velocity, b) 0 Contour V velocity

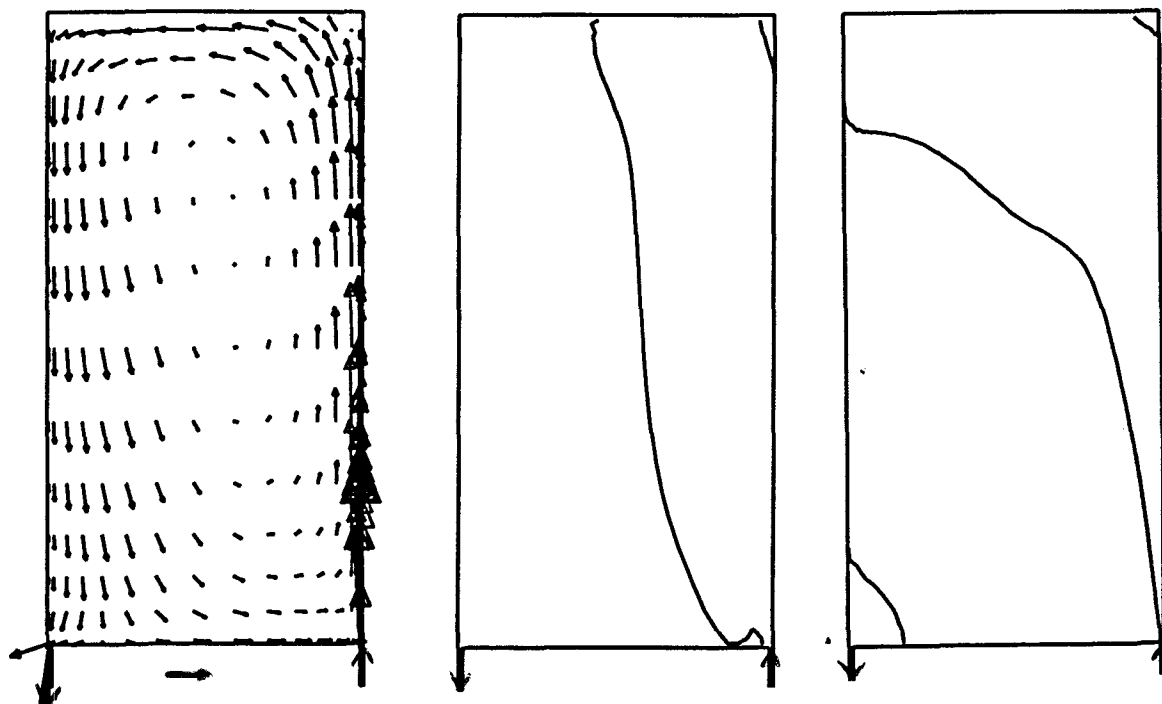


Figure 7.20 $Re_b = 1675$ 3D FLUENT $k - \epsilon$ Simulation $30 \times 40 \times 15$ Grid - a) (left side) Mean Velocity Dimensionless velocity vector $U/U_j = 1.0$ b) 0 Contour U velocity, c) 0 Contour V velocity

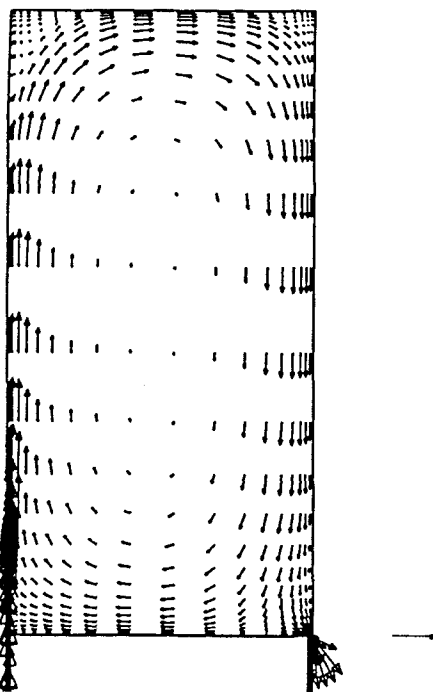


Figure 7.21 $Re_b = 1675$ 2D FLUENT ASM Simulation 86×78 Grid - Mean Velocity Dimensionless velocity vector $U/U_j = 0.5$. Grid lines removed for clarity.

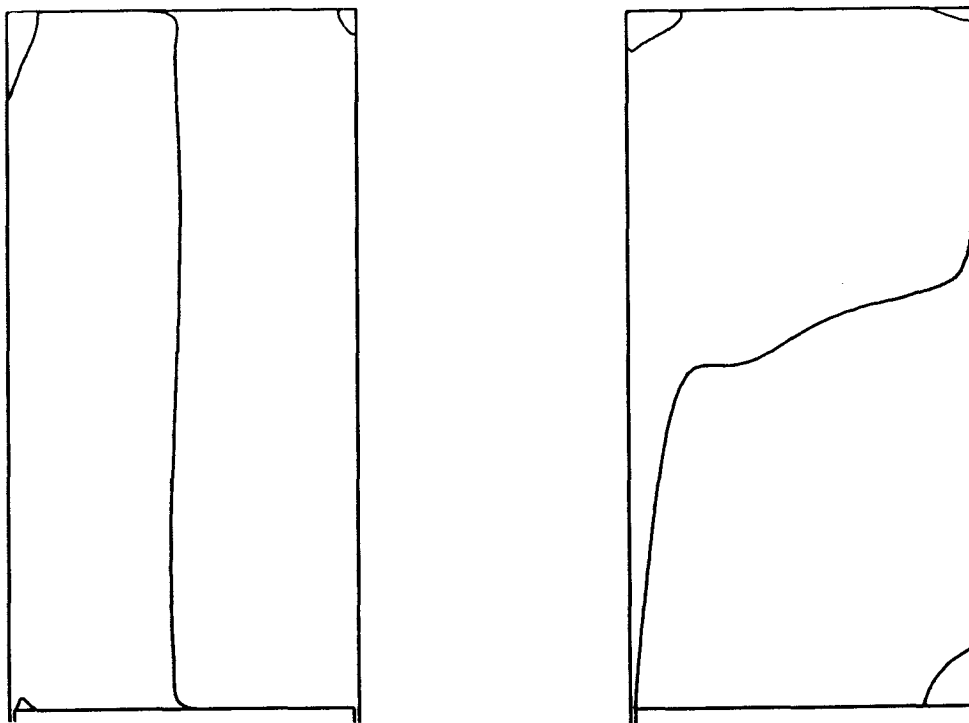


Figure 7.22 $Re_b = 1675$ 2D FLUENT ASM Simulation 86x78 Grid - Contours a) left side 0 Contour U velocity, b) 0 Contour V velocity

To complement the overall flow cavity figures, plots of four values of x were selected for detailed velocity measurements of $Re_b = 1675$. Figure 7.23 is a plot of U vs y at $x = .060$ m. These data show the steep velocity profile created by the incoming jet at the wall. The PSV data presented are individual velocity measurements at x values between .0575 and .0625 m. The PSV data agree with the LDA data well and the curve of the inlet wall jet is in excellent agreement with the LDA measurements. Velocity data is sparse in the central portion of the cavity because the slow moving fluid does not create a measurable streak in the longest time interval. The 44x40 2D $k - \epsilon$ and 30x40x15 3D $k - \epsilon$ simulations are seen to over-predict the peak jet velocity. As discussed earlier, the $k - \epsilon$ model simulations predict the peak velocity too close to the $y = 0$ wall whereas the ASM simulation is seen to

over-predict the velocities away from the wall boundaries. All $k - \epsilon$ simulations fail to predict the flow along the $y = .15$ m wall well.

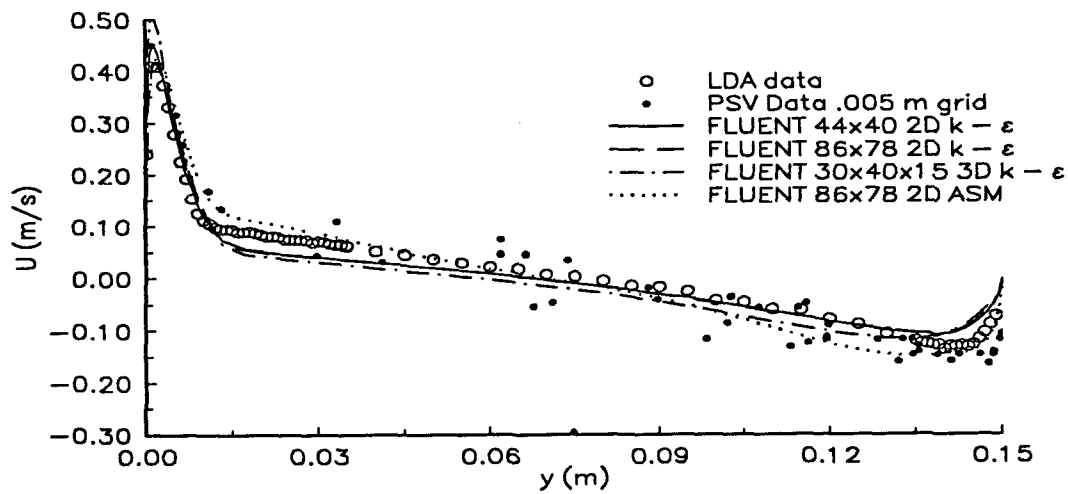


Figure 7.23 U versus y at $x = 0.06$ m $Re_b = 1675$

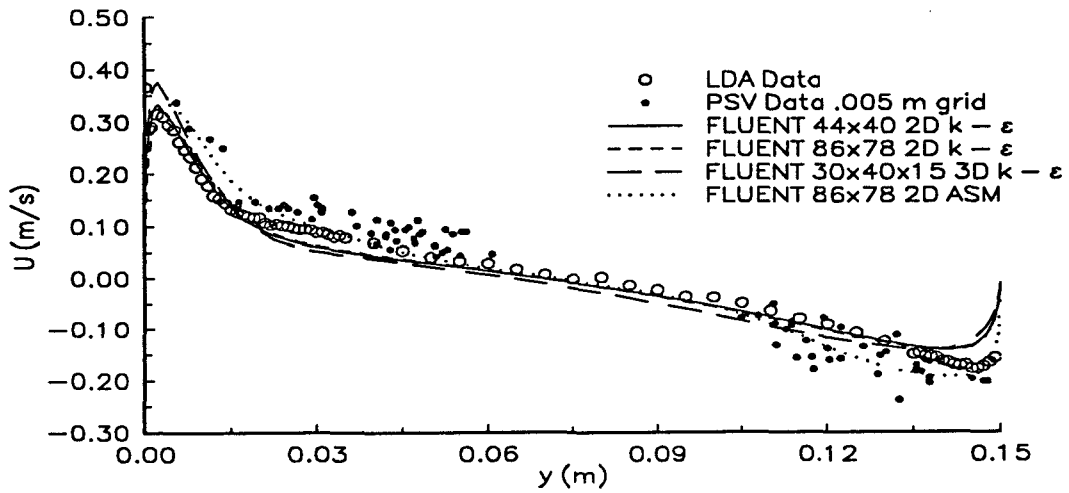


Figure 7.24 U versus y at $x = 0.12$ m $Re_b = 1675$

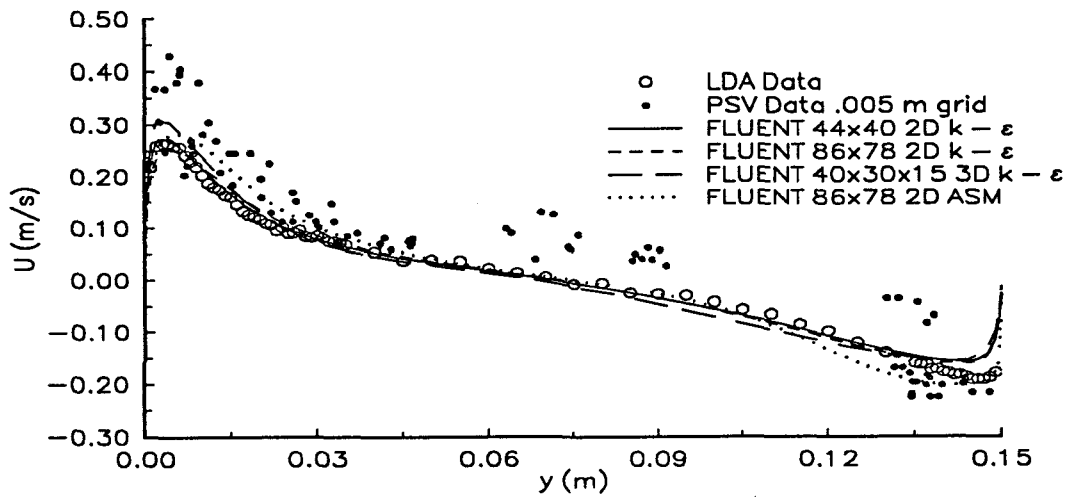


Figure 7.25 U versus y at $x = 0.18$ m $Re_b = 1675$

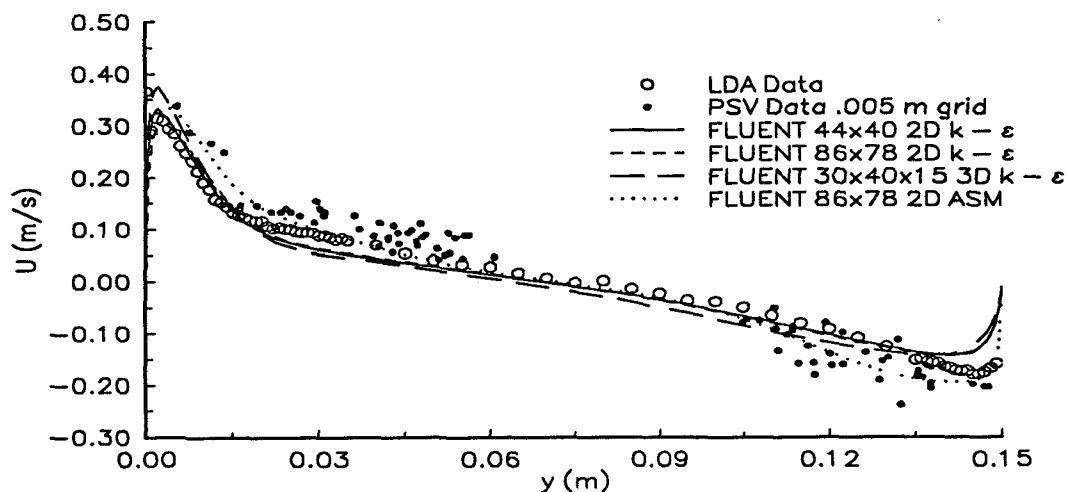


Figure 7.26 U versus y at $x = .24$ m $Re_b = 1675$

Similar results are found at $x = .12$ m (Figure 7.24) and $.18$ m (Figure 7.25) with the 44×40 2D and $30 \times 40 \times 15$ 3D $k - \epsilon$ simulations over-predicting the peak velocity in the jet and all $k - \epsilon$ simulations giving poor agreement along the $y = .15$ m wall. The ASM simulation predicts a broader jet profile than the experimental data at $x = .12$ m and $.18$ m. The jet profile predicted by the 86×78 2D $k - \epsilon$ simulation is in better agreement with the data. At $x = .24$ m (Figure 7.26) the experimental results show a steeper velocity gradient along the $y = 0$ wall than is predicted by all simulations and the ASM simulation again shows a broader jet profile. The PSV data measured generally shows higher velocities than the LDA data, partially because of the system bias previously discussed. The LDA data is an average of the V component of 8000 instantaneous particle velocity measurements in a very small distance (measuring volume of length $124 \mu\text{m}$ and diameter $26 \mu\text{m}$); whereas the PSV data are actual

measurements made of particle streaks. The requirement of a complete streak in the frame meant rejecting particles not travelling in the plane of light (.002 m thick). All particles with some V component were measured by the LDA. All these factors would account for some of the discrepancy in the measurements. The experimental PSV system as described has some bias toward higher velocity particles, as the longest time period available virtually eliminates slow moving particles (section 7.4.2.1).

Analysis of the LDA experimental data shows that continuity is satisfied at each x plane. Table 7.2 is the result of such continuity analysis. Ideally $\Sigma(Udy)/y$ should sum to 0.

Table 7.2 Continuity Analysis LDA Data $Re_b = 1675$

	.06 m	.12 m	.18 m	.24 m
$\Sigma(Udy)/y$.007414	.0068	-.00073	-.01092

Measurements of V vs x at y = .075 m are shown in Figure 7.27. Individual velocities obtained from PSV data are plotted with LDA results. The PSV results show the trend of the velocity and agree very well with the LDA data. The k - ϵ simulations are only able to predict the velocities away from the wall boundaries (x = 0 and x = .30 m). The ASM prediction is in excellent agreement with the experimental data.

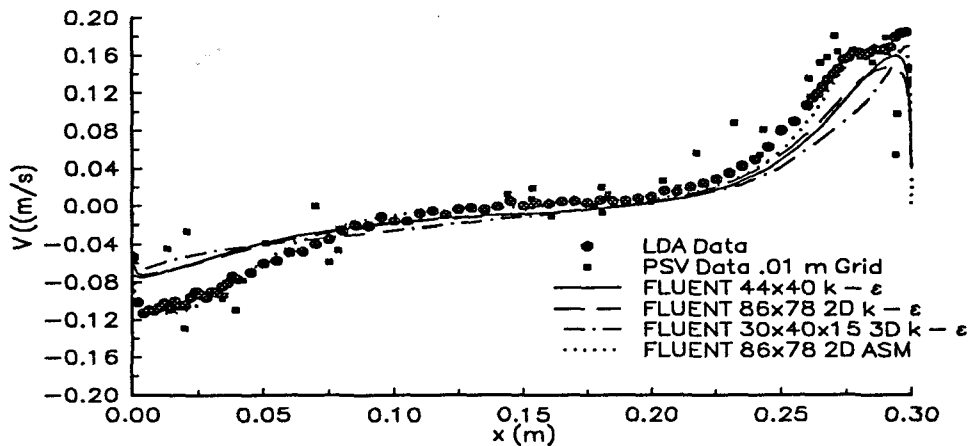


Figure 7.27 V versus x at $y = .075$ m $Re_b = 1675$

Measurements were also obtained in the z plane for U velocity for various x, y coordinates as shown in Figure 7.28. This measurement was made in an attempt to determine the three-dimensionality of the flow cavity. The results are compared to the three-dimensional $30 \times 40 \times 15$ FLUENT $k - \epsilon$ simulation. From the experimental data the cavity is seen to have good two-dimensional characteristics since the data do not vary widely across the depth of z plane, with the exception of the location $(x, y) = (.29, .01)$ where there is some scatter in the data because of the fluid turning and the small recirculation zone is developed. The simulation is in poor agreement with the data at this location and at the locations within the developing jet $(x, y) = (.06, .001)$ and $(x, y) = (.06, .002)$ where it over-predicts the peak velocity, as was previously seen in the U vs y plots.

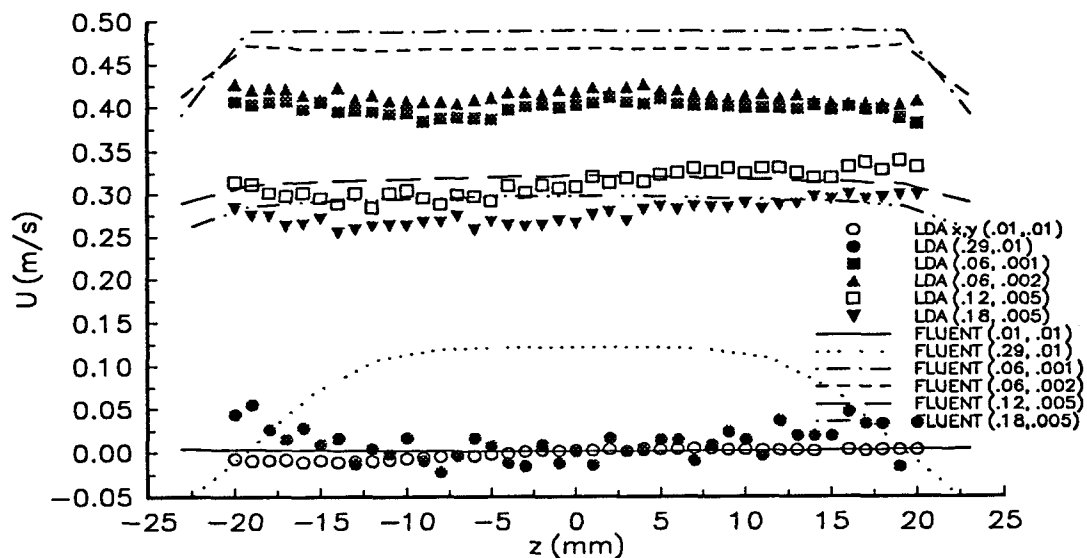


Figure 7.28 U versus z $Re_b = 1675$

Figure B7.1 [Additional cases for $Re_b = 1117$ are shown in Appendix B] shows the experimental results for the case of $Re_b = 1117$ for the overall flow field which is similar in many respects to the case of $Re_b = 1675$. Using the average inlet velocity both plots scale identically. Fluid enters the cavity from the inlet slot and entrains fluid in the cavity, reducing velocity and spreading in the y direction similar to the higher Re case. At $\sim x = .27$ m the bulk of the fluid turns and flows along the $x = .30$ m surface before turning once again and flowing along the $y = .15$ m wall with lower velocity but increased width. Upon approaching the exit some fluid is drawn to the exit and the remainder turns and re-enters the flow along the $x = 0$ wall. The centre recirculating core of the cavity is stagnant in comparison to the flow around the

walls. At the $x = .30$ wall, small recirculation zones exist; the area at $(.30,0)$ being $.020$ m in diameter, and the area at $(.30,.15)$ being somewhat smaller approximately $.010$ m in diameter. Three simulations of the flow cavity are presented in Figures B7.2-4. Figure B7.2 represents a two-dimensional FLUENT $k - \epsilon$ turbulence model simulation using a 44×40 grid. Figure B7.3 is a two-dimensional FLUENT $k - \epsilon$ turbulence model simulation using a 86×78 grid and Figure B7.4 is a three-dimensional FLUENT $k - \epsilon$ turbulence model simulation using a $30 \times 40 \times 15$ grid. The dense grid two-dimensional simulation was done to ensure that the solution was independent of the grid dimensions. Again the only significant difference between the simulations is the predicted size of both $x = .30$ m wall corner recirculation zones: the dense grid simulation predicts larger recirculation zones which are closer to the experimental data. Again, the three-dimensional simulation differs significantly from the experimental data and the two-dimensional numerical simulations, in that the flow toward the exit does not flow along the $y = .15$ m wall but flows on an angle toward the entrance slot. The main recirculation cell in the cavity is reduced in size and skewed in shape.

To complement the overall flow cavity plots four x values were selected for detailed velocity measurements for $Re_b = 1117$. Figure B7.5 is a plot of U velocity vs y for $x = .06$ m. This figure shows the steep velocity profile created by the incoming jet at the wall. Both two-dimensional simulations give excellent agreement with the experimental data, although the $30 \times 40 \times 15$ 3D simulation is seen to slightly under predict the peak jet velocity. The three-dimensional simulation fails to predict the

downward flow well for the reasons described above. Similar results are found at $x = .12$ m (Figure B7.6), $.18$ m (Figure B7.7), and $.24$ m (Figure B7.8). Better prediction is provided for the case of $Re_b = 1117$ than in the higher $Re_b = 1675$ case.

Analysis of the experimental data shows that continuity is satisfied at each cavity height. Table 7.3 is the result of continuity analysis.

Table 7.3 Continuity Analysis LDA Data $Re_b = 1117$

	.06 m	.12 m	.18 m	.24 m
$\Sigma(Udy)/y$.004416	.004495	-.00096	-.00244

Measurements of V vs x at $y = .075$ m are shown in Figure B7.9 for the case of $Re_b = 1117$. Again, the two-dimensional simulations predict the experimental trend well, although the width and magnitude of the velocity in the area of the $x = 0$ and $x = .30$ m walls is poorly predicted. The three-dimensional simulation is the poorest representation of the experimental data.

Measurements were also obtained in the z plane for U velocity for various x, y coordinates as shown in Figure B7.10. These measurements were made in an attempt to determine the three-dimensionality of the flow cavity. The results are compared to the three-dimensional FLUENT $k - \epsilon$ turbulence model simulation. From the experimental data the cavity is seen to have good two-dimensional characteristics, since the data do not vary widely across the depth of plane z , with the exception of the location chosen at $(.29, .01)$ where there is some scatter in the data due to the fluid

turning and the small recirculation zone is developed. The simulation is in poor agreement with the data at this location, but the prediction has improved at the locations within the developing jet (.06,.001) and (.06,.002) where it previously over-predicted the peak velocity in the $Re_b = 1675$ case.

Both cases collapse to one curve when plotted non-dimensionally, as shown in Figures 7.29 - 7.32. Here the mean velocities have been made non-dimensional with the average inlet velocity (.72 m/s for $Re_b = 1675$ and .48 m/s for $Re_b = 1117$). Only the 44x40 simulations are presented for the sake of clarity. Excellent agreement is seen in the first three cases of $x = .06, .12, \text{ and } .18$ m, with experimental results collapsing onto a single line, findings which suggest similarity in the two cases. $X = .24$ m has slight differences in the inlet side, but the results are similar in other respects.

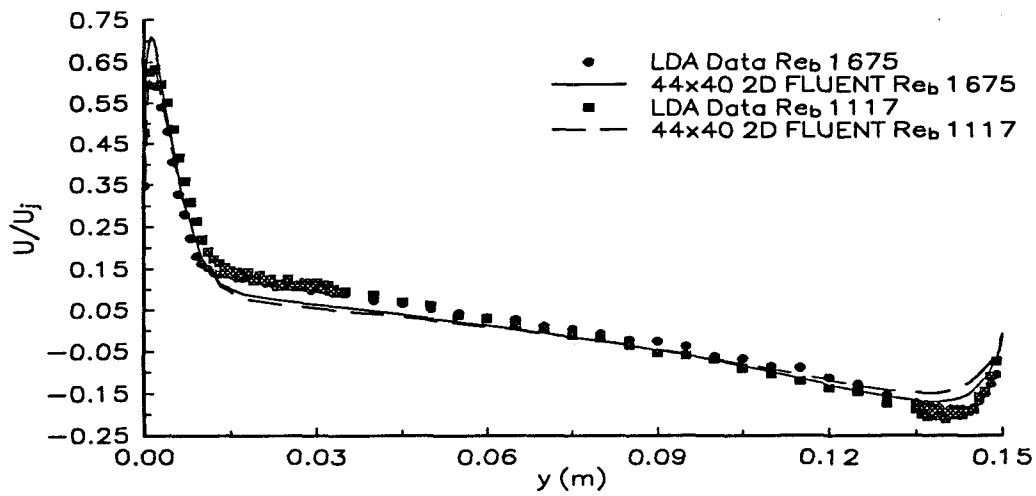


Figure 7.29 U/U_j versus y , $Re_b = 1675$ and 1117 , $x = .06$ m

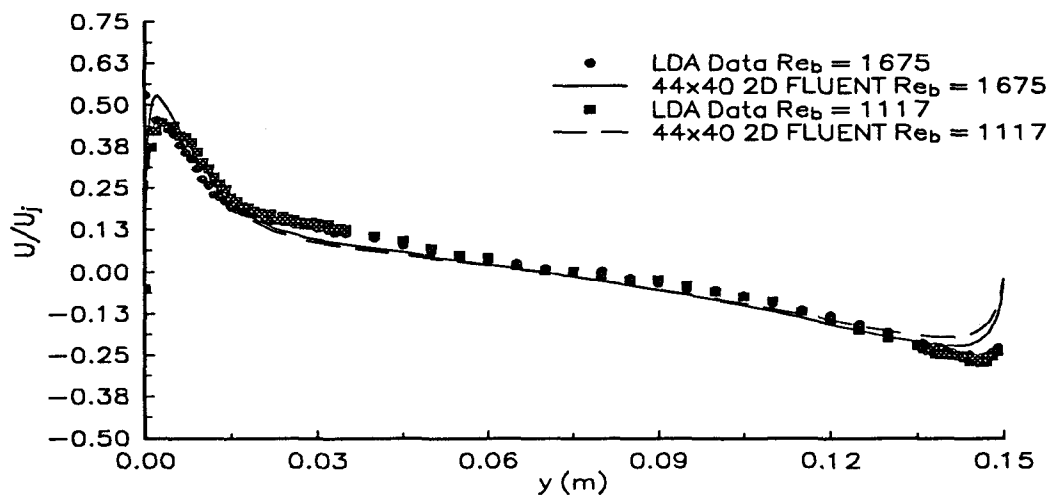


Figure 7.30 U/U_j versus y , $Re_b = 1675$ and 1117 , $x = .12$ m

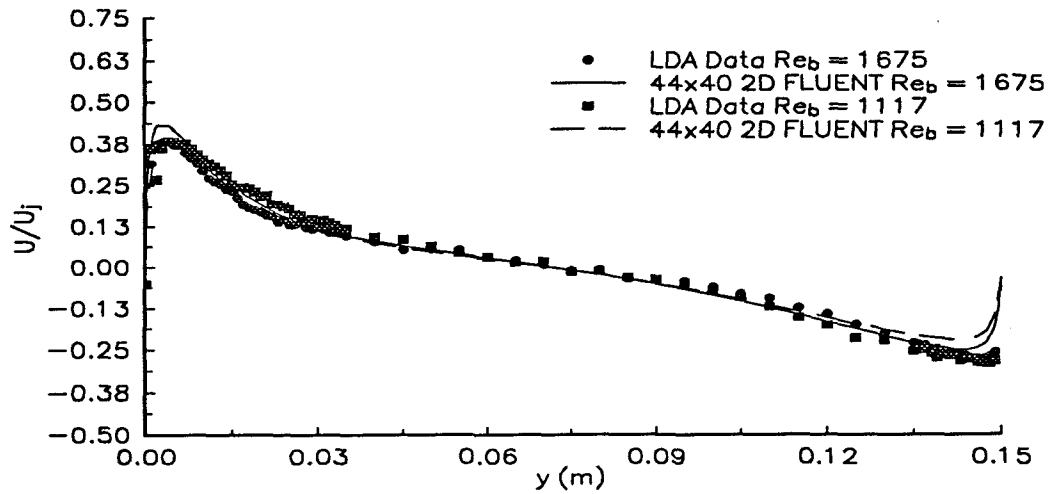


Figure 7.31 U/U_j versus y , $Re_b = 1675$ and 1117 , $x = .18$ m

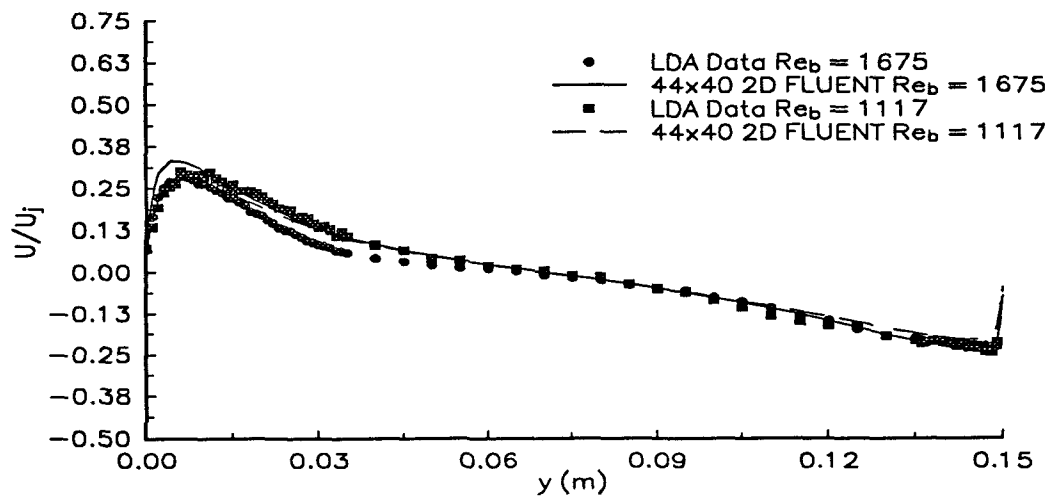


Figure 7.32 U/U_j versus y , $Re_b = 1675$ and 1117 , $x = .24$ m

Turbulent Energy

In the experimental cavity measurements $\overline{u^2}$ and $\overline{v^2}$ were obtained and $\overline{w^2}$ was not; as a result $k = 0.5 (\overline{u^2} + \overline{v^2})$. Consequently, k will be greater than the experimental data suggest. Experimental measurements of contours of turbulent kinetic energy $k = 0.5 (\overline{u^2} + \overline{v^2})$ are shown in Figure 7.33 for $Re_b = 1675$. The peak experimental k value from the entire cavity study was $.0068 \text{ m}^2/\text{s}^2$ and was found at $(.020, .005)$. Results from the 44×40 2D $k - \epsilon$ turbulence model simulation, 86×78 2D $k - \epsilon$ turbulence model simulation, the $30 \times 40 \times 15$ 3D $k - \epsilon$ turbulence model simulation and the 86×78 2D ASM turbulence model simulation are shown in Figures 7.34 - 7.37. Although all the simulations over-predict the k values, the 3D simulation is the closest in agreement with the experimental data. There was a limitation in the experimental data in that it was not possible to obtain data directly adjacent to the cavity boundary and the closest data point in the figure is $.005 \text{ m}$ from any cavity boundary. The numerical simulations show, in the inlet-wall boundary region, significant turbulent energy which was not measurable experimentally. Generally, in the y direction from the inlet into the cavity, the simulations show significant spreading of the turbulent energy which is not seen experimentally. Experimentally, this turbulent energy is confined to a narrow region along the $y = 0$ wall. This action is likely due to the damping of the turbulent velocity fluctuations normal to the wall because of the turbulent pressure reflections from the wall, as discussed in Launder and Rodi (1983). Standard $k - \epsilon$ turbulence models and ASM turbulent models, as used in these studies, do not specifically account for the damping of velocity fluctuations.

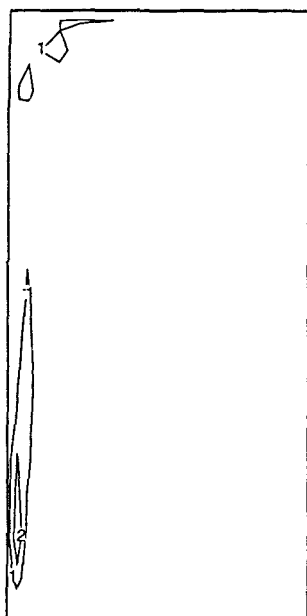


Figure 7.33 Contours of Kinetic Energy Entire Cavity - LDA Data $Re_b = 1675$
Kinetic Energy Contours (m^2/s^2) 1 - .001, 2 - .0025, 3 - .005

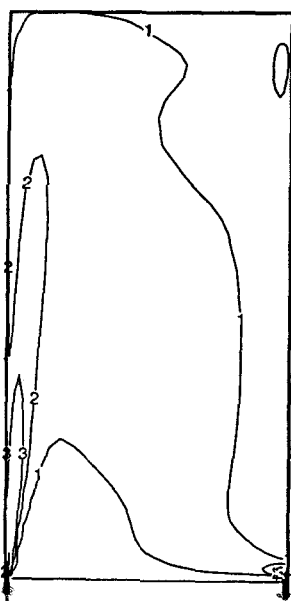


Figure 7.34 Contours of Kinetic Energy Entire Cavity - 44x40 2D $k - \epsilon$ Simulation
 $Re_b = 1675$ Kinetic Energy Contours (m^2/s^2) 1 - .001, 2 - .0025, 3 - .005

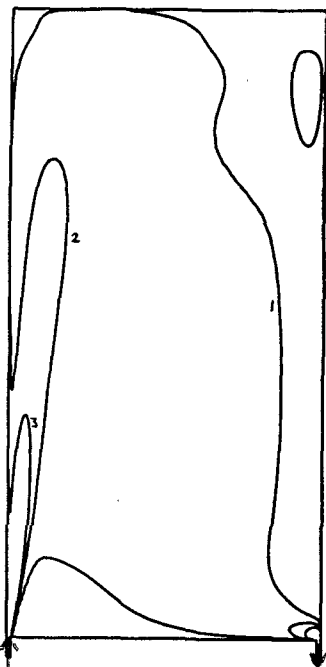


Figure 7.35 Contours of Kinetic Energy Entire Cavity - 86x78 2D $k - \epsilon$ Simulation
 $Re_b = 1675$ Kinetic Energy Contours (m^2/s^2) 1 - .001, 2 - .0025, 3 - .005

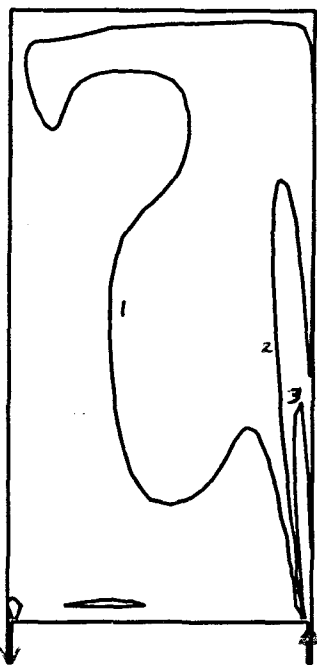


Figure 7.36 Contours of Kinetic Energy Entire Cavity - 30x40x15 3D $k - \epsilon$
 Simulation $Re_b = 1675$ Kinetic Energy Contours (m^2/s^2) 1 - .001, 2 -
 .0025, 3 - .005

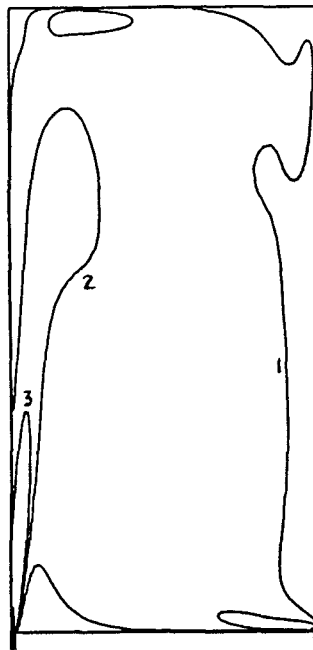


Figure 7.37 Contours of Kinetic Energy Entire Cavity - 86x78 2D ASM Simulation $Re_b = 1675$ Kinetic Energy Contours (m^2/s^2) 1 - .001, 2 - .0025, 3 - .005

Plots of kinetic energy versus y are presented in Figures 7.38 - 7.41 at the same four x values presented for the mean velocity plots for $Re_b = 1675$. For these experimental cases only $\overline{u^2}$ was measured and is presented for the profiles. In this case the assumption is made that $\overline{v^2}$ and $\overline{w^2}$ are of the same magnitude and $\overline{u^2} \approx \overline{v^2} + \overline{w^2}$ and $k = \overline{u^2}$, following the collated wall jet data of Launder and Rodi (1983). The three simulations are seen to over-predict the energy in the area adjacent to the wall where the jet enters. The experimental data show an increase in turbulent energy adjacent to the $y = .15$ m wall, a result which is not well simulated for the $x = .06$ m case (Figure 7.38). Some trends are well predicted by the simulations, such as the sharp decrease in energy very close to the $y = 0$ wall before the peak value occurs and the gradual decay of energy as x increases. All simulations show higher values of k in

the stagnant central core region of the cavity. Here the velocities are very low and the turbulence model assumptions may not apply. A modification of the models to include a low Reynolds number model (Jones and Launder, (1972), Patel *et al.*, (1984)) would improve the predictions in this region.

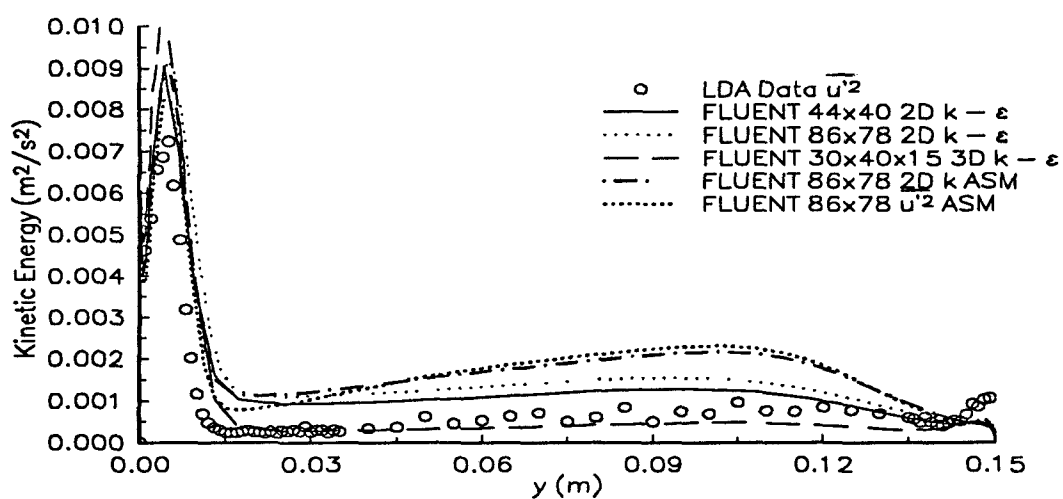


Figure 7.38 Kinetic Energy versus y at $x = .06$ m, $Re_b = 1675$

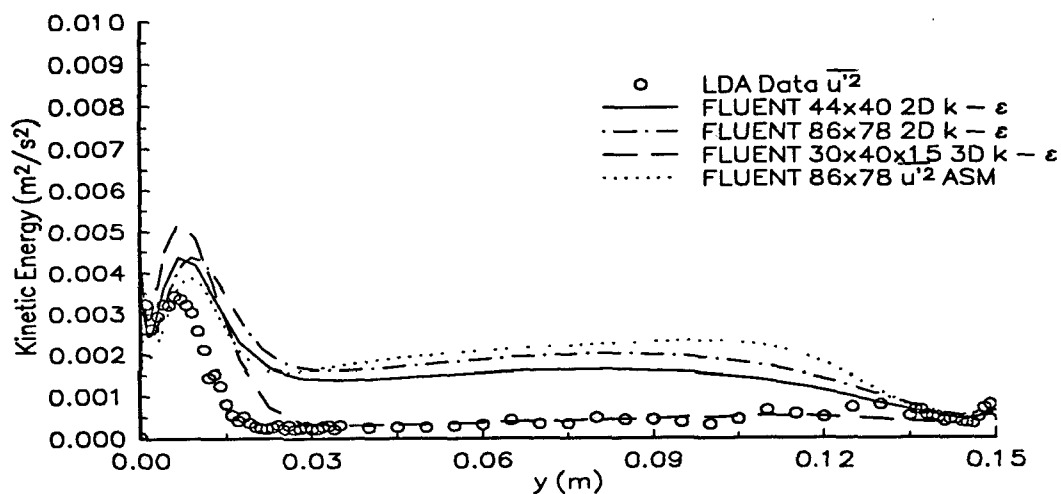


Figure 7.39 Kinetic Energy versus y at $x = .12$ m, $Re_b = 1675$

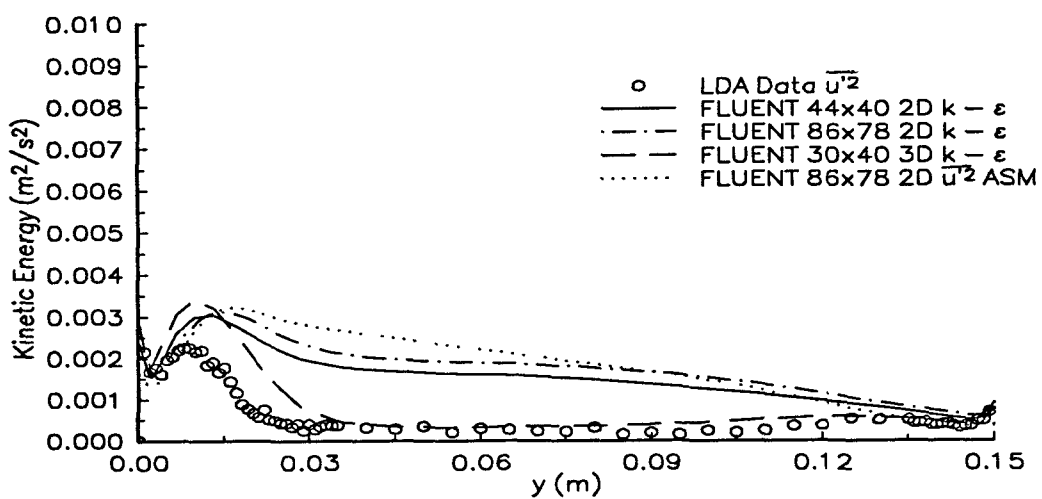


Figure 7.40 Kinetic Energy versus y at $x = .18$ m, $Re_b = 1675$

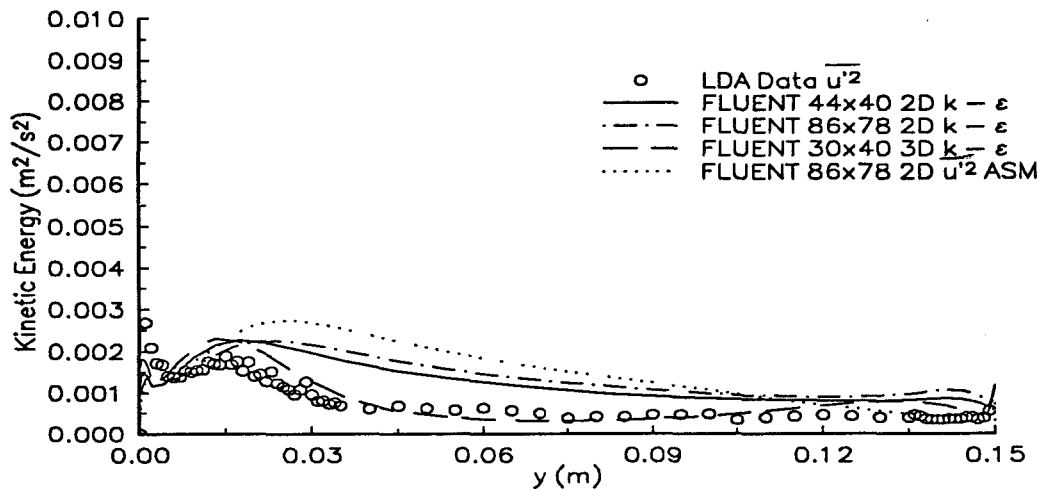


Figure 7.41 Kinetic Energy versus y at $x = .24$ m, $Re_b = 1675$

Contours of turbulent kinetic energy $k = 0.5(\overline{u'^2} + \overline{v'^2})$ are also presented for $Re_b = 1117$ (Figure B7.11). k values should be greater than those presented, as $\overline{w'^2}$ was not measured. The peak value of k was $.0038 \text{ m}^2/\text{s}^2$ and was found at $(.040, .005)$. Results from the 44×40 2D $k - \epsilon$ turbulence model simulation, 86×78 2D $k - \epsilon$ turbulence model simulation and the $30 \times 40 \times 15$ 3D $k - \epsilon$ turbulence model simulation are shown in Figures B7.12-B7.14. All the simulations over-predict the k values, although the 3D simulation is the closest agreement to the experimental data. The numerical simulations show significant turbulent energy in the inlet-wall boundary region which was not measurable experimentally. Again the two-dimensional simulations are very similar and the over-predictions of energy values in the main flow are not as drastic as the case of $Re_b = 1675$.

Plots of kinetic energy versus y are presented in Figures B7.15-18 for four x

values similar to the mean velocity plots previously presented. In the experimental case only $\overline{u^2}$ is presented for the profiles. The three simulations predict the energy levels with much better agreement than the higher flow case discussed above. Again the experimental data show an increase in turbulent energy adjacent to the opposite wall, which is not well simulated for the $x = .06$ m case (Figure B7.15). The simulations accurately predict the trends; such as the sharp decrease in energy very close to the wall before the peak value occurs and the gradual decay of energy as the cavity height is increased.

7.5 Conclusions and Recommendations

Two experimental test conditions have been examined for a recirculating cavity flow cell using flow visualization, laser Doppler anemometry (LDA), and particle streak velocimetry (PSV). Two and three dimensional numerical simulations have been completed using the commercial CFD code FLUENT using the $k - \epsilon$ turbulence model and the ASM turbulence model to augment the experimental work.

Results from the detailed wall jet measurements show a significantly higher growth rate than a unconfined wall jet in stagnant surroundings. The confining boundaries modify the jet development and may enhance the jet growth at the mid-plane ($z = 0$). Studies with different boundary arrangements might confirm this. Simulations with the $k - \epsilon$ and ASM turbulence models agree well with the measured data, whereas simulations of wall jets in stagnant surroundings have previously over-

predicted the growth of the jet.

The PSV data are in close agreement with the LDA data, although some bias towards higher velocity particle streaks was found. Improvements to the synchronization of the equipment would extend the velocity range available. Errors encountered because of manual streak digitization could be eliminated by means of a computational technique to locate the streaks, although this procedure would potentially increase the image processing time. The PSV technique is complementary to the LDA data because an instantaneous image of the entire flow field is obtained which is very valuable in probing areas where LDA measurements could not be obtained, such as adjacent to the wall boundaries.

Agreement between the measured and simulated mean velocities was found with the two-dimensional simulations but the three-dimensional simulation generally gave the poorest agreement with the experimental results. This latter finding may be a result of insufficient grid refinement in the z direction.

Although the levels of kinetic energy in the jet area were over-predicted in all simulations, the trends are reasonably represented. Kinetic energy levels remained high in the region adjacent to the $y = 0$ wall in the experimental data but the simulations showed significant spreading of the kinetic energy in the y direction with increasing x because of the model's inability to account for the wall damping of the v velocity fluctuations. High levels of kinetic energy were predicted by the simulations in the core of the cavity, possibly because of the inappropriateness of the modelling for the low velocity in this region.

8.0 Conclusions and Recommendations

Studies of jet flow in enclosures have been detailed for opposed jets impinging in a confined space and jet driven recirculating flow in a cavity.

Opposed jets impinging in a cavity was found to have three distinct flow regions based on dimensionless groups formed from the geometric and fluid parameters. The first region is the steady non-oscillatory region, consisting of several flow structures such as the free laminar jet, a curved shear layer, a stagnating impingement flow, a radial jet flow, recirculating flow and developing channel flow. The flow field of $Re_d < \sim 90$ was seen to be steady and unaffected by transient fluid velocities. The onset of the second region, or oscillatory phase, was found to be a function of the Re_d and the dimensionless length group L^* or D^* . Smaller values of L^* in the range of L^* studied delayed the onset of oscillations and the limit of oscillations. Incremental values of Re_d caused an increase in the dimensionless frequency St_d and amplitude of disc oscillation until a limit value was reached. The oscillations were postulated to occur as a result of pressure wave feedback from the point of jet impingement to the nozzle mouth, forcing the self-sustaining oscillations.

The third region occurred past the limit of finite oscillations. This region was characterized by a change in the overall flow structure because the jets no longer directly impinged for large values of L^* . An unsteady flow field was visualized and

no regular oscillations were found in velocity measurements, although the rms of the measured velocities continued to increase with increasing Re_d . Studies of the effect of geometrical parameters in the third region were obtained using commercial RIM nozzle blocks. Re_d typical of commercial RIM operation revealed the jets to be the only structure visible at $Re_d \sim 300$. Chamber diameter to nozzle diameter, needle position and a flow restriction were found to have a significant effect on the flow field, while the head position was found to have little effect past the point of impingement. The short nozzle was not found to have a significant effect on the jet development in an opposed jet configuration and no annular jet velocity profile was found for the nozzle needle settings examined; however unequal nozzle flow rate ratios were found to alter the flow field significantly.

Jet driven turbulent recirculating flow has been investigated and results from the developing wall jet measurements show a significantly higher growth rate than a unconfined wall jet in stagnant surroundings. In the former the confining boundaries modify the jet development and may enhance the jet growth. Studies with different boundary arrangements might confirm this. Simulations with the $k - \epsilon$ and ASM turbulence models agree well with the measured data, whereas simulations of wall jets in stagnant surroundings have previously over-predicted the growth of the jet.

The PSV data are in close agreement with the LDA data, although some bias towards higher velocity particle streaks was found. Equipment synchronization might extend the velocity range available. Errors encountered as a result of manual streak digitization could be reduced using a computational image analysis method. The PSV

technique is complementary to the LDA data since an instantaneous image of the entire flow field is obtained, and is very valuable in probing areas where LDA measurements could not be obtained. Agreement in the measured and simulated mean velocities was found with the two-dimensional simulations but the three-dimensional simulation generally gave the poorest agreement with the experimental results. This conclusion may be a result of insufficient grid refinement in the third dimension.

The levels of kinetic energy in the jet area were over predicted in all simulations, although the trends are reasonably represented. Kinetic energy levels remained high in the region adjacent to the $y = 0$ wall in the experimental data and the simulations showed significant spreading of the kinetic energy in the y direction with increasing x as both turbulence models are unable to account for the wall damping of the normal velocity fluctuations. High levels of kinetic energy were predicted by the simulations in the core of the cavity possibly because of the inappropriateness of the modelling for the low velocity in this region.

References

- Adamczyk, A.A., and Rimai, L., 2-Dimensional Particle Tracking Velocimetry (PTV): Technique and Image Processing Algorithms, *Experiments in Fluids*, **6**, 373-380, 1988.
- Adrian, R.J., Multi-point Optical Measurements of Simultaneous Vectors in Unsteady Flow - a Review, *International Journal of Heat and Fluid Flow*, **7**, 127-145, 1986.
- Adrian, R.J. Particle Imaging Techniques for Experimental Fluid Mechanics, *Annual Review of Fluid Mechanics*, **23**, 261-304, 1991.
- Agui, J.C., and Jimenez, J., On the Performance of Particle Tracking, *Journal of Fluid Mechanics*, **185**, 447-468, 1987.
- Akaike, S., Nemoto, M., and Ishiwata, R., Flow Visualization of Coaxial Impingement of Opposing Jets in Mixing Chamber, Flow Visualization IV, Proceedings of the Fourth International Symposium on Flow Visualization, Aug 26-29, Paris, France, 527-532, 1986.
- Akaike, S., and Nemoto, M., Potential Core of a Submerged Laminar Jet, *Transactions of the ASME Journal of Fluids Engineering*, **110**, 392-398, 1988.
- Andersson, H.I., Braseth, A.O., and Holmedal, B., Computation of the Inlet Wall Jet in a Rectangular Enclosure, *International Journal of Computational Fluid Dynamics*, **1**, 217-232, 1993.
- Arroyo, M.P., and Greated, C.A., Stereoscopic Particle Image Velocimetry, *Measurement Science and Technology*, **2**, 1181-1186, 1991.
- Baron, J., Benque, J.P., and Coeffe, Y., Turbulent Shear Flows Induced by a Jet in a Cavity - Measurements and 3D Numerical Simulation, Turbulent Shear Flows, Springer-Verlag, 1981.
- Becker, H.A., Cho, S.H., Ozum, B., and Tsujikawa, H., Turbulent Mixing in the Impingement Zone of Dual Opposed Free Jets and of the Normal Wall Impinging Jet, *Chemical Engineering Communications*, **67**, 291-313, 1988.
- Beltaos, S., and Rajaratnam, N., Plane Turbulent Impinging Jets, *Journal of Hydraulic Research*, **11**, 29-59, 1973.
- Boyle, D.R., and Golay, M.W., Measurement of a Recirculating, Two-dimensional, Turbulent Flow and Comparison to Turbulence Model Predictions I: Steady State Case, ASME Paper No. 83-WA/FE-8, 1983a.

- Boyle, D.R., and Golay, M.W., Measurement of a Recirculating, Two-dimensional, Turbulent Flow and Comparison to Turbulence Model Predictions II: Transient Case, ASME Paper No. 83-WA/FE-9, 1983b.
- Buchave, P., Particle Image Velocimetry - Status and Trends, *Experimental Thermal and Fluid Science*, 5, 586-604, 1992.
- Camp, C.E., Kolb, W.B., Sublette, K.L., and Cerro, R.L., The Measurement of Square Channel Velocity Profiles using a Microcomputer-based Image Analysis System, *Experiments in Fluids*, 10, 87-92, 1990.
- Cenedese, A., and Paglialunga, A., Digital Direct Analysis of a Multiexposed Photograph in PIV, *Experiments in Fluids*, 8, 273-280, 1990.
- Choi, H.L., Albright, L.D., Timmons, M.B., and Warhaft, Z., An Application of the K-Epsilon Turbulence Model to Predict Air Distribution in a Slot-Ventilated Enclosure, *Transactions of the ASAE*, 31, 1804-1814, 1988.
- Craig, R.R., Nejad, A.S., Hahn, E.Y., and Schwartzkopf, K.G., Approach for Obtaining Unbiased Laser Doppler Velocimetry Data in Highly Turbulent Flows, *Journal of Propulsion*, 2, 6, 541-545, 1986.
- Crow, S.C., and Champagne, F.H., Orderly Structure in Jet Turbulence, *Journal of Fluid Mechanics*, 48, 547-591, 1971.
- Davis, R.W., Moore, E.F., and Purtell, L.P., A Numerical-Experimental Study of Confined Flow Around Rectangular Cylinders, *Physics of Fluids*, 27, 1, 46-59, January, 1984.
- Denshchikov, V.A., Kondrat'ev, V.N., and Romashov, A.N., Interaction Between Two Opposed Jets, *Fluid Dynamics*, 6, 924-926, 1978.
- Denshchikov, V.A., Kondrat'ev, V.N., Romashov, A.N., and Chubarov, V.M., Auto-oscillations of Planar Colliding Jets, *Fluid Dynamics*, 3, 460-462, 1983.
- Deshpande, M.D., and Vaishnav, R.N., Submerged Laminar Jet Impingement on a Plane, *Journal of Fluid Mechanics*, 114, 213-236, 1982.
- Dimotakis, P.E., and Brown, G.L., The Mixing Layer at High Reynolds Number: Large-Structure Dynamics and Entrainment, *Journal of Fluid Mechanics*, 78, 535-560, 1976.
- DOSTEK, Model 1400 LDA Data Acquisition Interface, Waterloo, May, 1987.

Drain, L.E., The Laser Doppler Technique, John Wiley and Sons, Toronto, 1980.

Durao, D.F.G., and Pereira, J.C.F., A Numerical-Experimental Study of Confined Unsteady Laminar Flow Around a Squared Obstacle, in Numerical Methods in Laminar and Turbulent Flow, Proceedings of the Fifth International Conference, 6-10 July 1987, Montreal, Canada, C. Taylor, W.G. Habashi, and M.M. Hafez eds., Pineridge Press, Swansea, U.K., 5 ,part 1, 261-272, 1987.

Durst, F., Melling, A., and Whitelaw, J.H., Principles and Practice of Laser Doppler Anemometry, Second Edition, Academic Press, Toronto, 1981.

Eaton, J.K, and Johnston, J.P., Turbulent Flow Reattachment: An Experimental Study of the Flow and Structure Behind a Backward Facing Step, Thermosciences Div., Stanford University, Stanford, CA, Rept. MD-39, 1980.

Edwards, R.V., How Real are Particle Bias Errors ?, in Laser Velocimetry and Particle Sizing, (Thompson, H.D., Stevenson, W.H. eds.), 79-85, 1979.

FLUENT, version 4, Create Incorporated, Hanover, N.H., U.S.A, 1991.

Gosman, A.D., Nielsen, P.V., Restivo, A., and Whitelaw, J.H., The Flow Properties of Rooms with Small Ventilation Openings, *Transactions of the ASME Journal of Fluids Engineering*, 102, 316-323, 1980.

Gutmark, E., Wolfshtein, M., and Wygnanski, I., The Plane Turbulent Impinging Jet, *Journal of Fluid Mechanics*, 88, 737-756, 1978.

Gutmark, E., and Ho, C.M., Preferred Modes and the Spreading Rate of Jets, *Physics of Fluids*, 26, 10, 2932-2938, 1983.

Hassan, Y.A., and Canaan, R.E., Full-field Bubbly Flow Velocity Measurements Using a Multiframe Particle Tracking Technique, *Experiments in Fluids*, 12, 49-60, 1991.

Ho, A.S.K., The Effects of Flow and Geometrical Parameters on Impingement Mixing for Reaction Injection Molding, M.Eng. Thesis, McMaster University, Hamilton, Canada, 1992.

Ho, C.M., and Nosseir, N.S., Dynamics of an Impinging Jet. Part 1. The Feedback Phenomenon, *Journal of Fluid Mechanics*, 105, 119-142, 1981.

Irwin, H.P.A.H., Measurements in a Self-preserving Plane Wall Jet in a Positive Pressure Gradient, *Journal of Fluid Mechanics*, 61, 33-63, 1973.

- Johnson, D.A., An Experimental and Numerical Investigation of Turbulent Recirculating Flow Within a Cavity With an Inlet Wall Jet, M.Eng. Thesis, McMaster University, Hamilton, Canada, 1988.
- Johnson, D.A., and Shoukri, M., An Experimental and Numerical Investigation of Turbulent Recirculating Flow Within a Cavity With an Inlet Wall Jet, *Chemical Engineering Communications*, **86**, 225-239, 1989.
- Kawahashi, M., and Hosoi, K., Beam-sweep Laser Speckle Velocimetry, *Experiments in Fluids*, **8**, 109-111, 1989.
- Karlsson, R.I., Eriksson, J., and Persson, J., LDV Measurements in a Plane Wall Jet in a Large Enclosure, 6th International Symposium on Applications of Laser Techniques to Fluid Mechanics, Lisbon, 1.5.1-1.5.6, 1992.
- Kerstens, P.J.M., Interactive Image Processing and Pattern Recognition of Digitized Flow Patterns, M.Sci. Thesis, Dept. Computer Science and Electrical Engineering, Lehigh University, 1986.
- Kerstens, P.J.M., and Rockwell, D., Ensemble-averaging and Correlation Techniques for Flow Visualization Images, *Experiments in Fluids*, **6**, 409-419, 1988.
- Khalighi, B., Quantitative Fluid Velocity Measurements by Automatic Analysis of Flow Visualization Images, *Experiments in Fluids*, **7**, 142-144, 1989.
- Kolodziej, P., Macosko, C., and Ranz, W.E, The Influence of Impingement Mixing on Striation Thickness Distribution and Properties in Fast Polyurethane Polymerization, *Polymer Engineering and Science*, **22**, 6, 388-392, 1982.
- Lauder, B.E., and Spalding, D.B., Lectures in Mathematical Models of Turbulence, Academic Press, London, 1972.
- Lauder, B.E., and Spalding, D.B., The Numerical Computation of Turbulent Flows, *Computer Methods in Applied Mechanics and Engineering*, **3**, 269-289, 1974.
- Lauder, B.E., Reece, G.J., and Rodi, W., Progress in the Development of a Reynolds-Stress Turbulence Closure, *Journal of Fluid Mechanics*, **68**, 537-566, 1975.
- Lauder, B.E., and Rodi, W., The Turbulent Wall Jet, *Progress in Aerospace Sciences*, **19**, 81-128, 1981.
- Lauder, B.E., and Rodi, W., The Turbulent Wall Jet - Measurements and Modelling, *Annual Review of Fluid Mechanics*, **15**, 429-459, 1983.

- Law, H.S., and Masilyah, J.H., Mass Transfer Due to a Confined Laminar Impinging Axisymmetric Jet, *Industrial Engineering and Chemical Fundamentals*, **23**, 446-454, 1984.
- Lee, L.Y., Ottino, J.M., Ranz, W.E., and Macosko, C.W., Impingement Mixing in Reaction Injection Molding, *Polymer Engineering and Science*, **20**, 13, 868-874, 1980.
- Liou, T.M., and Wu, S.M., Flowfield in a Dual-Inlet Side-Dump Combustor, *Journal of Propulsion*, **4**, 1, 53-60, 1988.
- Liou, T.M., and Hwang, Y.H., Calculation of Flowfields in Side-Inlet Ramjet Combustors with an Algebraic Reynolds Stress Model, *Journal of Propulsion*, **5**, 6, 686-693, 1989.
- Liou, T.M., Wu, S.M., and Hwang, Y.H., Experimental and Theoretical Investigations of Turbulent Flow in a Side-Inlet Rectangular Combustor, *Journal of Propulsion*, **6**, 2, 131-138, 1990.
- Liou, T.M., Hwang, Y.H., and Chen, L., Prediction of Confined Three-Dimensional Impinging Flows with Various Turbulence Models, *Transactions of the ASME Journal of Fluids Engineering*, **114**, 220-230, 1992.
- Liou, T.M., Chen, L., and Wu, Y.Y., Effects of Momentum Ratio on Turbulent Nonreacting and Reacting Flows in a Ducted Rocket Combustor, *International Journal of Heat and Mass Transfer*, **36**, 10, 2589-2599, 1993.
- Liu, Z.C., Landreth, C.C., Adrian, R.J., and Hanratty, T.J., High Resolution Measurement of Turbulent Structure in a Channel with Particle Image Velocimetry, *Experiments in Fluids*, **10**, 301-312, 1991.
- Macosko, C.W., RIM Fundamentals of Reaction Injection Molding, Hanser, New York, 1989.
- Manjunath, A., Gowda, B.H.L., and Natarajan, R., Studies on the Mixing of Two Non-axial Plane Jets in a Confined Passage: Mean Flow Characteristics, *Experiments in Fluids*, **11**, 17-24, 1991.
- Manjunath, A., Gowda, B.H.L., and Natarajan, R., Studies on the Mixing of Two Non-axial Plane Jets in a Confined Passage: Turbulence Characteristics, *Experiments in Fluids*, **13**, 147-154, 1992.
- Marko, K.A., and Rimai, L., Video Recording and Quantitative Analysis of Seed Particle Track Images in Unsteady Flows, *Applied Optics*, **24**, 21, 3666-3672, 1985.

Miau, J.J., Sun, D.J., and Yao, L.S., Streamwise vortices generated by impinging flows in a confined duct, Technical Note, *Experiments in Fluids*, **7**, 497-500, 1989.

Michalke, A., On Spatially Growing Disturbances in an Inviscid Shear Layer, *Journal of Fluid Mechanics*, **23**, 521-544, 1965.

Muller, G. and Sochtig, W., Polyurethanes World Congress, 7-13, 1987.

Murai, K., Kawashima, Y., Nakanishi, S., and Taga, M., Self Oscillation Phenomena of Turbulent Jets in a Channel, *The Canadian Journal of Chemical Engineering*, **67**, 906 - 911, 1989.

Naudascher, E., From Flow Instability to Flow-Induced Excitation, *ASCE Proceedings Journal of the Hydraulics Division*, **93**, 15-40, 1967.

Nielsen, P.V., Restivo, A., and Whitelaw, J.H., The Velocity Characteristics of Ventilated Rooms, *Transactions of the ASME Journal of Fluids Engineering*, **100**, 291-298, 1978.

Nosseir, N.S., and Behar, S., Characteristics of Jet Impingement in a Side-Dump Combustor, *AIAA Journal*, **24**, 11, 1752-1757, 1986.

Nosseir, N., Peled, U., and Hildebrand, G., Pressure Field Generated by Jet on Jet Impingement, *AIAA Journal*, **25**, 10, 1312-1317, 1987.

Oertel, G., Ed., Polyurethane Handbook, Chapter 4, Hanser, Munich, 1985.

Ogawa, N., and Maki, H., Studies on Opposed Turbulent Jets, *Bulletin of JSME*, **29**, 255, 2872-2877, 1986.

Ogawa, N., Maki, H., and Hijikata, K., Studies on Opposed Turbulent Jets (Impact Position and Turbulent Component in Jet Centre), *JSME International Journal, Series II*, **35**, 2, 205-211, 1992.

Patankar, S.V., Numerical Heat Transfer and Fluid Flow, Hemisphere, New York, 1980.

Powell, A., Aerodynamic Noise and the Plane Boundary, *Journal of the Acoustical Society of America*, **32**, 982-990, 1960.

Racca, R.G., and Dewey, J.M., A Method for Automatic Particle Tracking in a Three-dimensional Flow Field, *Experiments in Fluids*, **6**, 25-32, 1988.

Rockwell, D., and Naudascher, E., Review - Self-Sustaining Oscillations of Flow Past Cavities, *Transactions of the ASME Journal of Fluids Engineering*, **100**, 152-165, June 1978.

Rockwell, D., and Naudascher, E., Self-Sustained Oscillations of Impinging Free Shear Layers, *Annual Review of Fluid Mechanics*, **11**, 67-94, 1979.

Rodi, W., Turbulence Models and their Applications in Hydraulics, IAHR State of the Art Paper, 1984.

Sandell, D.J., Macosko, C.W., and Ranz, W.E., Visualization Technique for Studying Impingement Mixing at Representative Reynolds Numbers, *Polymer Process Engineering*, **3**, (1&2), 57-70, 1985.

Schadow, K.C., and Gutmark, E., Combustion Instability Related to Vortex Shedding in Dump Combustors and Their Passive Control, *Progress in Energy and Combustion Science*, **18**, 117-132, 1992.

Schlichting, H., Boundary Layer Theory, McGraw-Hill, New York, p 218f, 1968.

Schwarz, W.H., The Radial Free Jet, *Chemical Engineering Science*, **18**, 779-786, 1963.

Sebastian, D.H., and Boukobbal, S., Mixhead Parameters Governing Impingement Mixing Effectiveness for Polyurethane Reactive Injection Molding Processes, *Polymer Process Engineering*, **4**, 53-70, 1986.

Shah, R.K., and London, A.L., Laminar Flow Forced Convection in Ducts, Academic Press, London, 1978.

Shapira, M., and Degani, D., Stability and Existence of Multiple Solutions for Viscous Flow in Suddenly Enlarged Channels, *Computers and Fluids*, **18**, 239-258, 1990.

Sinha, S.K., and Kuhlman, P.S., Investigating the use of Stereoscopic Particle Streak Velocimetry for Estimating the Three-dimensional Vorticity Fields, *Experiments in Fluids*, **12**, 377-384, 1992.

Stevenson, W.H., Thompson, H.D., and Gould, R.D., Laser Velocimeter Measurements and Analysis in Turbulent Flows with Combustion, Pt.II, AFWAL-TR-82-2076, July 1983.

Stuhmiller, J.H., Development and Validation of a Two-Variable Turbulence Model, Report SAI-74-509-LJ, Science Applications Inc., Palo Alto, California, 1974.

- Stull, F.D., Craig, R.R., Streby, G.D., and Vanka, S.P., Investigation of a Dual Inlet Side Dump Combustor Using Liquid Fuel Injection, *Journal of Propulsion*, **1**, 1, 83-88, 1985.
- Swamy, N.V.C., and Bandyopadhyay, P., Mean and Turbulence Characteristics of Three-dimensional Wall Jets, *Journal of Fluid Mechanics*, **71**, 541-562, 1975.
- Tanaka, N., Moriya, S., Katano, N., Maruoka, H., Wada, A., and Fujimoto, K., Thermal-hydraulic Characteristics in LMFBR Hot Plenum, Civil Engineering Laboratory, Central Research Institute of Electric Power Industry (CRIEPI), Chiba, Japan, 1983.
- Troutt, T.R., Bhattacharjee, S., and Scheelke, B., Modification of Vortex Interactions in a Reattaching Separated Flow, *Bulletin of the American Physical Society*, **29**, 9, 1541, 1984.
- Tucker, C.L., and Suh, N.P., Mixing for Reaction Injection Molding I. Impingement Mixing of Liquids, *Polymer Engineering and Science*, **20**, 13, 875-886, 1980.
- Ushijima, S., Kato, M., Fujimoto, K., and Moriya, S., Numerical Analyses of Two Dimensional Circulation Flows with a $k - \epsilon$ Model and Two Reynolds Stress Models, Central Research Institute of Electric Power Industry (CRIEPI) Report E385002, 1987.
- Utami, T., and Ueno, T., Experimental Study on the Coherent Structure of Turbulent Open-Channel Flow Using Visualization and Picture-Processing, *Journal of Fluid Mechanics*, **174**, 399-440, 1987.
- Walker, D.A., Measurements on an Axisymmetric Jet in a Slow Coflowing Stream, Ph.D. dissertation, The John Hopkins University, 1985.
- Walter, J.A., and Chen, C.J., Development of a Quantitative Velocity Imaging System and its Application to Offset Channel Flow, *IIHR Report No. 338*, Department of Mechanical Engineering, Iowa Institute of Hydraulic Research, University of Iowa, Iowa City, Iowa, April, 1990.
- Walter, J.A., and Chen, C.J., Visualization and Analysis of Flow in an Offset Channel, *Transactions of the ASME Journal of Heat Transfer*, **114**, 819-826, 1992.
- Westerweel, J., Efficient Detection of Spurious Vectors in Particle Image Velocimetry Data, *Experiments in Fluids*, **16**, 236-247, 1994.
- White, F.M., Heat Transfer, Addison-Wesley, Don Mills, Ontario, 1984.

Willert, C.E., and Gharib, M., Digital Particle Image Velocimetry, *Experiments in Fluids*, **10**, 181-193, 1991.

Willert, C.E., and Gharib, M., Three-dimensional Particle Imaging with a Single Camera, *Experiments in Fluids*, **12**, 353-358, 1992.

Winter, M., Lam, J.K., and Long, M.B., Techniques for High-Speed Digital Imaging of Gas Concentrations in Turbulent Flows, *Experiments in Fluids*, **5**, 177-183, 1987.

Wolfshtein, M., Some Solutions of the Plane Turbulent Impinging Jet, *Transactions of the ASME Journal of Basic Engineering*, **92**, 915-922, 1970.

Wood, P., Hrymak, A., Yeo, R., Johnson, D., and Tyagi, A., Experimental and Computational Studies of the Fluid Mechanics in an Opposed Jet Mixing Head, *Physics of Fluids A*, **3**, 1362-1368, 1991.

Yeo, R.W., A Numerical Study of Jet-To-Jet Impingement in a Mixing Head, Ph.D. Thesis, McMaster University, Hamilton, Canada, 1993.

Yu, J., Wu, M., Dai, G., and Zhang, L., An Investigation into Impingement Jets in Cylindrical Chamber, *Journal of Hydrodynamics*, **3**, 1, 90-94, 1991.

Appendix A

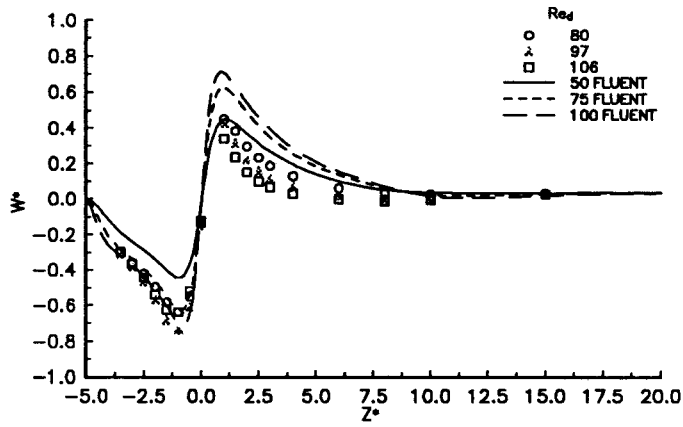


Figure A5.2.1 W^* versus Z^* Model 3, $d = 2 \text{ mm}$, $\mu = 50 \text{ cP}$

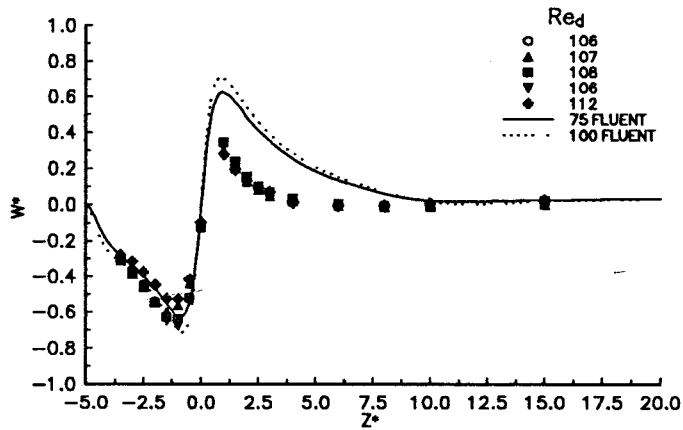


Figure A5.2.2 W^* versus Z^* Model 3, $d = 2 \text{ mm}$, $\mu = 50 \text{ cP}$

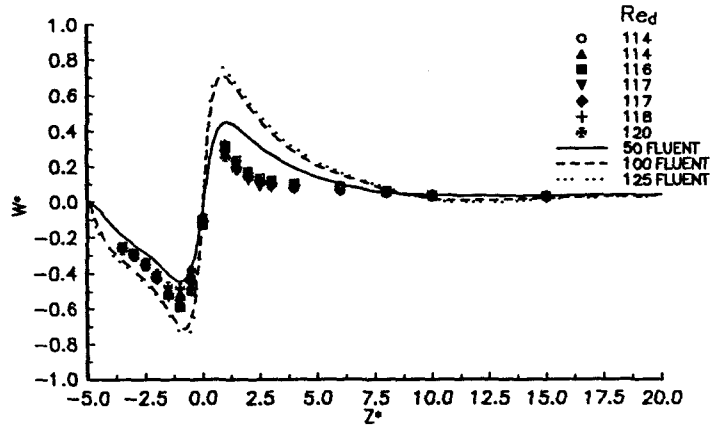


Figure A5.2.3 W^* versus Z^* Model 3, $d = 2$ mm, $\mu = 50$ cP

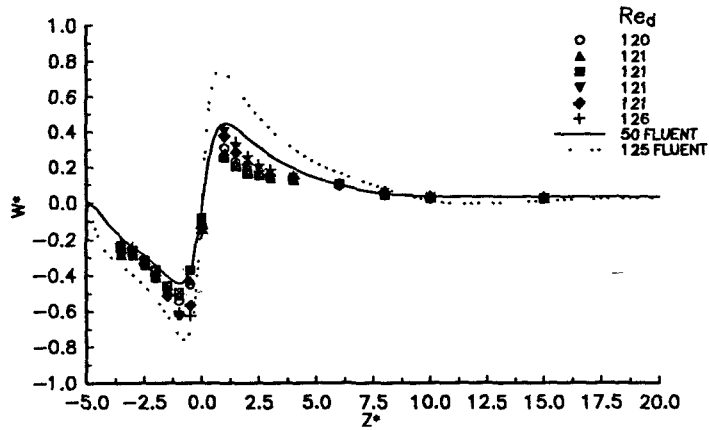


Figure A5.2.4 W^* versus Z^* Model 3, $d = 2$ mm, $\mu = 50$ cP

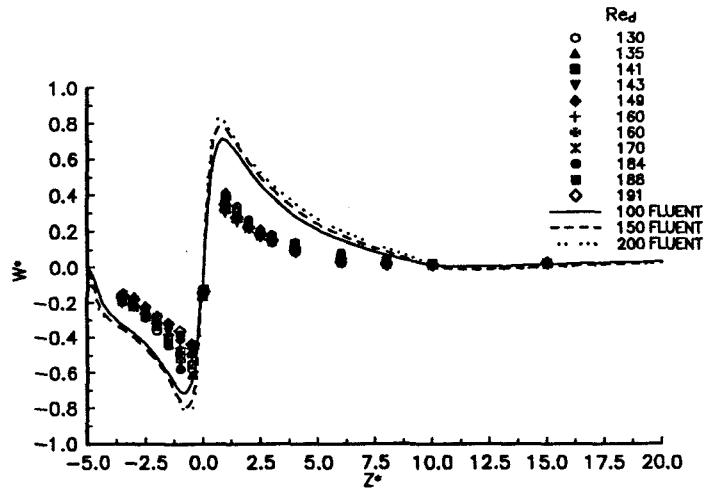


Figure A5.2.5 W^* versus Z^* Model 3, $d = 2$ mm, $\mu = 50$ cP

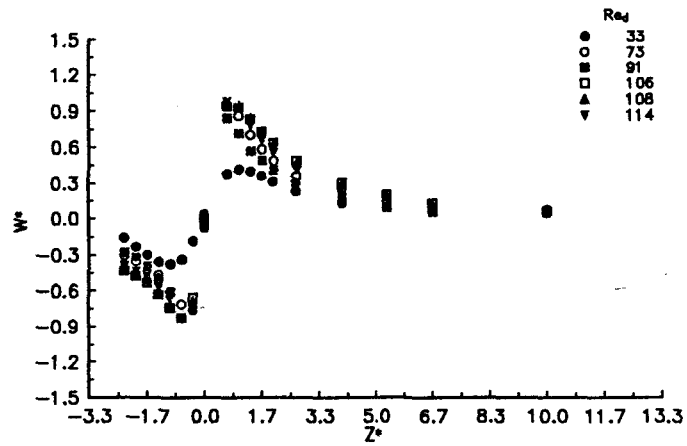


Figure A5.2.6 W^* versus Z^* Model 3, $d = 3$ mm, $\mu = 50$ cP

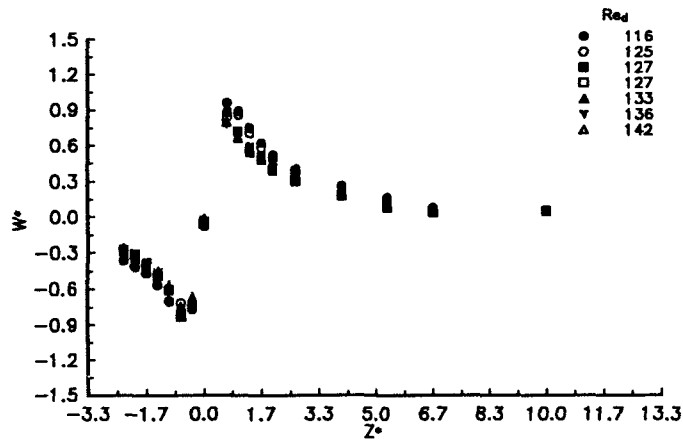


Figure A5.2.7 W^* versus Z^* Model 3, $d = 3$ mm, $\mu = 50$ cP

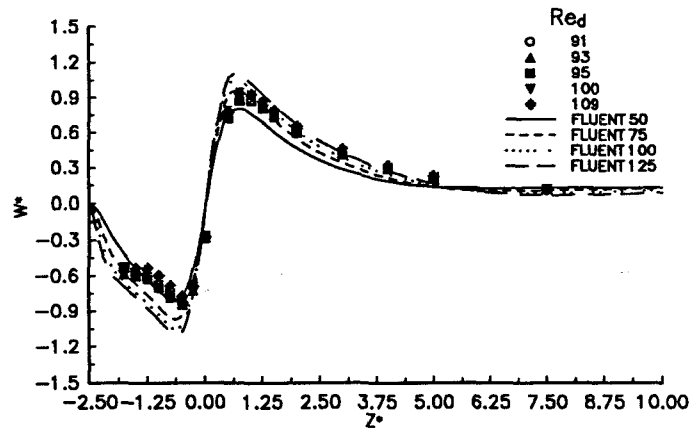


Figure A5.2.8 W^* versus Z^* Model 3, $d = 4$ mm, $\mu = 50$ cP

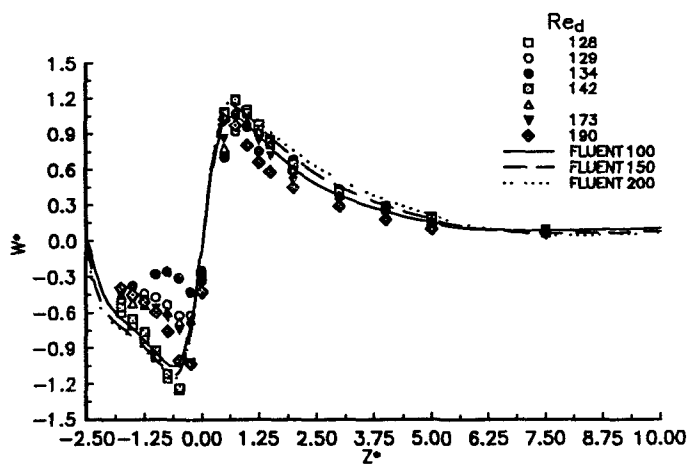


Figure A5.2.9 W^* versus Z^* Model 3, $d = 4$ mm, $\mu = 50$ cP

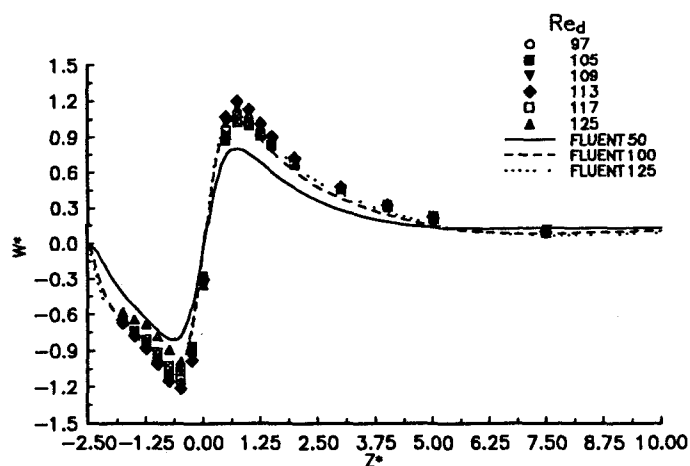


Figure A5.2.10 W^* versus Z^* Model 3, $d = 4$ mm, $\mu = 50$ cP

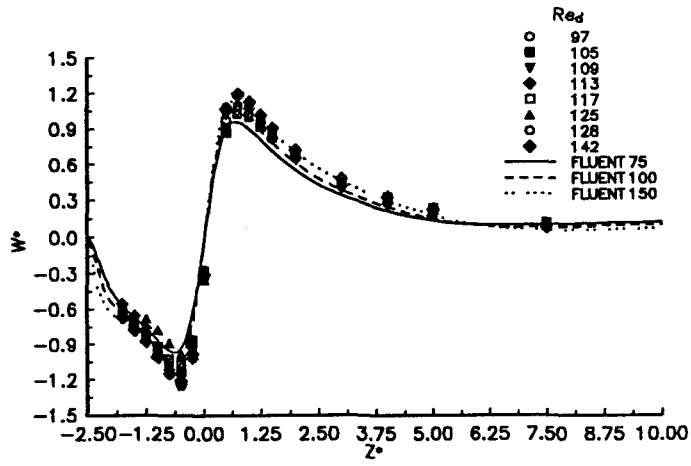


Figure A5.2.11 W^* versus Z^* Model 3, $d = 4$ mm, $\mu = 50$ cP

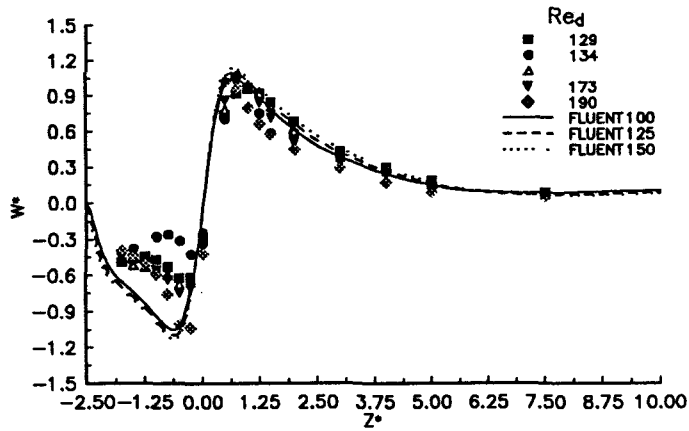


Figure A5.2.12 W^* versus Z^* Model 3, $d = 4$ mm, $\mu = 50$ cP

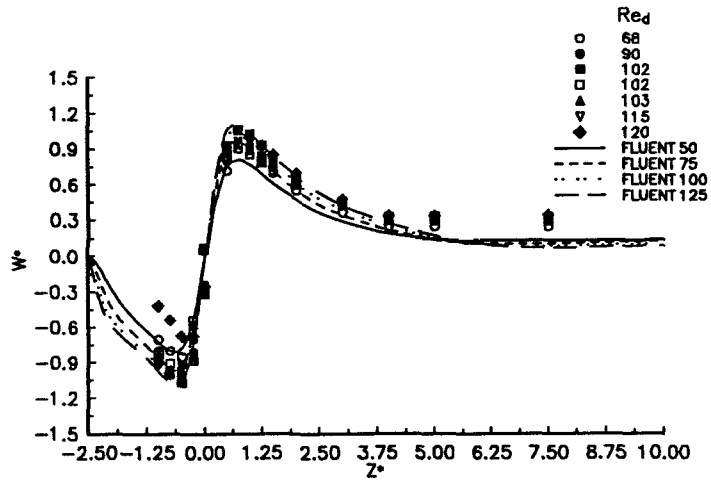


Figure A5.2.13 W^* versus Z^* Model 3, $d = 4$ mm, $\mu = 25$ cP

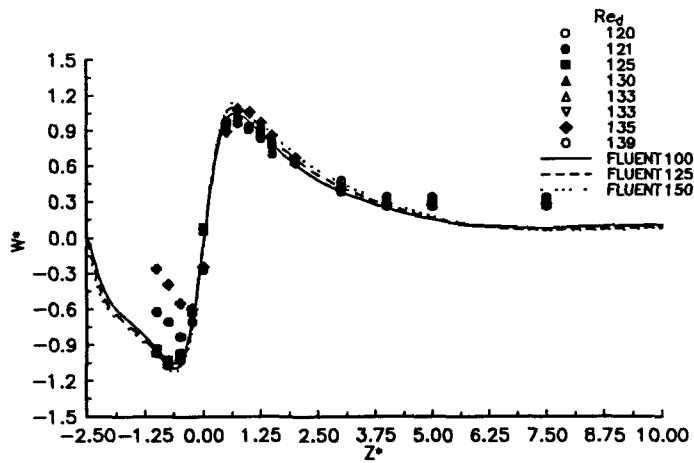


Figure A5.2.14 W^* versus Z^* Model 3, $d = 4$ mm, $\mu = 25$ cP

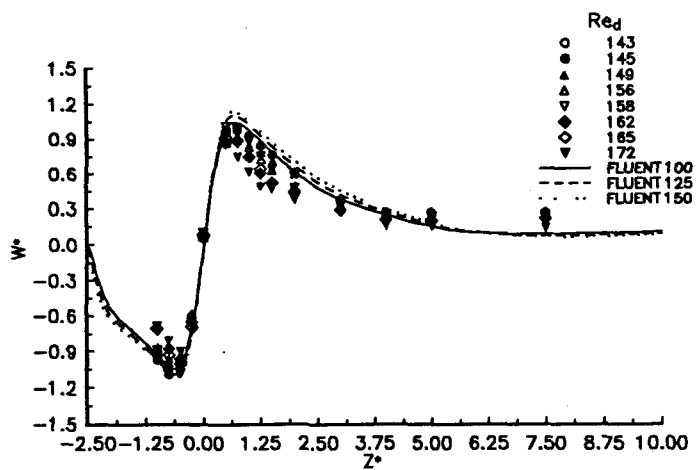


Figure A5.2.15 W^* versus Z^* Model 3, $d = 4$ mm, $\mu = 25$ cP

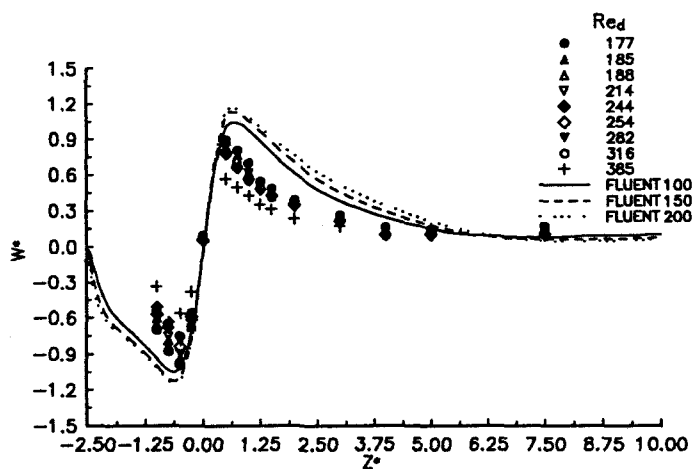


Figure A5.2.16 W^* versus Z^* Model 3, $d = 4$ mm, $\mu = 25$ cP

Appendix B

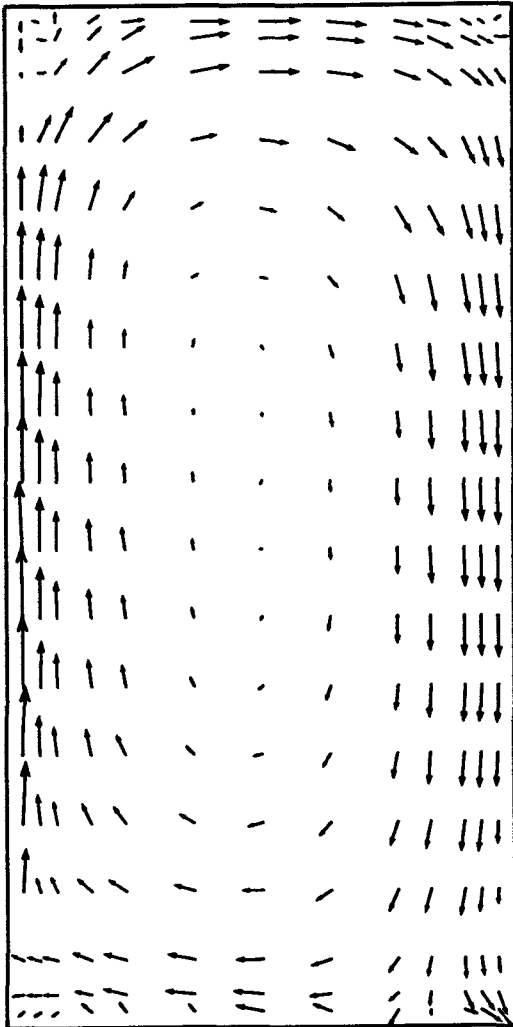


Figure B7.1 Velocity Vectors LDA Data $Re_b = 1117$
Dimensionless velocity vector $U/U_{avg} 0.5$

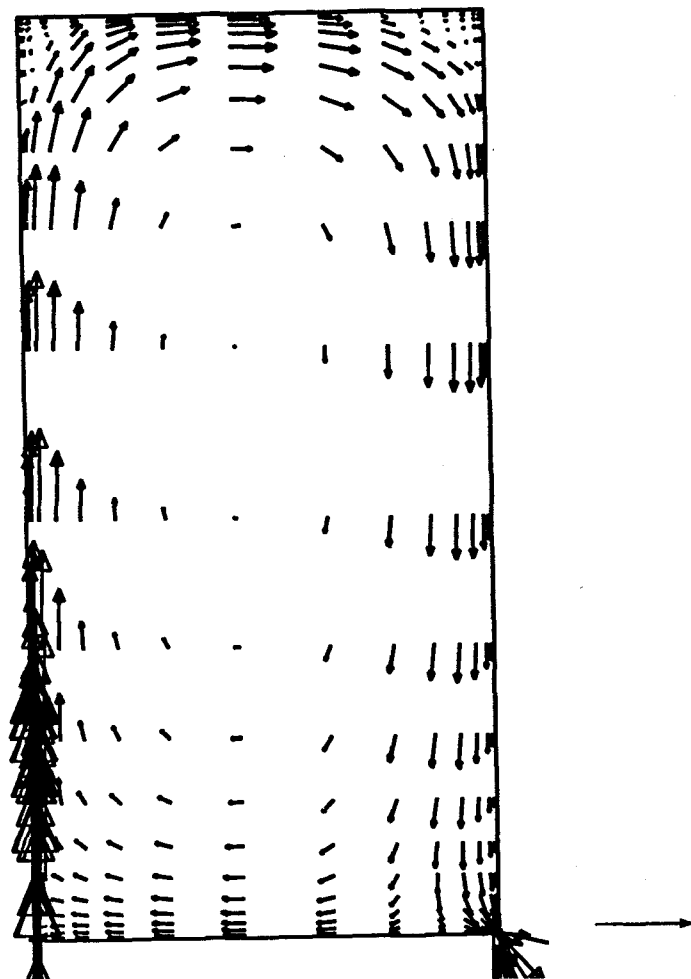


Figure B7.2 Velocity Vectors 44x40 2D $k - \epsilon$ Simulation $Re_b = 1117$
Dimensionless velocity vector U/U_{avg} 0.5 Grid lines removed for clarity

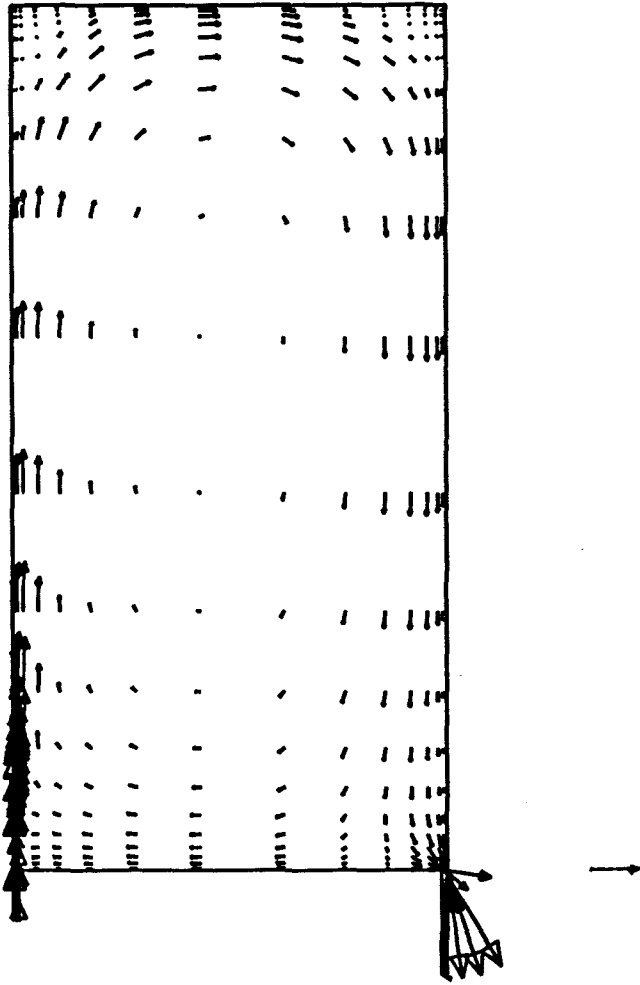


Figure B7.3 Velocity Vectors 86x78 2D k - ϵ Simulation $Re_b = 1117$
Dimensionless velocity vector U/U_{avg} 0.5 Grid lines removed for clarity

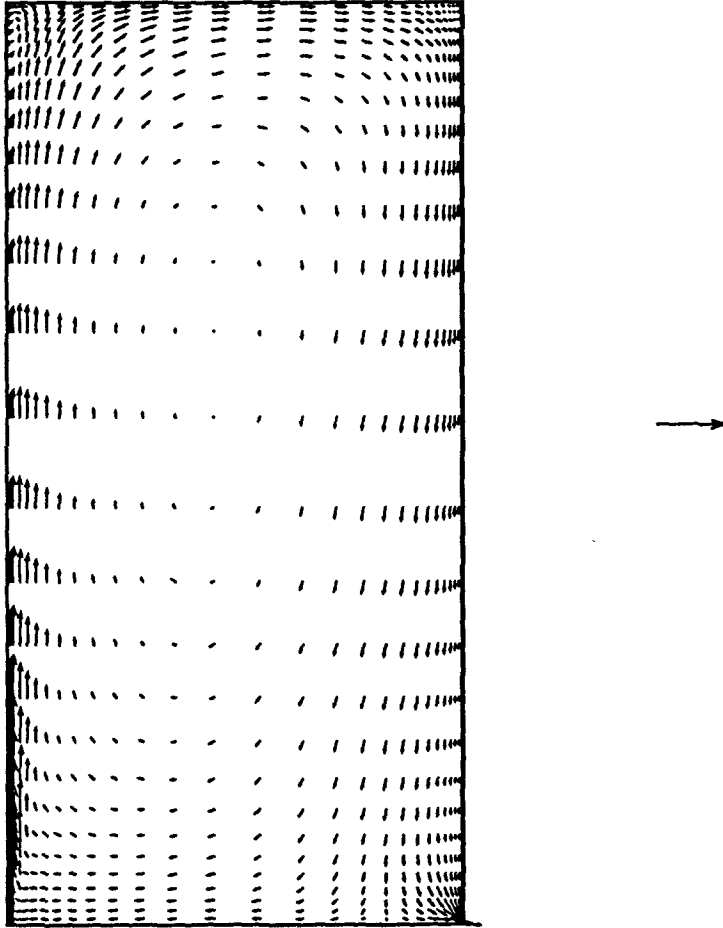


Figure B7.4 Velocity Vectors 30x40x15 3D k - ϵ Simulation $Re_b = 1117$
Dimensionless velocity vector $U/U_{avg} 1.0$

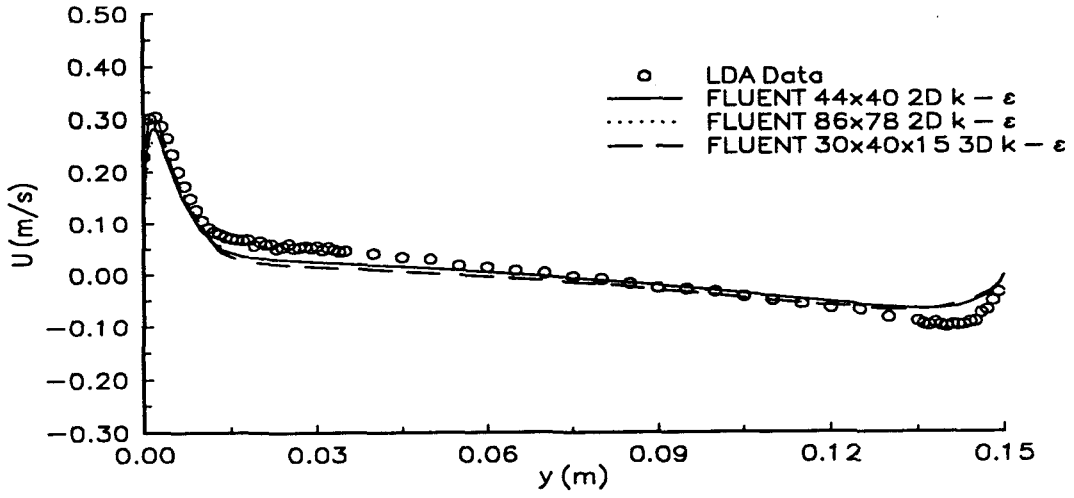


Figure B7.5 U versus y at x = .06 m $Re_b = 1117$

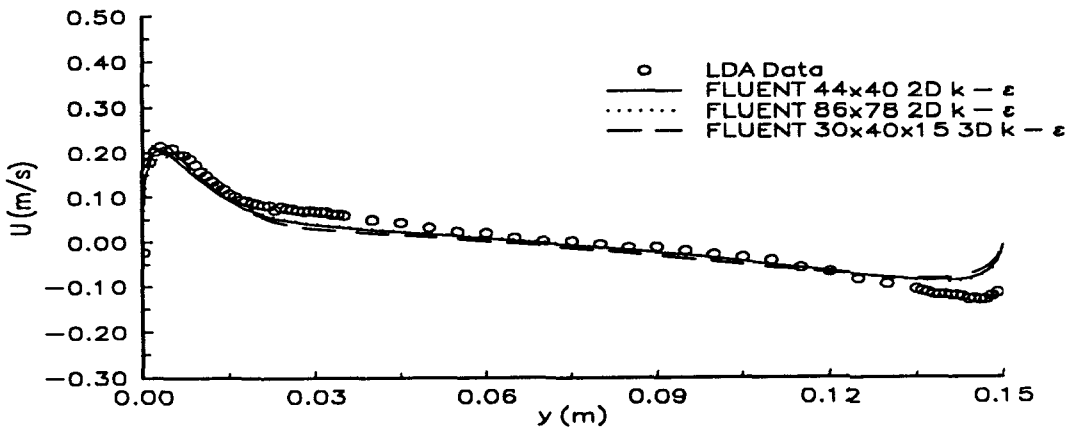


Figure B7.6 U versus y at x = .12 m $Re_b = 1117$